Three-dimensional Finite Element Simulation of Magnetotelluric Fields on Unstructured Grids

On the Efficient Formulation of the Boundary Value Problem

Von der Fakultät für Geowissenschaften, Geotechnik und Bergbau
der Technischen Universität Bergakademie Freiberg
genehmigte

DISSERTATION

zur Erlangung des akademischen Grades
doctor rerum naturalium
Dr. rer. nat.
vorgelegt

von Dipl.-Geophysikerin Antje Franke-Börner
geboren am 04.12.1978 in Karl-Marx-Stadt (heute Chemnitz)

Gutachter: Prof. Dr. rer. nat. habil. Klaus Spitzer, Freiberg
Prof. Dr. Philip E. Wannamaker, Ph.D., Salt Lake City, Utah, USA

Tag der Verleihung: 26.04.2013

To my mum and Clara

Contents

1 Introduction

Since the early 1950s, the magnetotelluric method has been used to investigate the deep interior of the earth. The registration of natural electromagnetic fields provides information about the subsurface distribution of the electrical conductivity. In general, to interpret magnetotelluric data, two- and three-dimensional numerical simulation and inversion is necessary. Numerical methods including the finite difference approach (e.g. Mackie et al., 1993), the integral equation technique (e.g. P. Wannamaker et al., 1984) and the finite element method (e.g. Mogi, 1996) have been developed since the 1970s. More recent advances in software development have focused on the efficiency, flexibility, and accuracy of the simulation algorithms (Siripunvaraporn et al., 2002; Key & Weiss, 2006; Nam et al., 2007; Farquharson & Miensopust, 2011).

This thesis aims at determining a most efficient three-dimensional boundary value problem among five formulations in terms of the electric field, the magnetic field, the magnetic vector potential and the electric scalar potential, the magnetic vector potential only, and the anomalous magnetic vector potential by means of convergence studies. Moreover, the convergence studies are examined regarding their capability to yield global and local error estimates for the numerical solution.

To solve the boundary value problems, a finite element approach on unstructured grids is applied which is considered to be very flexible in terms of smart mesh design and the accurate approximation of complicated-structured model geometries including surface topography and bathymetry (Franke et al., 2007). Since the solution of the three-dimensional boundary value problems requires much computational effort, the moderate-sized two-dimensional problems in terms of the electric and the magnetic field are also considered to gain valuable experience in performing convergence studies. To evaluate their efficiency, global and local convergence studies are executed for the two-dimensional models of a homogeneous and a layered halfspace as well as the three-dimensional COMMEMI 3-D-2 model.

Finally, convergence studies are applied to the finite element solution of the magnetotelluric boundary value problem in terms of the anomalous magnetic vector potential for a close-to-reality model of Stromboli area incorporating surface topography and sea floor bathymetry. They yield local error estimates for the off-diagonal elements of the impedance tensor even without knowing the exact solution.

2 Fundamental Physics of the Magnetotelluric Method Using Complete Maxwell's Equations

The magnetotelluric method or simply magnetotellurics (MT) that was developed by Tikhonov (1950) and Cagniard (1953) is one of the most capable geophysical tools to investigate the deep earth's interior nowadays. In MT, variations of the natural electromagnetic fields are measured for a typical frequency range of 10^{-4} to $10^{4}\,\mathrm{Hz}$. These data enable the reconstruction of the distribution of the electrical conductivity in the earth from some $100\,\mathrm{m}$ up to $100\,\mathrm{km}$ depth. Beside research on the earth's structure, applications of MT include hydrocarbon, mineral, geothermal, and groundwater exploration.

Interpretation of MT data involves transformation of time-series into frequency domain. In general, only numerical simulation and inversion of the frequency-domain data allow for two- or three-dimensional mapping of the subsurface conductivity structure. Therefore, the development and improvement of efficient and accurate numerical algorithms to solve the governing Maxwell's equations are in the focus of ongoing research.

2.1 Governing Equations

The behaviour of electric and magnetic fields is governed by Maxwell's equations. They can be written in differential form as

$$\nabla\times\mathbf{H} = \mathbf{j} = \mathbf{j}_c + \frac{\partial\mathbf{D}}{\partial t}, \tag{2.1a}$$

$$\nabla\times\mathbf{E} = -\frac{\partial\mathbf{B}}{\partial t}, \tag{2.1b}$$

$$\nabla\cdot\mathbf{D} = \rho, \tag{2.1c}$$

$$\nabla\cdot\mathbf{B} = 0, \tag{2.1d}$$

with

$\mathbf{E}$ ... electric field intensity (Vm^{-1}),
$\mathbf{H}$ ... magnetic field intensity (Am^{-1}),
$\mathbf{D}$ ... dielectric displacement (Cm^{-2}),
$\mathbf{B}$ ... magnetic flux density (T),
$\mathbf{j}$ ... electric current density (Am^{-2}) incorporating conduction currents $\mathbf{j}_c$ and diplacement currents $\frac{\partial\mathbf{D}}{\partial t}$,
ρ ... free charge density (Cm^{-3}).

$\frac{\partial}{\partial t}$ denotes the partial derivative with respect to time. Assuming a harmonic time dependency $e^{i\omega t}$ for the electric and the magnetic fields, it can be replaced by the factor $i\omega$ in the frequency domain.

In linear, homogeneous, and isotropic media, the following constitutive equations apply

$$\mathbf{B} = \mu\mathbf{H} = \mu_0\mu_r\mathbf{H} \tag{2.2}$$

and

$$\mathbf{D} = \varepsilon\mathbf{E} = \varepsilon_0\varepsilon_r\mathbf{E} \tag{2.3}$$

where

$\mu = \mu_0\mu_r$	...	magnetic permeability,
$\mu_0 = 4\,\pi \cdot 10^{-7}\mathrm{VsA^{-1}m^{-1}}$	...	magnetic field constant,
μ_r	...	relative magnetic permeability,
$\varepsilon = \varepsilon_0\varepsilon_r$	...	dielectric permittivity,
$\varepsilon_0 = 8.85{\cdot}10^{-12}\,\mathrm{AsV^{-1}m^{-1}}$	...	electric field constant,
ε_r	...	relative dielectric permittivity,

as well as a generalisation of Ohm's law incorporating conduction and displacement currents for alternating electric fields

$$\mathbf{j} = \mathbf{j}_c + \frac{\partial\mathbf{D}}{\partial t} = (\sigma + i\omega\varepsilon)\cdot\mathbf{E} \tag{2.4}$$

with electrical conductivity σ ($\mathrm{Sm^{-1}}$) and dielectric permittivity ε ($\mathrm{AsV^{-1}m^{-1}}$). Since

$$\nabla\cdot\nabla\times\mathbf{H} = \nabla\cdot\mathbf{j} = \nabla\cdot(\mathbf{j}_c + \frac{\partial\mathbf{D}}{\partial t}) = 0, \tag{2.5}$$

polarisation effects due to displacement currents $\frac{\partial\mathbf{D}}{\partial t}$ are balanced by conduction currents in conductive media:

$$\nabla\cdot\mathbf{j}_c = -\nabla\cdot\frac{\partial\mathbf{D}}{\partial t} = -\frac{\partial\rho}{\partial t}. \tag{2.6}$$

At interfaces between subdomains 1 and 2 representing jumps in the electromagnetic parameters, the following conditions of continuity hold

- The tangential components of the electric and magnetic fields are continuous:
  $\mathbf{n}_1\times\mathbf{E}_1 - \mathbf{n}_2\times\mathbf{E}_2 = 0$ and $\mathbf{n}_1\times\mathbf{H}_1 - \mathbf{n}_2\times\mathbf{H}_2 = 0$.
- The normal component of the dielectric displacement jumps if an electric surface charge δ occurs:
  $\mathbf{n}_1\cdot\mathbf{D}_1 - \mathbf{n}_2\cdot\mathbf{D}_2 = \varepsilon_1(\mathbf{n}_1\cdot\mathbf{E}_1) - \varepsilon_2(\mathbf{n}_2\cdot\mathbf{E}_2) = \delta$.
- The normal component of the electric current density is continuous:
  $\mathbf{n}_1\cdot\mathbf{j}_1 - \mathbf{n}_2\cdot\mathbf{j}_2 = \sigma_1(\mathbf{n}_1\cdot\mathbf{E}_1) - \sigma_2(\mathbf{n}_1\cdot\mathbf{E}_2) = 0$.
- Since there are no magnetic monopoles, the normal component of the magnetic flux density is continuous:
  $\mathbf{n}_1\cdot\mathbf{B}_1 - \mathbf{n}_2\cdot\mathbf{B}_2 = \mu_1(\mathbf{n}_1\cdot\mathbf{H}_1) - \mu_2(\mathbf{n}_2\cdot\mathbf{H}_2) = 0$.

$\mathbf{n}_1$ and $\mathbf{n}_2$ denote outward unit normal vectors on the interface between subdomains 1 and 2.

Applying $\nabla\times$ on eq. (2.1a), inserting the constitutive relations and Ohm's law (eqs (2.2) - (2.4)) yield

$$\nabla \times (\sigma + i\omega\varepsilon)^{-1}\nabla \times \mathbf{H} = \nabla \times \mathbf{E}. \tag{2.7}$$

Substituting $\nabla \times \mathbf{E}$ by eq. (2.1b), we obtain the equation of induction for the magnetic field

$$\nabla \times (\sigma + i\omega\varepsilon)^{-1}\nabla \times \mathbf{H} + i\omega\mu\mathbf{H} = 0. \tag{2.8}$$

The equation of induction for the electric field

$$\nabla \times \mu^{-1}\nabla \times \mathbf{E} + (i\omega\sigma - \omega^2\varepsilon)\mathbf{E} = 0 \tag{2.9}$$

can be derived in the same way starting from eq. (2.1b) and replacing $\nabla \times \mathbf{H}$ by eq. (2.1a).

From the horizontal electric and magnetic field components, the MT impedance tensor $\mathbf{Z}$

$$\begin{pmatrix} E_x \\ E_y \end{pmatrix} = \mathbf{Z}\begin{pmatrix} H_x \\ H_y \end{pmatrix} \quad \text{with} \quad \mathbf{Z} = \begin{pmatrix} Z_{xx} & Z_{xy} \\ Z_{yx} & Z_{yy} \end{pmatrix} \tag{2.10}$$

the apparent resistivity

$$\rho_{ij} = \frac{1}{\omega\mu}|Z_{ij}|^2, \quad i,j = x,y, \tag{2.11}$$

the phase

$$\phi_{ij} = \arg(Z_{ij}), \quad i,j = x,y, \tag{2.12}$$

and the magnetic transfer functions called tipper

$$H_z = \mathbf{T}\begin{pmatrix} H_x \\ H_y \end{pmatrix} \quad \text{with} \quad \mathbf{T} = \begin{pmatrix} T_x & T_y \end{pmatrix} \tag{2.13}$$

can be derived. Generally, the equation of induction for the electric or the magnetic field is solved numerically and the remaining field components are computed by numerical differentiation or integration in a subsequent procedure referred to as post-processing.

In the following subsections, the special cases of electromagnetic induction in one-dimensional (1-D) and two-dimensional (2-D) anomalous structures are discussed.

2.1.1 Electromagnetic Induction in 1-D Conductivity Structures

Considering a 1-D structure, i.e. a homogeneous or layered halfspace with $\sigma = \sigma(z)$, the electric and magnetic field values only depend on the z-direction of the coordinate system

$$-\frac{\partial}{\partial z}\left((\sigma + i\omega\varepsilon)^{-1}\frac{\partial \mathbf{H}}{\partial z}\right) + i\omega\mu\mathbf{H} = 0 \quad \text{and} \tag{2.14}$$

$$-\frac{\partial}{\partial z}\left(\mu^{-1}\frac{\partial \mathbf{E}}{\partial z}\right) + (i\omega\sigma - \omega^2\varepsilon)\mathbf{E} = 0. \tag{2.15}$$

Eqs (2.14) and (2.15) can be solved analytically. For constant parameters σ, μ, and ε, the analytical solution is

$$\mathbf{F} = \mathbf{F}_0 e^{-ik_z z} \quad \text{with} \quad \mathbf{F} = \mathbf{H}, \mathbf{E}, \quad \mathbf{F}_0 = \mathbf{H}_0, \mathbf{E}_0, \quad \text{and} \quad k_z^2 = \omega^2\mu\varepsilon - i\omega\mu\sigma, \tag{2.16}$$

where $\mathbf{H}_0$ and $\mathbf{E}_0$ are the field values at the earth's surface ($z = 0$) and k_z is the wave propagation constant or complex wave number for z-direction. To determine $k_z = \pm\sqrt{(k_z)^2}$, we need to ensure that the electric and magnetic field amplitudes $|\mathbf{F}| = |\mathbf{F}_0|\;|e^{-ik_z z}|$ vanish at infinity, i.e. for $z \to \infty$. Taking into account the complex wave number $k_z = k_z^R + ik_z^I$, the field amplitude is determined by the imaginary part k_z^I of k_z: $|\mathbf{F}| = |\mathbf{F}_0|\;|e^{-ik_z z}| = |\mathbf{F}_0| e^{k_z^I z}$. Using

$$k_z^2 \;=\; \omega^2\mu\varepsilon(1 - i\frac{\sigma}{\omega\varepsilon}) = (k_z^R + ik_z^I)^2 = (k_z^R)^2 + 2ik_z^I k_z^R - (k_z^I)^2 \tag{2.17}$$

and comparing real and imaginary parts yield a system of equations for k_z^R and k_z^I:

$$k_z^I = -\frac{1}{2}\frac{\omega\mu\sigma}{k_z^R} \tag{2.18}$$

$$(k_z^R)^2 - (k_z^I)^2 = \omega^2\mu\varepsilon. \tag{2.19}$$

Substituting eq. (2.18) into (2.19) and multiplying by $(k_z^R)^2$, we obtain a quadratic equation for $(k_z^R)^2$

$$(k_z^R)^4 - \omega^2\mu\varepsilon(k_z^R)^2 - \frac{1}{4}\omega^2\mu^2\sigma^2 = 0 \tag{2.20}$$

whose solution is

$$(k_z^R)^2 = \frac{\omega^2\mu\varepsilon}{2} \pm \sqrt{\left(\frac{\omega^2\mu\varepsilon}{2}\right)^2 + \left(\frac{\omega\mu\sigma}{2}\right)^2}. \tag{2.21}$$

Since k_z^R is required not to be 0 for $\omega \to \infty$, we choose

$$(k_z^R)^2 = \frac{\omega^2\mu\varepsilon}{2}\left(1 + \sqrt{1 + \left(\frac{\sigma}{\omega\varepsilon}\right)^2}\right) \tag{2.22}$$

and

$$k_z^R = \pm\sqrt{\frac{\omega^2\mu\varepsilon}{2}\left(\sqrt{1 + \left(\frac{\sigma}{\omega\varepsilon}\right)^2} + 1\right)}. \tag{2.23}$$

Applying eq. (2.19), we get

$$k_z^I = \pm\sqrt{\frac{\omega^2\mu\varepsilon}{2}\left(\sqrt{1 + \left(\frac{\sigma}{\omega\varepsilon}\right)^2} - 1\right)}. \tag{2.24}$$

Taking into account that $|\mathbf{F}| \to 0$ for $z \to \infty$ and $k_z = k_z^R = \frac{\omega}{c} = \frac{\omega}{\sqrt{\mu\varepsilon}}$ for $\omega \to \infty$ (c ... speed of electromagnetic waves), we finally arrive at

$$k_z = \omega\sqrt{\frac{\mu\varepsilon}{2}}\left(\sqrt{\sqrt{1+\left(\frac{\sigma}{\omega\varepsilon}\right)^2}+1} - i\sqrt{\sqrt{1+\left(\frac{\sigma}{\omega\varepsilon}\right)^2}-1}\right). \tag{2.25}$$

The electromagnetic skin depth δ which is a measure for the depth of penetration of the electromagnetic fields is defined as the depth where the amplitude of the surface field $|\mathbf{F}_0|$ has been attenuated to $e^{-1}|\mathbf{F}_0|$ (e ... Euler's number). It can be determined as

$$\delta = \left[\frac{\omega^2\mu\varepsilon}{2}\left(\sqrt{1+\left(\frac{\sigma}{\omega\varepsilon}\right)^2}-1\right)\right]^{-1/2}. \tag{2.26}$$

The quasistatic approximation

$$1 \ll \frac{\sigma}{\omega\varepsilon} \tag{2.27}$$

for low frequencies (f <10^5 Hz) yields

$$k_z = \sqrt{-i\omega\mu\sigma} \quad \text{and} \quad \delta = \sqrt{\frac{2}{\omega\mu\sigma}} \tag{2.28}$$

that can be estimated by

$$\delta[\mathrm{m}] \approx 503\sqrt{\frac{T[\mathrm{s}]}{\sigma[\mathrm{Sm}^{-1}]}} \tag{2.29}$$

for the period $T = 1/f$ given in s and the conductivity given in Sm^{-1}.

A more general analytic solution of eqs (2.14) and (2.15) for a layered halfspace as depicted in Fig. 2.1 was introduced by Wait (1953). The layered halfspace is composed of $n = 1...N$ layers. The parameters σ_n, μ_n, ε_n and the thickness d_n are assigned to layer n above its lower interface at depth z_n.

Two orthogonal horizontal components of the electric and the magnetic field, e.g. the x-component of the electric field E_x^n and the y-component of the magnetic field H_y^n, in layer n can be described by

$$E_x^n(z) = a_n e^{-ik_n(z-z_n)} + b_n e^{ik_n(z-z_n)} \tag{2.30}$$

and

$$H_y^n(z) = -\frac{1}{i\omega\mu}\frac{\partial E_x^n}{\partial z} = \frac{k_n}{\omega\mu}(a_n e^{-ik_n(z-z_n)} - b_n e^{ik_n(z-z_n)}) \tag{2.31}$$

for $z_n \leq z \leq z_{n-1}$. They are composed of a downward ($e^{-ik_n(z-z_n)}$) and an upward travelling, i.e. reflected ($e^{ik_n(z-z_n)}$) wave. The Nth layer is expanded to infinity and, hence, no reflection occurs at z_N. The apparent impedance $\hat{Z}_{xy}^n = \hat{Z}_n$ on top of layer n is calculated using the orthogonal horizontal

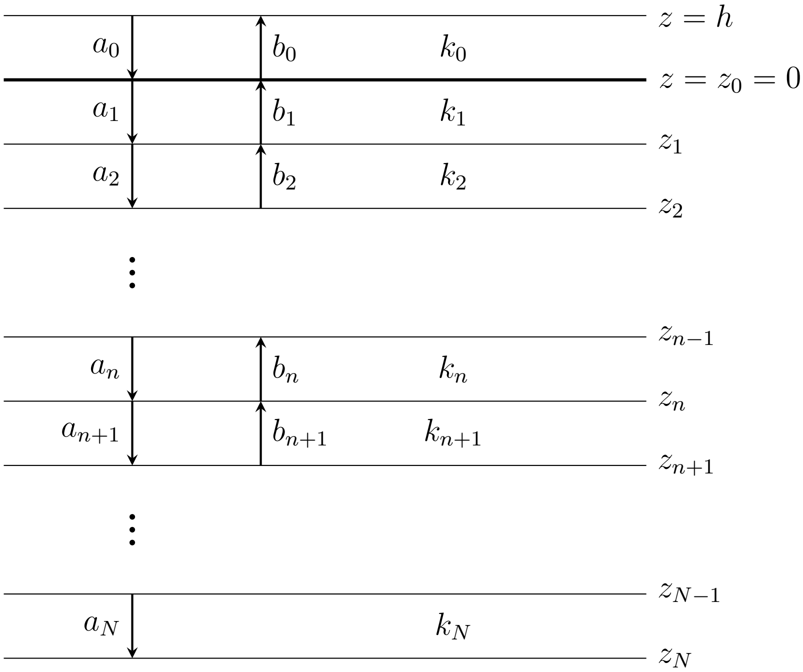

Fig. 2.1: Parameter distribution of the layered halfspace.

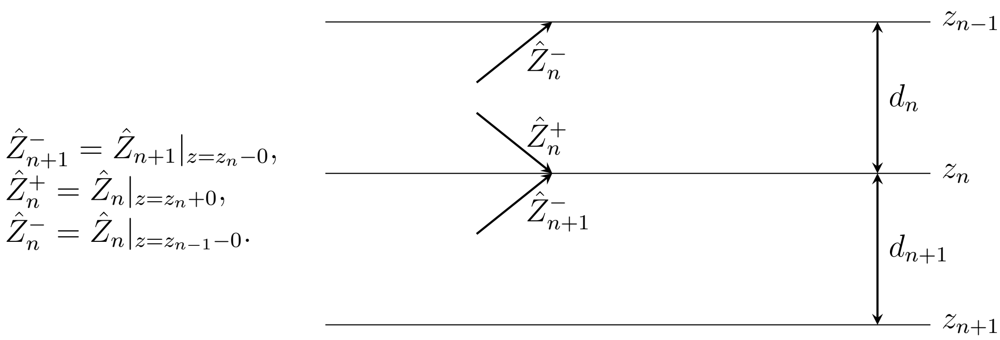

Fig. 2.2: Limits of the impedance at the interfaces

field components E_x^n and H_y^n

$$\hat{Z}_n = \frac{E_x^n(z)}{H_y^n(z)} = \frac{\omega\mu}{k_n} \frac{a_n e^{-ik_n(z-z_n)} + b_n e^{ik_n(z-z_n)}}{a_n e^{-ik_n(z-z_n)} - b_n e^{ik_n(z-z_n)}}. \tag{2.32}$$

Fig. 2.2 displays the notation for the limits of the apparent impedance at the interfaces used in the following. At the interfaces, the horizontal components of the electric and magnetic fields and, therefore, the apparent impedances are continuous: $\hat{Z}_n^+ = \hat{Z}_{n+1}^- = \hat{Z}_{n+1}$. The intrinsic impedance of the nth layer is obtained by $Z_n = \frac{\omega\mu}{k_n}$. In the following, a relation is derived to determine $\hat{Z}_n$ from $\hat{Z}_{n+1}$, Z_n and the parameters σ_n, μ_n, and ε_n. Starting point is eq. (2.32) at $z = z_n$:

$$\hat{Z}_n^+ = \frac{a_n + b_n}{\frac{k_n}{\omega\mu}(a_n - b_n)}. \tag{2.33}$$

Using $Z_n = \frac{\omega\mu}{k_n}$, this can be rearranged into

$$\frac{a_n + b_n}{a_n - b_n} = \frac{\hat{Z}_n^+}{Z_n}. \tag{2.34}$$

Applying eq. (2.32) at the upper interface yields

$$\hat{Z}_n^- = \frac{a_n e^{-ik_n(z_{n-1}-z_n)} + b_n e^{ik_n(z_{n-1}-z_n)}}{\frac{k_n}{\omega\mu}\left(a_n e^{-ik_n(z_{n-1}-z_n)} - b_n e^{ik_n(z_{n-1}-z_n)}\right)}. \tag{2.35}$$

Introducing the thickness d_n of layer n, we obtain

$$\hat{Z}_n^- = \frac{a_n e^{-ik_n(-d_n)} + b_n e^{ik_n(-d_n)}}{\frac{k_n}{\omega\mu}\left(a_n e^{-ik_n(-d_n)} - b_n e^{ik_n(-d_n)}\right)}. \tag{2.36}$$

The exponential expressions can be rewritten with the help of the hyperbolic functions $\cosh(x) = \frac{e^x+e^{-x}}{2}$ and $\sinh(x) = \frac{e^x-e^{-x}}{2}$:

$$\begin{aligned}
\hat{Z}_n^- &= \frac{a_n(\cosh(ik_nd_n) + \sinh(ik_nd_n)) + b_n(\cosh(ik_nd_n) - \sinh(ik_nd_n))}{1/Z_n(a_n(\cosh(ik_nd_n) + \sinh(ik_nd_n)) - b_n(\cosh(ik_nd_n) - \sinh(ik_nd_n)))} \\
&= \frac{(a_n + b_n)\cosh(ik_nd_n) + (a_n - b_n)\sinh(ik_nd_n)}{1/Z_n((a_n - b_n)\cosh(ik_nd_n) + (a_n + b_n)\sinh(ik_nd_n))}.
\end{aligned} \tag{2.37}$$

Considering eq. (2.34), we get

$$\hat{Z}_n^- = \frac{\cosh(ik_nd_n) + Z_n/\hat{Z}_n^+ \sinh(ik_nd_n)}{1/\hat{Z}_n^+ \cosh(ik_nd_n) + 1/Z_n \sinh(ik_nd_n)} = \frac{1 + Z_n/\hat{Z}_n^+ \tanh(ik_nd_n)}{1/\hat{Z}_n^+ + 1/Z_n \tanh(ik_nd_n)}. \tag{2.38}$$

Using $\hat{Z}_n^+ = \hat{Z}_{n+1}$, $\hat{Z}_n = \hat{Z}_n^-$ reads as

$$\hat{Z}_n = Z_n \frac{\hat{Z}_{n+1} + Z_n \tanh(ik_nd_n)}{Z_n + \hat{Z}_{n+1} \tanh(ik_nd_n)}. \tag{2.39}$$

Note that, the impedance $\hat{Z}_n$ at any layer interface only depends on the earth's properties below that interface and not on any above. For the underlying halfspace, $\hat{Z}_N = Z_N = \frac{\omega\mu}{k_N}$ applies at $z = z_{N-1}$. Based on this, the apparent impedances can be calculated recursively from the bottom up.

The reflection coefficients are to be determined from the impedances $\hat{Z}_{n+1}$ $(n = 1...N)$ applied at $z = z_n$

$$\frac{E_x^n}{H_y^n} = \frac{a_n + b_n}{\frac{k_n}{\omega\mu}(a_n - b_n)} = \hat{Z}_{n+1}. \tag{2.40}$$

Expansion with $\sqrt{a_n b_n}$ yields

$$\hat{Z}_{n+1} = \frac{1/\sqrt{R_n} + \sqrt{R_n}}{1/Z_n(1/\sqrt{R_n} - \sqrt{R_n})} = \frac{1 + R_n}{1/Z_n(1 - R_n)}, \quad R_n = \frac{b_n}{a_n}. \tag{2.41}$$

R_n can be expressed as

$$R_n = \frac{\hat{Z}_{n+1} - Z_n}{\hat{Z}_{n+1} + Z_n}. \tag{2.42}$$

In the next step, the condition of continuity for the electric field $E_x^n(z = z_n) = E_x^{n+1}(z = z_n)$ needs to be applied to calculate the coefficient a_{n+1} from a_n and the reflection coefficients R_n and R_{n+1}:

$$a_{n+1} = \frac{a_n(1 + R_n)}{e^{ik_{n+1}d_{n+1}} + R_{n+1}e^{-ik_{n+1}d_{n+1}}}. \tag{2.43}$$

In the case of an incident electric field of $E_0 = 1V \cdot m^{-1}$, we have $a_0 = 1$ and for the first layer

$$a_1 = \frac{(1 + R_0)e^{-ik_1d_1}}{1 + R_1e^{-2ik_1d_1}} \tag{2.44}$$

The formulae shown above describe the propagation of the electromagentic fields in a layered half-space with wave numbers k_n, conductivities σ_n, permeabilities μ_n, lower interfaces z_n, and thicknesses d_n of the layers as well as an incident electric field $E_x^0 = 1V \cdot m^{-1}$, whereas N is the number of layers and $n = 1...N$. In the air space, $k_0 = \sqrt{-i\omega\mu\sigma_0}$ with $\sigma_0 = 10^{-14}S \cdot m^{-1}$ and

$$Z_0 = \frac{\omega\mu}{k_0} \tag{2.45}$$

applies.
Without loss of generality, the incident magnetic field is fixed to $H_y^0 = 1Am^{-1}$. For the incident electric surface field follows

$$E_x^0 = \hat{Z}_1 \tag{2.46}$$

Now, we can use $b_n = R_na_n$ to compute the electric and magnetic field components in all layers:

$$\begin{aligned} E_x^n &= E_x^0a_n(e^{-ik_n(z-z_n)} + R_ne^{ik_n(z-z_n)}) \quad \text{and} \\ H_y^n &= \frac{k_n}{\omega\mu}E_x^0a_n(e^{-ik_n(z-z_n)} - R_ne^{ik_n(z-z_n)}). \end{aligned} \tag{2.47}$$

If the incident magnetic field component $H_x^0 = 1\,\mathrm{Am}^{-1}$ is oriented in x-direction, the orthogonal electric field component becomes $E_y^0 = -\hat{Z}_1$. Since

$$H_x^n(z) = \frac{1}{i\omega\mu}\frac{\partial E_y^n}{\partial z} = -\frac{k_n}{\omega\mu}(a_ne^{-ik_n(z-z_n)} - b_ne^{ik_n(z-z_n)}), \tag{2.48}$$

the electric and magnetic field components are calculated by

$$\begin{aligned} E_y^n &= E_y^0a_n(e^{-ik_n(z-z_n)} + R_ne^{ik_n(z-z_n)}) \quad \text{and} \\ H_x^n &= -\frac{k_n}{\omega\mu}E_y^0a_n(e^{-ik_n(z-z_n)} - R_ne^{ik_n(z-z_n)}). \end{aligned} \tag{2.49}$$

This analytical solution for the electric and magnetic fields propagating in a layered halfspace will be used later on to formulate boundary conditions for numerical simulations on bounded two-dimensional (2-D) and three-dimensional (3-D) domains.

2.1.2 Electromagnetic Induction in 2-D Conductivity Structures

In the case of 2-D isotropic structures, Maxwell's equations decouple into two independent modes. If y is the strike direction of a 2-D conductivity structure and assuming a harmonic time dependency $e^{i\omega t}$, eqs (2.1a) and (2.1b) reduce to

$$\frac{\partial H_x}{\partial z} - \frac{\partial H_z}{\partial x} = (\sigma + i\omega\varepsilon)E_y, \tag{2.50a}$$
$$-\frac{\partial E_y}{\partial z} = -i\omega\mu H_x, \tag{2.50b}$$
$$\frac{\partial E_y}{\partial x} = -i\omega\mu H_z, \tag{2.50c}$$

and

$$-\frac{\partial H_y}{\partial z} = (\sigma + i\omega\varepsilon)E_x, \tag{2.51a}$$
$$\frac{\partial H_y}{\partial x} = (\sigma + i\omega\varepsilon)E_z, \tag{2.51b}$$
$$\frac{\partial E_x}{\partial z} - \frac{\partial E_z}{\partial x} = -i\omega\mu H_y \tag{2.51c}$$

for a homogeneous region of the electromagnetic parameters σ, μ, and ε. Eqs (2.50) yield a complete description of the occuring electromagnetic fields in the case of E-polarisation, whereas eqs (2.51) hold for the case of H-polarisation (cf. Fig. 2.3). Combining eqs (2.50), the equation of induction for the electric field E_y reads as

$$-\frac{\partial}{\partial x}\mu^{-1}\frac{\partial E_y}{\partial x} - \frac{\partial}{\partial z}\mu^{-1}\frac{\partial E_y}{\partial z} + (i\omega\sigma - \omega^2\varepsilon)E_y = 0. \tag{2.52}$$

Eqs (2.51) yield the equation of induction for the magnetic field H_y

$$-\frac{\partial}{\partial x}(\sigma + i\omega\varepsilon)^{-1}\frac{\partial H_y}{\partial x} - \frac{\partial}{\partial z}(\sigma + i\omega\varepsilon)^{-1}\frac{\partial H_y}{\partial z} + i\omega\mu H_y = 0. \tag{2.53}$$

Once the strike-parallel components E_y and H_y have been computed, the remaining components H_x, H_z, E_x, and E_z can be derived from eqs (2.50b), (2.50c), and eqs (2.51b), (2.51c) by numerical differentiation. From the horizontal electric and magnetic fields, the MT impedances

$$Z_{xy} = \frac{E_x}{H_y} \quad \text{and} \quad Z_{yx} = \frac{E_y}{H_x} \tag{2.54}$$

yield the apparent resistivities

$$\rho_{xy} = \frac{1}{\omega\mu}\left|Z_{xy}\right|^2 \quad \text{and} \quad \rho_{yx} = \frac{1}{\omega\mu}\left|Z_{yx}\right|^2 \tag{2.55}$$

as well as the phases

$$\phi_{xy} = \arg(Z_{xy}) \quad \text{and} \quad \phi_{yx} = \arg(Z_{yx}). \tag{2.56}$$

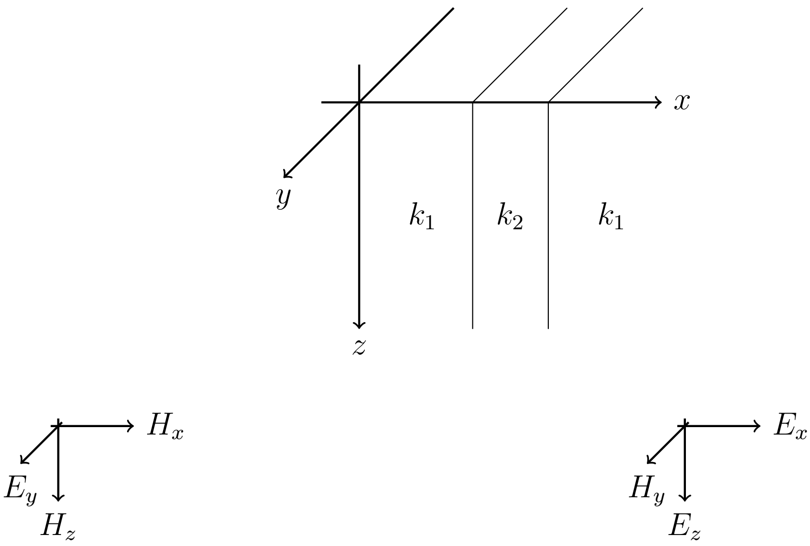

Fig. 2.3: Orientation of field components occuring for E- (left) and H- (right) polarisation for a 2-D model as exemplarily described on top.

Furthermore, the ratio of vertical to horizontal magnetic field components provides the magnetic transfer function called tipper:

$$T_{zx} = \frac{H_z}{H_x}. \tag{2.57}$$

As can be seen from the inspection of eqs (2.50) and (2.51), Z_{xx}, Z_{yy}, and T_{zy} are zero in the 2-D case.

3 Formulations of the Magnetotelluric Boundary Value Problem

From Maxwell's equations, different formulations of the magnetotelluric (MT) boundary value problem (BVP) arise that similarly describe the propagation of the electromagnetic fields. In this chapter, the equation of induction is derived in terms of the electric field, the magnetic field, the magnetic vector potential and the electric scalar potential, the magnetic vector potential only, or the anomalous magnetic vector potential. Incorporating adequate boundary conditions of Dirichlet and Neumann type, the appropriate two-dimensional (2-D) BVPs are formulated in terms of the electric and the magnetic field, respectively, whereas in the three-dimensional (3-D) case five different BVPs are introduced. The latter represent a variety of BVPs that are suited to simulate MT fields (Haber et al., 2000; Schwarzbach, 2009; Mackie et al., 1994; Mogi, 1996) without intending to be exhaustive. However, it enables the analysis of the different formulations regarding the numerical simulation of electric versus magnetic field values, the approximation of electromagnetic potentials versus electromagnetic fields, the consideration of a stabilised approach versus unstabilised formulations, and the simulation of an anomalous electromagnetic potential versus total field approaches. These points are among the issues that are most intensively discussed in the community of geo-electromagnetic code developers nowadays.

3.1 The Two-Dimensional Boundary Value Problem

To calculate the electric and magnetic field components from eqs (2.52) and (2.53), respectively, in a bounded domain $\Omega \subset \mathbb{R}^2$ the following 2-D BVPs can be formulated for E-polarisation

$$
\begin{aligned}
-\frac{\partial}{\partial x}\mu^{-1}\frac{\partial E_y}{\partial x} - \frac{\partial}{\partial z}\mu^{-1}\frac{\partial E_y}{\partial z} + (i\omega\sigma - \omega^2\varepsilon)E_y &= 0 \quad \text{in} \quad \Omega && \text{(3.1a)}\\
E_y &= E_n(x,z) \quad \text{on} \quad \Gamma_\mathrm{D} && \text{(3.1b)}\\
\mathbf{n}_1 \times \mathbf{H}_1 + \mathbf{n}_2 \times \mathbf{H}_2 = \mathbf{n}_1 \cdot (\mu_1^{-1}\nabla E_{y,1}) + \mathbf{n}_2 \cdot (\mu_2^{-1}\nabla E_{y,2}) &= 0 \quad \text{on} \quad \Gamma_\mathrm{int} && \text{(3.1c)}
\end{aligned}
$$

and H-polarisation

$$
\begin{aligned}
-\frac{\partial}{\partial x}(\sigma + i\omega\varepsilon)^{-1}\frac{\partial H_y}{\partial x} - \frac{\partial}{\partial z}(\sigma + i\omega\varepsilon)^{-1}\frac{\partial H_y}{\partial z} + i\omega\mu H_y &= 0 \quad \text{in} \quad \Omega && \text{(3.2a)}\\
H_y &= H_n(x,z) \quad \text{on} \quad \Gamma_\mathrm{D} && \text{(3.2b)}\\
\mathbf{n}_1 \times \mathbf{E}_1 + \mathbf{n}_2 \times \mathbf{E}_2 &= \\
\mathbf{n}_1 \cdot \big((\sigma_1 + i\omega\varepsilon)^{-1}\nabla H_{y,1}\big) + \mathbf{n}_2 \cdot \big((\sigma_2 + i\omega\varepsilon)^{-1}\nabla H_{y,2}\big) &= 0 \quad \text{on} \quad \Gamma_\mathrm{int}, && \text{(3.2c)}
\end{aligned}
$$

respectively. For the outer boundaries Γ_D, to which inhomogeneous boundary conditions of the Dirichlet type apply, the normal field values E_n and H_n are computed according to the algorithm presented in the previous section. $\mathbf{n}_1$ and $\mathbf{n}_2$ denote outward unit normal vectors on the interface Γ_int seperating subdomains 1 and 2, i.e. regions of different electrical conductivity.

3.2 The Three-Dimensional Boundary Value Problem

To solve eqs (2.8) or (2.9) for the magnetic or the electric fields, respectively, in a bounded domain $\Omega \subset \mathbb{R}^3$ respecting the boundary conditions described in subsection 2.1.1 for two orthogonal horizontal electric and magnetic field components, several BVPs can be formulated. The BVP in terms of the magnetic field reads

BVP (i) Find $\mathbf{H}$ such that

$$\begin{aligned}
\nabla \times (\sigma + i\omega\varepsilon)^{-1}\nabla \times \mathbf{H} + i\omega\mu\mathbf{H} &= 0 \quad \text{in} \quad \Omega && \text{(3.3a)}\\
\mathbf{n} \times \mathbf{E} &= 0 \quad \text{on} \quad \Gamma_{\perp} && \text{(3.3b)}\\
\mathbf{n} \times \mathbf{H} &= 0 \quad \text{on} \quad \Gamma_{||} && \text{(3.3c)}\\
\mathbf{H} &= \mathbf{H}_n(x,y,z) \quad \text{on} \quad \Gamma_{\text{top}} \cup \Gamma_{\text{bottom}} && \text{(3.3d)}\\
\mathbf{n}_1 \times \mathbf{E}_1 - \mathbf{n}_2 \times \mathbf{E}_2 &= 0 \quad \text{on} \quad \Gamma_{\text{int}} && \text{(3.3e)}
\end{aligned}$$

where $\Gamma_{\perp}$ denotes all boundaries oriented perpendicular to the current flow, $\Gamma_{||}$ includes all boundaries parallel to the current flow, Γ_{top} and Γ_{bottom} are the horizontal top and bottom boundaries, respectively. On all the interior boundaries, Γ_{int} representing possible jumps in the electromagnetic model parameters the conditions of continuity of the tangential field components apply. Furthermore, $\mathbf{E} = (\sigma + i\omega\epsilon)^{-1}\nabla \times \mathbf{H}$ is valid.

The BVP for the electric field reads as

BVP (ii) Find $\mathbf{E}$ such that

$$\begin{aligned}
\nabla \times \mu^{-1}\nabla \times \mathbf{E} + (i\omega\sigma - \omega^2\varepsilon)\mathbf{E} &= 0 \quad \text{in} \quad \Omega && \text{(3.4a)}\\
\mathbf{n} \times \mathbf{E} &= 0 \quad \text{on} \quad \Gamma_{\perp} && \text{(3.4b)}\\
\mathbf{n} \times \mathbf{H} &= 0 \quad \text{on} \quad \Gamma_{||} && \text{(3.4c)}\\
\mathbf{H} &= \mathbf{H}_n(x,y,z) \quad \text{on} \quad \Gamma_{\text{top}} \cup \Gamma_{\text{bottom}} && \text{(3.4d)}\\
\mathbf{n}_1 \times \mathbf{H}_1 - \mathbf{n}_2 \times \mathbf{H}_2 &= 0 \quad \text{on} \quad \Gamma_{\text{int}} && \text{(3.4e)}
\end{aligned}$$

using the same notation as above. Here, $\mathbf{H} = (-i\omega\mu)^{-1}\nabla \times \mathbf{E}$ applies.

The divergence-free field $\mathbf{B}$ can be expressed as curl of the vector potential $\mathbf{A}$

$$\mathbf{B} = \nabla \times \mathbf{A}. \tag{3.5}$$

Since $\nabla \times (\mathbf{E} + i\omega\mathbf{A}) = 0$ (cf. eq. 2.1b), we can introduce the scalar potential ϕ so that

$$\mathbf{E} = -\nabla\phi - i\omega\mathbf{A}. \tag{3.6}$$

Substituting the electric field in eq. (2.9) yields the equation of induction for the magnetic vector potential $\mathbf{A}$

$$\nabla\times \mu^{-1}\nabla\times \mathbf{A} + (i\omega\sigma - \omega^2\varepsilon)\mathbf{A} + (\sigma + i\omega\varepsilon)\nabla\phi = 0. \tag{3.7}$$

To solve for both unkowns $\mathbf{A}$ and ϕ, the equation of continuity
$\nabla\cdot (\nabla\times \mathbf{H}) = \nabla\cdot \left((\sigma + i\omega\varepsilon)\mathbf{E}\right) = 0$ needs to be applied additionally

$$-\nabla\cdot \big((i\omega\sigma - \omega^2\varepsilon)\mathbf{A} + (\sigma + i\omega\varepsilon)\nabla\phi\big) = 0. \tag{3.8}$$

Choosing $\tilde{\mathbf{A}} = \mathbf{A} + \nabla\Psi$ and $\tilde{\phi} = \phi - \dot{\Psi}$ with the gauge condition $\Psi = -i\phi/\omega$, we obtain

$$\tilde{\mathbf{A}} = \mathbf{A} - \frac{i}{\omega}\nabla\phi \quad \text{and} \quad \tilde{\phi} = 0 \tag{3.9}$$

that determine the same electromagnetic fields as $\mathbf{A}$ and ϕ (cf. eqs 3.5 and 3.6). With the help of eq. (3.9), eq. (3.7) can be rearranged into an elliptic second-order partial differential equation for $\tilde{\mathbf{A}}$

$$\nabla\times\mu^{-1}\nabla\times\tilde{\mathbf{A}} + (i\omega\sigma - \omega^2\varepsilon)\tilde{\mathbf{A}} = 0. \tag{3.10}$$

Therewith, two more BVPs can be formulated

BVP (iii) Find $\mathbf{A}$ and ϕ such that

$$\begin{aligned}
\nabla\times\mu^{-1}\nabla\times\mathbf{A} + (i\omega\sigma - \omega^2\varepsilon)\mathbf{A} + (\sigma + i\omega\varepsilon)\nabla\phi &= 0 \quad \text{in} \quad \Omega && (3.11a)\\
-\nabla\cdot\left((i\omega\sigma - \omega^2\varepsilon)\mathbf{A} + (\sigma + i\omega\varepsilon)\nabla\phi\right) &= 0 \quad \text{in} \quad \Omega && (3.11b)\\
\mathbf{n}\times\mathbf{H} = 0 \quad \text{and} \quad \mathbf{n}\cdot\mathbf{j} &= 0 \quad \text{on} \quad \Gamma_{||} && (3.11c)\\
\mathbf{n}\times\mathbf{A} = 0 \quad \text{and} \quad \phi &= \phi_0 \quad \text{on} \quad \Gamma_{\perp} && (3.11d)\\
\mathbf{H} = \mathbf{H}_n(x,y,z) \quad \text{and} \quad \mathbf{n}\cdot\mathbf{j} = -\nabla\cdot(\mathbf{n}\times\mathbf{H}) &= 0 \quad \text{on} \quad \Gamma_{\text{top}}\cup\Gamma_{\text{bottom}} && (3.11e)\\
\mathbf{n}_1\times\mathbf{H}_1 - \mathbf{n}_2\times\mathbf{H}_2 = 0 \quad \text{and} \quad \mathbf{n}_1\cdot\mathbf{j}_1 - \mathbf{n}_2\cdot\mathbf{j}_2 &= 0 \quad \text{on} \quad \Gamma_{\text{int}} && (3.11f)
\end{aligned}$$

where $\mathbf{H} = \mu^{-1}\nabla\times\mathbf{A}$ and $\mathbf{j} = -\left((i\omega\sigma - \omega^2\varepsilon)\mathbf{A} + (\sigma + i\omega\varepsilon)\nabla\phi\right)$.

BVP (iv) Find $\tilde{\mathbf{A}}$ such that

$$\begin{aligned}
\nabla\times\mu^{-1}\nabla\times\tilde{\mathbf{A}} + (i\omega\sigma - \omega^2\varepsilon)\tilde{\mathbf{A}} &= 0 \quad \text{in} \quad \Omega && (3.12a)\\
\mathbf{n}\times\mathbf{H} &= 0 \quad \text{on} \quad \Gamma_{||} && (3.12b)\\
\mathbf{n}\times\tilde{\mathbf{A}} &= 0 \quad \text{on} \quad \Gamma_{\perp} && (3.12c)\\
\mathbf{H} &= \mathbf{H}_n(x,y,z) \quad \text{on} \quad \Gamma_{\text{top}}\cup\Gamma_{\text{bottom}} && (3.12d)\\
\mathbf{n}_1\times\mathbf{H}_1 - \mathbf{n}_2\times\mathbf{H}_2 &= 0 \quad \text{on} \quad \Gamma_{\text{int}} && (3.12e)
\end{aligned}$$

with $\mathbf{H} = \mu^{-1}\nabla\times\mathbf{A}$. In the following, $\tilde{\mathbf{A}}$ is substituted by $\mathbf{A}$ in eqs (3.12a) and (3.12c). How much $\mathbf{A}$ computed from BVP (iii) and BVP (iv) differ, i.e. which influence the scalar potential ϕ has on the solution (cf. eq. 3.9), will be examined in chapter 5.

Assuming a harmonic time dependency $e^{i\omega t}$ in eqs (2.1a) and (2.1b), the separation of the electric and magnetic fields $\mathbf{E}$ and $\mathbf{H}$, respectively, into normal ($\mathbf{E}_n$, $\mathbf{H}_n$) and anomalous ($\mathbf{E}_a$, $\mathbf{H}_a$) contributions

$$\mathbf{E} = \mathbf{E}_a + \mathbf{E}_n \quad \text{and} \quad \mathbf{H} = \mathbf{H}_a + \mathbf{H}_n \tag{3.13}$$

where

$$\nabla\times\mathbf{E}_n = -i\omega\mu_n\mathbf{H}_n \quad \text{and} \quad \nabla\times\mathbf{H}_n = (\sigma_n + i\omega\epsilon_n)\mathbf{E}_n \tag{3.14}$$

with

$$\varepsilon = \varepsilon_n + \varepsilon_a, \quad \sigma = \sigma_n + \sigma_a, \quad \mu = \mu_n + \mu_a$$

results in

$$\begin{aligned}\nabla\times \mathbf{E}_a = \nabla\times(\mathbf{E}-\mathbf{E}_n) &= -i\omega\mu\mathbf{H} + i\omega\mu_n\mathbf{H}_n \\ &= -i\omega\mu\mathbf{H}_a - i\omega\mu_a\mathbf{H}_n \qquad \text{and} \qquad (3.15)\\ \nabla\times \mathbf{H}_a = \nabla\times(\mathbf{H}-\mathbf{H}_n) &= (\sigma+i\omega\varepsilon)\mathbf{E} - (\sigma_n+i\omega\varepsilon_n)\mathbf{E}_n \\ &= (\sigma+i\omega\varepsilon)\mathbf{E}_a + (\sigma_a+i\omega\varepsilon_a)\mathbf{E}_n. \qquad (3.16)\end{aligned}$$

Multiplying eq. (3.15) by μ^{-1}, taking $\nabla\times$ and combining it with eq. (3.16) yield the equation of induction for the anomalous electric field $\mathbf{E}_a$

$$\nabla\times\mu^{-1}\nabla\times\mathbf{E}_a + (i\omega\sigma-\omega^2\varepsilon)\mathbf{E}_a + i\omega\,\nabla\times\mu_a\mu^{-1}\mathbf{H}_n = -(i\omega\sigma_a-\omega^2\varepsilon_a)\mathbf{E}_n. \qquad (3.17)$$

Assuming $\phi_a = 0$ (cf. eq. 3.9) and substituting $\mathbf{E}_a = -i\omega\mathbf{A}_a$, we obtain the equation of induction for the anomalous potential $\mathbf{A}_a$

$$\nabla\times\mu^{-1}(\nabla\times\mathbf{A}_a - \mu_a\mathbf{H}_n) + (i\omega\sigma-\omega^2\varepsilon)\mathbf{A}_a = (\sigma_a+i\omega\varepsilon_a)\mathbf{E}_n. \qquad (3.18)$$

The non-zero horizontal components of the normal electromagnetic fields $\mathbf{E}_n$ und $\mathbf{H}_n$ are computed for a 1-D layered halfspace with parameter distributions σ_n, μ_n, and ε_n analytically as shown in subsection 2.1.1. Considering eq. (3.18) in the domain Ω with the outer boundary Γ_{D} and all internal boundaries Γ_{int}, for which the conditions of continuity for the magnetic field are valid, yields the BVP BVP (v) Find $\mathbf{A}_a$ such that

$$\begin{aligned}\nabla\times\mu^{-1}(\nabla\times\mathbf{A}_a - \mu_a\mathbf{H}_n) \;&+\; (i\omega\sigma-\omega^2\varepsilon)\mathbf{A}_a = (\sigma_a+i\omega\varepsilon_a)\mathbf{E}_n \quad \text{in } \Omega \qquad (3.19a)\\ \mathbf{n}\times\mathbf{A}_a \;&=\; 0 \quad \text{on} \quad \Gamma_{\mathrm{D}} \qquad (3.19b)\\ \mathbf{n}_1\times\mathbf{H}_{a,1} - \mathbf{n}_2\times\mathbf{H}_{a,2} \;&=\; 0 \quad \text{on} \quad \Gamma_{\mathrm{int}} \qquad (3.19c)\end{aligned}$$

where $\mathbf{H}_a = \mu^{-1}\nabla\times\mathbf{A}_a$.
Analogous to eqs (3.5) and (3.6), we can find an electric vector potential $\mathbf{T}$ and a magnetic scalar potential Ω to describe the electric current density and the magnetic field:

$$\mathbf{j} = \nabla\times\mathbf{T} \quad \text{and} \quad \mathbf{H} = \mathbf{T} - \nabla\,\Omega. \qquad (3.20)$$

A solution to the BVP using this approach is presented by Mitsuhata and Uchida (2004) and will not be explicitly discussed in this thesis.
Additional BVPs can be formulated using anomalous field approaches (Newman & Alumbaugh, 1996) that are quite similar to the anomalous potential technique. Furthermore, the numerical solution of the stabilised equation of induction for the electric field has been introduced by Schwarzbach (2009).

4 The Finite Element Method

For the accurate computation of electromagnetic fields and potentials on the earth's surface and the sea floor, it is desireable to incorporate the topographic and bathymetric relief into the model. Unstructured triangular and tetrahedral grids are superior to tensor-product grids when approximating close-to-reality topographic and bathymetric undulations. Moreover, in connection with an *a-posteriori* error estimator provided by convergence theory applied to the finite element (FE) method, unstructured grids allow for elaborate mesh design by adaptive refinement concentrating elements and their associated degrees of freedom (DOF) in the regions of importance. To benefit from these advantages, for solving the introduced boundary value problems (BVPs), the FE method is applied.

Based on the weak formulation of the two-dimensional (2-D) and three-dimensional (3-D) BVPs introduced in the previous chapter, the FE method is used to approximate the solution of the partial differential equations. In the following, the derivation of the weak form of the 2-D and 3-D BVPs is demonstrated. The FE analysis leads to a discrete matrix-vector formulation of the BVPs that is solved numerically. In the 2-D case, Lagrange elements are applied to approximate scalar field components. For the 3-D BVPs, however, curl-conforming vector finite elements are better suited for the approximation of vector fields. From convergence theory it is expected that, a finer discretisation yields a more accurate solution. Hence, at the end of this chapter, applicable mesh refinement strategies are presented.

Detailed descriptions of the application of the FE method to solve Maxwell's equations can be found in Monk (2003) and Jin (1993).

4.1 Weak Form of the Boundary Value Problems

4.1.1 Weak Form of the Two-Dimensional Boundary Value Problems

We seek for solutions E_y and H_y of the BVPs described by eqs (3.1) and (3.2), respectively. An equivalent formulation of the BVP for E-polarisation on the domain Ω requires the validity of eq. (3.1a) only in the sense of the L^2-inner product $(u, v) = \int_\Omega u\bar{v}\ d\mathbf{x}$ with an arbitrary complex test function v of a function space V and its complex conjugate $\bar{v}$, which leads to

$$\int_\Omega \left(-\nabla \cdot \left(\mu^{-1}\nabla E_y\right)\bar{v} + (i\omega\sigma - \omega^2\varepsilon)E_y\bar{v}\right)\ d\mathbf{x} = 0 \quad \forall v \in V. \tag{4.1}$$

From the vector identity $\nabla \cdot (c\,\nabla uv) = \nabla \cdot (c\,\nabla u)\,v + c\,\nabla u \cdot \nabla v$ and Green's theorem, we obtain

$$\int_\Omega \left(\mu^{-1}\nabla E_y \cdot \nabla\bar{v} + (i\omega\sigma - \omega^2\varepsilon)E_y\bar{v}\right)\ d\mathbf{x} - \int_{\partial\Omega} \mathbf{n} \cdot \left(\mu^{-1}\nabla E_y\right)\bar{v}\,dl = 0 \quad \forall v \in V. \tag{4.2}$$

The integral over all boundaries $\partial\Omega = \Gamma_{\mathrm{D}} \cup \Gamma_{\mathrm{int}}$ of the region Ω

$$\begin{aligned}\int_{\partial\Omega} \mathbf{n}\cdot\left(\mu^{-1}\nabla E_y\right)\bar{v}\,dl &= \int_{\Gamma_{\mathrm{D}}} \mathbf{n}\cdot\left(\mu^{-1}\nabla E_y\right)\bar{v}\,dl \\ &+ \int_{\Gamma_{\mathrm{int}}} \left(\mathbf{n}_1\cdot\left(\mu_1^{-1}\nabla E_{y,1}\right) + \mathbf{n}_2\cdot\left(\mu_2^{-1}\nabla E_{y,2}\right)\right)\bar{v}\,dl \end{aligned} \tag{4.3}$$

vanishes if $v \equiv 0$ on the Dirichlet boundary Γ_{D}. On that condition, the original problem of solving eqs (3.1a)-(3.1c) can be replaced by the so-called weak formulation which consists of finding $E_y \in U$ such that:

$$b(E_y, v) = \int_{\Omega} \left(\mu^{-1}\nabla E_y\cdot\nabla\bar{v} + (i\omega\sigma - \omega^2\varepsilon)E_y\bar{v}\right)\,d\mathbf{x} = 0 \quad \forall v \in V, \tag{4.4}$$

where

$$U \;:=\; \{E_y \in H^1(\Omega) : E_y = E_n(x,z) \quad \text{on} \quad \Gamma_{\mathrm{D}}\} \quad \text{and} \tag{4.5}$$
$$V \;:=\; \{v \in H^1(\Omega) : v \equiv 0 \quad \text{on} \quad \Gamma_{\mathrm{D}}\} \tag{4.6}$$

are the trial and the test space, respectively. H^1 denotes the finite-dimensional Hilbert space

$$H^1(\Omega) := \{v \in L^2(\Omega), \nabla v \in (L^2(\Omega))^2\} \tag{4.7}$$

that is linear with respect to the scalar product $(u,v) = \int_\Omega (u\,v + \nabla u\cdot\nabla v)\,d\mathbf{x}$. For the solution E_y of the weak form (4.4) and its first partial derivatives ∇E_y, it is sufficient to be square integrable instead of twice continously differentiable ($E_y \in C^2(\Omega)$, cf. eq. 3.1a). The material parameters $\sigma, \mu, \varepsilon \in L^2(\Omega)$ are required to be square integrable. Satisfying eqs (3.1), the electromagnetic fields are solutions to eq. (4.4) as well.
In the H-Polarisation case, the weak form of the BVP described by eqs (3.2) is: Find $H_y \in U$ such that

$$b(H_y, v) = \int_{\Omega} \left((\sigma + i\omega\varepsilon)^{-1}\nabla H_y\cdot\nabla\bar{v} + i\omega\mu H_y\bar{v}\right)\,d\mathbf{x} = 0 \quad \forall v \in V, \tag{4.8}$$

where

$$U \;:=\; \{H_y \in H^1(\Omega) : H_y = H_n(x,z) \quad \text{on} \quad \Gamma_{\mathrm{D}}\} \quad \text{and} \tag{4.9}$$
$$V \;:=\; \{v \in H^1(\Omega) : v \equiv 0 \quad \text{on} \quad \Gamma_{\mathrm{D}}\} \tag{4.10}$$

with the same finite-dimensional Hilbert space H^1 as above

$$H^1(\Omega) := \{v \in L^2(\Omega), \nabla v \in (L^2(\Omega))^2\}. \tag{4.11}$$

4.1.2 Weak Form of the Three-Dimensional Boundary Value Problems

Seeking for a solution $\mathbf{H}$ of BVP (i) (eqs 3.3) in the domain Ω requires the validity of (3.3a) only in the sense of the L^2-inner product $(\mathbf{u},\mathbf{v}) = \int_\Omega \mathbf{u}\cdot\bar{\mathbf{v}}\,d\mathbf{x}$ with an arbitrary complex- and vector-valued test function $\mathbf{v}$ of a function space V, which leads to

$$\int_{\Omega} \left[\left(\nabla\times(\sigma + i\omega\varepsilon)^{-1}\nabla\times\mathbf{H}\right)\cdot\bar{\mathbf{v}} + i\omega\mu\,\mathbf{H}\cdot\bar{\mathbf{v}}\right]d\mathbf{x} = 0 \quad \forall\mathbf{v} \in V \tag{4.12}$$

where $\bar{\mathbf{v}}$ is the complex conjugate of $\mathbf{v}$. From the vector identity $\nabla\times\mathbf{w}\cdot\mathbf{v} = \nabla\cdot(\mathbf{w}\times\mathbf{v}) + \mathbf{w}\cdot\nabla\times\mathbf{v}$ and Green's theorem we obtain

$$\begin{aligned}\int_\Omega [(\sigma + i\omega\varepsilon)^{-1}\nabla\times\mathbf{H}\cdot\nabla\times\bar{\mathbf{v}} \quad &+ \quad i\omega\mu\,\mathbf{H}\cdot\bar{\mathbf{v}}]\,d\mathbf{x} \\ &+ \int_{\partial\Omega}\mathbf{n}\times\big((\sigma+i\omega\varepsilon)^{-1}\nabla\times\mathbf{H}\big)\cdot\bar{\mathbf{v}}\,d\mathbf{x} = 0 \quad \forall\mathbf{v}\in V.\end{aligned} \tag{4.13}$$

$\mathbf{n}$ denotes the outward unit normal vector. Portions of the integral over all boundaries $\partial\Omega = \Gamma_\perp \cup \Gamma_{||}\cup\Gamma_{\text{top}}\cup\Gamma_{\text{bottom}}\cup\Gamma_{\text{int}}$ of the domain Ω

$$\begin{aligned}\int_{\partial\Omega}\mathbf{n}\times\big((\sigma+i\omega\varepsilon)^{-1}\nabla\times\mathbf{H}\big)\cdot\bar{\mathbf{v}}\,d\mathbf{x} \quad &= \quad -\int_{\partial\Omega\setminus\Gamma_{\text{int}}}(\mathbf{n}\times\bar{\mathbf{v}})\cdot\big((\sigma+i\omega\varepsilon)^{-1}\nabla\times\mathbf{H}\big)\ d\mathbf{x} \\ &\quad + \int_{\Gamma_{\text{int}}}(\mathbf{n}_1\times\mathbf{E}_1 - \mathbf{n}_2\times\mathbf{E}_2)\cdot\bar{\mathbf{v}}\,d\mathbf{x}\end{aligned} \tag{4.14}$$

vanish on $\Gamma_\perp$ and Γ_{int} (cf. eqs 3.3b and 3.3e). To generally eliminate this term from eq. (4.13), we choose $\mathbf{n}\times\mathbf{v} = 0$ on $\Gamma_{||}$, Γ_{top} and Γ_{bottom} since no information about $\mathbf{n}\times((\sigma+i\omega\varepsilon)^{-1}\nabla\times\mathbf{H})$ is given on these boundaries. On that condition, the original problem (eqs (3.3)) can be replaced by the so-called weak formulation

BVP (i) Find $\mathbf{H}\in U$ such that

$$\int_\Omega[(\sigma+i\omega\varepsilon)^{-1}\nabla\times\mathbf{H}\cdot\nabla\times\mathbf{v} + i\omega\mu\,\mathbf{H}\cdot\mathbf{v}]\,d\mathbf{x} = 0 \quad \forall\mathbf{v}\in V \tag{4.15}$$

where

$$\begin{aligned} U \quad &:= \quad \{\mathbf{H}\in H(\text{curl},\Omega) : \mathbf{H} = \mathbf{H}(x,y,z) \quad \text{on} \quad \Gamma_{\text{top}}\cup\Gamma_{\text{bottom}}, \\ &\qquad\qquad \mathbf{n}\times\mathbf{H} = 0 \quad \text{on} \quad \Gamma_{||}\}, &&(4.16a)\\ V \quad &:= \quad \{\mathbf{v}\in H(\text{curl},\Omega) : \mathbf{n}\times\mathbf{v} = 0 \quad \text{on} \quad \Gamma_{\text{top}}\cup\Gamma_{\text{bottom}}\cup\Gamma_{||}\} \quad \text{and} &&(4.16b)\\ H(\text{curl},\Omega) \quad &:= \quad \{\mathbf{v}\in(L^2(\Omega))^3, \nabla\times\mathbf{v}\in(L^2(\Omega))^3\}. &&(4.16c)\end{aligned}$$

The weak form of BVP (ii) (eqs 3.4) can be derived in the same manner. Starting from the L^2-inner product with an arbitrary complex- and vector-valued test function $\mathbf{v}$

$$\int_\Omega\big[\big(\nabla\times\mu^{-1}\nabla\times\mathbf{E}\big)\cdot\bar{\mathbf{v}} + (i\omega\sigma - \omega^2\epsilon)\,\mathbf{E}\cdot\bar{\mathbf{v}}\big]\,d\mathbf{x} = 0 \quad \forall\mathbf{v}\in V, \tag{4.17}$$

we get after applying vector calculus

$$\begin{aligned}\int_\Omega[\mu^{-1}\nabla\times\mathbf{E}\cdot\nabla\times\bar{\mathbf{v}} \quad &+ \quad (i\omega\sigma-\omega^2\varepsilon)\,\mathbf{E}\cdot\bar{\mathbf{v}}]\,d\mathbf{x} \\ &+ \int_{\partial\Omega}\mathbf{n}\times\big(\mu^{-1}\nabla\times\mathbf{E}\big)\cdot\bar{\mathbf{v}}\,d\mathbf{x} = 0 \quad \forall\mathbf{v}\in V\end{aligned} \tag{4.18}$$

whereas

$$\int_{\partial\Omega} \mathbf{n} \times \left(\mu^{-1}\nabla\times \mathbf{E}\right) \cdot \bar{\mathbf{v}}\, d\mathbf{x} = -\int_{\partial\Omega\setminus\Gamma_{\text{int}}} (\mathbf{n} \times \bar{\mathbf{v}}) \cdot \left(\mu^{-1}\nabla\times \mathbf{E}\right)\, d\mathbf{x} + \int_{\Gamma_{\text{int}}} (\mathbf{n}_1 \times \mathbf{H}_1 - \mathbf{n}_2 \times \mathbf{H}_2) \cdot \bar{\mathbf{v}}\, d\mathbf{x}. \tag{4.19}$$

Portions of the boundary integral vanish on $\Gamma_{||}$ and Γ_{int} (cf. eqs 3.4c and 3.4e) as well as on $\Gamma_{\perp}$ if we choose $\mathbf{n} \times \mathbf{v} = 0$ there. On Γ_{top} and Γ_{bottom}, eq. (3.4d) gives $\mu^{-1}\nabla\times \mathbf{E} = \mathbf{H}_n(x, y, z)$. Taking the boundary-integral term to the right-hand side, the original problem (eqs (3.4)) can be replaced by its weak form

BVP (ii) Find $\mathbf{E} \in U$ such that

$$\int_{\Omega} \left(\mu^{-1}\nabla\times \mathbf{E} \cdot \nabla\times \mathbf{v}\right) + (i\omega\sigma - \omega^2\varepsilon)\, \mathbf{E} \cdot \mathbf{v}\, d\mathbf{x} = \int_{\Gamma_{\text{top}}} (\mathbf{n} \times \bar{\mathbf{v}}) \cdot \mathbf{H}_n\, d\mathbf{x} + \int_{\Gamma_{\text{bottom}}} (\mathbf{n} \times \bar{\mathbf{v}}) \cdot \mathbf{H}_n\, d\mathbf{x} \quad \forall \mathbf{v} \in V \tag{4.20}$$

where

$$U := \{\mathbf{E} \in H(\text{curl}, \Omega) : \mathbf{n} \times \mathbf{E} = 0 \quad \text{on} \quad \Gamma_{\perp}\}, \tag{4.21a}$$

$$V := \{\mathbf{v} \in H(\text{curl}, \Omega) : \mathbf{n} \times \mathbf{v} = 0 \quad \text{on} \quad \Gamma_{\perp}\} \quad \text{and} \tag{4.21b}$$

$$H(\text{curl}, \Omega) := \{\mathbf{v} \in (L^2(\Omega))^3, \nabla \times \mathbf{v} \in (L^2(\Omega))^3\}. \tag{4.21c}$$

Due to the homogeneous boundary condition (3.4b) for $\mathbf{n} \times \mathbf{E}$ on $\Gamma_{\perp}$, the trial and the test functions can be chosen from the same function space V.

To find the weak form of BVP (iii) (eqs (3.11)), we need to formulate eqs (3.11a) and (3.11b) in the sense of the L^2-inner products $(\mathbf{u}, \mathbf{v}) = \int_{\Omega} \mathbf{u} \cdot \bar{\mathbf{v}}\, d\mathbf{x}$ and $(f, w) = \int_{\Omega} f\bar{w}\, d\mathbf{x}$ using an arbitrary complex-valued vector test function $v \in V$, its complex conjugate $\bar{\mathbf{v}}$, an arbitrary complex-valued scalar test function $w \in W$ and its complex conjugate $\bar{w}$, respectively,

$$\int_{\Omega} \left[\left(\nabla\times \mu^{-1}\nabla\times \mathbf{A}\right) \cdot \bar{\mathbf{v}} + (i\omega\sigma - \omega^2\epsilon)\, \mathbf{A} \cdot \bar{\mathbf{v}} + (\sigma + i\omega\epsilon)\nabla\, \phi \cdot \bar{\mathbf{v}}\right] d\mathbf{x} = 0 \quad \forall \mathbf{v} \in V, \tag{4.22a}$$

$$\int_{\Omega} \left[-\nabla\cdot\, \left((i\omega\sigma - \omega^2\varepsilon)\, \mathbf{A} + (\sigma + i\omega\varepsilon)\, \nabla\, \phi\right) \cdot w\right] d\mathbf{x} = 0. \tag{4.22b}$$

Applying the vector identities $\nabla\times \mathbf{w} \cdot \mathbf{v} = \nabla\cdot (\mathbf{w} \times \mathbf{v}) + \mathbf{w} \cdot \nabla\times \mathbf{v}$ and $\nabla\cdot (w\mathbf{v}) = w\nabla\cdot \mathbf{v} + \mathbf{v} \cdot \nabla\, w$, respectively, and Green's theorem yield

$$\int_{\Omega} [\mu^{-1}\nabla\times \mathbf{A} \cdot \nabla\times \bar{\mathbf{v}} + (i\omega\sigma - \omega^2\varepsilon)\, \mathbf{A} \cdot \bar{\mathbf{v}} + (\sigma + i\omega\varepsilon)\nabla\, V \cdot \bar{\mathbf{v}}]\, d\mathbf{x} + \int_{\partial\Omega} \mathbf{n} \times \left(\mu^{-1}\nabla\times \mathbf{A}\right) \cdot \bar{\mathbf{v}}\, d\mathbf{x} = 0 \quad \forall \mathbf{v} \in V \tag{4.23a}$$

$$\int_{\Omega} [(i\omega\sigma - \omega^2\varepsilon)\, \mathbf{A} \cdot \nabla\, \bar{w} + (\sigma + i\omega\varepsilon)\, \nabla\, \phi \cdot \nabla\, \bar{w}]\, d\mathbf{x} + \int_{\partial\Omega} \mathbf{n} \cdot [(i\omega\sigma - \omega^2\varepsilon)\, \mathbf{A} + (\sigma + i\omega\varepsilon)\, \nabla\, \phi] \cdot \bar{w}\, d\mathbf{x} = 0 \quad \forall w \in W. \tag{4.23b}$$

$\mathbf{n}$ represents the outward unit normal vector again. Portions of the integrals over all boundaries $\partial\Omega =$

$\Gamma_\perp \cup \Gamma_{||} \cup \Gamma_{\text{top}} \cup \Gamma_{\text{bottom}} \cup \Gamma_{\text{int}}$ of the domain Ω

$$\begin{aligned} \int_{\partial\Omega} \mathbf{n} \times \left(\mu^{-1}\nabla\times \mathbf{A}\right) \cdot \bar{\mathbf{v}}\, d\mathbf{x} &= -\int_{\partial\Omega\setminus\Gamma_{\text{int}}} (\mathbf{n}\times\bar{\mathbf{v}}) \cdot \left(\mu^{-1}\nabla\times \mathbf{A}\right)\, d\mathbf{x} \\ &+ \int_{\Gamma_{\text{int}}} (\mathbf{n}_1 \times \mathbf{H}_1 - \mathbf{n}_2 \times \mathbf{H}_2) \cdot \bar{\mathbf{v}}\, d\mathbf{x}, \qquad (4.24a) \end{aligned}$$

$$\begin{aligned} \int_{\partial\Omega} \mathbf{n} \cdot [(i\omega\sigma - \omega^2\varepsilon)\,\mathbf{A} + (\sigma &+ i\omega\varepsilon)\,\nabla\,\phi] \cdot w\, d\mathbf{x} = \int_{\Gamma_{\text{int}}} (\mathbf{n}_1\cdot\mathbf{j}_1 - \mathbf{n}_2\cdot\mathbf{j}_2) w\, d\mathbf{x} \\ &+ \int_{\partial\Omega\setminus\Gamma_{\text{int}}} \mathbf{n}\cdot\left[(i\omega\sigma - \omega^2\varepsilon)\,\mathbf{A} + (\sigma + i\omega\varepsilon)\,\nabla\,\phi\right] \cdot w\, d\mathbf{x} \end{aligned}$$
(4.24b)

vanish on $\Gamma_{||}$ and Γ_{int} (cf. eqs (3.11c) and (3.11f)). To eliminate the portion of the boundary integral on $\Gamma_\perp$ as well, $\mathbf{n}\times\bar{\mathbf{v}} = 0$ is chosen there. On Γ_{top} and Γ_{bottom}, we have data for $\mu^{-1}\nabla\times\mathbf{A} = \mathbf{H}_n(x,y,z)$, however, $\mathbf{n}\cdot((i\omega\sigma - \omega^2\varepsilon)\,\mathbf{A} + (\sigma + i\omega\varepsilon)\nabla\,\phi) = \mathbf{n}\cdot\mathbf{j} = 0$ applies to the lower integral (cf. eq. 3.11e). Therewith, the weak formulation of BVP (iii) described by eqs (3.11) reads as follows

BVP (iii) Find $\mathbf{A} \in U$ and $\phi \in F$ such that

$$\begin{aligned} \int_\Omega (\mu^{-1}\nabla\times\mathbf{A}\cdot\nabla\times\mathbf{v} &+ (i\omega\sigma - \omega^2\varepsilon)\,\mathbf{A}\cdot\mathbf{v} + (\sigma + i\omega\varepsilon)\,\nabla\,\phi\cdot\mathbf{v})\, d\mathbf{x} \\ &= \int_{\Gamma_{\text{top}}} (\mathbf{n}\times\bar{\mathbf{v}})\cdot\mathbf{H}_n\, d\mathbf{x} + \int_{\Gamma_{\text{bottom}}} (\mathbf{n}\times\bar{\mathbf{v}})\cdot\mathbf{H}_n\, d\mathbf{x} \quad \text{and} \qquad (4.25a) \\ \int_\Omega ((i\omega\sigma - \omega^2\varepsilon)\,\mathbf{A}\cdot\nabla\,w &+ (\sigma + i\omega\varepsilon)\,\nabla\,\phi\cdot\nabla\,w)\, d\mathbf{x} = 0 \quad \forall\mathbf{v}\in V \quad \text{and} \quad w \in W \qquad (4.25b) \end{aligned}$$

where

$$\begin{aligned} U &:= \{\mathbf{A}\in H(\text{curl},\Omega) : \mathbf{n}\times\mathbf{A} = 0 \quad \text{on} \quad \Gamma_\perp\}, && (4.26a) \\ F &:= \{\phi\in H^1(\Omega) : \phi = 0 \quad \text{on} \quad \Gamma_\perp\}, && (4.26b) \\ V &:= \{\mathbf{v}\in H(\text{curl},\Omega) : \mathbf{n}\times\mathbf{v} = 0 \quad \text{on} \quad \Gamma_\perp\}, && (4.26c) \\ W &:= \{w\in H^1(\Omega) : w \equiv 0 \quad \text{on} \quad \Gamma_\perp\}, && (4.26d) \\ H(\text{curl},\Omega) &:= \{\mathbf{v}\in (L^2(\Omega))^3, \nabla\times\mathbf{v}\in (L^2(\Omega))^3\} \quad \text{and} && (4.26e) \\ H^1(\Omega) &:= \{w\in L^2(\Omega), \nabla w\in (L^2(\Omega))^3\}. && (4.26f) \end{aligned}$$

Due to the homogeneous boundary conditions for $\mathbf{n}\times\mathbf{A}$ and ϕ on $\Gamma_\perp$, the trial and test functions can be chosen from the same function spaces V and W, respectively.

Following the derivation of BVP (ii), the weak formulation of BVP (iv) (eqs (3.12)) is obtained as

BVP (iv) Find $\mathbf{A} \in U$ such that

$$\begin{aligned} \int_\Omega (\mu^{-1}\nabla\times\mathbf{A}\cdot\nabla\times\mathbf{v} + (i\omega\sigma - \omega^2\varepsilon)\,\mathbf{A}\cdot\mathbf{v})\, d\mathbf{x} &= \int_{\Gamma_{\text{top}}} (\mathbf{n}\times\bar{\mathbf{v}})\cdot\mathbf{H}_n\, d\mathbf{x} \\ &+ \int_{\Gamma_{\text{bottom}}} (\mathbf{n}\times\bar{\mathbf{v}})\cdot\mathbf{H}_n\, d\mathbf{x} \quad \forall\mathbf{v}\in V \quad (4.27) \end{aligned}$$

where

$$\begin{aligned} U &:= \{\mathbf{A} \in H(\text{curl}, \Omega) : \mathbf{n} \times \mathbf{A} = 0 \quad \text{on} \quad \Gamma_\perp\}, && \text{(4.28a)}\\ V &:= \{\mathbf{v} \in H(\text{curl}, \Omega) : \mathbf{n} \times \mathbf{v} = 0 \quad \text{on} \quad \Gamma_\perp\} \quad \text{and} && \text{(4.28b)}\\ H(\text{curl}, \Omega) &:= \{\mathbf{v} \in (L^2(\Omega))^3, \nabla \times \mathbf{v} \in (L^2(\Omega))^3\}. && \text{(4.28c)} \end{aligned}$$

The homogeneous boundary conditions for $\mathbf{n} \times \mathbf{A}$ on $\Gamma_\perp$ allow to choose the trial and test functions from the same function space V.

Finally, for BVP (v) represented by eqs (3.19), we obtain a weak formulation basing on the L^2-inner product $(\mathbf{u}, \mathbf{v}) = \int_\Omega \mathbf{u} \cdot \bar{\mathbf{v}} \, d\mathbf{x}$ with an arbitrary complex-valued vector test function $\mathbf{v}$ and its complex conjugate $\bar{\mathbf{v}}$

$$\int_\Omega \left[\left(\nabla\times \mu^{-1}(\nabla\times \mathbf{A}_a - \mu_a \mathbf{H}_n)\right) \cdot \bar{\mathbf{v}} + (i\omega\sigma - \omega^2\epsilon)\, \mathbf{A}_a \cdot \bar{\mathbf{v}}\right] d\mathbf{x} = \int_\Omega (\sigma_a + i\omega\varepsilon_a)\mathbf{E}_n \cdot \bar{\mathbf{v}} \quad \forall \mathbf{v} \in V. \tag{4.29}$$

Vector calculus yields

$$\begin{aligned} \int_\Omega [\mu^{-1}(\nabla\times \mathbf{A}_a - \mu_a \mathbf{H}_n) \cdot \nabla\times \bar{\mathbf{v}} \quad &+ \quad (i\omega\sigma - \omega^2\varepsilon)\, \mathbf{A}_a \cdot \bar{\mathbf{v}}]\, d\mathbf{x} \\ &+ \quad \int_{\partial\Omega} \mathbf{n} \times \left(\mu^{-1}(\nabla\times \mathbf{A}_a - \mu_a \mathbf{H}_n)\right) \cdot \bar{\mathbf{v}}\, d\mathbf{x} \\ &= \quad \int_\Omega (\sigma_a + i\omega\varepsilon_a)\mathbf{E}_n \cdot \bar{\mathbf{v}} \quad \forall \mathbf{v} \in V \end{aligned} \tag{4.30}$$

where

$$\begin{aligned} \int_{\partial\Omega} \mathbf{n} \times \left(\mu^{-1}(\nabla\times \mathbf{A}_a - \mu_a \mathbf{H}_n)\right) \cdot \bar{\mathbf{v}}\, d\mathbf{x} \quad &= \quad -\int_{\partial\Omega\setminus\Gamma_{\text{int}}} \mathbf{n} \times \left(\mu^{-1}(\nabla\times \mathbf{A}_a - \mu_a \mathbf{H}_n)\right) \cdot \bar{\mathbf{v}}\, d\mathbf{x} \\ &+ \quad \int_{\Gamma_{\text{int}}} (\mathbf{n}_1 \times \mathbf{H}_1 - \mathbf{n}_2 \times \mathbf{H}_2) \cdot \bar{\mathbf{v}}\, d\mathbf{x}. \end{aligned} \tag{4.31}$$

The boundary integral vanishes on Γ_{int} (cf. eq. 3.19c). On all other boundaries $\partial\Omega \setminus \Gamma_{\text{int}}$ the integral is eliminated from eq. (4.30) by choosing $\mathbf{v} \equiv 0$. Arranging all terms with known field values on the right-hand side, the weak form of BVP (v) reads as

BVP (v) Find $\mathbf{A}_a \in U$ such that

$$\begin{aligned} \int_\Omega (\mu^{-1}\nabla\times \mathbf{A}_a \cdot \nabla\times \bar{\mathbf{v}} \quad &+ \quad (i\omega\sigma - \omega^2\varepsilon)\, \mathbf{A}_a \cdot \bar{\mathbf{v}})\, d\mathbf{x} \\ &= \quad \int_\Omega ((\sigma_a + i\omega\varepsilon_a)\, \mathbf{E}_n \cdot \bar{\mathbf{v}} + \mu_a\, \mathbf{H}_n \cdot \nabla\times \bar{\mathbf{v}})\ d\mathbf{x} \quad \forall \mathbf{v} \in V \end{aligned} \tag{4.32}$$

where

$$\begin{aligned} U &:= \{\mathbf{A}_a \in H(\text{curl}, \Omega) : \mathbf{A}_a = 0 \quad \text{on} \quad \Gamma_{\text{top}},\ \Gamma_{\text{bottom}},\ \Gamma_\perp,\ \Gamma_{||}\}, && \text{(4.33a)}\\ V &:= \{\mathbf{v} \in H(\text{curl}, \Omega) : \mathbf{v} \equiv 0 \quad \text{on} \quad \Gamma_{\text{top}},\ \Gamma_{\text{bottom}},\ \Gamma_\perp,\ \Gamma_{||}\} \quad \text{and} && \text{(4.33b)}\\ H(\text{curl}, \Omega) &:= \{\mathbf{v} \in (L^2(\Omega))^3, \nabla \times \mathbf{v} \in (L^2(\Omega))^3\}. && \text{(4.33c)} \end{aligned}$$

Since the boundary conditions for $\mathbf{A}_a$ are homogeneous on the outer boundaries $\partial\Omega \setminus \Gamma_{\text{int}}$, the trial and test functions can be chosen from the same function space V.

4.2 Finite Element Analysis

4.2.1 Two-dimensional Finite Element Approximation Using Lagrange Elements

We seek discrete formulations of eqs (4.4) and (4.8) which read in general form as follows

$$b(u,v) = \int_\Omega (c\,\nabla u \cdot \nabla \bar{v} + a\,u\bar{v})\;d\mathbf{x} = 0 \quad \forall v \in V, \tag{4.34}$$

with function spaces

$$U := \{u \in H^1(\Omega) : u = r \quad \text{on} \quad \Gamma_\mathrm{D}\}, \tag{4.35a}$$
$$V := \{v \in H^1(\Omega) : v \equiv 0 \quad \text{on} \quad \Gamma_\mathrm{D}\} \quad \text{and} \tag{4.35b}$$
$$H^1(\Omega) := \{v \in L^2(\Omega), \nabla v \in (L^2(\Omega))^2\} \tag{4.35c}$$

and where the functions u and v and the coefficients a and c are associated with the electromagnetic field components and the electrical conductivity as well as the magnetic permeability as follows

E-Polarisation:

$$u := E_y, \quad c := \mu^{-1}, \quad a := i\omega\sigma - \omega^2\varepsilon, \tag{4.36}$$

H-Polarisation:

$$u := H_y, \quad c := (\sigma + i\omega\varepsilon)^{-1}, \quad a := i\omega\mu. \tag{4.37}$$

Preliminarily, the solution u and the test function v are both required to belong to the same infinite-dimensional function space V, i.e. $r \equiv 0$ in eq. (4.35a). The inhomogeneous Dirichlet boundary conditions $u = r \not\equiv 0$ will be taken into account later. Projection of the weak form onto an N_p-dimensional function subspace V_{N_p} means requiring $u, v \in V_{N_p}$. Taking N_p test functions $\psi_i \in V_{N_p}$ that form a basis of V_{N_p} and u^h as a linear combination of these basis functions and the scalar complex expansion coefficients U_j

$$u^h(\mathbf{x}) = \sum_{j=1}^{N_p} U_j \psi_j(\mathbf{x}), \tag{4.38}$$

we obtain the system of equations

$$\sum_{j=1}^{N_p} \left(\int_\Omega \big((c\,\nabla\psi_j) \cdot \nabla\bar{\psi}_i + a\,\psi_j\bar{\psi}_i \big)\, d\mathbf{x} \right) U_j = 0, \quad i = 1, \ldots, N_p. \tag{4.39}$$

It can be rewritten in matrix form

$$(\mathbf{K} + \mathbf{M})\mathbf{U} = \mathbf{0}, \tag{4.40}$$

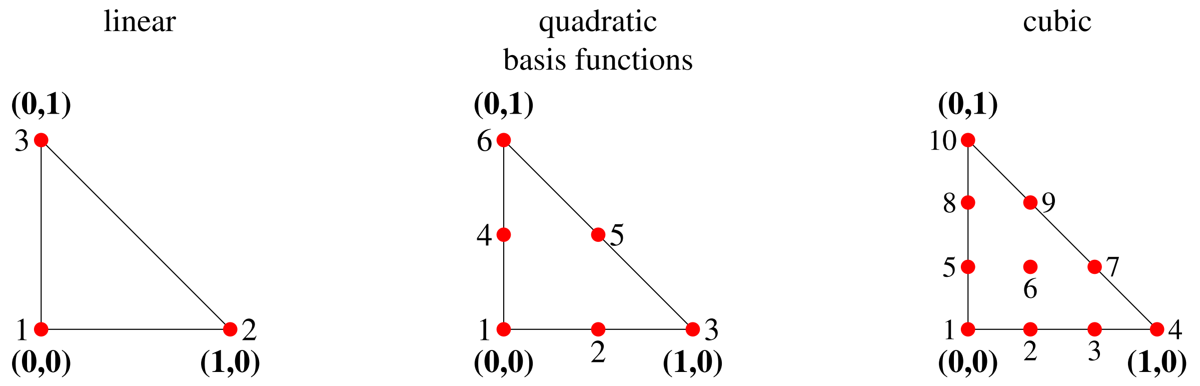

Fig. 4.1: Graphical representation of DOF: $l_i(u) = u(\mathbf{x}_i)$ for linear (left), quadratic (middle), and cubic (right) Lagrange elements.

with the stiffness matrix

$$K_{i,j} = \int_\Omega (c\,\nabla\psi_j)\cdot\nabla\bar{\psi}_i d\mathbf{x} \quad i,j = 1,...,N_p \tag{4.41}$$

and the mass matrix

$$M_{i,j} = \int_\Omega a\,\psi_j\bar{\psi}_i d\mathbf{x} \quad i,j = 1,...,N_p. \tag{4.42}$$

In the 2-D MT case, i.e. for simulating scalar field components in source-free regions, Lagrange elements whose degrees of freedom $l_n(\psi_j)$ are defined as values $\psi_j(\mathbf{x})$ at location $\mathbf{x}$ are well suited. In the 3-D case that is discussed in the following section, however, the application of curl-conforming vector elements seems to be more natural due to the conditions of continuity of the electromagnetic vector fields. Furthermore, we choose V_{N_p} to be a space of piecewise linear ($p = 1$), quadratic ($p = 2$), or cubic ($p = 3$) functions. The basis functions are designed such that

$$l_n(\psi_j) = \delta_{n,j} = \begin{cases} 1 & \text{if} \quad n = j \\ 0 & \text{if} \quad n \neq j \end{cases} \quad \text{and} \quad \sum_n l_n(\psi_j) = 1 \quad j = 1,...,N_p. \tag{4.43}$$

Using $l_i(\psi_i) = \psi_i(\mathbf{x_i}) = 1$ in eq. (4.38) with $\mathbf{x}_i$ denoting the location of the degrees of freedom leads to

$$u^h(\mathbf{x_i}) = \sum_{j=1}^{N_p} U_j\psi_j(\mathbf{x_i}) = U_i. \tag{4.44}$$

Hence, solving eq. (4.40) yields values of the approximate solution $u^h(\mathbf{x})$ for all DOF. In the case of linear ($p = 1$) basis functions, DOF are placed in the vertices of the triangles. Additional DOF appear at the edges for quadratic ($p = 2$) and cubic ($p = 3$) basis functions (cf. Fig. 4.1). Tab. 4.1 lists the coordinates of the DOF positions in the reference triangle (0,0) – (1,0) – (0,1). The integrals in eqs (4.41) and (4.42) are computed on each triangle ϑ by numerical quadrature. The system matrices $\mathbf{K}$ and $\mathbf{M}$ are assembled from the local matrices $\mathbf{K}^\vartheta$ and $\mathbf{M}^\vartheta$, respectively.

p	1 (linear)			2 (quadratic)						
no. of DOF	1	2	3	1	2	3	4	5	6	
x	0	1	0	0	0.5	1	0	0.5	0	
y	0	0	1	0	0	0	0.5	0.5	1	
p	3 (cubic)									
no. of DOF	1	2	3	4	5	6	7	8	9	10
x	0	0.33	0.67	1	0	0.33	0.67	0	0.33	0
y	0	0	0	0	0.33	0.33	0.33	0.67	0.67	1

Tab. 4.1: List of DOF positions for 2-D Lagrange elements in the reference triangle at (0,0) – (1,0) – (0,1).

The inhomogeneous Dirichlet boundary conditions with $r \not\equiv 0$ still need consideration. So far, the vector $\mathbf{U}$ contains N_p elements for the interior points in region $\Omega \setminus \Gamma_{\mathrm{D}}$ and $N_{\Gamma_{\mathrm{D}}}$ elements for the points on Γ_{D} whose values vanish (cf. eq. (4.35b)). Eq. (3.1b) provides the $N_{\Gamma_{\mathrm{D}}}$ non-zero values on Γ_{D} in $\mathbf{U}_{\Gamma_{\mathrm{D}}}$ which comprises N_p zero-elements for all the interior points. Applying

$$\mathbf{U} = \mathbf{U}_{\Omega\setminus\Gamma_{\mathrm{D}}} + \mathbf{U}_{\Gamma_{\mathrm{D}}} \tag{4.45}$$

to eq. (4.40), we derive a system of linear equations for $\mathbf{U}_{\Omega\setminus\Gamma_{\mathrm{D}}}$:

$$(\mathbf{K}+\mathbf{M})\mathbf{U}_{\Omega\setminus\Gamma_{\mathrm{D}}} = -(\mathbf{K}+\mathbf{M})\mathbf{U}_{\Gamma_{\mathrm{D}}}. \tag{4.46}$$

4.2.2 Three-dimensional Finite Element Approximation Using Vector Elements

In the following, the general form of BVP (i), BVP (ii), BVP (iv), and BVP (v)

$$\begin{aligned} b(\mathbf{u},\mathbf{v}) &= \int_\Omega ((c\,\nabla\times\mathbf{u})\cdot\nabla\times\bar{\mathbf{v}} + a\,\mathbf{u}\cdot\bar{\mathbf{v}})\,d\mathbf{x} = \int_\Omega \mathbf{q}_1\cdot\bar{\mathbf{v}}\,d\mathbf{x} + \int_\Omega \mathbf{q}_2\cdot\nabla\times\bar{\mathbf{v}}\,d\mathbf{x} \\ &+ \int_{\Gamma_{\text{top}}} (\mathbf{n}\times\bar{\mathbf{v}})\cdot\mathbf{g}_1\,d\mathbf{x} + \int_{\Gamma_{\text{bottom}}} (\mathbf{n}\times\bar{\mathbf{v}})\cdot\mathbf{g}_2\,d\mathbf{x} \quad \forall\mathbf{v}\in V \end{aligned} \tag{4.47}$$

where

$$\begin{aligned} U_{\text{(i)}} &:= \{\mathbf{u}\in H(\text{curl},\Omega) : \mathbf{u}=\mathbf{u}(x,y,z) \text{ on } \Gamma_{\text{top}}\cup\Gamma_{\text{bottom}}, \\ &\qquad \mathbf{n}\times\mathbf{u}=0 \text{ on } \Gamma_{||}\}, && (4.48a) \\ V_{\text{(i)}} &:= \{\mathbf{v}\in H(\text{curl},\Omega) : \mathbf{n}\times\mathbf{v}=0 \text{ on } \Gamma_{\text{top}}\cup\Gamma_{\text{bottom}}\cup\Gamma_{||}\}, && (4.48b) \\ U_{\text{(ii),(iv)}} &:= \{\mathbf{u}\in H(\text{curl},\Omega) : \mathbf{n}\times\mathbf{u}=0 \text{ on } \Gamma_{\perp}\}, && (4.48c) \\ V_{\text{(ii),(iv)}} &:= \{\mathbf{v}\in H(\text{curl},\Omega) : \mathbf{n}\times\mathbf{v}=0 \text{ on } \Gamma_{\perp}\}, && (4.48d) \\ U_{\text{(v)}} &:= \{\mathbf{u}\in H(\text{curl},\Omega) : \mathbf{u}=0 \text{ on } \Gamma_{\perp}\}, && (4.48e) \\ V_{\text{(v)}} &:= \{\mathbf{v}\in H(\text{curl},\Omega) : \mathbf{v}=0 \text{ on } \Gamma_{\perp}\}, \quad \text{and} && (4.48f) \\ H(\text{curl},\Omega) &:= \{\mathbf{v}\in (L^2(\Omega))^3, \nabla\times\mathbf{v}\in (L^2(\Omega))^3\}. && (4.48g) \end{aligned}$$

and

(i): $\mathbf{u} := \mathbf{H},\ a := i\omega\mu,\ c := (\sigma + i\omega\varepsilon)^{-1},\ \mathbf{q}_1 := 0,\ \mathbf{q}_2 := 0,\ \mathbf{g}_1 := 0,\ \mathbf{g}_2 := 0,$

(ii): $\mathbf{u} := \mathbf{E},\ a := i\omega\sigma - \omega^2\varepsilon,\ c := \mu^{-1},\ \mathbf{q}_1 := 0,\ \mathbf{q}_2 := 0,\ \mathbf{g}_1 := \mathbf{H}_n,\ \mathbf{g}_2 := \mathbf{H}_n,$

(iv): $\mathbf{u} := \mathbf{A},\ a := i\omega\sigma - \omega^2\varepsilon,\ c := \mu^{-1},\ \mathbf{q}_1 := 0,\ \mathbf{q}_2 := 0,\ \mathbf{g}_1 := \mathbf{H}_n,\ \mathbf{g}_2 := \mathbf{H}_n,$

(v): $\mathbf{u} := \mathbf{A}_a,\ a := i\omega\sigma - \omega^2\varepsilon,\ c := \mu^{-1},\ \mathbf{q}_1 := (\sigma_a + i\omega\varepsilon_a)\mathbf{E}_n,\ \mathbf{q}_2 := c\mu_a\mathbf{H}_n,$
$\mathbf{g}_1 := 0,\ \mathbf{g}_2 := 0.$

is considered. For BVP (i), we choose $\mathbf{u} \in U_{\text{(i)}}$ and $\mathbf{v} \in V_{\text{(i)}}$. Since the boundary conditions for $\mathbf{n} \times \mathbf{u}$ and $\mathbf{u}$ are homogeneous in the cases of BVP (ii), (iv), and (v), the trial and the test function spaces are $\mathbf{u},\ \mathbf{v} \in V_{\text{(ii),(iv)}}$ and $\mathbf{u},\ \mathbf{v} \in V_{\text{(v)}}$, respectively. The special case of BVP (iii) will be discussed in the appropriate place.
As in the 2-D case, we seek an approximation $\mathbf{u}^h \in V_{N_p}$ to $\mathbf{u} \in V$ with V_{N_p} being an N_p-dimensional function subspace of V. The inhomogeneous Dirichlet boundary conditions on Γ_{top} and Γ_{bottom} for BVP (i) (cf. eq (4.16a)) will be regarded later. Taking N_p complex-valued test functions $\boldsymbol{\psi}_i \in V_{N_p}$ that form a basis of V_{N_p} and $\mathbf{u}^h$ as a linear combination of these basis functions and the complex-valued expansion coefficients U_j

$$\mathbf{u}^h = \sum_{j=1}^{N_p} U_j \boldsymbol{\psi}_j, \tag{4.49}$$

the system of equations reads as

$$\sum_{j=1}^{N_p} \left(\int_\Omega \left((c\,\nabla\times \boldsymbol{\psi}_j) \cdot \nabla\times \bar{\boldsymbol{\psi}}_i + a\,\boldsymbol{\psi}_j \cdot \bar{\boldsymbol{\psi}}_i \right) d\mathbf{x} \right) U_j = L_i, \quad i = 1, ..., N_p. \tag{4.50}$$

with $\bar{\boldsymbol{\psi}}_i$ being the complex conjugate of $\boldsymbol{\psi}_i$. In matrix form we have

$$\mathbf{K}\mathbf{U} = \mathbf{L} \tag{4.51}$$

with

$$K_{i,j} \;=\; \int_\Omega (c\,\nabla \times \boldsymbol{\psi}_j \cdot \nabla \times \bar{\boldsymbol{\psi}}_i + a\,\boldsymbol{\psi}_j \cdot \bar{\boldsymbol{\psi}}_i) d\mathbf{x}, \tag{4.52}$$

$$L_i \;=\; \left\{ \begin{array}{cll} 0 & \text{for} & \text{bvp (i)} \\ \int_{\Gamma_{\text{top}}} (\mathbf{n} \times \bar{\boldsymbol{\psi}}_i) \cdot \mathbf{H}_n \, d\mathbf{x} + \int_{\Gamma_{\text{bottom}}} (\mathbf{n} \times \bar{\boldsymbol{\psi}}_i) \cdot \mathbf{H}_n \, d\mathbf{x} & \text{for} & \text{bvp (ii), (iv)} \\ \int_\Omega (\mu^{-1}\,\mu_a \mathbf{H}_n \cdot \nabla\times \bar{\boldsymbol{\psi}}_i + (\sigma_a + i\omega\varepsilon_a)\,\mathbf{E}_n \cdot \bar{\boldsymbol{\psi}}_i)\, d\mathbf{x} & \text{for} & \text{bvp (v)} \end{array} \right. . \tag{4.53}$$

Since the tangential components of $\mathbf{u}^h$ are expected to be continuous, we choose curl-conforming vector elements to approximate the solution of eq. (4.50). Their DOF are defined as integrals of $\mathbf{u}^h$ over edges, faces and the volume of each tetrahedron ϑ in case of V_{N_p} being a space of piecewise linear ($p = 1$), quadratic ($p = 2$) or cubic ($p = 3$) functions (cf. Fig. 4.2). The assumed DOF positions in the reference tetrahedron (0,0,0) – (1,0,0) – (0,1,0) – (0,0,1) are listed in Tab. 4.2.
As in the 2-D case, the basis functions are characterised by

$$l_n(\boldsymbol{\psi}_j) = \delta_{n,j} = \left\{ \begin{array}{ll} 1 \ \text{if} & n = j \\ 0 \ \text{if} & n \neq j \end{array} \right. \quad \text{and} \quad \sum_n l_n(\boldsymbol{\psi}_j) = 1 \quad j = 1, ..., N_p. \tag{4.54}$$

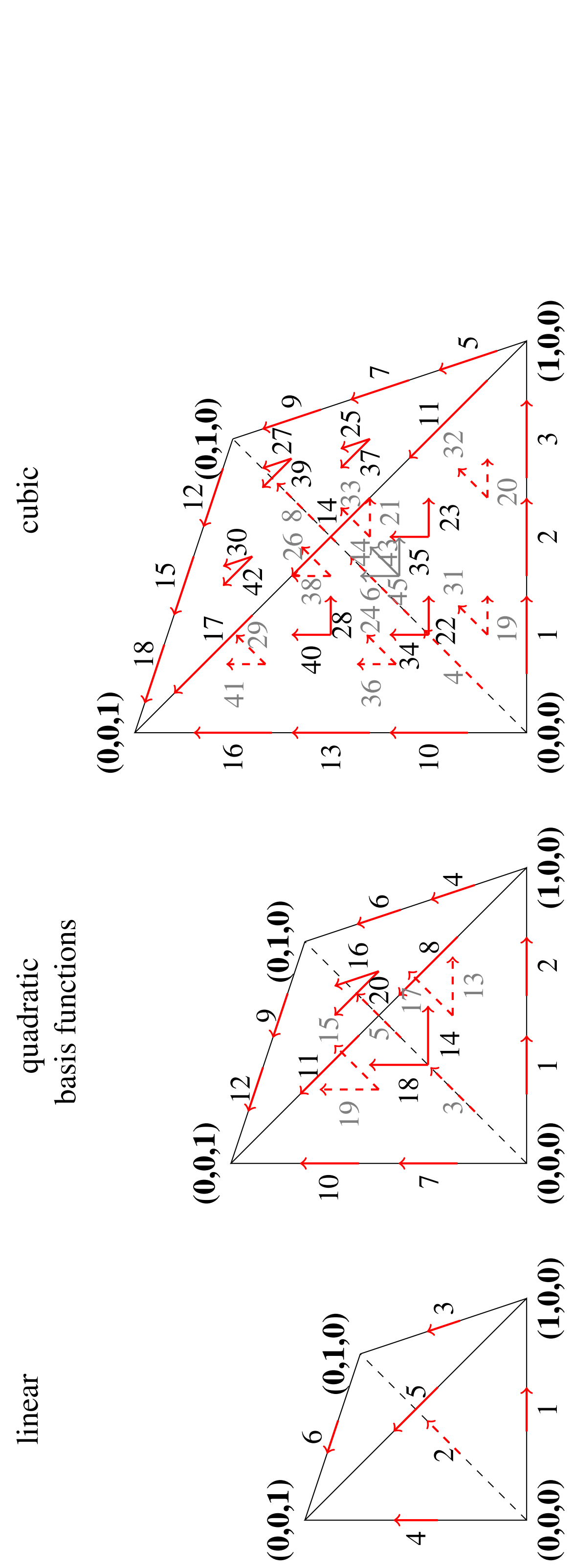

Fig. 4.2: Graphical representation of DOF: Integrals over $\mathbf{u}^h$ along edges and over faces for first-order and second-order curl-conforming vector elements. Additional volume associated DOF occur for cubic basis functions.

p	1 (linear)						2 (quadratic)						
no. of DOF	1	2	3	4	5	6	1	2	3	4	5	6	7
x	0.5	0	0.5	0	0.5	0	0.33	0.67	0	0.67	0	0.33	0
y	0	0.5	0.5	0	0	0.5	0	0	0.33	0.33	0.67	0.67	0
z	0	0	0	0.5	0.5	0.5	0	0	0	0	0	0	0.33
p	2 (quadratic)												
no. of DOF	8	9	10	11	12	13	14	15	16	17	18	19	20
x	0.67	0	0	0.33	0	0.33	0.33	0	0.33	0.33	0.33	0	0.33
y	0	0.67	0	0	0.33	0.33	0	0.33	0.33	0.33	0	0.33	0.33
z	0.33	0.33	0.67	0.67	0.67	0	0.33	0.33	0.33	0	0.33	0.33	0.33
p	3 (cubic)												
no. of DOF	1	2	3	4	5	6	7	8	9	10	11	12	13
x	0.25	0.5	0.75	0	0.75	0	0.5	0	0.25	0	0.75	0	0
y	0	0	0	0.25	0.25	0.5	0.5	0.75	0.75	0	0	0.75	0
z	0	0	0	0	0	0	0	0	0	0.25	0.25	0.25	0.5
p	3 (cubic)												
no. of DOF	14	15	16	17	18	19	20	21	22	23	24	25	26
x	0.5	0	0	0.25	0	0.25	0.5	0.25	0.25	0.5	0	0.5	0
y	0	0.5	0	0	0.25	0.25	0.25	0.5	0	0	0.25	0.25	0.5
z	0.5	0.5	0.75	0.75	0.75	0	0	0	0.25	0.25	0.25	0.25	0.25
p	3 (cubic)												
no. of DOF	27	28	29	30	31	32	33	34	35	36	37	38	39
x	0.25	0.25	0	0.25	0.25	0.5	0.25	0.25	0.5	0	0.5	0	0.25
y	0.5	0	0.25	0.25	0.25	0.25	0.5	0	0	0.25	0.25	0.5	0.5
z	0.25	0.5	0.5	0.5	0	0	0	0.25	0.25	0.25	0.25	0.25	0.25
p	3 (cubic)												
no. of DOF	40	41	42	43	44	45							
x	0.25	0	0.25	0.25	0.25	0.25							
y	0	0.25	0.25	0.25	0.25	0.25							
z	0.5	0.5	0.5	0.25	0.25	0.25							

Tab. 4.2: List of DOF positions for 3-D curl-conforming vector elements in the reference tetrahedron at (0,0,0) – (1,0,0) – (0,1,0) – (0,0,1) for polynomial degrees $p = 1$, $p = 2$, $p = 3$.

Solving eq. (4.50) yields the discrete approximate solution U_i at locations $\mathbf{x}_i$ of the DOF

$$\mathbf{u}^h(\mathbf{x}_i) = \sum_{j=1}^{N_p} U_j \boldsymbol{\psi}_j(\mathbf{x}_i) = U_i. \tag{4.55}$$

To compute the elements of the local stiffness matrix $\mathbf{K}^\vartheta$ and the local load vector $\mathbf{L}^\vartheta$, eqs (4.52), (4.53) and the integrals occuring in the definition of the DOF are evaluated by numerical quadrature on each tetrahedron ϑ. $\mathbf{K}$ and $\mathbf{L}$ are assembled from $\mathbf{K}^\vartheta$ and $\mathbf{L}^\vartheta$, respectively, taking into account the relation between local and global numbering of the DOF.

In the case of BVP (i), the incorporation of the inhomogeneous Dirichlet boundary conditions $\mathbf{U}_{\Gamma_\mathrm{D}}$ with $\mathbf{U} = \mathbf{U}_{\Omega\setminus\Gamma_\mathrm{D}} + \mathbf{U}_{\Gamma_\mathrm{D}}$ where $\mathbf{U}_{\Omega\setminus\Gamma_\mathrm{D}}$ is the solution in the interior region $\Omega \setminus \Gamma_\mathrm{D}$ yields a linear system of equations for $\mathbf{U}_{\Omega\setminus\Gamma_\mathrm{D}}$

$$\mathbf{K}\mathbf{U}_{\Omega\setminus\Gamma_\mathrm{D}} = -\mathbf{K}\mathbf{U}_{\Gamma_\mathrm{D}}. \tag{4.56}$$

BVP (iii) needs special treatment because two types of finite elements are applied to approximate $\mathbf{A}$ and ϕ. Using the notation of eqs (4.25) and (4.26), the general form of BVP (iii) reads as

$$\begin{aligned}\int_\Omega (c\,\nabla\times\mathbf{u}\cdot\nabla\times\bar{\mathbf{v}} \;&+\; a\,\mathbf{u}\cdot\bar{\mathbf{v}} + b\,\nabla f\cdot\bar{\mathbf{v}})\,d\mathbf{x} \\ &= \int_{\Gamma_\mathrm{top}} (\mathbf{n}\times\bar{\mathbf{v}})\cdot\mathbf{g}_1\,d\mathbf{x} + \int_{\Gamma_\mathrm{bottom}} (\mathbf{n}\times\bar{\mathbf{v}})\cdot\mathbf{g}_2\,d\mathbf{x} \quad \text{and}\end{aligned} \tag{4.57a}$$

$$\int_\Omega (a\,\mathbf{u}\cdot\nabla w \;+\; b\,\nabla f\cdot\nabla w)\,d\mathbf{x} = 0 \quad \forall\mathbf{v}\in V, \quad \forall w\in W \tag{4.57b}$$

where

$$\begin{aligned} U &:= \{\mathbf{A}\in H(\text{curl},\Omega) : \mathbf{n}\times\mathbf{A} = 0 \quad \text{on} \quad \Gamma_\perp\}, && (4.58a)\\ F &:= \{\phi\in H^1(\Omega) : \phi = 0 \quad \text{on} \quad \Gamma_\perp\}, && (4.58b)\\ V &:= \{\mathbf{v}\in H(\text{curl},\Omega) : \mathbf{n}\times\mathbf{v} = 0 \quad \text{on} \quad \Gamma_\perp\}, && (4.58c)\\ W &:= \{w\in H^1(\Omega) : w \equiv 0 \quad \text{on} \quad \Gamma_\perp\}, && (4.58d)\\ H(\text{curl},\Omega) &:= \{\mathbf{v}\in (L^2(\Omega))^3, \nabla\times\mathbf{v}\in (L^2(\Omega))^3\} \quad \text{and} && (4.58e)\\ H^1(\Omega) &:= \{w\in L^2(\Omega), \nabla w\in (L^2(\Omega))^3\} && (4.58f)\end{aligned}$$

with

$$\mathbf{u} := \mathbf{A},\; f := \phi,\; a := i\omega\sigma - \omega^2\varepsilon,\; b := \sigma + i\omega\varepsilon,\; c := \mu^{-1},\; \mathbf{g}_1 := \mathbf{H}_n,\; \mathbf{g}_2 := \mathbf{H}_n. \tag{4.59}$$

To find approximations $\mathbf{u}^h \in V_{N_p}$ to $\mathbf{u}\in V$ and $f^h \in W_{M_p}$ to $f\in W$, we take N_p test functions $\boldsymbol{\psi}_i \in V_{N_p}$ that form a basis of V_{N_p}, M_p test functions $\upsilon_i \in W_{M_p}$ that form a basis of W_{M_p} and $\mathbf{u}^h$ and f^h as linear combinations of these basis functions with expansion coefficients U_i and F_i, respectively

$$\mathbf{u}^h = \sum_{i=1}^{N_p} U_i\boldsymbol{\psi}_i, \qquad f^h = \sum_{i=1}^{M_p} F_i\upsilon_i. \tag{4.60}$$

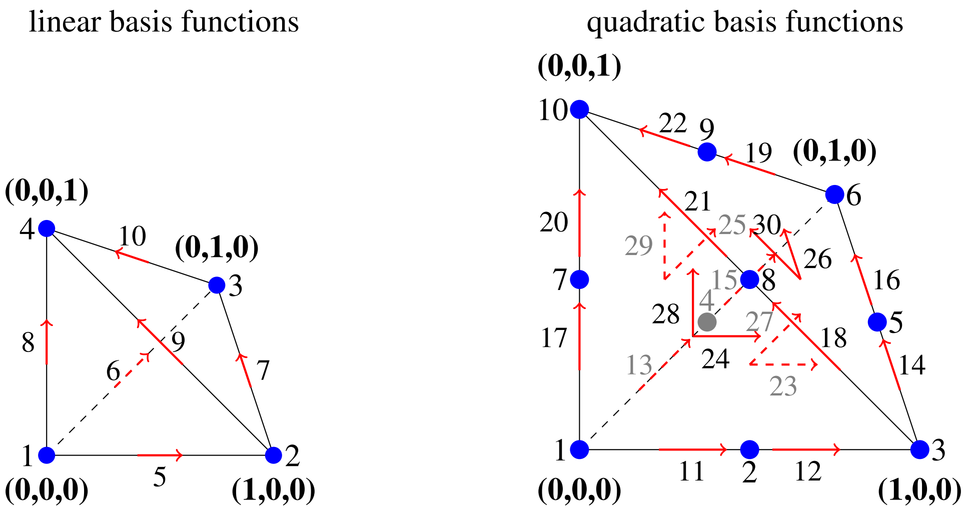

Fig. 4.3: Graphical representation of DOF: Integrals over $\mathbf{u}^h$ along edges and over faces as well as locations of f^h for first-order (left) and second-order (right) curl-conforming vector elements.

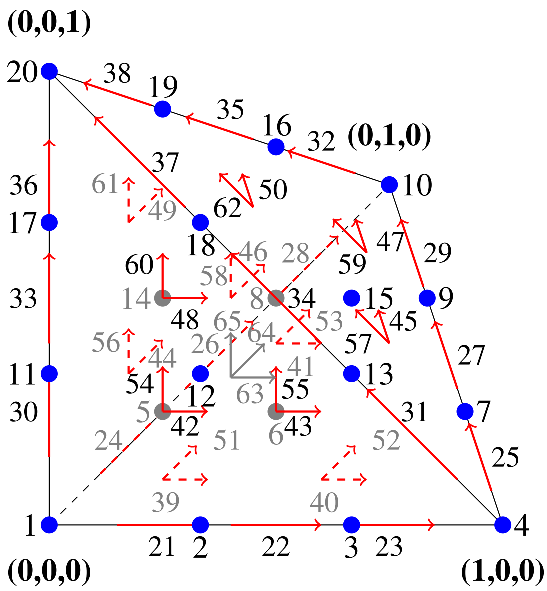

Fig. 4.4: Graphical representation of DOF for cubic basis functions: Integrals over $\mathbf{u}^h$ along edges, over faces and associated with the volume as well as locations of f^h for third-order curl-conforming vector elements.

p	1 (linear)										2 (quadratic)		
type	scalar				vector						scalar		
no. of DOF	1	2	3	4	5	6	7	8	9	10	1	2	3
x	0	1	0	0	0.5	0	0.5	0	0.5	0	0	0.5	1
y	0	0	1	0	0	0.5	0.5	0	0	0.5	0	0	0
z	0	0	0	1	0	0	0	0.5	0.5	0.5	0	0	0

p	2 (quadratic)												
type	scalar							vector					
no. of DOF	4	5	6	7	8	9	10	11	12	13	14	15	16
x	0	0.5	0	0	0.5	0	0	0.33	0.67	0	0.67	0	0.33
y	0.5	0.5	1	0	0	0.5	0	0	0	0.33	0.33	0.67	0.67
z	0	0	0	0.5	0.5	0.5	1	0	0	0	0	0	0

p	2 (quadratic)												
type	vector												
no. of DOF	17	18	19	20	21	22	23	24	25	26	27	28	29
x	0	0.67	0	0	0.33	0	0.33	0.33	0	0.33	0.33	0.33	0
y	0	0	0.67	0	0	0.33	0.33	0	0.33	0.33	0.33	0	0.33
z	0.33	0.33	0.33	0.67	0.67	0.67	0	0.33	0.33	0.33	0	0.33	0.33

p	2	3 (cubic)											
type	vector	scalar											
no. of DOF	30	1	2	3	4	5	6	7	8	9	10	11	12
x	0.33	0	0.33	0.67	1	0	0.33	0.67	0	0.33	0	0	0.33
y	0.33	0	0	0	0	0.33	0.33	0.33	0.67	0.67	1	0	0
z	0.33	0	0	0	0	0	0	0	0	0	0	0.33	0.33

p	3 (cubic)												
type	scalar								vector				
no. of DOF	13	14	15	16	17	18	19	20	21	22	23	24	25
x	0.67	0	0.33	0	0	0.33	0	0	0.25	0.5	0.75	0	0.75
y	0	0.33	0.33	0.67	0	0	0.33	0	0	0	0	0.25	0.25
z	0.33	0.33	0.33	0.33	0.67	0.67	0.67	1	0	0	0	0	0

Tab. 4.3: List of DOF positions for 3-D vector and Lagrange elements in the reference tetrahedron at (0,0,0) – (1,0,0) – (0,1,0) – (0,0,1) for polynomial degrees $p = 1$, $p = 2$, $p = 3$, part I.

p	3 (cubic)												
type	vector												
no. of DOF	26	27	28	29	30	31	32	33	34	35	36	37	38
x	0	0.5	0	0.25	0	0.75	0	0	0.5	0	0	0.25	0
y	0.5	0.5	0.75	0.75	0	0	0.75	0	0	0.5	0	0	0.25
z	0	0	0	0	0.25	0.25	0.25	0.5	0.5	0.5	0.75	0.75	0.75
p	3 (cubic)												
type	vector												
no. of DOF	39	40	41	42	43	44	45	46	47	48	49	50	51
x	0.25	0.5	0.25	0.25	0.5	0	0.5	0	0.25	0.25	0	0.25	0.25
y	0.25	0.25	0.5	0	0	0.25	0.25	0.5	0.5	0	0.25	0.25	0.25
z	0	0	0	0.25	0.25	0.25	0.25	0.25	0.25	0.5	0.5	0.5	0
p	3 (cubic)												
type	vector												
no. of DOF	52	53	54	55	56	57	58	59	60	61	62	63	64
x	0.5	0.25	0.25	0.5	0	0.5	0	0.25	0.25	0	0.25	0.25	0.25
y	0.25	0.5	0	0	0.25	0.25	0.5	0.5	0	0.25	0.25	0.25	0.25
z	0	0	0.25	0.25	0.25	0.25	0.25	0.25	0.5	0.5	0.5	0.25	0.25
p	3												
type	vector												
no. of DOF	65												
x	0.25												
y	0.25												
z	0.25												

Tab. 4.4: List of DOF positions for 3-D vector and Lagrange elements in the reference tetrahedron at (0,0,0) – (1,0,0) – (0,1,0) – (0,0,1), part II.

U_i and F_i are complex-valued. The resulting system of equations reads as

$$\begin{pmatrix} \mathbf{K}^1 & \mathbf{K}^2 \\ \mathbf{M}^1 & \mathbf{M}^2 \end{pmatrix} \begin{pmatrix} \mathbf{U} \\ \mathbf{F} \end{pmatrix} = \begin{pmatrix} \mathbf{L} \\ \mathbf{N} \end{pmatrix} \tag{4.61}$$

with

$$K^1_{i,j} = \int_\Omega ((c\nabla \times \boldsymbol{\psi}_j) \cdot \nabla \times \bar{\boldsymbol{\psi}}_i + a\,\boldsymbol{\psi}_j \cdot \bar{\boldsymbol{\psi}}_i) d\mathbf{x}, \tag{4.62}$$

$$K^2_{i,j} = \int_\Omega (b\,\nabla \upsilon_i \cdot \bar{\boldsymbol{\psi}}_j) d\mathbf{x}, \tag{4.63}$$

$$M^1_{i,j} = \int_\Omega (a\,\boldsymbol{\psi}_i \cdot \nabla \upsilon_j) d\mathbf{x}, \tag{4.64}$$

$$M^2_{i,j} = \int_\Omega (b\,\nabla \upsilon_i \cdot \nabla \upsilon_j) d\mathbf{x}, \tag{4.65}$$

$$L_i = \int_{\Gamma_{\text{top}}} (\mathbf{n} \times \bar{\boldsymbol{\psi}}_i) \cdot \mathbf{H}_n \; d\mathbf{x} + \int_{\Gamma_{\text{bottom}}} (\mathbf{n} \times \bar{\boldsymbol{\psi}}_i) \cdot \mathbf{H}_n \; d\mathbf{x}, \tag{4.66}$$

$$N_i = 0. \tag{4.67}$$

4.3 Equation Solver

To solve eqs (4.46), (4.56), and (4.61) numerically, direct, iterative, or geometrical multigrid methods can be applied. Based on Gauss elimination, direct solvers yield exact results whereas iterative techniques start from an initial guess and aim at reducing the residual to a certain tolerance. A variety of equation solvers of both types is available as software packages, e.g. UMFPACK (Davis, 2004a), SPOOLES (Ashcraft et al., 1999), GMRES (Saad & Schultz, 1986). They include elaborate techniques of matrix factorisation, pre-ordering, pivoting and even employ parallelisation as PARDISO (Schenk & Gärtner, 2004). Geometrical multigrid methods work on a hierarchy of nested grids. Their implementation is strongly dependent on the nature of the partial differential equation to be solved. In the case of Maxwell's equations, the null-space of the curl-curl operator requires hand-tailored treatment (Hiptmair, 1998) and no general software packages are available.

Direct solvers yield accurate results in a reasonable time but demand lots of memory. Since computer memory capacity is still growing, direct factorisation methods are of great interest also to compute pre-conditioning matrices to increase the convergence rate of iterative solvers. The examples shown in this thesis are restricted to the application of the direct equation solvers UMFPACK (Davis, 2004a) incorporated in the COMSOL Multiphysics® package for the 2-D simulations and PARDISO (Schenk & Gärtner, 2004) in the case of solving the 3-D BVPs. In the following, a LU-decomposition as the basic Gauss algorithm and a LDL^T-decomposition for symmetric matrices are presented.

4.3.1 LU-Decomposition

We consider the system of equations

$$\mathbf{A}\mathbf{x} = \mathbf{b}, \tag{4.68}$$

where $\mathbf{A}$ is the system matrix, $\mathbf{x}$ is the vector of unknown fields and $\mathbf{b}$ is an arbitrary vector describing sources or inhomogeneous Dirichlet boundary conditions. The solution of the eq. (4.68) is based on a so-called LU-decomposition of matrix $\mathbf{A}$ in an upper and a lower triangular matrix $\mathbf{U}$ and $\mathbf{L}$, respectively:

$$\mathbf{A} = \mathbf{L}\mathbf{U}. \tag{4.69}$$

The system of equations

$$\mathbf{A}\mathbf{x} = \mathbf{L}\mathbf{U}\mathbf{x} = \mathbf{b} \tag{4.70}$$

is solved substituting

$$\mathbf{U}\mathbf{x} = \mathbf{y} \quad \text{into} \quad \mathbf{L}\mathbf{U}\mathbf{x} = \mathbf{L}\mathbf{y} = \mathbf{b}. \tag{4.71}$$

In detail is

$$y_1 = \frac{b_1}{l_{11}}, \qquad y_2 = \frac{1}{l_{22}}\left(b_2 - l_{21}y_1\right) \tag{4.72}$$

and in general

$$y_i = \frac{1}{l_{ii}}\left(b_i - \sum_{k=1}^{i-1} l_{ik}y_k\right) \qquad (i > 1) \tag{4.73}$$

applies. The back substitution yields $\mathbf{x}$

$$x_n = \frac{y_n}{u_{nn}} \tag{4.74}$$

and

$$x_i = \frac{1}{u_{ii}}\left(y_i - \sum_{k=i+1}^{n} u_{ik}x_k\right) \qquad (i < n). \tag{4.75}$$

$\mathbf{L}$ and $\mathbf{U}$ remain to be determined:

$$\begin{pmatrix} l_{11} & & & & \\ l_{21} & l_{22} & & 0 & \\ \vdots & \vdots & \ddots & & \\ l_{n1} & l_{n2} & l_{n3} & \dots & l_{nn} \end{pmatrix} \begin{pmatrix} u_{11} & u_{12} & u_{13} & \dots & u_{1n} \\ & u_{22} & u_{23} & \dots & u_{2n} \\ 0 & & \ddots & & \vdots \\ & & & & u_{nn} \end{pmatrix} = \begin{pmatrix} a_{11} & \dots & a_{1n} \\ \vdots & & \vdots \\ & & \\ a_{n1} & \dots & a_{nn} \end{pmatrix} \tag{4.76}$$

This system consists of n^2 equations for $\frac{2n(n-1)}{2} + 2n = n^2 + n$ unknowns l_{ij} and u_{ij}. n unknowns are chosen to be $u_{ii} = 1$ ($i = 1, 2, ..., n$). Thus, we obtain

$$\begin{array}{llll} l_{11} = a_{11}, & l_{21} = a_{21} & \text{and} & l_{22} = a_{22} - l_{21}u_{12} \quad \text{as well as} \\ u_{12} = \frac{a_{12}}{l_{11}}, & u_{13} = \frac{a_{13}}{l_{11}} & \text{and} & u_{23} = \frac{1}{l_{22}}\left(a_{23} - l_{21}u_{13}\right). \end{array} \tag{4.77}$$

Hence, $\mathbf{L}$ and $\mathbf{U}$ are calculated as

$$\begin{array}{ll} l_{ij} = a_{ij} - \sum_{k=1}^{j-1} l_{ik}u_{kj} & (i \geq j) \quad \text{and} \\ u_{ij} = \frac{1}{l_{ii}}\left(a_{ij} - \sum_{k=1}^{i-1} l_{ik}u_{kj}\right) & (i < j). \end{array} \tag{4.78}$$

4.3.2 LDL^T-Decomposition

The factorisation of symmetric matrices does without the computation of $\mathbf{U}$. Since $a_{ij} = a_{ji}$,

$$l_{21} = a_{21} \qquad \text{and} \qquad l_{11}u_{21} = a_{12} = a_{21} = l_{21} \tag{4.79}$$

applies (cf. eq. 4.77) and eq. (4.78) reads as

$$u_{ij} = \frac{1}{l_{ii}}\left(a_{ij} - \sum_{k=1}^{i-1} l_{ik}u_{kj}\right) = \frac{l_{ji}}{l_{ii}} \qquad (i < j). \tag{4.80}$$

Furthermore, $\mathbf{L}$ can be decomposed into $\hat{\mathbf{L}}$ and an diagonal matrix $\mathbf{D}$

$$\mathbf{L} = \hat{\mathbf{L}}\mathbf{D} = \begin{pmatrix} 1 & & & \\ \hat{l}_{21} & 1 & & 0 \\ \hat{l}_{31} & \hat{l}_{32} & 1 & \\ \vdots & \vdots & & \ddots \\ \hat{l}_{n1} & \hat{l}_{n2} & \dots & & 1 \end{pmatrix} \begin{pmatrix} l_{11} & & & \\ & l_{22} & & \\ 0 & & l_{33} & & 0 \\ & & & \ddots & \\ & & & & l_{nn} \end{pmatrix} \tag{4.81}$$

$$\text{where} \qquad \hat{l}_{ij} = \frac{l_{ij}}{l_{jj}} \qquad (i > j).$$

The upper triangular matrix $\mathbf{U}$ is derived by transposing $\hat{\mathbf{L}}$: $\mathbf{U} = \hat{\mathbf{L}}^T$ and, hence, $\mathbf{UL} = \hat{\mathbf{L}}\mathbf{D}\hat{\mathbf{L}}^T$. Solving

$$\hat{\mathbf{L}}\mathbf{y} = \mathbf{b} \qquad \text{and} \qquad \mathbf{D}\hat{\mathbf{L}}^T\mathbf{x} = \mathbf{y} \tag{4.82}$$

is carried out in the same manner as presented in the previous section.
$\mathbf{A}$ is typically sparse since each grid node of the FE mesh has a small number of neighbours compared to the total number of nodes. Storing all non-zero elements and their position is sufficient and more efficient than keeping the whole matrix in the computer memory. Furthermore, for the 2-D BVPs as well as BVPs (i) and (ii) in 3-D, $\mathbf{A}$ is symmetric.
The numerical stability of an algorithm implementing a LU or LDL^T decomposition is increased by pivoting, i.e. allocating the largest absolute values to the matrix diagonal by exchanging columns (Schenk & Gärtner, 2006). Additionally, clever matrix factorisation techniques as multifrontal methods (Davis & Duff, 1997) and pre-ordering techniques (Ashcraft & Liu, 1998; Davis, 2004b) further improve the efficiency of direct equation solvers.

4.4 Convergence of the FE Solution

4.4.1 Error Estimation for the 2-D FE Solution

Assuming the exact solution $u \in H^k(\Omega)$ with regularity k and $u^h \in V_{N_p}$ being the 2-D FE solution, for a family of quasi-uniform meshes, the L^2-norm of the error $e_h := u - u^h$ of the numerical solution is bounded

$$||e_h||_{L^2} = ||u - u^h||_{L^2} \leq C_1 N^\alpha \tag{4.83}$$

where C_1 is a constant that is dependent on the regularity of the exact solution, the polynomial degree p of the basis functions, the modelling domain Ω, and the triangulation but does not depend on the exact solution u itself and the number N of DOF (Babuška & Aziz, 1972). In the case of quasi-uniform meshes, the ratio of size h_{max} of the largest element to the size h_{min} of the smallest element is bounded, i.e. the refinement applies to all parts of the mesh. The number N of degrees of freedom is proportional to h^{-2} in the 2-D case where h denotes the mesh size, e.g. the circumdiameter of a triangle. Considering N contrary to h for the error bound in eq. (4.83) allows to examine the convergence of the numerical solution not only in dependence on the mesh size (h-refinement) but also on the polynomial order of the finite elements (p-refinement).
The exponent

$$\alpha = -\frac{1}{d} \min\{k, p+1\} \tag{4.84}$$

with dimensionality $d = 2$ for the 2-D case is called the asymptotic rate of convergence or simply convergence rate. Sufficient regularity of the exact solution provided, i.e. $k > p + 1$, the convergence rate α is governed by the order of the finite elements. Optimum convergence rates are listed in Tab. 4.5. Note that, ∇u yielding the derived field components is calculated by differentiation of the basis functions and, hence, exhibits convergence behaviour that is one order lower than that of the FE solution itself. H^1-norm error estimates

$$||e_h||_{H^1} = ||u - u^h||_{L^2} + ||\nabla u - \nabla u^h||_{L^2} \leq C_2 N^\beta \quad \text{with} \quad \beta = -\frac{1}{2} \min\{k, p\} \tag{4.85}$$

result in the same optimum convergence rates as the L^2-norm estimates of the error of ∇u. C_2 is a constant with similar characteristics as C_1.

p	u	∇u
1	-1.00	-0.50
2	-1.50	-1.00
3	-2.00	-1.50

Tab. 4.5: Optimum convergence rate α for the simulated field component u and the derived field components that are proportional to ∇u in dependence of the polynomial degree p of the finite elements.

For further details on the FE method and a-priori error estimates, the reader is referred to Babuška and Aziz (1972), Ciarlet (1978), and Strang and Fix (1973).

4.4.2 Error Estimation for the 3-D FE Solution

The error of the 3-D vector FE solution is bounded as well (cf. Monk, 2003). Assuming the exact solution $\mathbf{u} \in H^k(\Omega)$ with regularity k and $\mathbf{u}^h \in V_{N_p}$ being the FE solution, for a family of quasi-uniform meshes, similar convergence rates for the error $\mathbf{e}_h := \mathbf{u} - \mathbf{u}^h$ of the numerical solution are implied by the L^2- und the $H(curl)$-norm

$$\begin{aligned} ||e_h||_{L^2} &= ||\mathbf{u} - \mathbf{u}^h||_{L^2} \leq C_1 N^\alpha && (4.86) \\ ||e_h||_{H(curl)} &= ||\mathbf{u} - \mathbf{u}^h||_{L^2} + ||\nabla\times \mathbf{u} - \nabla\times \mathbf{u}^h||_{L^2} \leq C_2 N^\alpha && (4.87) \end{aligned}$$

with

$$\alpha = -\frac{1}{d} \min\{k, p\} \quad \text{and} \quad d = 3 \tag{4.88}$$

using the same notation as above where the mesh size h is represented e.g. by the diameter of the surrounding sphere where a tetrahedron is embedded. The optimum convergence rates are as follows

$$\alpha = \begin{cases} -0.33, & p = 1 \\ -0.67, & p = 2 \\ -1.00, & p = 3. \end{cases} \tag{4.89}$$

4.4.3 Mesh Refinement Strategies

The quality of the FE solution might be improved by increasing the number of degrees of freedom N if the exact solution provides sufficient regularity. This is achieved by (i) increasing the number of mesh elements, i.e. reducing the size h of the mesh elements (h-refinement) or (ii) choosing higher-order basis functions (p-refinement). In the scope of this thesis, the order of the basis functions is restricted to $p = 1$ (linear basis functions), $p = 2$ (quadratic basis functions), and $p = 3$ (cubic basis functions). The h-refinement can be applied globally so that each element of the FE mesh is refined (uniform mesh refinement). On the basis of an error indicator function, elements with large errors can be chosen for refinement such that the mesh is refined adaptively in regions only where strong variations of the solution occur. Meshes are created by the COMSOL Multiphysics® mesh generator. The initial mesh is based on a Delaunay triangulation algorithm.

Uniform Mesh Refinement

Two refinement methods are used to subdivide all mesh elements:

1. The regular refinement divides each edge of the element into two new ones. Hence, in the 2-D case, we obtain four new triangles from a previous coarse triangle (cf. Fig. 4.5, left-hand side). In the 3-D case, one tetrahedron is subdivided into eight new elements (cf. Fig. 4.6, left-hand side).

2. The longest-edge bisection devides only the longest edge of the elements. Therefore, we get two new triangles in the 2-D case (cf. Fig. 4.5, right-hand side) and two new tetrahedra in the 3-D case as well (cf. Fig. 4.6, right-hand side).

Fig. 4.5: Visualization of the regular grid refinement technique (left) and the longest-edge bisection (right) for 2-D triangular elements.

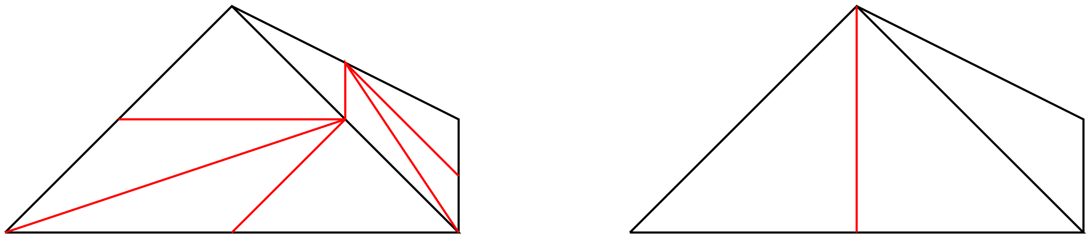

Fig. 4.6: Visualization of the regular grid refinement technique (left) and the longest-edge bisection (right) for 3-D tetrahedral elements.

Adaptive Mesh Refinement

According to an error indicator function based on *a-posteriori* error estimation (e.g. Monk, 2003), mesh elements with the largest errors are chosen for refinement so that the number of elements is increased by a given factor (e.g. 1.7). The selected elements are further subdivided by either the regular mesh refinement or the longest-edge bisection as described above for the uniform mesh refinement. The error $\mathbf{e}^h = \mathbf{u} - \mathbf{u}^h$ of the FE approximation satisfies the variational formulation

$$b(\mathbf{e}^h, \mathbf{v}) = b(\mathbf{u}, \mathbf{v}) - b(\mathbf{u}^h, \mathbf{v}) = -b(\mathbf{u}^h, \mathbf{v}) = \mathbf{R}^h(\mathbf{v}) \quad \forall \mathbf{v} \in V, \tag{4.90}$$

where $\mathbf{R}^h$ is called the weak residual.
In the 2-D case, according to eq. (4.34), eq. (4.90) can be rewritten as

$$b(e^h, v) = -\int_\Omega \left(c\nabla u^h \cdot \nabla v + au^h v\right) \, d\mathbf{x} \quad \forall v \in V. \tag{4.91}$$

Splitting the domain integral into contributions of each element ϑ that is part of the triangulation $\mathcal{T}_\mathrm{h}$ yields

$$b(e^h, v) = \sum_{\vartheta \in \mathcal{T}_\mathrm{h}} \left(-\int_\vartheta \left(c\nabla u^h \cdot \nabla v + au^h v\right) \, d\mathbf{x} \right) \quad \forall v \in V. \tag{4.92}$$

The vector identity $\nabla \cdot (c\nabla uv) = \nabla \cdot (c\nabla u)\, v + (c\nabla u) \cdot \nabla v$ and Green's theorem lead to

$$b(e^h, v) \;=\; \sum_{\vartheta \in \mathcal{T}_\mathrm{h}} \int_\vartheta \left(\nabla \cdot \left(c\nabla u^h\right) - au^h\right) v \, d\mathbf{x} - \sum_{\tau \in \Gamma_\mathrm{int}} \int_\tau \mathbf{n}_\tau c \nabla u^h v \, dl \quad \forall v \in V, \tag{4.93}$$

where $\tau \subset \Gamma_\mathrm{int}$ includes all interior edges in the domain Ω. For the exterior boundaries, $v \equiv 0$

holds (cf. eq. (4.35b)). According to interpolation theory (Johnson, 1987), the error that arises from projecting $v \in V$ onto $v^h \in V_{N_p}$ can be estimated as $\nu_1 h_\vartheta \|v\|$ on all triangles ϑ and $\nu_2 \sqrt{h_\tau}\|v\|$ on all edges τ with $\nu_1, \nu_2 \in R$ being constant for a triangulation. h_ϑ and h_τ denote the local mesh size and the length of edge τ, respectively. A typical measure for the local mesh size h_ϑ is the circumradius of the triangle ϑ. Using these estimates and the Cauchy-Schwarz inequality, we derive

$$b(e^h, v) \leq \|v\| \left(\nu_1 \sum_{\vartheta \in \mathcal{T}_\mathrm{h}} \|\nabla \cdot (c\nabla u^h) - au^h\|^2 h_\vartheta^2 + \nu_2 \sum_{\tau \in \Gamma_\mathrm{int}} \| - \mathbf{n}_\tau c \nabla u^h\|^2 h_\tau \right)^{1/2} \quad \forall v \in V. \tag{4.94}$$

Employing the inequality $\kappa\|v\|^2 \leq b(v, v)$ ($\kappa \in R, \kappa =$ const.) and substituting e^h in place of v, an element-wise local error indicator $E(\vartheta)$ can be obtained

$$\|e^h\|^2 \leq E^2(\vartheta) = \alpha\|\nabla \cdot (c\nabla u^h) - au^h\|^2 h_\vartheta^2 + \beta \frac{1}{2} \sum_{\tau \in \Gamma_\mathrm{int}} \| - \mathbf{n}_\tau \cdot c\nabla u^h\|^2 h_\tau, \tag{4.95}$$

where $\alpha = \nu_1^2/\kappa^2$ and $\beta = \nu_2^2/\kappa^2$. The error indicator function depends on the local mesh size $h_\vartheta = h_\vartheta(\mathbf{x})$, the length h_τ of edge τ, the residual $\nabla \cdot (c\nabla u^h) - au^h$ on the triangle ϑ, and the jump in the tangential electromagnetic fields $\mathbf{n}_\tau \cdot c\nabla u^h$ across the element edge τ that is distributed equally to both triangles sharing the edge by the factor $\frac{1}{2}$. By $\| \cdot \|$ the L^2-norm is denoted. The real coefficients α, β, ν_1, ν_2, and κ are independent of the triangulation. In case of linear basis functions, $\nabla \cdot (c\nabla u^h)$ vanishes.

According to eq. (4.47), the weak residual $\mathbf{R}^h$ in the 3-D case for bvp (i), (ii), (iv), and (v) reads as

$$\mathbf{R}^h = b(\mathbf{e}^h, \mathbf{v}) = -\int_\Omega \left(\left(c\,\nabla\times \mathbf{u}^h \right) \cdot \nabla\times \mathbf{v} + a\,\mathbf{u}^h \cdot \mathbf{v} \right) d\mathbf{x} \quad \forall \mathbf{v} \in V. \tag{4.96}$$

Recently, Botha and Davidson (2005) have presented an elemental error indicator function η_i for vector elements

$$\eta_i^2 = h_i^2 \|\mathbf{R}_V\|^2 + \frac{1}{2} \sum_{f \subset \partial K_i} h_f \|\mathbf{R}_f\|^2 \tag{4.97}$$

that is composed of volume and face residuals $\mathbf{R}_V$ and $\mathbf{R}_f$, respectively, where

$$\mathbf{R}_V = -\nabla\times c\nabla\times \mathbf{u}^h - a\mathbf{u}^h \quad \text{and} \tag{4.98}$$

$$\mathbf{R}_f = -\mathbf{n} \times \left(c_1^{-1} \nabla\times \mathbf{u}_1^h - c_2^{-1} \nabla\times \mathbf{u}_2^h \right). \tag{4.99}$$

h_i and h_f denote the diameters of tetrahedron K_i and face f, respectively.

A similar error indicator function that is applicable to BVP (iii) is proposed by Beck et al. (2000)

$$\eta_i^2 = h_i^2 \|\mathbf{R}_V\|^2 + \frac{1}{2} \sum_{f \subset \partial K_i} h_f \left(\|\mathbf{R}_f^1\|^2 + \|\mathbf{R}_f^2\|^2 \right). \tag{4.100}$$

where

$$\mathbf{R}_V = -\nabla\times c\nabla\times \mathbf{u}^h - a\mathbf{u}^h - b\,\nabla\, f^h, \tag{4.101}$$

$$\mathbf{R}_f^1 = -\mathbf{n} \cdot \left((a_1 \mathbf{u}_1^h + b_1 \nabla\, f_1^h) - (a_2 \mathbf{u}_2^h - b\,\nabla\, f_2^h) \right) \quad \text{and} \tag{4.102}$$

$$\mathbf{R}_f^2 = -\mathbf{n} \times \left(c_1^{-1} \nabla\times \mathbf{u}_1^h - c_2^{-1} \nabla\times \mathbf{u}_2^h \right). \tag{4.103}$$

In Monk (2003), error indicator functions for Maxwell's equations are presented as well.
In the COMSOL Multiphysics® package (COMSOL, 2006) version 3.5a, however, a hierarchical basis error estimator (cf. Verfürth, 1996) is included to be applied to vector elements, i.e. to BVP (i)–(v). The volume and face residuals mentioned above are evaluated for a mapping of the solution to an auxiliary FE space consisting of higher-order finite elements. The polynomial order of the basis functions is increased by one. To compute the error indicator function, the discrete residuals are averaged per element.

4.5 Post-Processing Procedure

After having computed the 2-D FE solutions of eqs (3.1) and (3.2), the remaining field components still need to be determined in order to be able to calculate MT data such as the impedance tensor, the apparent resistivity, and the phase. From Maxwell's equations (eqs (2.1a),(2.1b)), we see that this can be done by numerical differentiation. In the 2-D case, the gradients of the basis functions are averaged per element. To yield the derivatives of the simulated field in a mesh point, the gradients of adjacent triangles are weighted by the area of the triangles.
In the 3-D case, however, the test function $\mathbf{v}$ and its curl $\nabla\times\mathbf{v}$ are both included in the FE formulation (cf. eqs (4.51), (4.52), (4.61), and (4.62)). Hence, no subsequent procedure performing a numerical differentiation or integration is necessary to obtain additional field components.

5 Comparison of the Numerical Solution for Different Formulations of the Magnetotelluric Boundary Value Problem by Convergence Studies

The quality of a numerical simulation approach is mainly prescribed by the accuracy of the solution and the computational cost, i.e. memory requirements and run time. In this chapter, the two-dimensional (2-D) and three-dimensional (3-D) boundary value problems (BVPs) introduced in section 3 are examined under these aspects in terms of convergence studies. First, a 2-D homogeneous-halfspace model with $\sigma = 0.01\,\mathrm{Sm}^{-1}$ is considered. Using several steps of uniform or adaptive geometrical mesh refinement (h-refinement) and increasing the polynomial degree of the basis functions (p-refinement) up to $p = 3$, the convergence of the FE solution towards the analytical solution is demonstrated for the frequencies $f = 1, 0.1, 0.01\,\mathrm{Hz}$. Second, since in general the true solution is unknown, the convergence of the numerical result to the finest-grid solution is analysed. Third, a convergence study for a 2-D layered-halfspace model illustrates that even simple conductivity structures affect the convergence behaviour. Finally, the numerical solutions of BVP (i) - (v) for the COMMEMI 3-D-2 model are examined regarding their convergence to the finest-grid solution in order to investigate the convergence behaviour in the presence of 3-D conductivity structures on the one hand and to compare the different formulations of the magnetotelluric (MT) BVP on the other hand.
All computaions are performed on a 2.4 GHz shared memory 32-cores computer using 2 of 8 processors each accommodating 4 cores.

5.1 Introduction to the Convergence Studies

In the following sections, convergence curves show the error of the numerical solution with respect to the analytical solution as a function of the number of degrees of freedom (DOF). The relative root-mean-square (rms) error is calculated by

$$\text{relative rms}^2 = \frac{\sum_{i=1}^{N} |u_i - F_i|^2}{\sum_{i=1}^{N} |F_i|^2}, \tag{5.1}$$

where u_i denotes the numerical solution for all DOF i ($i = 1, ..., N$) including boundary DOF represented by Dirichlet boundary conditions and $F_i = E_i, H_i$ is the analytical solution for the electric and magnetic field, respectively. The relative rms error for each mesh is determined on the finest grid of the hierarchy, i.e. each FE solution is mapped onto the finest grid and the error is computed for all DOF locations there. Hence, for one hierarchy of grids, F_i ($i = 1, ..., N$) and the associated norms $|F_i|$ ($i = 1, ..., N$) are constant for all meshes. Therefore, the optimum convergence rates presented in section 4.4 are expected to apply for the discrete relative rms error measure (eq. (5.1)) in the same manner as for the L^2-norm $||\cdot||_{L^2}$ that performs an area integration over the whole modelling domain to ensure a fixed reference value.

Note that, in order to estimate the errors of the simulated fields first, for the H-polarisation case in 2-D and the 3-D BVP (i), the magnetic field H_i is considered, whereas we examine the electric field E_i in the 2-D E-polarisation case and for 3-D BVP (ii) – (iv). In the case of BVP (iii) and (iv), E_i is calculated by using eq. (3.6) and eq. (3.9). In a second step, the errors for the derived field components (H-polarisation, BVP (i): E_i, E-polarisation, BVP (ii) – (iv): H_i) are computed.

From eq. (4.83) the asymptotic convergence rate α_{as} is determined as the slope of a linear function

$$\log(\text{relative rms}) = \alpha_{\text{as}} \log(N) + \beta, \tag{5.2}$$

fitting the data for sufficiently large numbers N of DOF in a least-squares sense. $\log(\cdot)$ denotes the common logarithm. Additionally, a limiting convergence rate α_{lim} is computed by

$$\alpha_{\text{lim}} = \frac{\log(\text{relative rms}(n)) - \log(\text{relative rms}(n-1))}{\log(N(n)) - \log(N(n-1))}, \tag{5.3}$$

for the finest (n) and the second-finest ($n-1$) grid of the appropriate hierarchy of meshes. If α_{lim} is significantly smaller than α_{as}, a stagnation of the relative rms error is indicated and, hence, the limit of the discretisation error of the boundary value problem is reached.

Considering the convergence to the finest-grid solution, a relative rms deviation is calculated by

$$\text{relative dev}^2 = \frac{\sum_{i=1}^{N} |u_i - u_i^n|^2}{\sum_{i=1}^{N} |u_i^n|^2}, \tag{5.4}$$

where u_i^n is the numerical solution on the finest grid of the hierarchy. Assuming that the finest grid yields the most accurate solution, the coarser-grid solutions are required to converge to the finest-grid solution. Eq. (5.4) is also applied to BVP (v) solved for the COMMEMI 3-D-2 model, where the simulated field is E_i and the derived field is H_i.

The asymptotic convergence rate α_{as} is then obtained as the slope of

$$\log(\text{relative dev}) = \alpha_{\text{as}} \log(N) + \beta, \tag{5.5}$$

and the limiting convergence rate α_{lim} can be computed as

$$\alpha_{\text{lim}} = \frac{\log(\text{relative dev}(n-1)) - \log(\text{relative dev}(n-2))}{\log(N(n-1)) - \log(N(n-2))}. \tag{5.6}$$

for the second-finest ($n-1$) and the third-finest ($n-2$) grid.

5.2 The 2-D Homogeneous-Halfspace Model: Comparison with the Analytical Solution

The following convergence studies are carried out for a homogeneous halfspace with electrical conductivity $\sigma = 0.01\,\text{Sm}^{-1}$. The 2-D model extends from $x_1 = -100\,\text{km}$ to $x_2 = 100\,\text{km}$. The homogeneous halfspace is chosen to be $100\,\text{km}$ deep. In the case of E-polarisation, an air space of $50\,\text{km}$ height is added.

5.2.1 h-Refinement versus p-Refinement

Fig. 5.1 displays convergence curves for the simulated field components in the case of E-polarisation (left-hand side) and H-polarisation (right-hand side). The polynomial order p of the basis functions varies among $p = 1$ (+), $p = 2$ (×), and $p = 3$ (□).

Obviously, the relative rms error decreases with increasing number N of DOF for E- and H-polarisation. For a given mesh, the number of DOF is enlarged by rising the polynomial order of the finite elements. Hence, smaller numerical errors are to be expected. The absolute value of the convergence rate, i.e. the slope of the linear trend line, however, is also increased with the polynomial degree of the basis functions. Thus, even with a similar number of DOF, the relative rms error is smaller using higher-order basis functions. Note that, the computational effort is not only increased with the number N of DOF but also depends on the sparsity pattern of the system matrix which becomes more complex for higher-order finite elements. The number of non-zero elements grows with the polynomial degree of the basis functions (cf. Fig. 5.2). With the matrix bandwith also the computational cost caused by direct solvers increases and opposes to the gain of accuracy with higher-order elements.

The convergence rates α_{as} and α_{lim} listed in Tab. 5.1 reflect the depicted behaviour. The asymptotic convergence rate α_{as} is calculated as the slope of a linear function that fits the data for appropriate numbers N of DOF in a least-squares sense. Data that do not exhibit a linear trend are neglected. In the present case, this applies to very coarse grids ($N < 300$). The asymptotic convergence rate is approximately the same for E- and H-polarisation and its absolute value increases with the order of the finite elements as expected from convergence theory (cf. section 4.4). The linear trends are displayed as black lines (–) in Fig. 5.1. The limiting convergence rate α_{lim} is computed as the slope between the largest and the second-largest number N of DOF. It does not differ by orders of magnitude from the asymptotic convergence rate α_{as} for all considered cases ($p = 1, 2, 3$, E- and H-polarisation). Hence, the limit of the discretisation error which will be indicated by a stagnation of the convergence curves, i.e. a small absolute value of the limiting convergence rate, is below $2.4 \cdot 10^{-9}$ and $1.0 \cdot 10^{-8}$ for E- and H-polarisation, respectively.

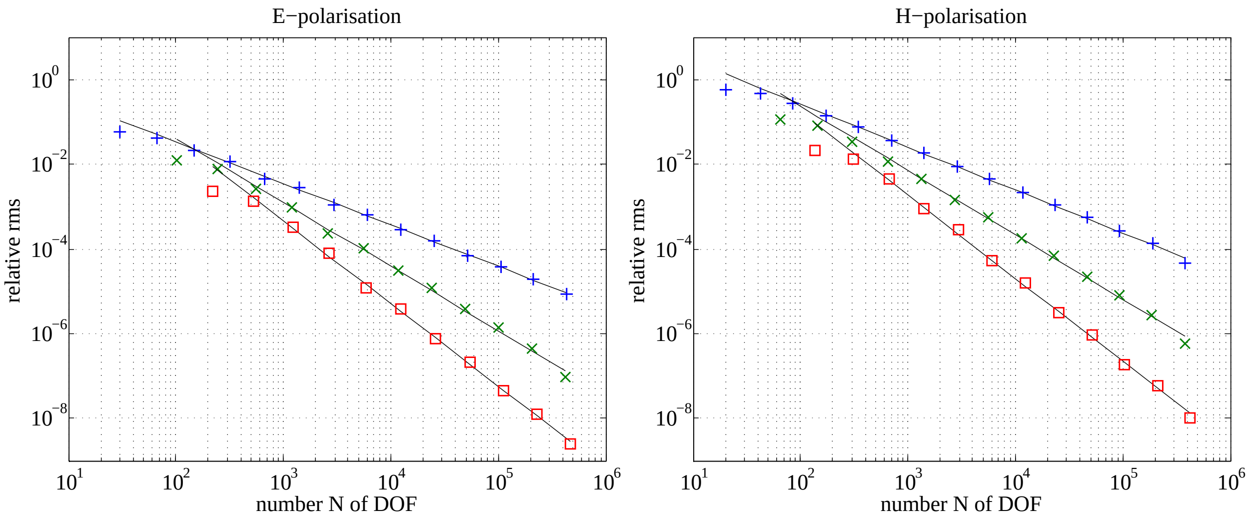

Fig. 5.1: Convergence curves of the global relative rms error of the simulated field components for E-polarisation (left) and H-polarisation (right) using linear ($p = 1$, +), quadratic ($p = 2$, ×) and cubic ($p = 3$, □) basis functions. Black lines (–) indicate the linear trend of each convergence curve for sufficiently large N. The frequency is $f = 0.1\,\text{Hz}$.

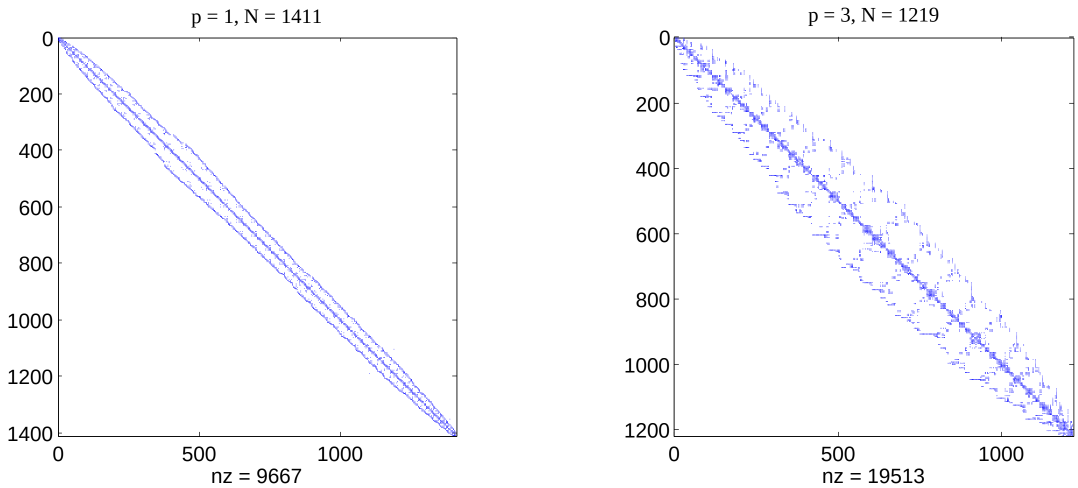

Fig. 5.2: Sparsity patterns for the system matrices $\mathbf{K} + \mathbf{M}$ for linear ($p = 1$, $N = 1411$, left) and cubic ($p = 3$, $N = 1219$, right) basis functions. Numbers nz of non-zero elements are 9687 and 19513 for $p = 1$ and $p = 3$, respectively.

	asymptotic conv. rate α_{as}			limiting conv. rate α_{lim}		
p	1 (linear)	2 (quadratic)	3 (cubic)	1 (linear)	2 (quadratic)	3 (cubic)
E-polarisation	-0.98	-1.51	-1.95	-1.06	-2.22	-2.32
H-polarisation	-1.01	-1.52	-1.96	-1.59	-2.23	-2.54

Tab. 5.1: Asymptotic (α_{as}) and limiting (α_{lim}) convergence rate for the simulated field components in the case of E- and H-polarisation depending on the polynomial degree p of the basis functions.

5.2.2 Frequency Dependence

The size of the computational domain used for the presented simulations is well suited for the frequency of $0.1\,\mathrm{Hz}$. The model boundaries are chosen to be 5 to 10 times the skin depth away from the center of the model (cf. P. E. Wannamaker, 1989). Since exact boundary conditions are applied in the case of the homogeneous halfspace, we ensure that no error is introduced by boundary effects. Therefore, the dependence of the discretisation error on the frequency is examined exclusively in the following. The frequency is chosen to be $f = 1, 0.1,$ or $0.01\,\mathrm{Hz}$.
Fig. 5.3 shows that, for one mesh, the relative rms errors decrease if the frequency is reduced. This is due to an enlarged skin depth δ ($\delta \propto \sqrt{T} \propto \sqrt{f^{-1}}$, cf. eq. (2.29)) in which a larger number of DOF is distributed for a given mesh. The asymptotic convergence rate α_{as}, however, is almost independent of the frequency. Using higher-order finite elements, the difference in the accuracy of the numerical solutions for varying frequencies is even more significant as Fig. 5.4 illustrates for cubic basis functions.
Tab. 5.2 quantifies the slopes of the convergence curves, i.e. the convergence rates. The asymptotic convergence rate α_{as} proves to be independent of the frequency and its absolute value increases with the order p of the finite elements. The limiting convergence rate α_{lim} does not indicate that the limit of the discretisation error is reached. Hence, it is expected to smaller than $7.9 \cdot 10^{-11}$ and $8.6 \cdot 10^{-11}$ for E- and H-polarisation, respectively (cf. Fig. 5.4).

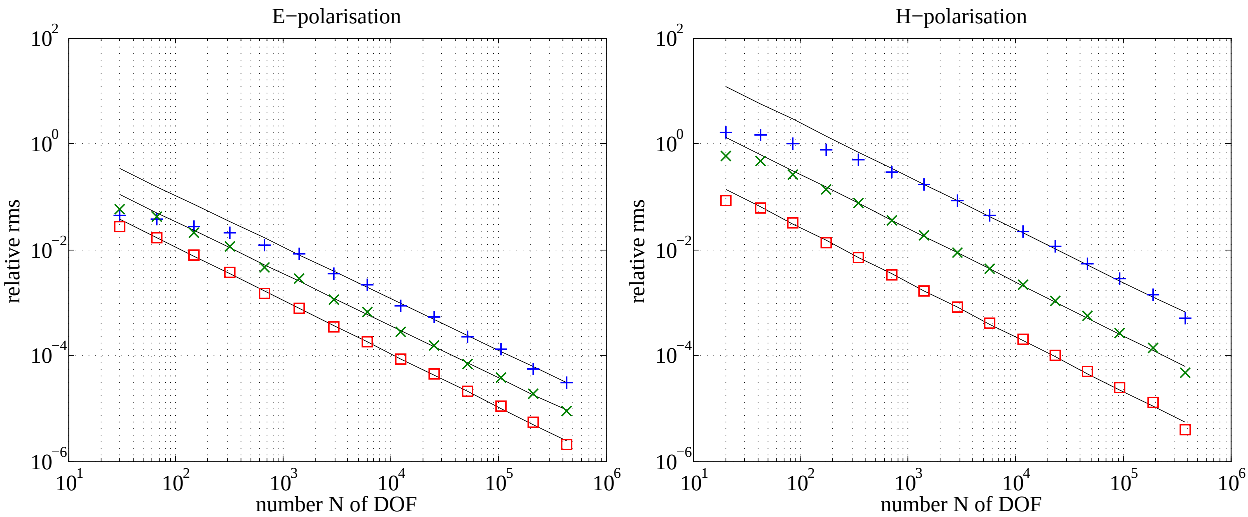

Fig. 5.3: Convergence curves of the global relative rms error of the simulated field component for E-polarisation (left) and H-polarisation (right) using linear ($p = 1$) basis functions. Frequencies are $f = 1\,\mathrm{Hz}$ (+), $f = 0.1\,\mathrm{Hz}$ (×), $f = 0.01\,\mathrm{Hz}$ (□). Black lines (–) indicate the linear trend of each convergence curve for sufficiently large N.

		asymptotic conv. rate α_{as}			limiting conv. rate α_{lim}		
	$f\,[\mathrm{Hz}]$	1	0.1	0.01	1	0.1	0.01
$p = 1$ (Fig. 5.3)	E-polarisation	-0.97	-0.98	-1.01	-0.87	-1.06	-1.37
	H-polarisation	-0.99	-1.01	-1.03	-1.50	-1.59	-1.70
$p = 2$ (no figure)	E-polarisation	-1.55	-1.51	-1.52	-2.12	-2.22	-2.24
	H-polarisation	-1.51	-1.52	-1.53	-2.15	-2.23	-2.29
$p = 3$ (Fig. 5.4)	E-polarisation	-1.94	-1.97	-2.01	-2.40	-2.32	-2.22
	H-polarisation	-1.98	-2.00	-2.01	-2.62	-2.54	-2.45

Tab. 5.2: Asymptotic (α_{as}) and limiting (α_{lim}) convergence rate for the simulated field component in the case of E- and H-polarisation depending on the polynomial degree p of the basis functions and the frequency f.

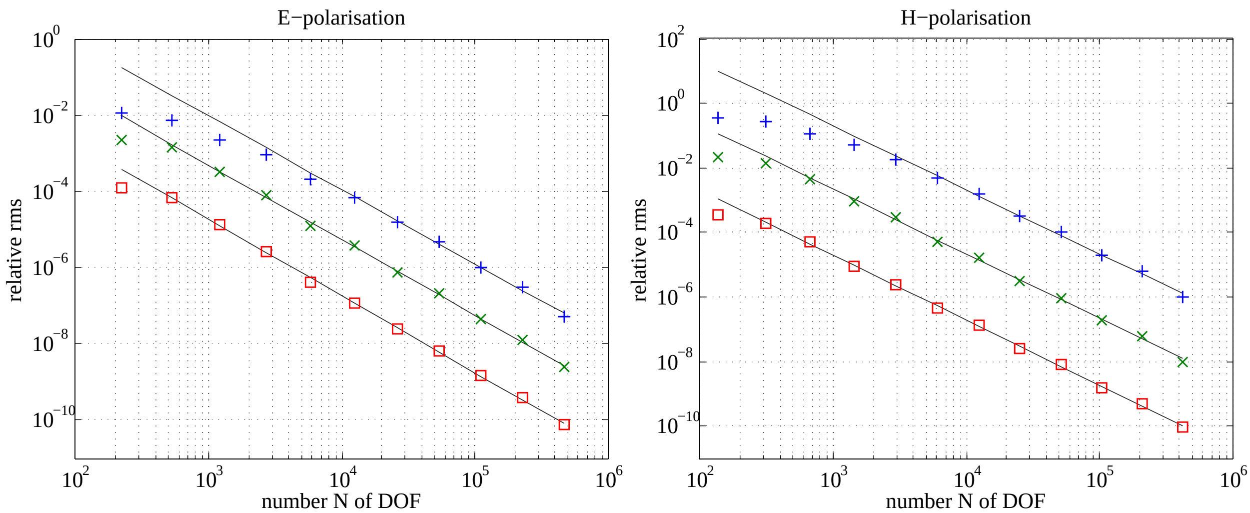

Fig. 5.4: Convergence curves of the global relative rms error of the simulated field components for E-polarisation (left) and H-polarisation (right) using cubic ($p = 3$) basis functions. Frequencies are $f = 1\,\mathrm{Hz}$ (+), $f = 0.1\,\mathrm{Hz}$ (×), $f = 0.01\,\mathrm{Hz}$ (□). Black lines (–) indicate the linear trend of each convergence curve for sufficiently large N until it stagnates.

5.2.3 Grid Refinement Methods

All convergence studies presented so far have been carried out applying a uniform longest-edge bisection as mesh refinement method. To compare this with other refinement strategies, Fig. 5.5 displays convergence curves for linear basis functions using the uniform refinement with the longest-edge bisection (+), the uniform regular refinement method (×), the adaptive mesh refinement in combination with the longest-edge bisection (□), and the adaptive regular mesh refinement (△), respectively, for generating the family of grids. In general, the regular mesh refinement (× and △) yields smaller errors than the longest-edge bisection (+ and □) considering both techniques for uniform (+ and ×) or adaptive mesh refinement (□ and △).
Advantages of the adaptive mesh refinement are obvious for cubic basis functions and a frequency of $f = 1\,\mathrm{Hz}$ (Fig. 5.6): It yields higher absolute values of the convergence rates (cf. Tab. 5.3) and provides significantly smaller errors than the uniform refinement in the H-polarisation case (Fig. 5.6, right-hand diagram).

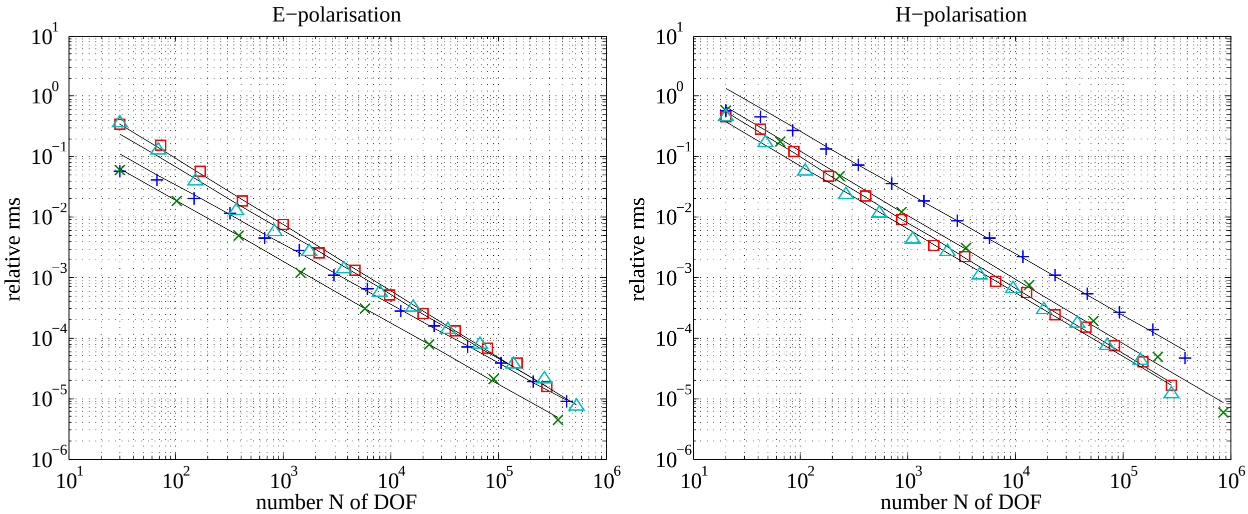

Fig. 5.5: Convergence curves of the global relative rms error of the simulated field components for E-polarisation (left) and H-polarisation (right) using linear ($p = 1$) basis functions. For generating the family of grids, the uniform refinement with the longest-edge bisection (+), the uniform regular refinement method (×), the adaptive mesh refinement in combination with the longest-edge bisection (□), and the adaptive regular mesh refinement (△) are applied, respectively. The frequency is $f = 0.1\,\mathrm{Hz}$. Black lines (–) indicate the linear trend of each convergence curve for sufficiently large N.

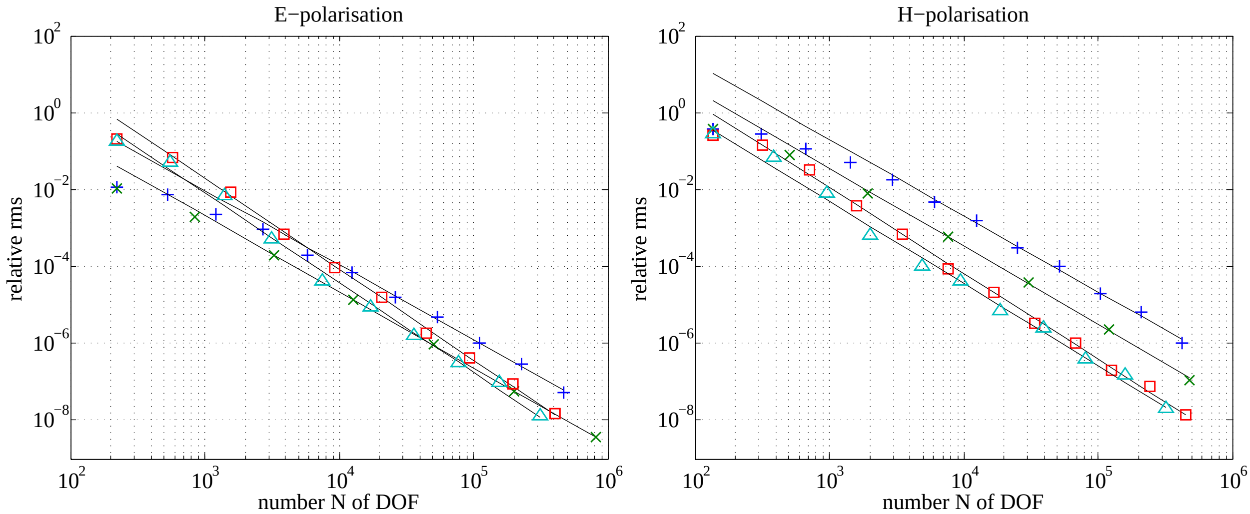

Fig. 5.6: Convergence curves of the global relative rms error of the simulated field components for E-polarisation (left) and H-polarisation (right) using cubic ($p = 3$) basis functions. For generating the family of grids, the uniform refinement with the longest-edge bisection (+), the uniform regular refinement method (×), the adaptive mesh refinement in combination with the longest-edge bisection (□), and the adaptive regular mesh refinement (△) are applied, respectively. The frequency is $f = 1\,\mathrm{Hz}$. Black lines (–) indicate the linear trend of each convergence curve for sufficiently large N.

p	$f\,[\mathrm{Hz}]$		asymptotic conv. rate α_{as}				limiting conv. rate α_{lim}			
		refinement method	uniform		adaptive		uniform		adaptive	
			longest edge	regular	longest edge	regular	longest edge	regular	longest edge	regular
1	0.1	E-polarisation	−0.98	−1.01	−1.09	−1.06	−1.06	−1.11	−1.47	−1.51
(Fig. 5.5)		H-polarisation	−1.01	−1.06	−1.08	−1.05	−1.59	−1.53	−1.53	−1.92
3	0.01	E-polarisation	−2.00	−2.02	−2.19	−2.09	−2.22	−1.12	−3.08	−3.14
(no figure)		H-polarisation	−2.02	−2.03	−2.05	−2.04	−2.45	−1.93	−2.02	−2.69
3	1	E-polarisation	−1.94	−1.97	−2.36	−2.33	−2.40	−1.97	−2.56	−2.85
(Fig. 5.6)		H-polarisation	−1.98	−2.03	−2.23	−2.13	−2.62	−2.24	−2.85	−2.89

Tab. 5.3: Asymptotic (α_{as}) and limiting (α_{lim}) convergence rate for the simulated field component in the case of E- and H-polarisation depending on the mesh refinement technique, the polynomial degree p of the basis functions and the frequency f.

5.2.4 Derived Field Components

After having discussed the convergence behaviour for the simulated field components, we turn to the non-zero derived field components now, i.e. the horizontal electric field for H-polarisation and the horizontal magnetic field for E-polarisation, respectively. Here, the vertical field components are of less importance and will not be considered due to them being zero in the homogeneous case.

h-Refinement versus p-Refinement

In general, the derived field components show the same behaviour as the simulated field components. However, the relative rms errors are larger (cf. e.g. Figs 5.7 and 5.1) and the absolute values of the convergence rates are lower for the derived field components (cf. e.g. Tabs 5.4 and 5.1). The asymptotic convergence rates α_{as} are in good agreement with the predicted values listed in Tab. 4.5 in section 4.4. Slightly reduced absolute values of the limiting convergence rates α_{lim} might indicate that the relative rms errors are approaching their limits. Due to limited computer memory capacity, it is not possible to perform further refinement steps to assess the limit of the relative rms error.

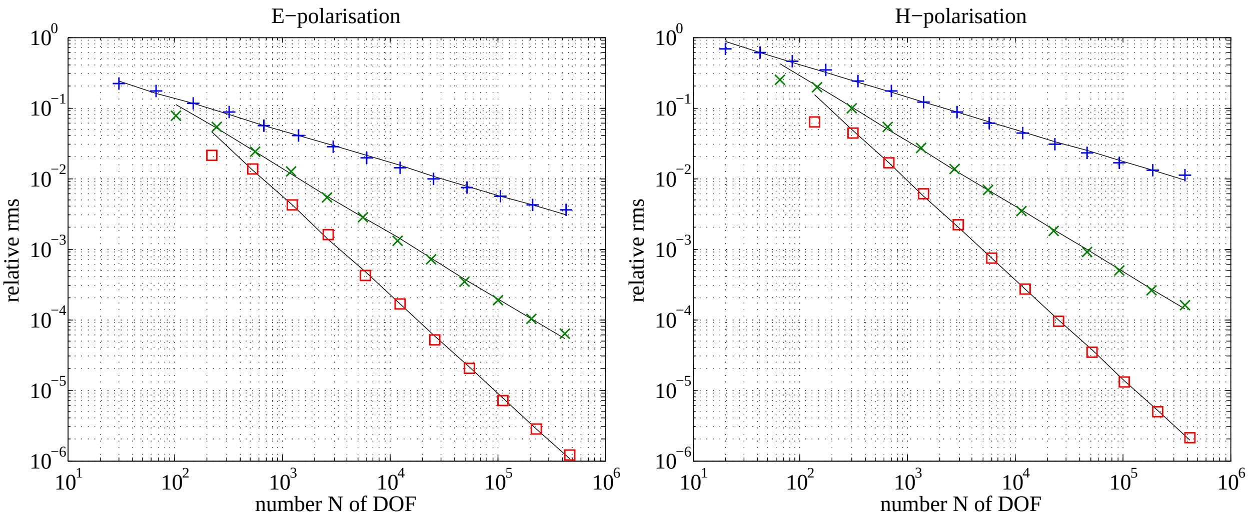

Fig. 5.7: Convergence curves of the global relative rms error of the derived field components for E-polarisation (left) and H-polarisation (right) using linear ($p = 1$, +), quadratic ($p = 2$, ×) and cubic ($p = 3$, □) basis functions. Black lines (–) indicate the linear trend of each convergence curve for sufficiently large N. The frequency is $f = 0.1$ Hz.

	asymptotic conv. rate α_{as}			limiting conv. rate α_{lim}		
p	1 (linear)	2 (quadratic)	3 (cubic)	1 (linear)	2 (quadratic)	3 (cubic)
E-polarisation	-0.46	-0.92	-1.39	-0.23	-0.69	-1.21
H-polarisation	-0.46	-0.93	-1.40	-0.25	-0.73	-1.20

Tab. 5.4: Asymptotic (α_{as}) and limiting (α_{lim}) convergence rate of the derived field components for E- and H-polarisation depending on the polynomial degree p of the basis functions.

Frequency Dependence

Figs 5.8 and 5.9 present convergence curves for linear ($p = 1$) and cubic ($p = 3$) basis functions, respectively. The dependence on the frequency appears in the same manner as in Figs 5.3 and 5.4.

For one mesh, the relative rms errors increase with decreasing frequency. Again, the slope of the convergence curves, i.e. the convergence rate, is independent of the frequency (cf. Tab. 5.5). The absolute values of the limiting convergence rates α_{lim} are slightly reduced. The relative rms may start to stagnate for large numbers N of DOF ($N > 100,000$). They are neglected for estimating the asymptotic convergence rates.

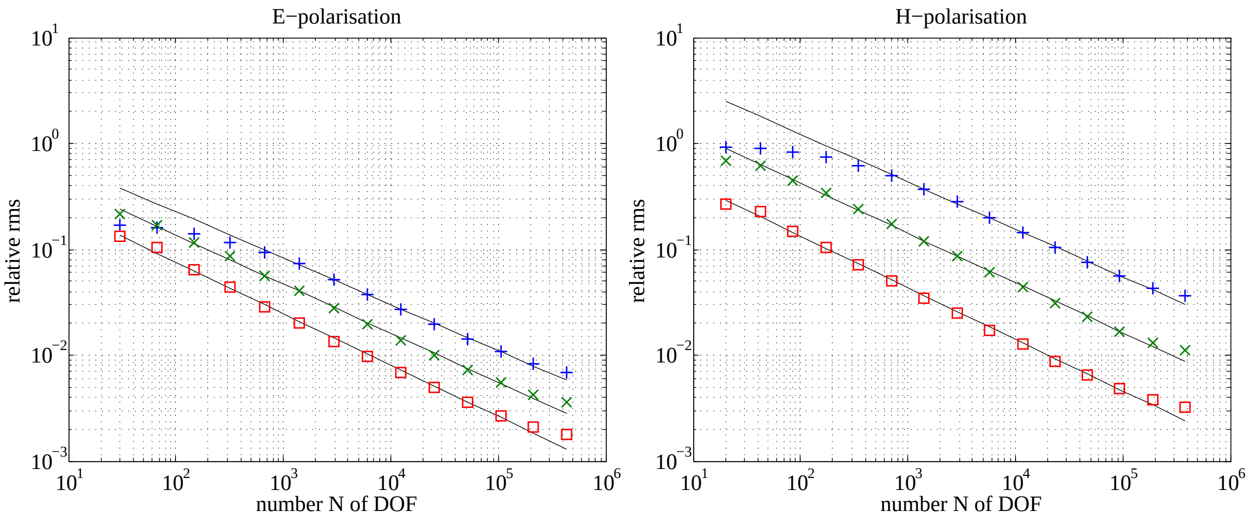

Fig. 5.8: Convergence curves of the global relative rms error of the derived field components for E-polarisation (left) and H-polarisation (right) using linear ($p = 1$) basis functions. Frequencies are $f = 1\,\text{Hz}$ (+), $f = 0.1\,\text{Hz}$ (×), $f = 0.01\,\text{Hz}$ (□). Black lines (–) indicate the linear trend of each convergence curve for sufficiently large N until it starts to stagnate.

p		asymptotic conv. rate α_{as}			limiting conv. rate α_{lim}		
	f[Hz]	1	0.1	0.01	1	0.1	0.01
1 (Fig. 5.8)	E-polarisation	-0.44	-0.46	-0.48	-0.25	-0.23	-0.21
	H-polarisation	-0.45	-0.47	-0.49	-0.25	-0.25	-0.24
2 (no figure)	E-polarisation	-0.88	-0.92	-0.97	-0.68	-0.69	-0.68
	H-polarisation	-0.90	-0.93	-0.97	-0.72	-0.73	-0.73
3 (Fig. 5.9)	E-polarisation	-1.32	-1.39	-1.47	-1.17	-1.21	-1.20
	H-polarisation	-1.38	-1.40	-1.47	-1.15	-1.20	-1.19

Tab. 5.5: Asymptotic (α_{as}) and limiting (α_{lim}) convergence rate of the derived field components for E- and H-polarisation depending on the polynomial degree p of the basis functions and the frequency f.

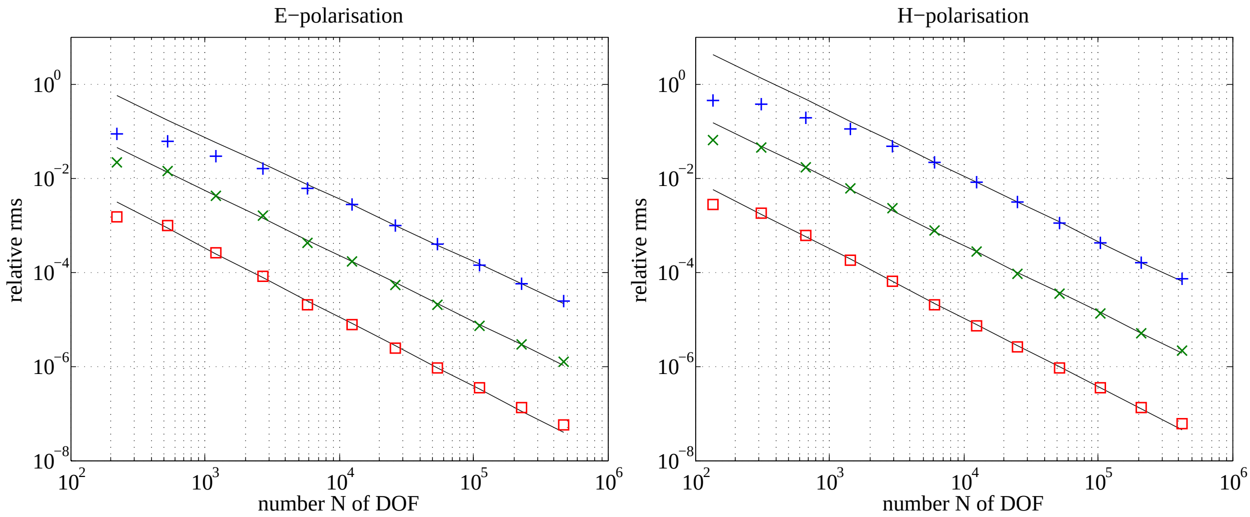

Fig. 5.9: Convergence curves of the global relative rms error for E-polarisation (left) and H-polarisation (right) using cubic ($p = 3$) basis functions. Frequencies are $f = 1\,\mathrm{Hz}$ (+), $f = 0.1\,\mathrm{Hz}$ (×), $f = 0.01\,\mathrm{Hz}$ (□). Black lines (–) indicate the linear trend of each convergence curve for sufficiently large N until it starts to stagnate.

Grid Refinement Methods

Considering different types of grid refinement for first-order ($p = 1$) and third-order ($p = 3$) finite elements at frequencies $f = 0.1\,\mathrm{Hz}$ and $f = 1\,\mathrm{Hz}$, respectively, similar conclusions can be drawn for the derived field components (Figs 5.10 and 5.11) as for the simulated field components (Figs 5.5 and 5.6). Adaptive mesh refinement strategies are advantageous especially for higher-order finite elements and high frequencies.

Fig. 5.10 shows most clearly that we need to expect a limit for the discretisation error. Tab. 5.6 also displays reduced limiting convergence rates α_{lim} for this case ($p = 1$, $f = 0.1\,\mathrm{Hz}$). The asymptotic convergence rates are estimated neglecting large numbers of DOF ($N > 100,000$). The limit of the discretisation error may be dependent on the frequency since Fig. 5.11 does not exhibit a stagnation of the rms errors for $f = 1\,\mathrm{Hz}$. Computations using more DOF are necessary to verify this and to estimate the limit of the error.

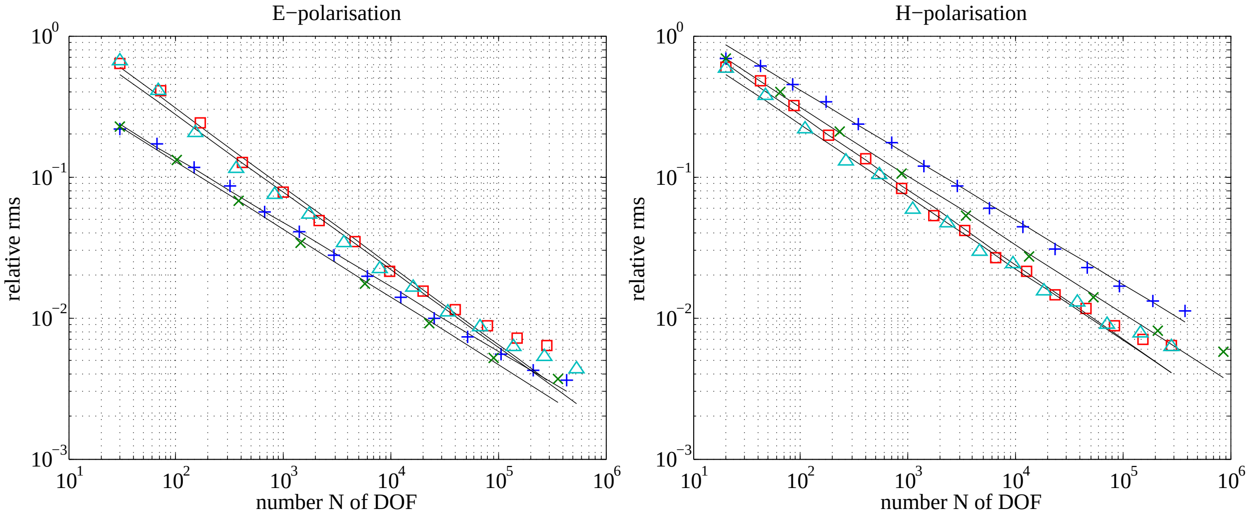

Fig. 5.10: Convergence curves of the global relative rms error of the derived field components for E-polarisation (left-hand side) and H-polarisation (right-hand side) using linear ($p = 1$) basis functions. For generating the family of grids, the uniform refinement with the longest-edge bisection (+), the uniform regular refinement method (×), the adaptive mesh refinement in combination with the longest-edge bisection (□), and the adaptive regular mesh refinement (△) are applied, respectively. The frequency is $f = 0.1\,\mathrm{Hz}$. Black lines (–) indicate the linear trend of each convergence curve for sufficiently large N until it starts to stagnate.

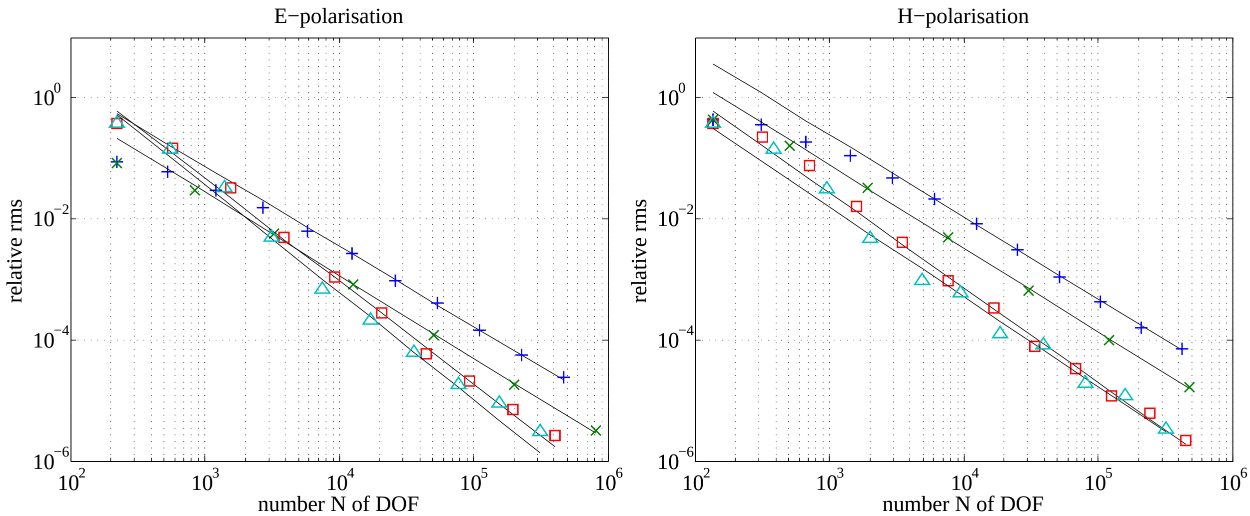

Fig. 5.11: Convergence curves of the global relative rms error of the derived field components for E-polarisation (left-hand side) and H-polarisation (right-hand side) using cubic ($p = 3$) basis functions. For generating the family of grids, the uniform refinement with the longest-edge bisection (+), the uniform regular refinement method (×), the adaptive mesh refinement in combination with the longest-edge bisection (□), and the adaptive regular mesh refinement (△) are applied, respectively. The frequency is $f = 1\,\mathrm{Hz}$. Black lines (–) indicate the linear trend of each convergence curve for sufficiently large N.

p	$f\,[\mathrm{Hz}]$		asymptotic conv. rate α_{as}				limiting conv. rate α_{lim}			
		refinement	uniform		adaptive		uniform		adaptive	
		method	longest edge	regular	longest edge	regular	longest edge	regular	longest edge	regular
1	0.1	E-polarisation	−0.46	−0.48	−0.56	−0.55	−0.23	−0.26	−0.21	−0.29
(Fig. 5.10)		H-polarisation	−0.46	−0.49	−0.53	−0.51	−0.25	−0.25	−0.15	−0.35
3	0.01	E-polarisation	−1.47	−1.45	−1.57	−1.52	−1.20	−1.27	−1.51	−1.41
(no figure)		H-polarisation	−1.45	−1.41	−1.49	−1.44	−1.19	−1.26	−1.29	−1.49
3	1	E-polarisation	−1.32	−1.37	−1.70	−1.78	−1.17	−1.27	−1.36	−1.55
(Fig. 5.11)		H-polarisation	−1.36	−1.38	−1.56	−1.49	−1.15	−1.29	−1.73	−1.79

Tab. 5.6: Asymptotic (α_{as}) and limiting (α_{lim}) convergence rate for the derived field components in the case of E- and H-polarisation depending on the mesh refinement technique, the polynomial degree p of the basis functions and the frequency f.

5.2.5 Local Convergence

In contrast to the global convergence that has been verified according to the expectations from convergence theory in the previous section, we focus on the local convergence in this section. Convergence curves are considered for all DOF located on the earth's surface and for one point $(0, 0)$ on the earth's surface that is chosen independently of the positions of the DOF. From the geophysical point of view, local convergence, i.e. convergence of the solution in some arbitrarily chosen data points, is even more important than global convergence that includes DOF in regions of the model, e.g. at large depths, where no measured data exist.

h-Refinement versus p-Refinement

Considering the left-hand and right-hand diagram of Fig. 5.12, quite similar convergence behaviour is obtained for all DOF located on the earth's surface (left-hand side) and for the point $(0, 0)$ (right-hand side) in the case of E-polarisation for the frequency of $f = 0.1\,\mathrm{Hz}$. The appropriate convergence rates are listed in Tab. 5.7. They are similar to the global convergence rates in Tab. 5.1. Convergence theory is not applicable in a local sense, however, in most cases local convergence rates are similar to global ones. Here, the absolute values of the asymptotic convergence rates α_{as} for the DOF on the earth's surface are lower than those for all DOF (cf. Tab. 5.1). For the point $(0, 0)$, the absolute values of the asymptotic convergence rates α_{as} are as high as the global ones, however, the relative rms error exhibits a more and more non-exponential behaviour with increasing order of the finite elements (cf. Fig. 5.12, right-hand side).

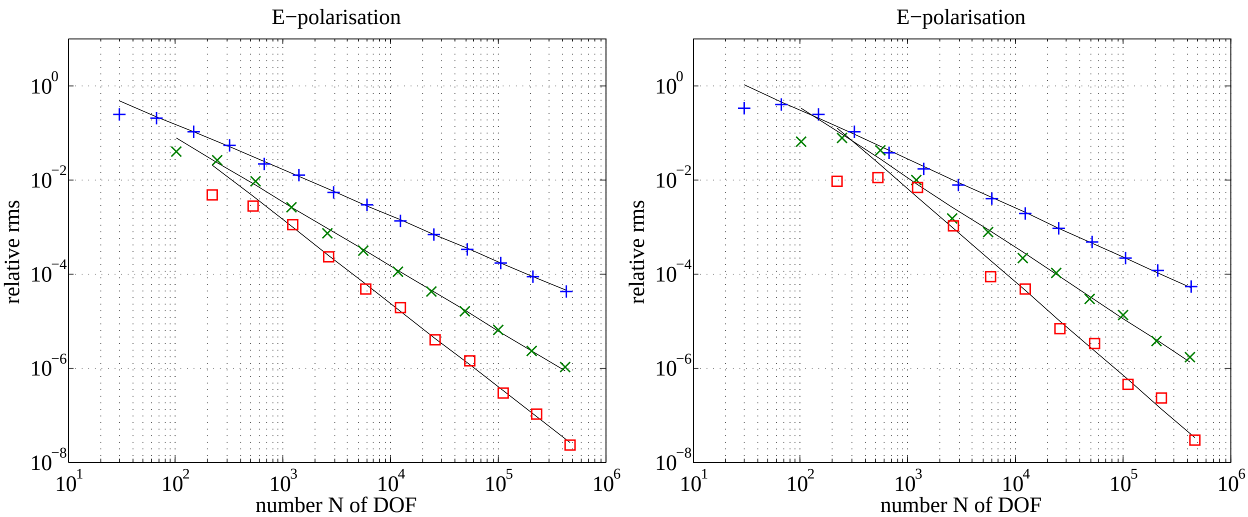

Fig. 5.12: Convergence curves of the local relative rms error of the electric field for E-polarisation for all DOF on the earth's surface (left) and for the point $(0, 0)$ (right) using linear ($p = 1$, +), quadratic ($p = 2$, ×) and cubic ($p = 3$, □) basis functions. Black lines (–) indicate the linear trend of each convergence curve for sufficiently large N. The frequency is $f = 0.1\,\mathrm{Hz}$.

Derived Field Components

Anomalous convergence behaviour can be observed in Fig. 5.13 for the derived field components. Here, the application of cubic ($p = 3$) basis functions does not yield the smallest errors for all numbers N of DOF. Especially, regarding the convergence in the point $(0, 0)$ (right-hand diagram), more

	asymptotic conv. rate α_{as}			limiting conv. rate α_{lim}		
p	1 (linear)	2 (quadratic)	3 (cubic)	1 (linear)	2 (quadratic)	3 (cubic)
earth's surface	-0.97	-1.36	-1.78	-0.99	-1.11	-2.07
point $(0,0)$	-1.04	-1.49	-1.98	-1.13	-1.09	-2.88

Tab. 5.7: Asymptotic (α_{as}) and limiting (α_{lim}) convergence rate of the electric field for E-polarisation at all DOF on the earth's surface and at the point $(0,0)$ depending on the polynomial degree p of the basis functions.

accurate results are obtained from the numerical solution computed with quadratic ($p = 2$) basis functions than from that computed with cubic ($p = 3$) basis functions for all N. Moreover, the relative rms error for quadratic ($p = 2$) basis functions does not decrease strictly monotonically. All DOF on the earth's surface seem to be a sufficiently large number of points to almost reflect the global convergence behaviour, whereas the convergence for only one point is more arbitrary.

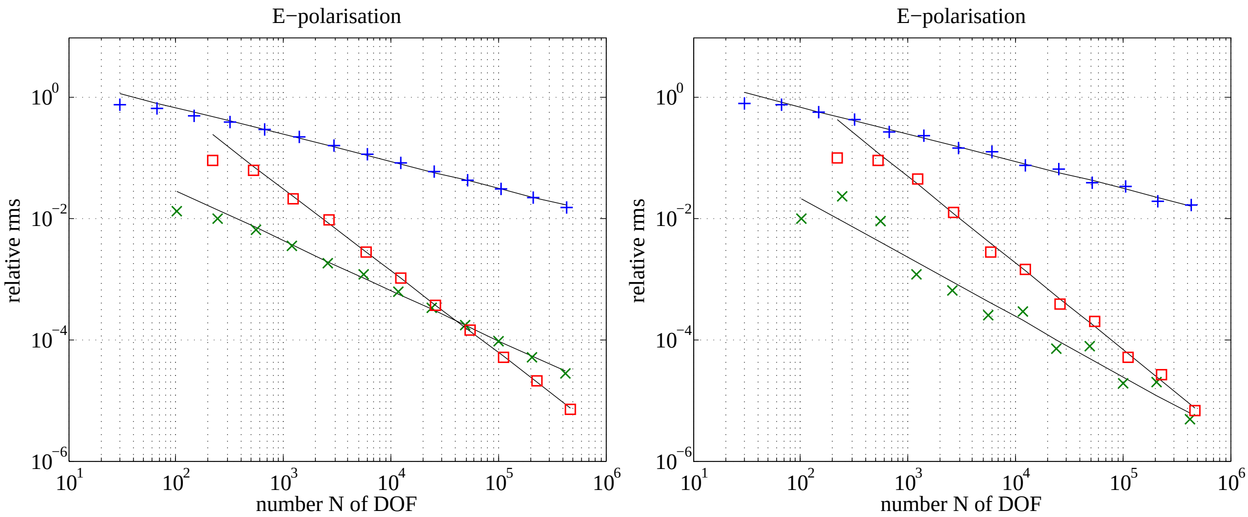

Fig. 5.13: Convergence curves of the local relative rms error of the magnetic field for E-polarisation for all DOF on the earth's surface (left) and for the point $(0,0)$ (right) using linear ($p = 1$, $+$), quadratic ($p = 2$, $\times$) and cubic ($p = 3$, $\square$) basis functions. Black lines (–) indicate the linear trend of each convergence curve for sufficiently large N. The frequency is $f = 0.1\,\text{Hz}$.

For completeness, Fig. 5.14 shows the local convergence of the derived field components for H-polarisation. Here, the local convergence behaviour is as expected from the global convergence studies. For the simulated magnetic fields, the error on the earth's surface is zero because the boundary conditions for the numerical solution are represented by the analytical solution on the air-earth interface.

Tab. 5.8 summarises the local convergence rates for the derived field components for E- and H-polarisation. They agree well with the rates for global convergence listed in Tab. 5.4.

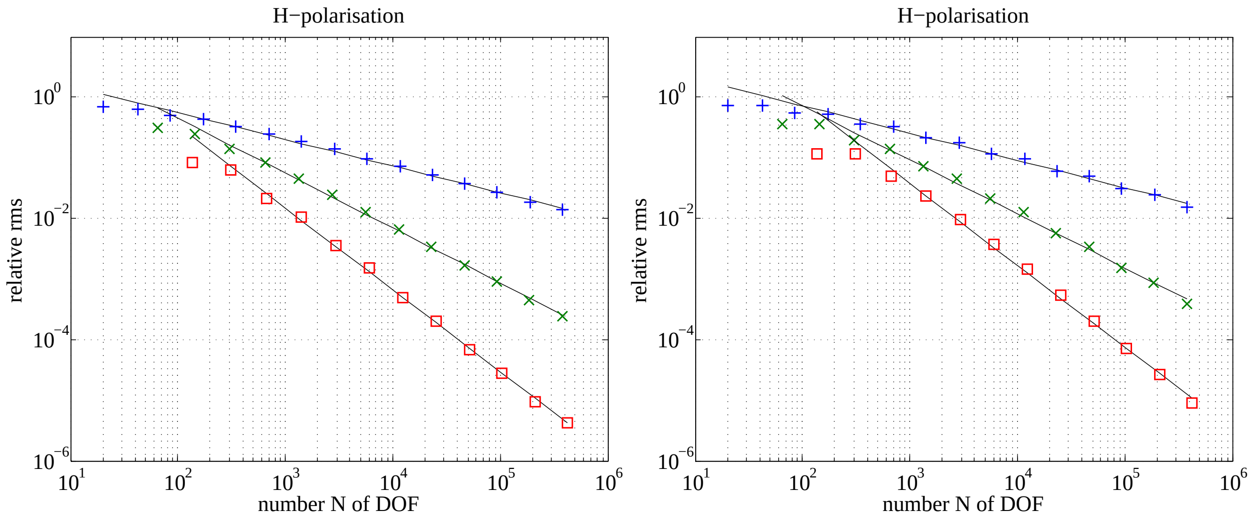

Fig. 5.14: Convergence curves of the local relative rms error of the electric field for H-polarisation for all DOF on the earth's surface (left) and for the point $(0, 0)$ (right) using linear ($p = 1$, +), quadratic ($p = 2$, ×) and cubic ($p = 3$, □) basis functions. Black lines (–) indicate the linear trend of each convergence curve for sufficiently large N. The frequency is $f = 0.1\,\mathrm{Hz}$.

		asymptotic conv. rate α_{as}			limiting conv. rate α_{lim}		
	p	1 (linear)	2 (quadratic)	3 (cubic)	1 (linear)	2 (quadratic)	3 (cubic)
E-polarisation (Fig. 5.13)	earth's surface	-0.44	-0.82	-1.36	-0.48	-0.85	-1.49
	point $(0,0)$	-0.45	-0.98	-1.43	-0.20	-2.05	-1.96
H-polarisation (Fig. 5.14)	earth's surface	-0.44	-0.91	-1.36	-0.46	-0.84	-1.20
	point $(0,0)$	-0.45	-0.89	-1.35	-0.69	-1.14	-1.51

Tab. 5.8: Asymptotic (α_{as}) and limiting (α_{lim}) convergence rate of the derived field components for E- and H-polarisation at all DOF on the earth's surface and at the point $(0,0)$ depending on the polynomial degree p of the basis functions.

Grid Refinement Methods

When comparing different mesh refinement techniques for linear ($p = 1$) basis functions (Fig. 5.15), the adaptive mesh refinement turns out to be advantageous for the local accuracy of the numerical solution in the E- and H-polarisation case. Since the mesh adaption affects regions close to the earth's surface where large gradients of the electromagnetic fields occur, the relative rms error of the numerical solution is decreased mainly there (cf. Fig. 5.5 for global convergence). Considering one data point that is not necessarily located in the same position as a DOF (Fig. 5.15, right-hand panel), the relative rms error does not decrease monotonically in the case of adaptive mesh refinement even for the simulated field components. Looking at the derived field components as well (Fig. 5.16), the non-monotonical behaviour becomes even worse for the adaptive mesh refinement in combination with the longest-edge bisection (Fig. 5.16, right-hand diagram). Hence, the accuracy of the numerical solution is influenced by the spatial mesh geometry especially for linear ($p = 1$) basis functions. The derived field components computed by the derivative of the numerical solution itself reflect a strong dependency on the grid as well.
For H-polarisation, the behaviour of the convergence curves for the derived field components is smoother (cf. Fig. 5.17).

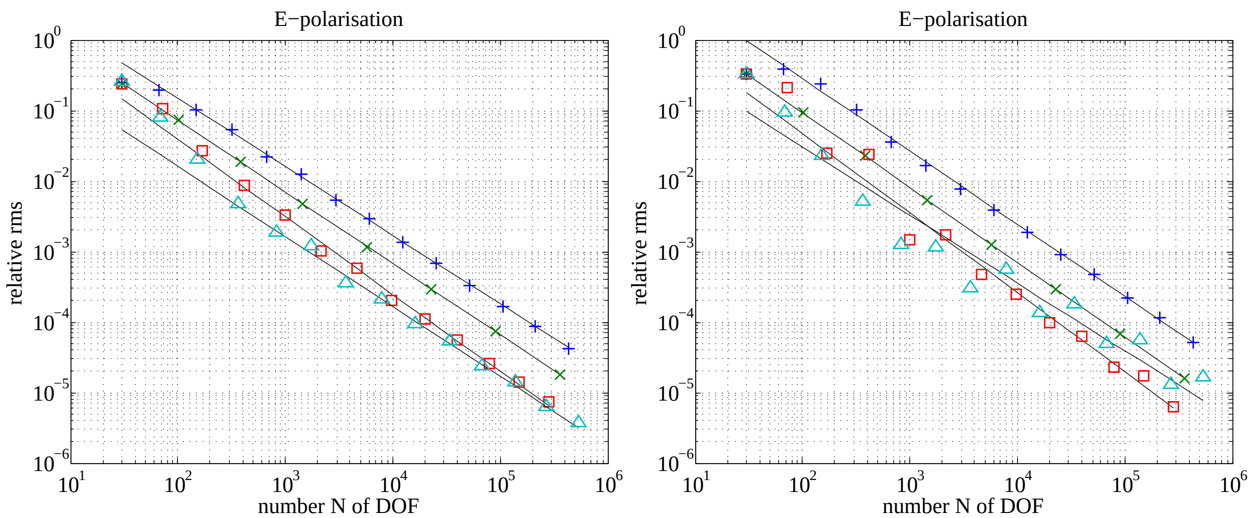

Fig. 5.15: Convergence curves of the local relative rms error of the electric field for E-polarisation for all DOF on the earth's surface (left) and for the point $(0, 0)$ (right) using linear ($p = 1$) basis functions. For generating the family of grids, the uniform refinement with the longest-edge bisection (+), the uniform regular refinement method (×), the adaptive mesh refinement in combination with the longest-edge bisection (□), and the adaptive regular mesh refinement (△) are applied, respectively. The frequency is $f = 0.1$ Hz. Black lines (–) indicate the linear trend of each convergence curve for sufficiently large N.

Tab. 5.9 displays the asymptotic (α_{as}) and limiting (α_{lim}) convergence rates depending on the mesh refinement strategy for the local accuracy of the numerical solution for all DOF located on the earth's surface ($z = 0$) and for the point $(0, 0)$ that does not coincide with a DOF. For first-order ($p = 1$) finite elements, the local convergence rates agree well with the global ones (cf. Tabs 5.3 and 5.6 for global convergence). In the case of cubic ($p = 3$) basis functions, the absolute value of local asymptotic convergence rate α_{as} for the simulated field using uniform mesh refinement is lower than the absolute value of the global asymptotic convergence rate. For adaptive mesh refinement, however, the numerical solution exhibits significantly better local convergence. Apart from the non-monotonic

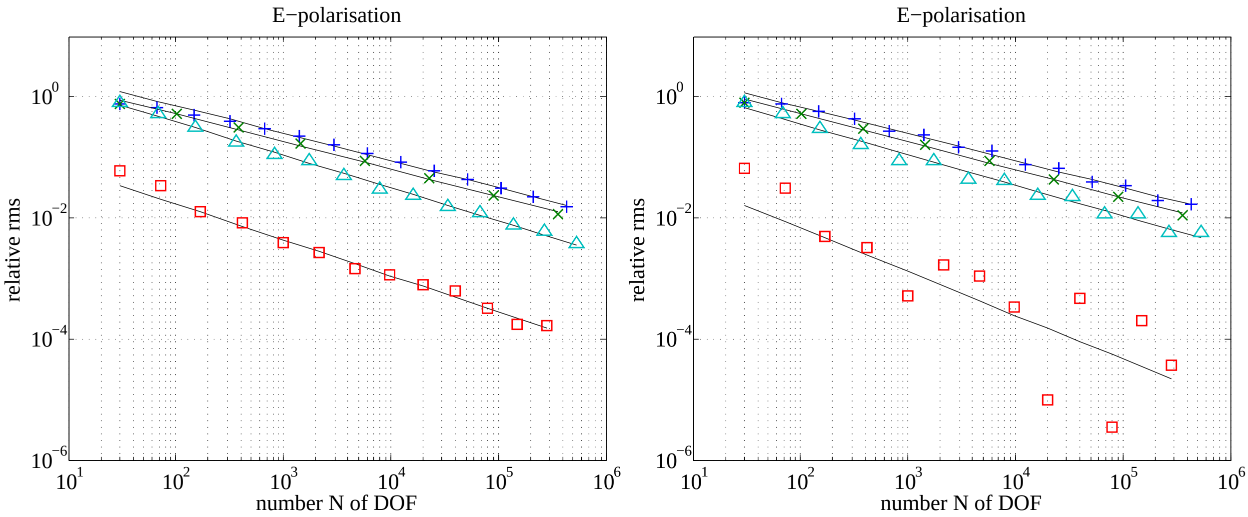

Fig. 5.16: Convergence curves of the local relative rms error of the magnetic field for E-polarisation for all DOF on the earth's surface (left) and for the point $(0, 0)$ (right) using linear ($p = 1$) basis functions. For generating the family of grids, the uniform refinement with the longest-edge bisection (+), the uniform regular refinement method (×), the adaptive mesh refinement in combination with the longest-edge bisection (□), and the adaptive regular mesh refinement (△) are applied, respectively. The frequency is $f = 0.1\,\mathrm{Hz}$. Black lines (–) indicate the linear trend of each convergence curve for sufficiently large N.

convergence behaviour, the adaptive mesh refinement in combination with the longest-edge bisection seems to be advantageous also considering the derived field components.

p	f [Hz]	pola-risa-tion	refinement method	asymptotic conv. rate α_{as}				limiting conv. rate α_{lim}			
				uniform		adaptive		uniform		adaptive	
				longest edge	regular	longest edge	regular	longest edge	regular	longest edge	regular
1 (Fig. 5.15)	0.1	E	$\mathbf{E}(z=0)$	-0.97	-1.01	-1.10	-0.99	-0.99	-1.00	-0.99	-0.77
			$\mathbf{E}$(0,0)	-1.03	-1.06	-1.13	-0.97	-1.13	-1.06	-1.63	0.33
1 (Fig. 5.16)	0.1	E	$\mathbf{H}(z=0)$	-0.45	-0.45	-0.59	-0.54	-0.48	-0.50	$-9.0 \cdot 10^{-2}$	-0.65
			$\mathbf{H}$(0,0)	-0.44	-0.46	-0.72	-0.50	-0.20	-0.50	-2.64	$-1.1 \cdot 10^{-2}$
1 (Fig. 5.17)	0.1	H	$\mathbf{E}(z=0)$	-0.46	-0.48	-0.50	-0.50	-0.46	-0.50	-0.46	-0.68
			$\mathbf{E}$(0,0)	-0.46	-0.49	-0.53	-0.52	-0.69	-0.50	-0.51	$3.9 \cdot 10^{-3}$
3 (no figure)	0.01	E	$\mathbf{H}(z=0)$	-1.42	-1.45	-1.55	-1.51	-1.51	-1.36	-1.77	-1.51
			$\mathbf{H}$(0,0)	-1.46	-1.49	-1.54	-1.52	-1.98	-1.48	-2.14	-3.24
3 (no figure)	1	E	$\mathbf{E}(z=0)$	-1.63	-1.78	-2.30	-2.41	-2.01	-1.81	-1.54	-2.02
			$\mathbf{E}$(0,0)	-1.77	-1.78	-2.30	-2.48	-2.80	-1.99	-3.11	$7.1 \cdot 10^{-2}$

Tab. 5.9: Asymptotic (α_{as}) and limiting (α_{lim}) convergence rate of the derived field components for E- and H-polarisation at all DOF on the earth's surface and at the point $(0,0)$ depending on the mesh refinement technique, the polynomial degree p of the basis functions.

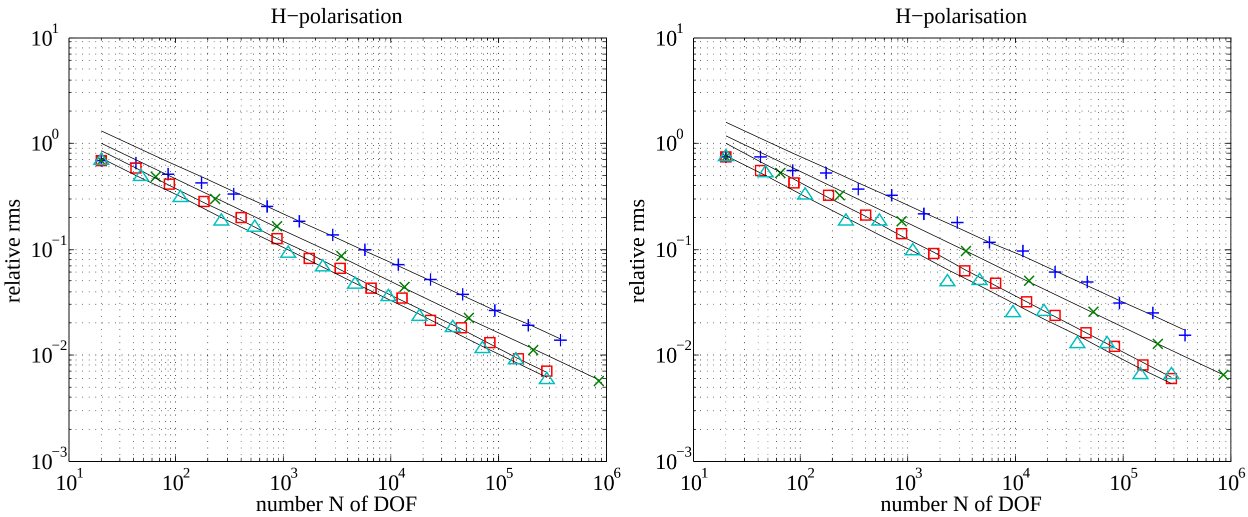

Fig. 5.17: Convergence curves of the local relative rms error of the electric field for H-polarisation for all DOF on the earth's surface (left) and for the point $(0, 0)$ (right) using linear ($p = 1$) basis functions. For generating the family of grids, the uniform refinement with the longest-edge bisection (+), the regular refinement method (×), the adaptive mesh refinement in combination with the longest-edge bisection (□), and the adaptive regular mesh refinement (△) are applied, respectively. The frequency is $f = 0.1\,\mathrm{Hz}$. Black lines (–) indicate the linear trend of each convergence curve for sufficiently large N.

5.3 The 2-D Homogeneous-Halfspace Model: Comparison with the Numerical Finest-Grid Solution

In most cases, especially when considering models that are close to reality, no analytical solution is available to compare with and to estimate the discretisation error of the numerical solution. Therefore, in this section, the convergence of the numerical solution towards the finest-grid solution of the 2-D homogeneous-halfspace model introduced in section 5.2 is examined. The numerical finest-grid solution is assumed to be close to the true solution. Hence, similar convergence behaviour is expected for the relative deviation as for the relative rms error.

5.3.1 h-Refinement versus p-Refinement

Fig. 5.18 and Tab. 5.10 show the same behaviour for the convergence towards the finest-grid solution as Fig. 5.1 and Tab. 5.1, respectively, for the convergence to the analytical solution. Note that, the convergence curves for the comparison with the numerical finest-grid solution are supported by one point less than the ones for the comparison with the analytical solution since the finest-grid solution is needed to compute the relative deviation (eq. (5.4)).

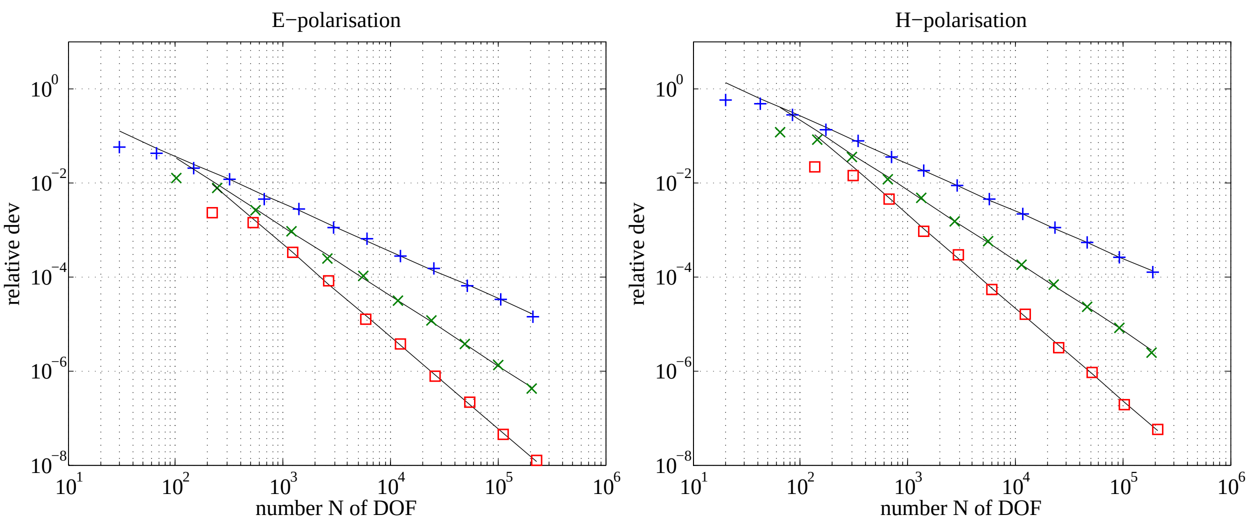

Fig. 5.18: Convergence curves of the global relative deviation of the simulated field components from the finest-grid solutions for E-polarisation (left) and H-polarisation (right) using linear ($p = 1$, +), quadratic ($p = 2$, ×) and cubic ($p = 3$, □) basis functions. Black lines (–) indicate the linear trend of each convergence curve for sufficiently large N. The frequency is $f = 0.1\,\mathrm{Hz}$.

	asymptotic conv. rate α_{as}			limiting conv. rate α_{lim}		
p	1 (linear)	2 (quadratic)	3 (cubic)	1 (linear)	2 (quadratic)	3 (cubic)
E-polarisation	-1.01	-1.47	-1.95	-1.21	-1.67	-1.80
H-polarisation	-1.01	-1.49	-1.98	-1.02	-1.72	-1.67

Tab. 5.10: Asymptotic (α_{as}) and limiting (α_{lim}) convergence rate for the simulated field components in the case of E- and H-polarisation depending on the polynomial degree p of the basis functions.

5.3.2 Frequency Dependence

Figs 5.19 and 5.20 illustrate that, the convergence behaviour is independent of the frequency for linear ($p = 1$) and cubic ($p = 3$) basis functions, respectively. The convergence rates listed in Tab. 5.11 only vary with the polynomial degree p of the basis functions but not with the frequency. Moreover, larger relative deviations are observed for higher frequencies.

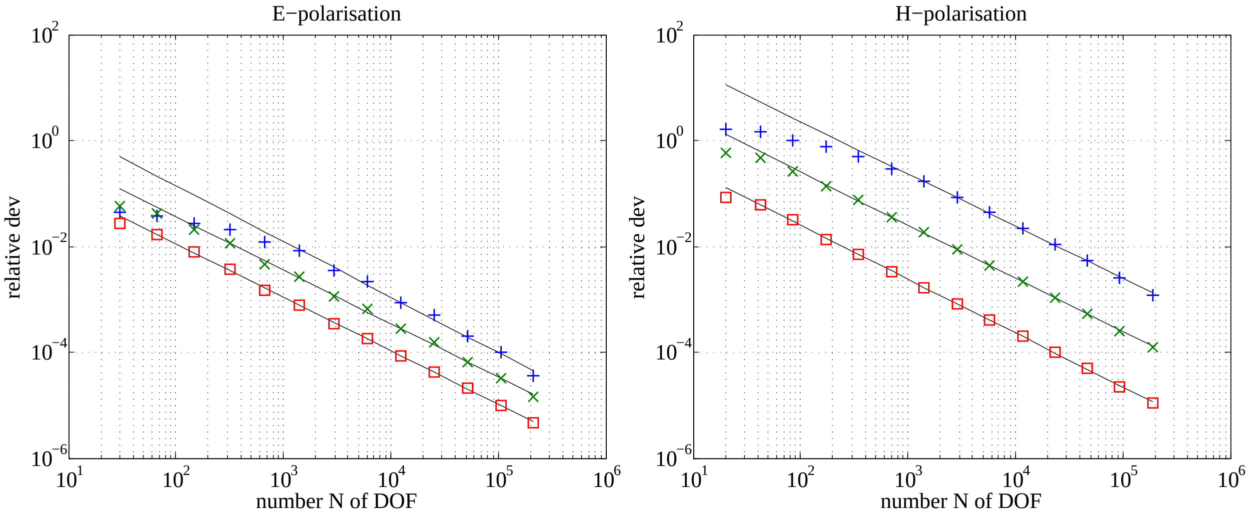

Fig. 5.19: Convergence curves of the global relative deviation of the simulated field components from the finest-grid solutions for E-polarisation (left) and H-polarisation (right) using linear ($p = 1$) basis functions. Frequencies are $f = 1\,\text{Hz}$ (+), $f = 0.1\,\text{Hz}$ (×), $f = 0.01\,\text{Hz}$ (□). Black lines (–) indicate the linear trend of each convergence curve for sufficiently large N.

		asymptotic conv. rate α_{as}			limiting conv. rate α_{lim}		
	f[Hz]	1	0.1	0.01	1	0.1	0.01
p = 1 (Fig. 5.19)	E-polarisation	−1.05	−1.01	−1.01	−1.50	−1.21	−1.06
	H-polarisation	−0.99	−1.01	−1.02	−1.08	−1.02	−1.02
$p = 2$ (no figure)	E-polarisation	−1.50	−1.47	−1.51	−1.74	−1.67	−1.65
	H-polarisation	−1.46	−1.49	−1.50	−1.78	−1.72	−1.66
$p = 3$ (Fig. 5.20)	E-polarisation	−1.89	−1.95	−2.03	−1.73	−1.80	−1.91
	H-polarisation	−1.92	−1.98	−2.01	−1.63	−1.67	−1.70

Tab. 5.11: Asymptotic (α_{as}) and limiting (α_{lim}) convergence rate for the simulated field components in the case of E- and H-polarisation depending on the polynomial degree p of the basis functions and the frequency f.

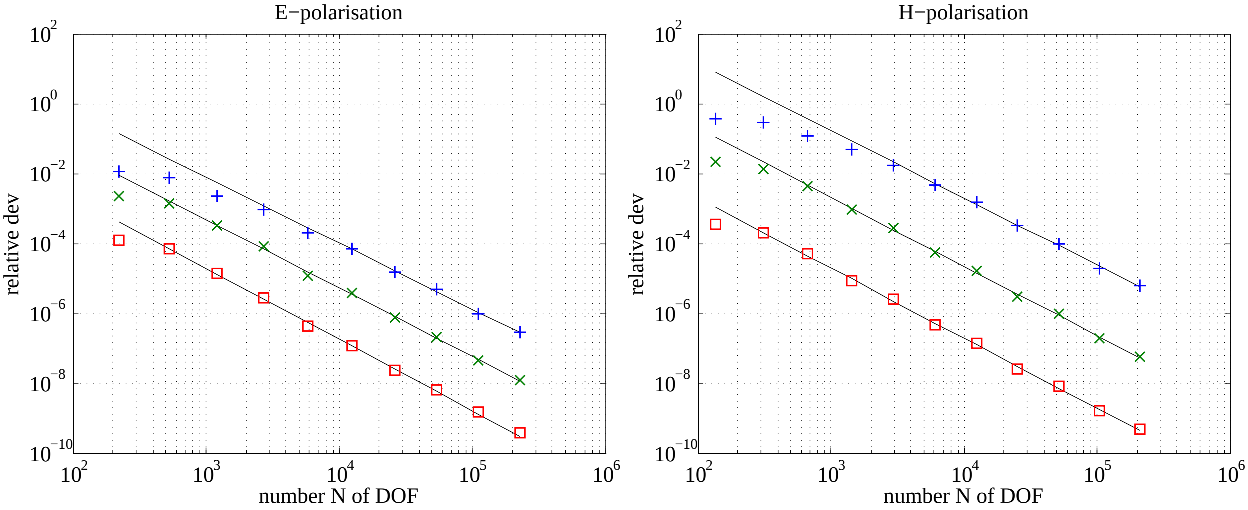

Fig. 5.20: Convergence curves of the global relative deviation of the simulated field components from the finest-grid solutions for E-polarisation (left) and H-polarisation (right) using cubic ($p = 3$) basis functions. Frequencies are $f = 1\,\mathrm{Hz}$ (+), $f = 0.1\,\mathrm{Hz}$ (×), $f = 0.01\,\mathrm{Hz}$ (□). Black lines (–) indicate the linear trend of each convergence curve for sufficiently large N.

5.3.3 Grid Refinement Methods

Examining different mesh refinement methods (Figs. 5.21 – 5.23 and Tab. 5.12), we come to similar conclusions as for the convergence towards the analytical solution in the previous section:

- The adaptive mesh refinement (□ and △) is advantageous for high frequencies ($f = 1, 0.1\,\mathrm{Hz}$) and higher-order ($p = 3$) finite elements. For $f = 1\,\mathrm{Hz}$ and $p = 3$, the asymptotic convergence rate is significantly increased for adaptively refined meshes (cf. Tab. 5.12).
- Smaller relative deviations are obtained by regular mesh refinement methods (× and △).
- For the lowest frequency of $f = 0.01\,\mathrm{Hz}$ and cubic ($p = 3$) basis functions, the uniform regular mesh refinement (×) yields smallest relative deviations.

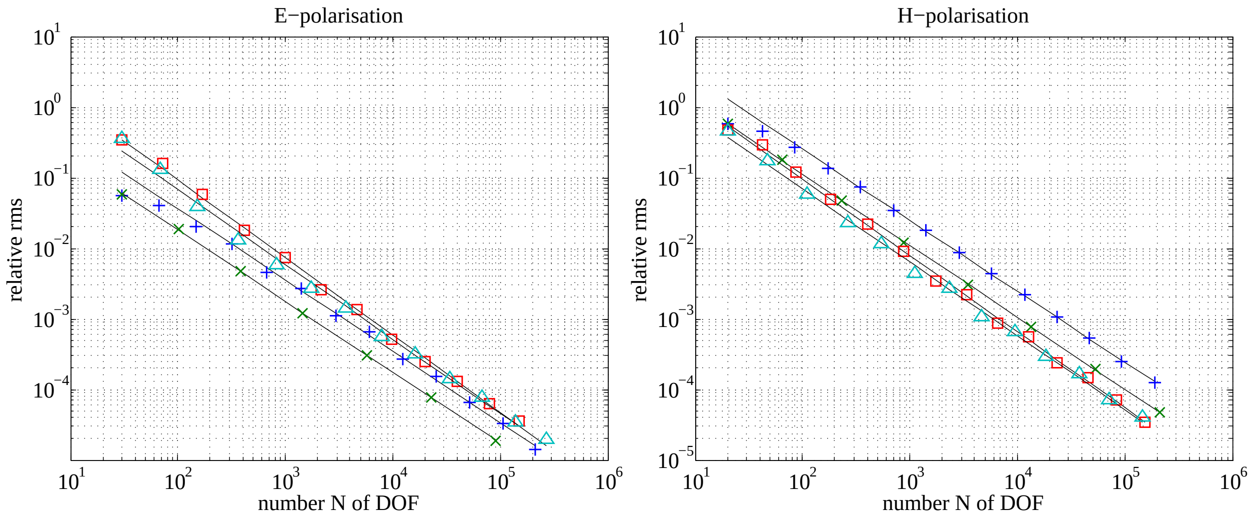

Fig. 5.21: Convergence curves of the global relative deviation of the simulated field components from the finest-grid solutions for E-polarisation (left) and H-polarisation (right) using linear ($p = 1$) basis functions. For generating the family of grids, the uniform refinement with the longest-edge bisection (+), the uniform regular refinement method (×), the adaptive mesh refinement in combination with the longest-edge bisection (□), and the adaptive regular mesh refinement (△) are applied, respectively. The frequency is $f = 0.1\,\mathrm{Hz}$. Black lines (–) indicate the linear trend of each convergence curve for sufficiently large N.

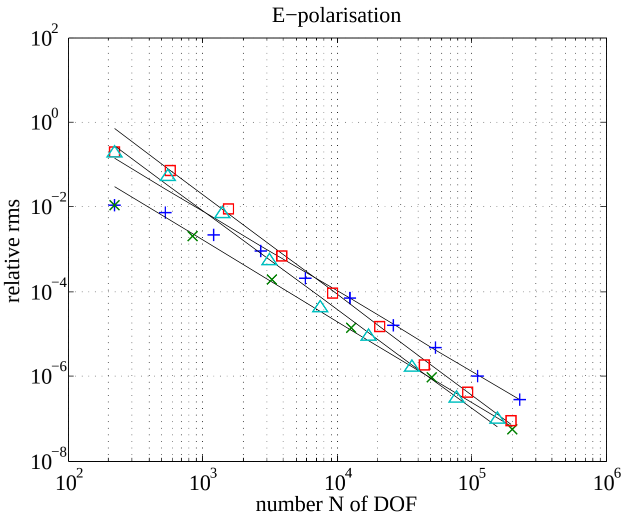

Fig. 5.22: Convergence curves of the global relative deviation of the simulated field components from the finest-grid solutions for E-polarisation (left) and H-polarisation (right) using cubic ($p = 3$) basis functions. For generating the family of grids, uniform refinement with the longest-edge bisection (+), the uniform regular refinement method (×), the adaptive mesh refinement in combination with the longest-edge bisection (□), and the adaptive regular mesh refinement (△) are applied, respectively. The frequency is $f = 1\,\mathrm{Hz}$. Black lines (–) indicate the linear trend of each convergence curve for sufficiently large N.

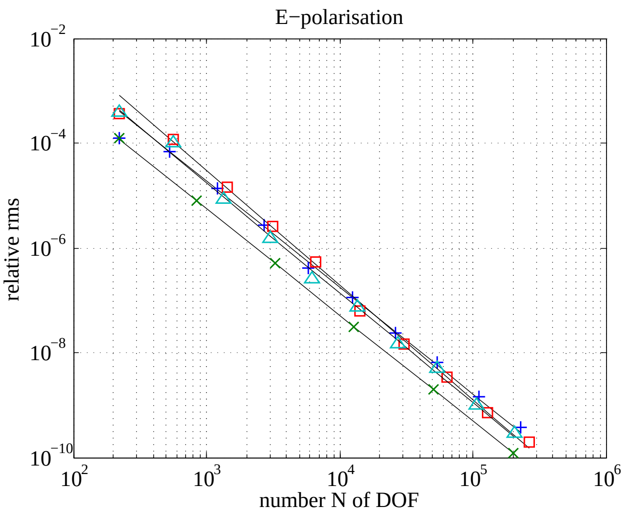

Fig. 5.23: Convergence curves of the global relative deviation of the simulated field components from the finest-grid solution for E-polarisation (left-hand side) and H-polarisation (right-hand side) using cubic ($p = 3$) basis functions. For generating the family of grids, the uniform refinement longest-edge bisection (+), the uniform regular refinement method (×), the adaptive mesh refinement in combination with the longest-edge bisection (□), and the adaptive regular mesh refinement (△) are applied, respectively. The frequency is $f = 0.01\,\mathrm{Hz}$. Black lines (–) indicate the linear trend of each convergence curve for sufficiently large N until it stagnates.

p	$f\,[\mathrm{Hz}]$		asymptotic conv. rate α_{as}				limiting conv. rate α_{lim}			
		refinement	uniform		adaptive		uniform		adaptive	
		method	longest edge	regular	longest edge	regular	longest edge	regular	longest edge	regular
1	0.1	E-polarisation	-1.01	-1.01	-1.10	-1.06	-1.20	-1.01	-0.88	-0.84
(Fig. 5.21)		H-polarisation	-1.01	-1.02	-1.08	-1.04	-1.03	-1.01	-1.19	-0.88
3	0.01	E-polarisation	-2.03	-2.02	-2.19	-2.10	-1.91	-2.03	-1.80	-1.84
(Fig. 5.23)		H-polarisation	-2.01	-2.03	-2.08	-1.99	-1.70	-2.03	-2.56	-1.68
3	1	E-polarisation	-1.89	-1.91	-2.37	-2.33	-1.73	-2.02	-2.08	-1.70
(Fig. 5.22)		H-polarisation	-1.92	-1.91	-2.23	-2.13	-1.63	-2.02	-1.52	-1.42

Tab. 5.12: Asymptotic (α_{as}) and limiting (α_{lim}) convergence rate for the simulated field components in the case of E- and H-polarisation depending on the mesh refinement techique, the polynomial degree p of the basis functions and the frequency f.

5.3.4 Derived Field Components

h-Refinement versus p-Refinement

Considering the convergence of the derived field components, i.e. the horizontal magnetic field for E-polarisation and the horizontal electric field for H-polarisation, respectively, to the vertical derivative of the numerical solution on the finest grid of the family, the same general convergence behaviour can be observed as for the comparison with the analytical solution (cf. e.g. Figs 5.24 and 5.7). The asymptotic convergence rates α_{as} in Tab. 5.13 and Tab. 5.4 are in good agreement as well. The absolute values of the limiting convergence rates α_{lim} in Tab. 5.13, however, are as large as the absolute values of the asymptotic ones, hence, no stagnation of the relative deviation is indicated.

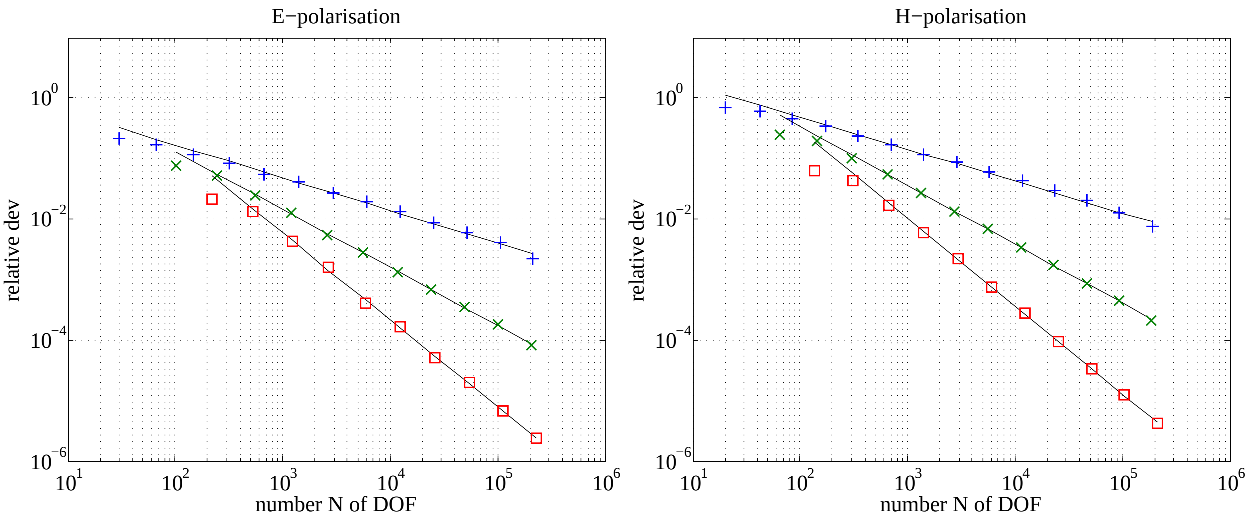

Fig. 5.24: Convergence curves of the global relative deviation of the derived field components from the finest-grid solution for E-polarisation (left) and H-polarisation (right) using linear ($p = 1$, +), quadratic ($p = 2$, ×) and cubic ($p = 3$, □) basis functions. Black lines (–) indicate the linear trend of each convergence curve for sufficiently large N. The frequency is $f = 0.1$ Hz.

	asymptotic conv. rate α_{as}			limiting conv. rate α_{lim}		
p	1 (linear)	2 (quadratic)	3 (cubic)	1 (linear)	2 (quadratic)	3 (cubic)
E-polarisation	-0.54	-0.96	-1.43	-0.84	-1.10	-1.44
H-polarisation	-0.53	-0.97	-1.46	-0.76	-1.11	-1.51

Tab. 5.13: Asymptotic (α_{as}) and limiting (α_{lim}) convergence rate of the derived field components for E- and H-polarisation depending on the polynomial degree p of the basis functions.

Frequency Dependence

Fig. 5.25 illustrates that the asymptotic convergence rate α_{as} is independent of the frequency (cf. Tab. 5.14) as is the case in the comparison with the analytical solution.

Grid Refinement Methods

Comparing different mesh refinement strategies, Figs 5.26 and 5.10 as well as Tabs 5.15 and 5.6 display similar asymptotic convergence rates α_{as}. Hence, also regarding mesh refinement techniques,

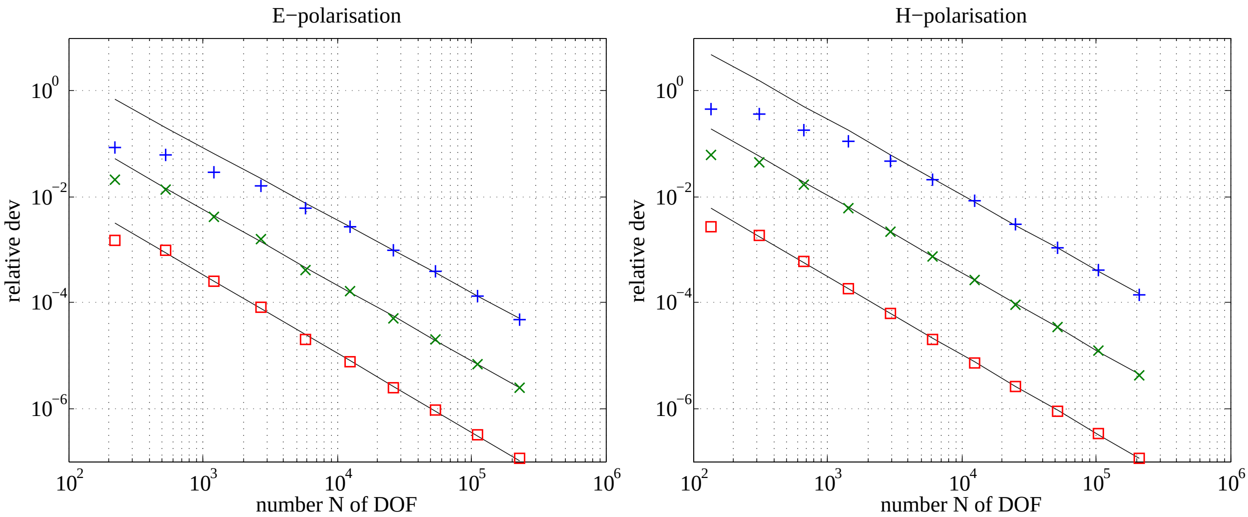

Fig. 5.25: Convergence curves of the global relative deviation of the derived field components from the finest-grid solution for E-polarisation (left) and H-polarisation (right) using cubic ($p = 3$) basis functions. Frequencies are $f = 1$ Hz (+), $f = 0.1$ Hz (×), $f = 0.01$ Hz (□). Black lines (–) indicate the linear trend of each convergence curve for sufficiently large N.

p		asymptotic conv. rate α_{as}			limiting conv. rate α_{lim}		
	f [Hz]	1	0.1	0.01	1	0.1	0.01
1 (no figure)	E-polarisation	-0.55	-0.54	-0.54	-0.81	-0.84	-0.87
	H-polarisation	-0.53	-0.53	-0.53	-0.81	-0.76	-0.76
2 (no figure)	E-polarisation	-0.92	-0.96	-0.99	-1.12	-1.10	-1.12
	H-polarisation	-0.95	-0.97	-0.99	-1.16	-1.11	-1.08
3 (Fig. 5.25)	E-polarisation	-1.37	-1.43	-1.49	-1.45	-1.44	-1.44
	H-polarisation	-1.42	-1.46	-1.48	-1.51	-1.51	-1.52

Tab. 5.14: Asymptotic (α_{as}) and limiting (α_{lim}) convergence rate of the derived field components for E- and H-polarisation depending on the polynomial degree p of the basis functions and the frequency f.

convergence towards the finest-grid solution exhibits similar behaviour as convergence with respect to the analytical solution.

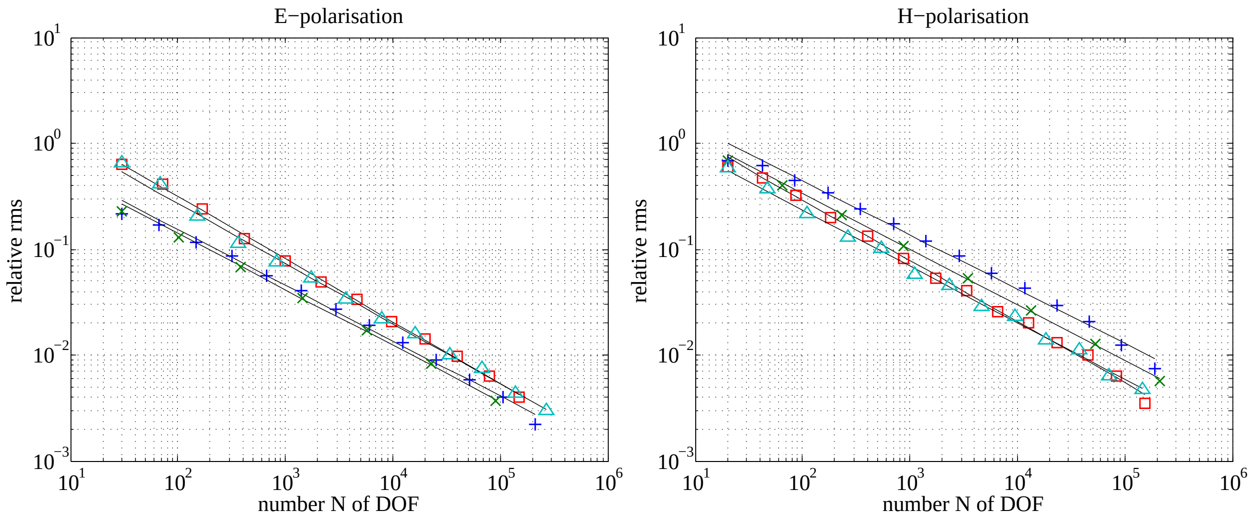

Fig. 5.26: Convergence curves of the global relative deviation of the derived field components from the finest-grid solution for E-polarisation (left) and H-polarisation (right) using linear ($p = 1$) basis functions. For generating the family of grids, the uniform refinement with the longest-edge bisection (+), the uniform regular refinement method ($\times$), the adaptive mesh refinement in combination with the longest edge bisection ($\square$), and the adaptive regular mesh refinement ($\triangle$) are applied, respectively. The frequency is $f = 0.1\,\mathrm{Hz}$. Black lines (–) indicate the linear trend of each convergence curve for sufficiently large N.

p	$f\,[\mathrm{Hz}]$	refinement	asymptotic conv. rate α_{as}				limiting conv. rate α_{lim}			
			uniform		adaptive		uniform		adaptive	
		method	longest edge	regular	longest edge	regular	longest edge	regular	longest edge	regular
1	0.1	E-polarisation	−0.54	−0.53	−0.59	−0.57	−0.84	−0.59	−0.73	−0.55
(Fig. 5.26)		H-polarisation	−0.53	−0.52	−0.57	−0.53	−0.76	−0.58	−0.99	−0.44
3	0.01	E-polarisation	−1.49	−1.48	−1.61	−1.53	−1.45	−1.41	−1.43	−1.35
(no figure)		H-polarisation	−1.48	−1.48	−1.55	−1.46	−1.53	−1.41	−1.66	−1.11
3	1	E-polarisation	−1.37	−1.41	−1.76	−1.85	−1.46	−1.38	−1.63	−1.10
(no figure)		H-polarisation	−1.42	−1.42	−1.64	−1.65	−1.51	−1.40	−1.11	−0.78

Tab. 5.15: Asymptotic (α_{as}) and limiting (α_{lim}) convergence rate for the derived field components in the case of E- and H-polarisation depending on the mesh refinement technique, the polynomial degree p of the basis functions and the frequency f.

5.3.5 Local Convergence

Fig. 5.27 and Tab. 5.16 illustrate the same local convergence behaviour with respect to the finest-grid solution as Fig. 5.12 and Tab. 5.7 considering the numerical solution in comparison to the analytical solution. The asymptotic convergence rates α_{as} are similar.

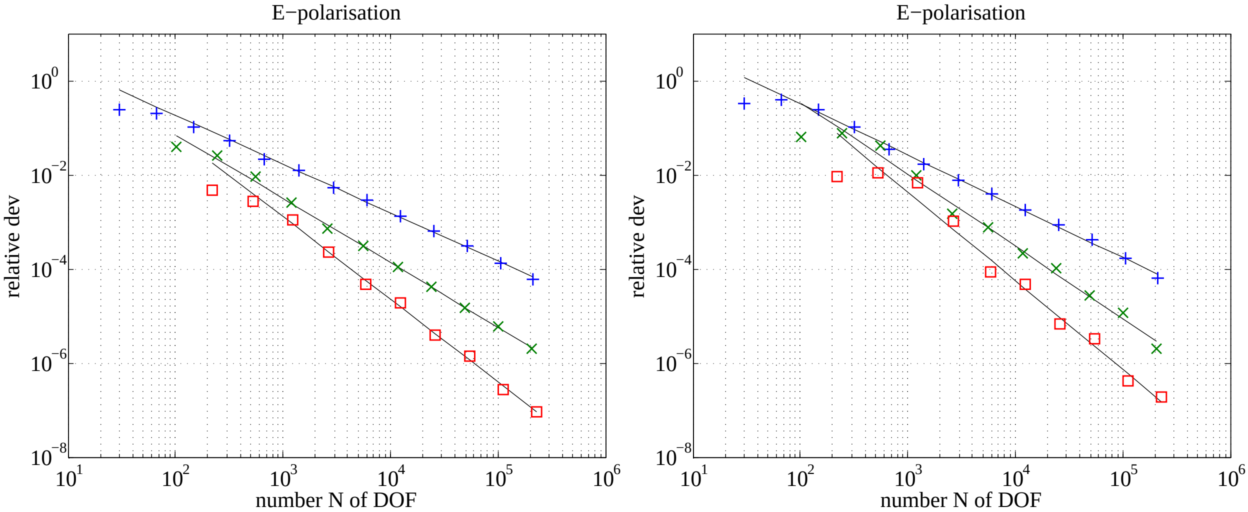

Fig. 5.27: Convergence curves of the local relative deviation of the electric field from the finest-grid solution for E-polarisation for all DOF on the earth's surface (left) and for the point $(0, 0)$ (right) using linear ($p = 1$, +), quadratic ($p = 2$, ×) and cubic ($p = 3$, □) basis functions. Black lines (–) indicate the linear trend of each convergence curve for sufficiently large N. The frequency is $f = 0.1\,\mathrm{Hz}$.

	asymptotic conv. rate α_{as}			limiting conv. rate α_{lim}		
p	1 (linear)	2 (quadratic)	3 (cubic)	1 (linear)	2 (quadratic)	3 (cubic)
earth's surface	-1.03	-1.36	-1.75	-1.12	-1.53	-1.55
point $(0, 0)$	-1.09	-1.53	-1.88	-1.37	-2.50	-1.06

Tab. 5.16: Asymptotic (α_{as}) and limiting (α_{lim}) convergence rate of the electric field for E-polarisation at all DOF on the earth's surface and at the point $(0, 0)$ depending on the polynomial degree p of the basis functions.

Derived Field Components

For the derived field components, same anomalous convergence behaviour can be observed for E-polarisation in Fig. 5.28 as in Fig. 5.13 representing the comparison with the analytical solution: The application of quadratic ($p = 2$) basis functions yields smaller relative deviations than using third-order ($p = 3$) finite elements up to $N = 40,000$ for $z = 0$ and $N = 200,000$ for the point $(0, 0)$. However, higher absolute values of the convergence rates (cf. Tab. 5.17) let expect smallest relative deviations for cubic ($p = 3$) basis functions for larger numbers N of DOF. For H-polarisation, the convergence behaviour is smoother (Fig. 5.29) and similar to that displayed in Fig. 5.14 illustrating the comparison of the numerical solution to the analytical solution.

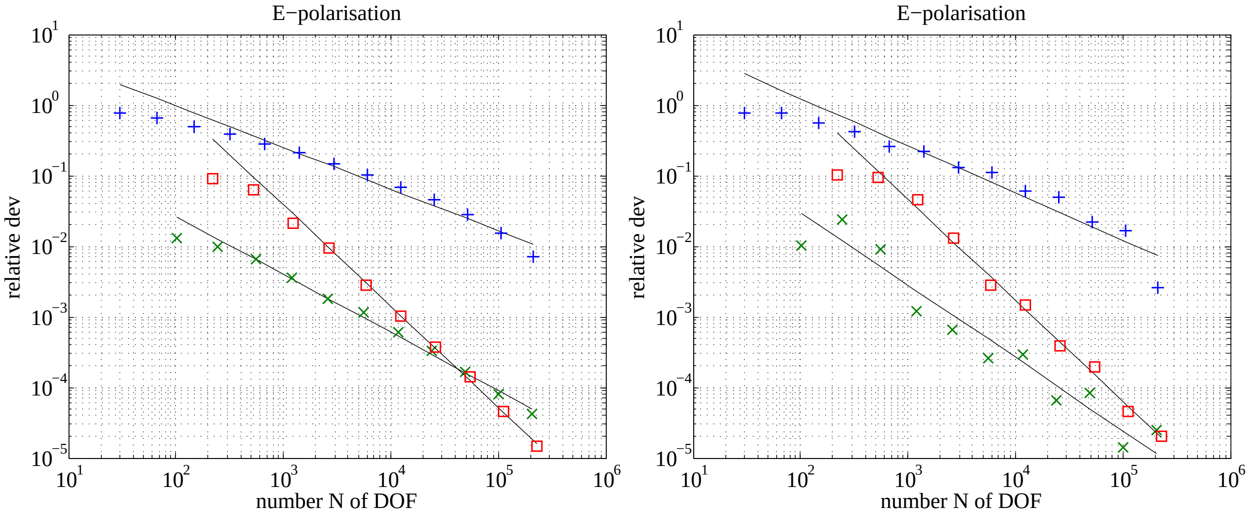

Fig. 5.28: Convergence curves of the local relative deviation of the magnetic field for E-polarisation for all DOF on the earth's surface (left) and for the point $(0, 0)$ (right) using linear ($p = 1$, +), quadratic ($p = 2$, ×) and cubic ($p = 3$, □) basis functions. Black lines (–) indicate the linear trend of each convergence curve for sufficiently large N. The frequency is $f = 0.1\,\text{Hz}$.

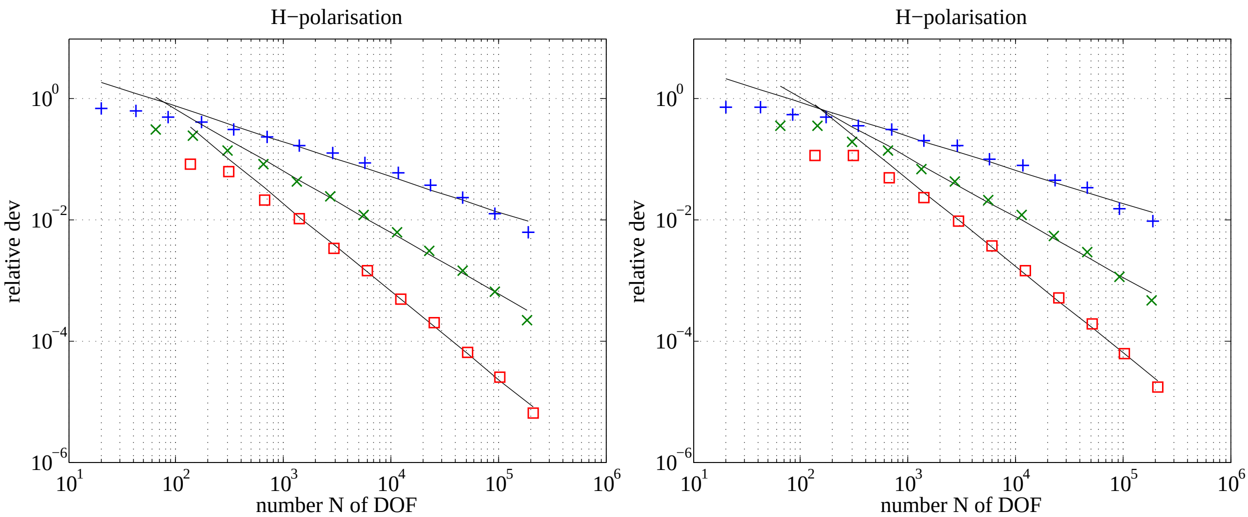

Fig. 5.29: Convergence curves of the local relative deviation of the electric field for H-polarisation for all DOF on the earth's surface (left) and for the point $(0, 0)$ (right) using linear ($p = 1$, +), quadratic ($p = 2$, ×) and cubic ($p = 3$, □) basis functions. Black lines (–) indicate the linear trend of each convergence curve for sufficiently large N. The frequency is $f = 0.1\,\text{Hz}$.

		asymptotic conv. rate α_{as}			limiting conv. rate α_{lim}		
	p	1 (linear)	2 (quadratic)	3 (cubic)	1 (linear)	2 (quadratic)	3 (cubic)
E-polarisation (Fig. 5.28)	earth's surface	-0.59	-0.82	-1.43	-1.07	-0.93	-1.58
	point $(0, 0)$	-0.67	-1.03	-1.43	-2.66	0.83	-1.12
H-polarisation (Fig. 5.29)	earth's surface	-0.58	-1.02	-1.45	-1.06	-1.56	-1.96
	point $(0, 0)$	-0.56	-0.99	-1.43	-0.68	-1.26	-1.83

Tab. 5.17: Asymptotic (α_{as}) and limiting (α_{lim}) convergence rate of the derived field components for E- and H-polarisation at all DOF on the earth's surface and at the point $(0, 0)$ depending on the polynomial degree p of the basis functions.

Grid Refinement Methods

Concerning the grid refinement technique, convergence of the numerical solution to the finest-grid solution implies similar conclusions as the convergence to the analytical solution that was examined in subsection 5.2.5:

- Adaptive mesh refinement is advantageous for the local accuracy of the numerical results for E- and H-polarisation (cf. Figs 5.30 for the electric field in the E-polarisation case and 5.31 for the electric field in the H-polarisation case).
- The local convergence curves may exhibit non-monotonical behaviour (Fig. 5.30, right-hand side for the point $(0, 0)$).
- For $f = 1\,\mathrm{Hz}$ and $p = 3$, the adaptive mesh refinement yields significantly increased absolute values of convergence rates (cf. Fig. 5.32 and Tab. 5.18).

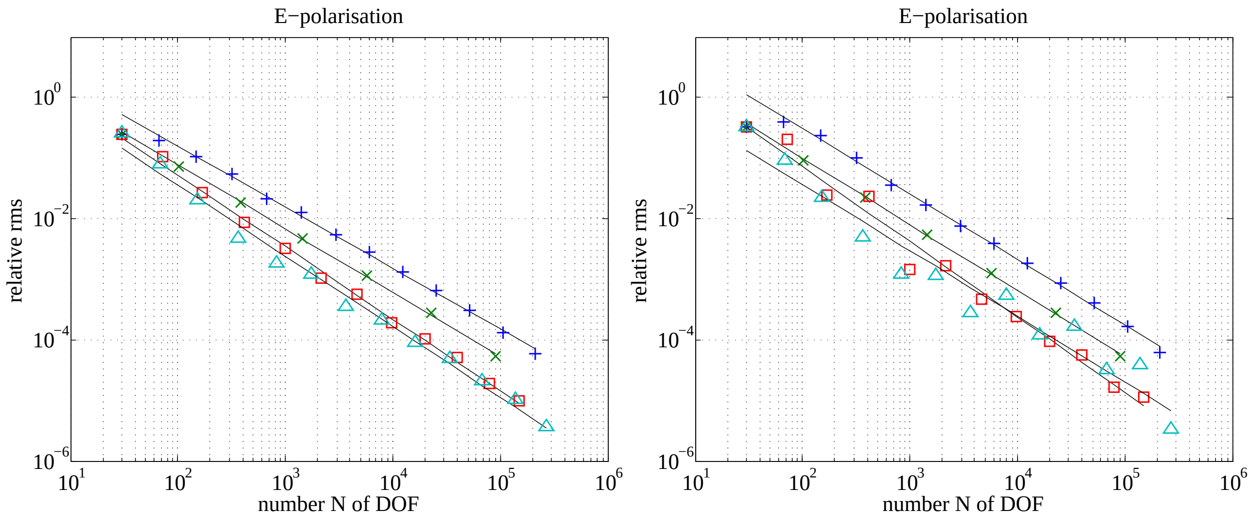

Fig. 5.30: Convergence curves of the local relative deviation of the electric field for E-polarisation for all DOF on the earth's surface (left) and for the point $(0, 0)$ (right) using linear ($p = 1$) basis functions. For generating the family of grids, the uniform refinement with the longest-edge bisection (+), the uniform regular refinement method (×), the adaptive mesh refinement in combination with the longest-edge bisection (□), and the adaptive regular mesh refinement (△) are applied, respectively. The frequency is $f = 0.1\,\mathrm{Hz}$. Black lines (–) indicate the linear trend of each convergence curve for sufficiently large N.

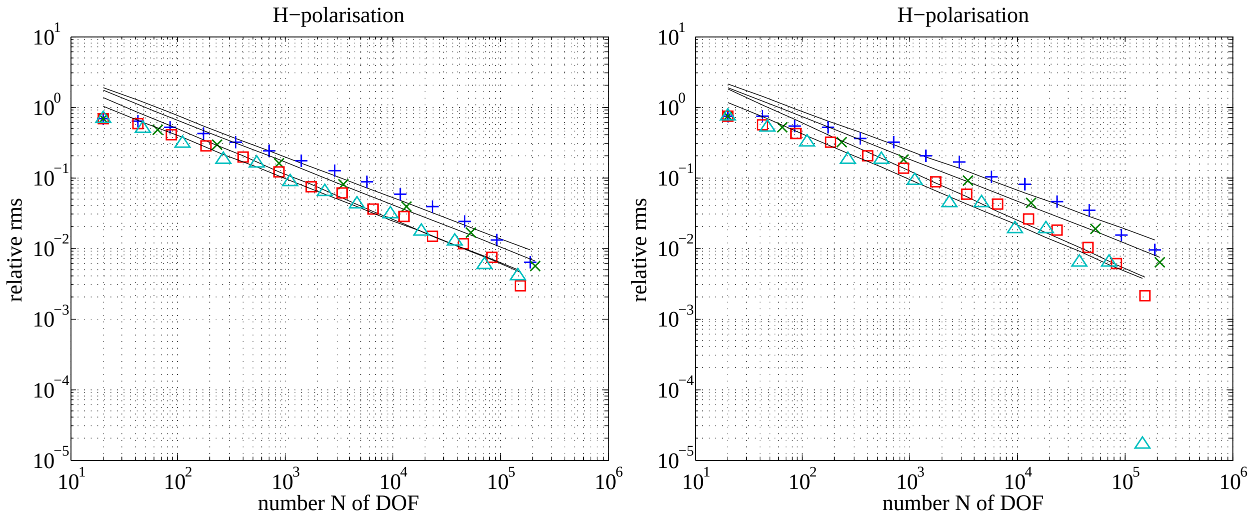

Fig. 5.31: Convergence curves of the local relative deviation of the electric field for H-polarisation for all DOF on the earth's surface (left) and for the point $(0, 0)$ (right) using linear ($p = 1$) basis functions. For generating the family of grids, the uniform refinement with the longest-edge bisection (+), the uniform regular refinement method (×), the adaptive mesh refinement in combination with the longest-edge bisection (□), and the adaptive regular mesh refinement (△) are applied, respectively. The frequency is $f = 0.1\,\mathrm{Hz}$. Black lines (–) indicate the linear trend of each convergence curve for sufficiently large N.

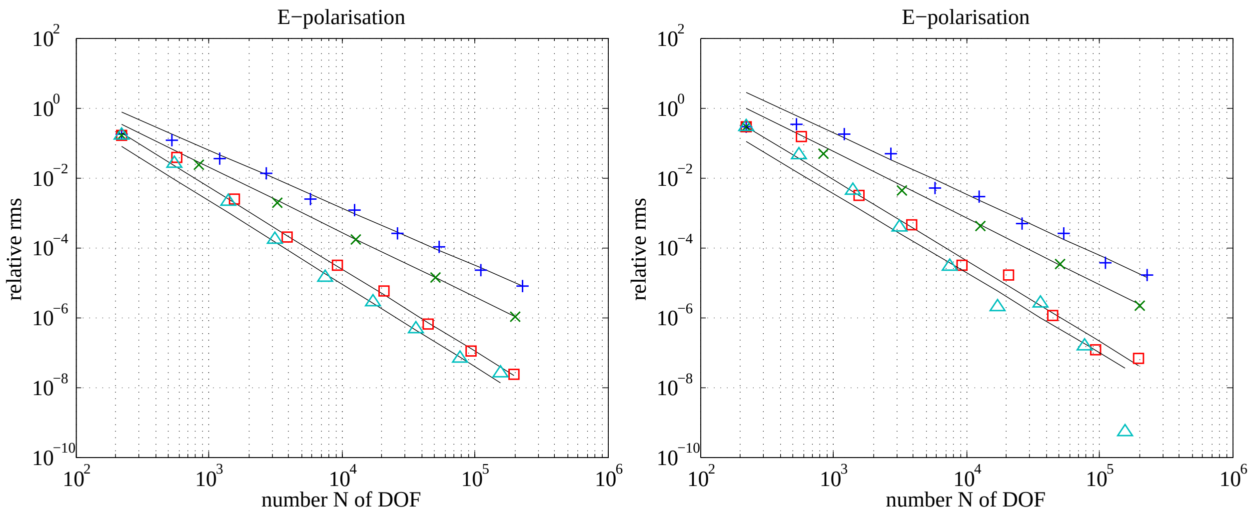

Fig. 5.32: Convergence curves of the local relative deviation of the electric field for E-polarisation for all DOF on the earth's surface (left) and for the point $(0, 0)$ (right) using cubic ($p = 3$) basis functions. For generating the family of grids, the uniform refinement with the longest-edge bisection (+), the uniform regular refinement method (×), the adaptive mesh refinement in combination with the longest-edge bisection (□), and the adaptive regular mesh refinement (△) are applied, respectively. The frequency is $f = 1\,\mathrm{Hz}$. Black lines (–) indicate the linear trend of each convergence curve for sufficiently large N until it stagnates.

p	f[Hz]	polarisation	refinement method	asymptotic conv. rate α_{as} uniform longest edge	uniform regular	adaptive longest edge	adaptive regular	limiting conv. rate α_{lim} uniform longest edge	uniform regular	adaptive longest edge	adaptive regular
1 (Fig. 5.30)	0.1	E	$\mathbf{E}(z=0)$	-1.01	-1.05	-1.19	-1.17	-1.12	-1.16	-1.09	-1.50
			$\mathbf{E}$(0,0)	-1.08	-1.09	-1.24	-1.09	-1.37	-1.20	-0.55	-3.53
1 (no figure)	0.1	E	$\mathbf{H}(z=0)$	-0.59	-0.60	-0.72	-0.67	-1.07	-0.79	-0.17	-0.53
			$\mathbf{H}$(0,0)	-0.67	-0.60	-0.72	-0.66	-2.66	-0.79	3.01	-7.29
1 (Fig. 5.31)	0.1	H	$\mathbf{E}(z=0)$	-0.58	-0.60	-0.64	-0.60	-1.06	-0.79	-1.52	-0.56
			$\mathbf{E}$(0,0)	-0.56	-0.60	-0.69	-0.65	-0.68	-0.79	-1.73	-9.11
3 (no figure)	0.01	E	$\mathbf{H}(z=0)$	-1.49	-1.47	-1.54	-1.56	-1.60	-1.47	-1.48	-1.69
			$\mathbf{H}$(0,0)	-1.49	-1.54	-1.48	-1.63	-1.12	-1.58	-1.19	$1.0 \cdot 10^{-4}$
3 (Fig. 5.32)	1	E	$\mathbf{E}(z=0)$	-1.64	-1.86	-2.35	-2.38	-1.48	-1.88	-2.14	-1.45
			$\mathbf{E}$(0,0)	-1.75	-1.90	-2.31	-2.28	-1.03	-1.96	-0.83	-8.11

Tab. 5.18: Asymptotic (α_{as}) and limiting (α_{lim}) convergence rate of the derived field components for E- and H-polarisation at all DOF on the earth's surface and at the point $(0, 0)$ depending on the mesh refinement technique, the polynomial degree p of the basis functions.

5.4 The 2-D Layered-Halfspace Model

In this section, the model of a layered halfspace consisting of three layers of conductivities $\sigma_1 = 0.1\,\mathrm{Sm}^{-1}$, $\sigma_2 = 0.01\,\mathrm{Sm}^{-1}$, and $\sigma_3 = 100\,\mathrm{Sm}^{-1}$ and thicknesses $d_1 = 10\,\mathrm{km}$, $d_2 = 20\,\mathrm{km}$ (cf. Fig. 5.33) is examined regarding the convergence behaviour of the numerical solution. These convergence studies are restricted to the comparison with the finest-grid solution since, for the homogeneous-halfspace model in the previous section, these results have proved to reflect the convergence behaviour with respect to the true solution that is usually unknown for close-to-reality models. At the vertical conductivity contrasts, the horizontal components of the electric and magnetic fields are continuous, however, the tangential component of the magnetic field is not continuously differentiable (cf. eq. (2.1a)) which affects the regularity of the numerical solution. Hence, the convergence behaviour is expected to be different than that for the homogeneous halfspace.

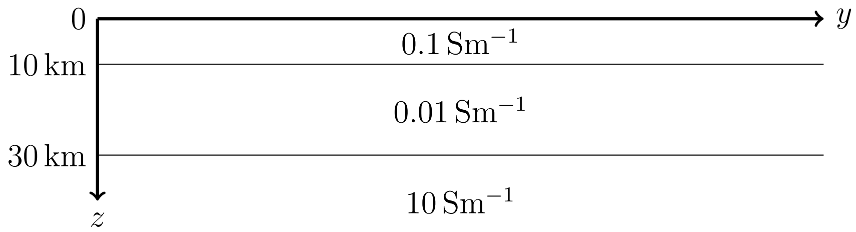

Fig. 5.33: 2D layered-halfspace model.

5.4.1 h-Refinement versus p-Refinement

Fig. 5.34 displays convergence curves for linear ($p = 1$, $+$), quadratic ($p = 2$, $\times$) and cubic ($p = 3$, $\square$) basis functions in the case of E-polarisation (left-hand diagram) and H-polarisation (right-hand diagram) at a frequency of $f = 0.1\,\mathrm{Hz}$. The convergence rate, i.e. the slope of the convergence curves, does not vary with p in the same way as for the homogeneous-halfspace model (cf. Fig. 5.18). Tab. 5.19 illustrates that the convergence rate α_{as} is almost constant for $p \geq 2$ in the E-polarisation case and even for all polynomial degrees p in the case of H-polarisation. This observation is in accordance with the expectations from convergence theory (cf. section 4.4). If the true solution is not sufficiently regular, an increase of the polynomial order of the finite elements does not necessarily result in a higher absolute value of the convergence rate. For $f = 1\,\mathrm{Hz}$ (Fig. 5.35) and $f = 0.01\,\mathrm{Hz}$ (Fig. 5.36), the convergence behaviour is almost similar to that for the homogeneous-halfspace model due to the small skin depth for $f = 1\,\mathrm{Hz}$ and the large skin depth $f = 0.01\,\mathrm{Hz}$ for which the layered-halfspace model appears to be an asymptotically homogeneous halfspace with electrical conductivity σ_1 or σ_3, respectively.

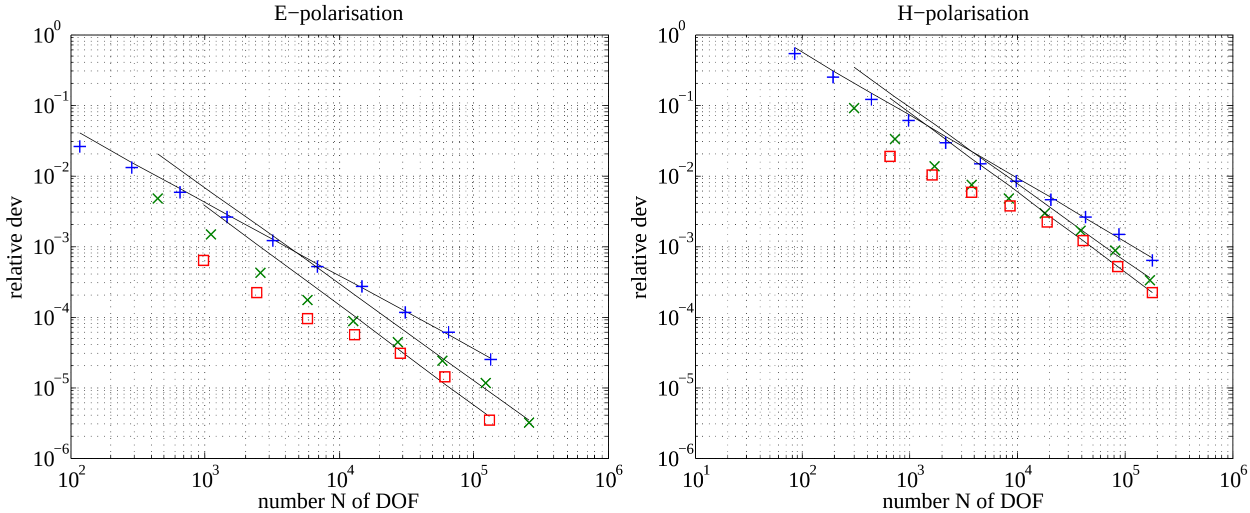

Fig. 5.34: Convergence curves of the global relative deviation of the simulated field components for E-polarisation (left) and H-polarisation (right) using linear ($p = 1$, +), quadratic ($p = 2$, ×) and cubic ($p = 3$, □) basis functions. Black lines (–) indicate the linear trend of each convergence curve for sufficiently large N. The frequency is $f = 0.1\,\mathrm{Hz}$.

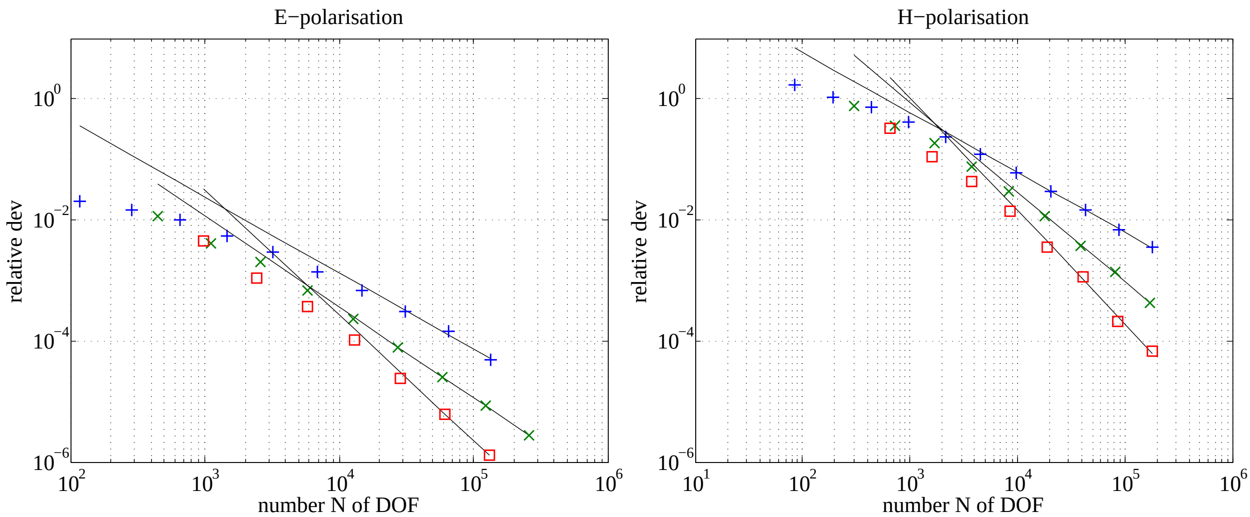

Fig. 5.35: Convergence curves of the global relative deviation of the simulated field components for E-polarisation (left) and H-polarisation (right) using linear ($p = 1$, +), quadratic ($p = 2$, ×) and cubic ($p = 3$, □) basis functions. Black lines (–) indicate the linear trend of each convergence curve for sufficiently large N. The frequency is $f = 1\,\mathrm{Hz}$.

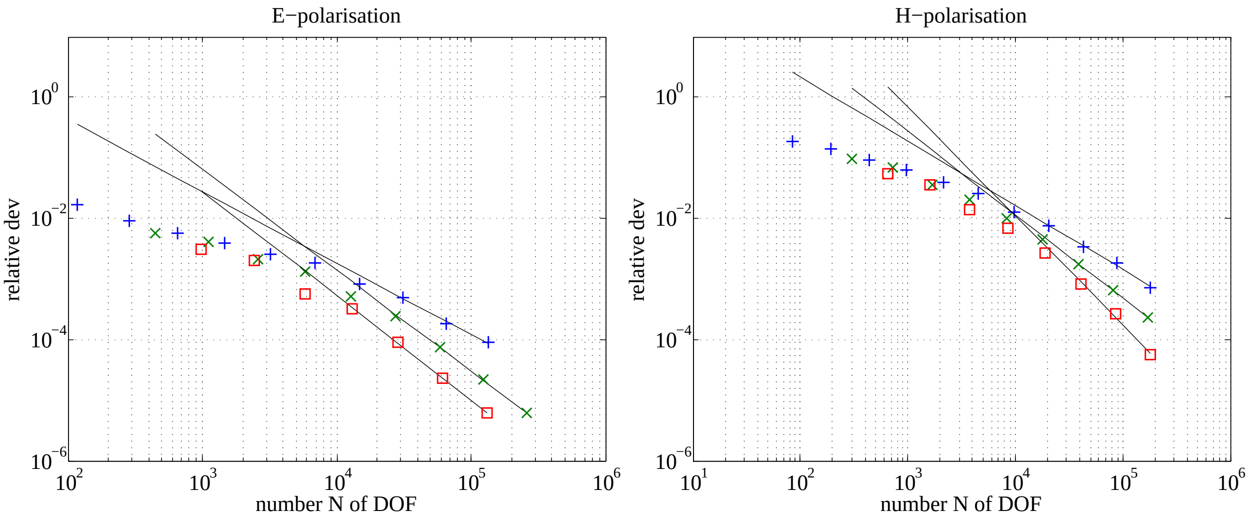

Fig. 5.36: Convergence curves of the global relative deviation of the simulated field components for E-polarisation (left) and H-polarisation (right) using linear ($p = 1$, +), quadratic ($p = 2$, ×) and cubic ($p = 3$, □) basis functions. Black lines (–) indicate the linear trend of each convergence curve for sufficiently large N. The frequency is $f = 0.01\,\mathrm{Hz}$.

		asymptotic conv. rate α_{as}			limiting conv. rate α_{lim}		
$f\,[\text{Hz}]$	p	1 (linear)	2 (quadratic)	3 (cubic)	1 (linear)	2 (quadratic)	3 (cubic)
0.01	E-polarisation	-1.18	-1.66	-1.72	-1.02	-1.68	-1.72
(Fig. 5.36)	H-polarisation	-1.06	-1.38	-1.80	-1.34	-1.44	-2.09
0.1	E-polarisation	-1.04	-1.36	-1.41	-1.24	-1.75	-1.86
(Fig. 5.34)	H-polarisation	-0.89	-1.09	-1.13	-1.17	-1.34	-1.15
1	E-polarisation	-1.26	-1.50	-2.06	-1.48	-1.52	-2.06
(Fig. 5.35)	H-polarisation	-0.99	-1.49	-1.87	-0.90	-1.62	-1.54

Tab. 5.19: Asymptotic (α_{as}) and limiting (α_{lim}) convergence rate for the simulated field components in the case of E- and H-polarisation depending on the polynomial degree p of the basis functions.

5.4.2 Grid Refinement Methods

When applying adaptive mesh refinement strategies, the absolute values of the convergence rates increase with the order p of the finite elements independently of the frequency (cf. Fig. 5.37 and Tab. 5.20) to even higher values than predicted by eq. (4.84) and Tab. 4.5 in section 4.4.

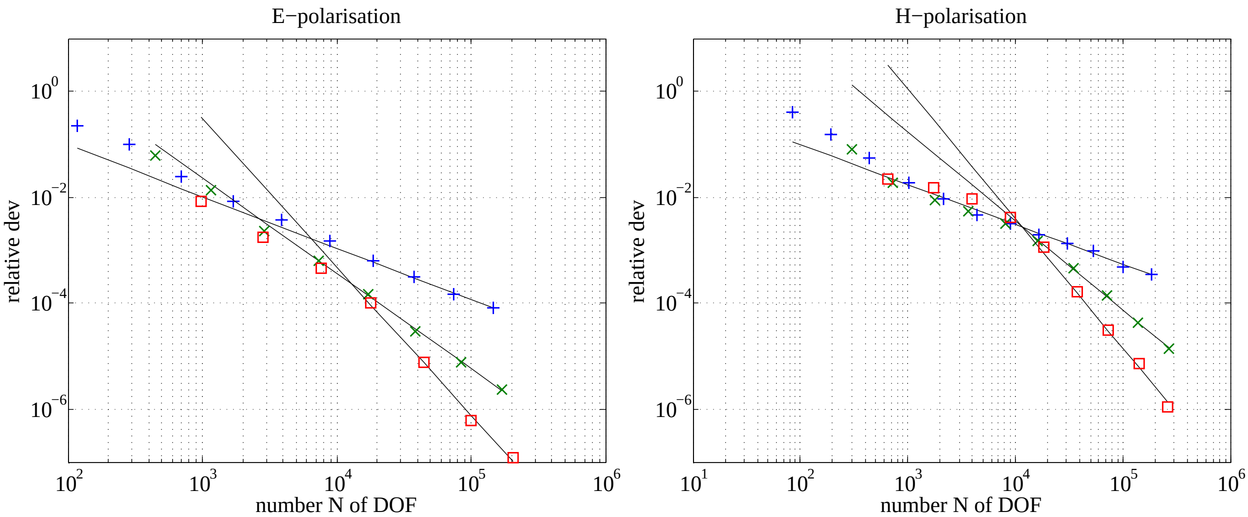

Fig. 5.37: Convergence curves of the global relative deviation of the simulated field components for E-polarisation (left) and H-polarisation (right) using linear ($p = 1$, +), quadratic ($p = 2$, ×) and cubic ($p = 3$, □) basis functions. Black lines (–) indicate the linear trend of each convergence curve for sufficiently large N. The frequency is $f = 0.1\,\mathrm{Hz}$. Adaptive mesh refinement.

		asymptotic conv. rate α_{as}			limiting conv. rate α_{lim}		
$f\,[\text{Hz}]$	p	1 (linear)	2 (quadratic)	3 (cubic)	1 (linear)	2 (quadratic)	3 (cubic)
0.01 (no figure)	E-polarisation	-1.12	-1.69	-2.52	-1.01	-1.54	-2.60
	H-polarisation	-1.07	-1.72	-2.45	-1.37	-1.89	-1.93
0.1 (Fig. 5.37)	E-polarisation	-0.97	-1.80	-2.79	-0.82	-1.75	-2.24
	H-polarisation	-0.75	-1.69	-2.44	-0.59	-1.80	-3.05
1 (no figure)	E-polarisation	-0.99	-1.69	-2.00	-0.85	-1.71	-2.02
	H-polarisation	-0.99	-1.64	-2.24	-0.73	-1.54	-1.23

Tab. 5.20: Asymptotic (α_{as}) and limiting (α_{lim}) convergence rate for the simulated field components in the case of E- and H-polarisation depending on the polynomial degree p of the basis functions. Adaptive mesh refinement.

5.4.3 Derived Field Components

Considering the convergence of the derived field components for the frequency $f = 0.1\,\mathrm{Hz}$ in Fig. 5.38, the same convergence behaviour can be observed as for the simulated field components. The absolute value of the convergence rate α_{as} hardly increases with the order p of the finite elements (cf. Tab. 5.21). For $f = 1\,\mathrm{Hz}$ (Fig. 5.39) and $f = 0.01\,\mathrm{Hz}$ (Fig. 5.40) the convergence curves and rates resemble those for the homogeneous-halfspace model more. Again, the adaptive mesh refinement provides better convergence as illustrated in Fig. 5.41 and Tab. 5.22.

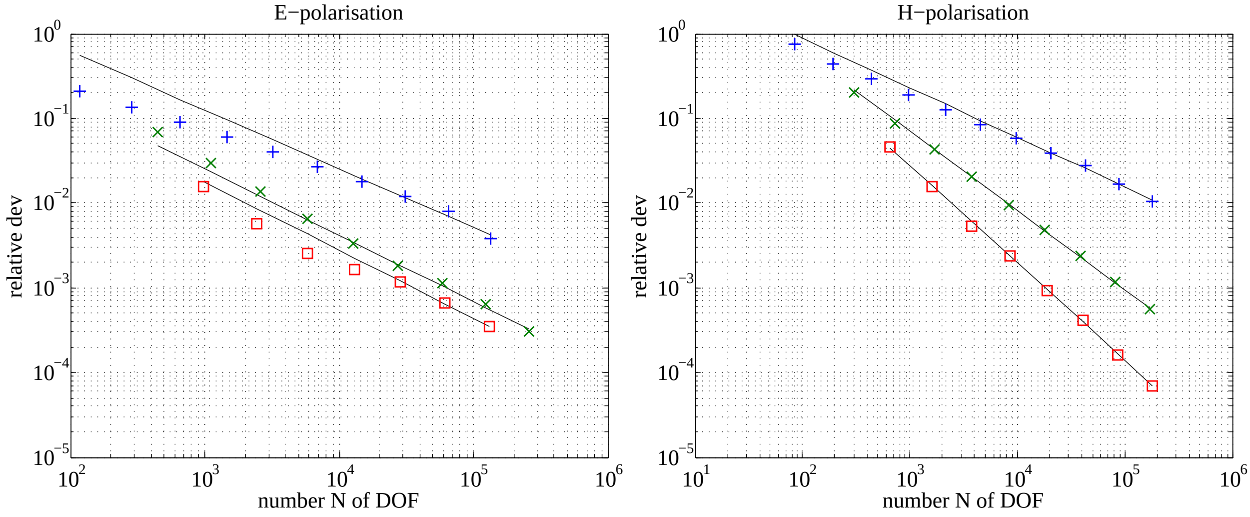

Fig. 5.38: Convergence curves of the global relative deviation of the derived field components for E-polarisation (left) and H-polarisation (right) using linear ($p = 1$, +), quadratic ($p = 2$, ×) and cubic ($p = 3$, □) basis functions. Black lines (–) indicate the linear trend of each convergence curve for sufficiently large N. The frequency is $f = 0.1\,\mathrm{Hz}$.

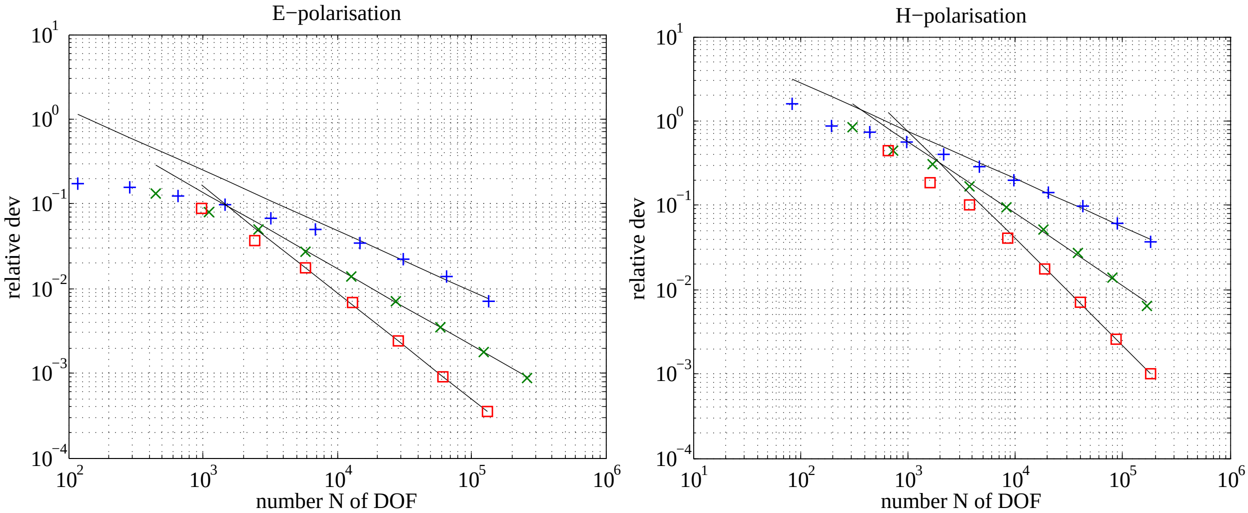

Fig. 5.39: Convergence curves of the global relative deviation of the derived field components for E-polarisation (left) and H-polarisation (right) using linear ($p = 1$, +), quadratic ($p = 2$, ×) and cubic ($p = 3$, □) basis functions. Black lines (–) indicate the linear trend of each convergence curve for sufficiently large N. The frequency is $f = 1\,\text{Hz}$.

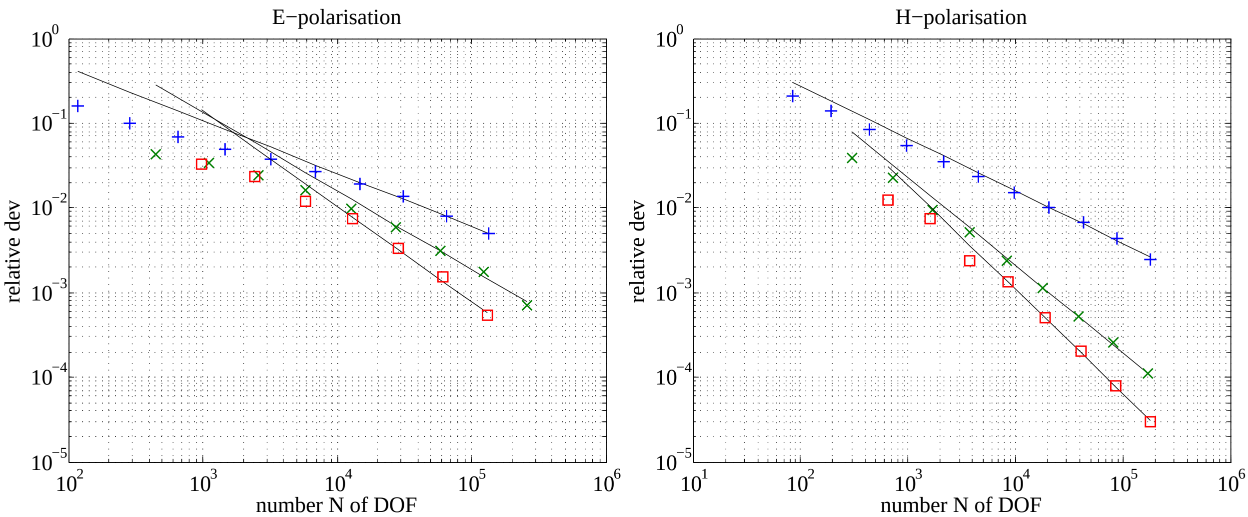

Fig. 5.40: Convergence curves of the global relative deviation of the derived field components for E-polarisation (left) and H-polarisation (right) using linear ($p = 1$, +), quadratic ($p = 2$, ×) and cubic ($p = 3$, □) basis functions. Black lines (–) indicate the linear trend of each convergence curve for sufficiently large N. The frequency is $f = 0.01\,\text{Hz}$.

		asymptotic conv. rate α_{as}			limiting conv. rate α_{lim}		
f[Hz]	p	1 (linear)	2 (quadratic)	3 (cubic)	1 (linear)	2 (quadratic)	3 (cubic)
0.01	E-polarisation	-0.62	-0.93	-1.12	-0.68	-1.24	-1.39
(Fig. 5.40)	H-polarisation	-0.62	-1.04	-1.23	-0.79	-1.14	-1.30
0.1	E-polarisation	-0.69	-0.78	-0.80	-1.00	-0.98	-0.87
(Fig. 5.38)	H-polarisation	-0.58	-0.94	-1.15	-0.67	-1.01	-1.14
1	E-polarisation	-0.71	-0.90	-1.25	-0.96	-0.95	-1.26
(Fig. 5.39)	H-polarisation	-0.57	-0.86	-1.27	-0.70	-1.05	-1.30

Tab. 5.21: Asymptotic (α_{as}) and limiting (α_{lim}) convergence rate of the derived field components for E- and H-polarisation depending on the polynomial degree p of the basis functions.

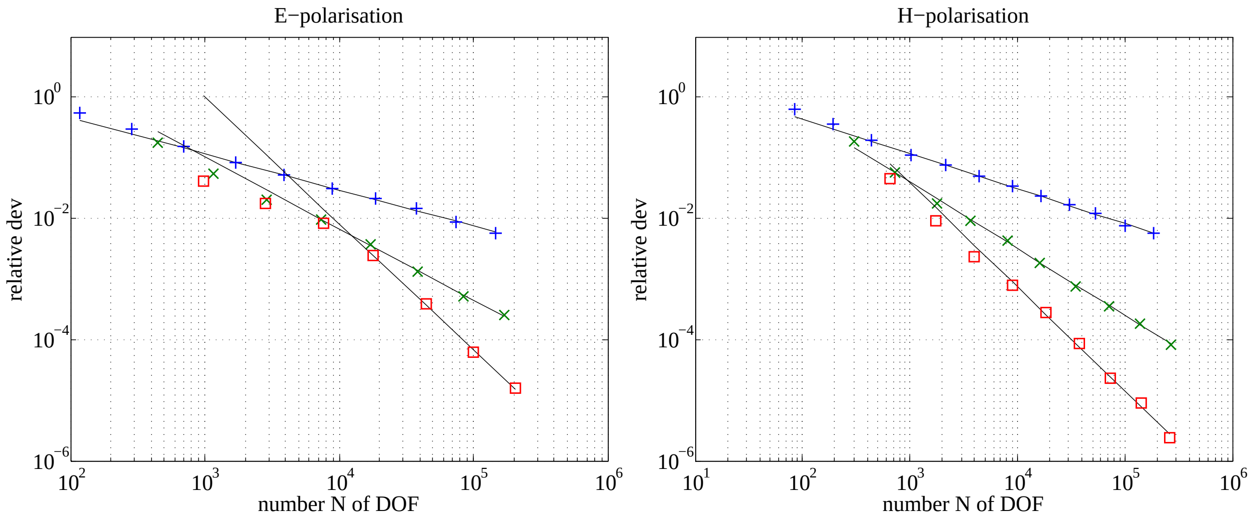

Fig. 5.41: Convergence curves of the global relative deviation of the derived field components for E-polarisation (left) and H-polarisation (right) using linear ($p = 1$, +), quadratic ($p = 2$, ×) and cubic ($p = 3$, □) basis functions. Black lines (–) indicate the linear trend of each convergence curve for sufficiently large N. The frequency is $f = 0.1\,\mathrm{Hz}$. Adaptive mesh refinement.

		asymptotic conv. rate α_{as}			limiting conv. rate α_{lim}		
f [Hz]	p	1 (linear)	2 (quadratic)	3 (cubic)	1 (linear)	2 (quadratic)	3 (cubic)
0.01 (no figure)	E-polarisation	-0.62	-1.07	-1.74	-0.66	-1.01	-1.41
	H-polarisation	-0.61	-1.02	-1.63	-0.64	-1.05	-1.84
0.1 (Fig. 5.41)	E-polarisation	-0.59	-1.18	-2.08	-0.59	-1.02	-1.88
	H-polarisation	-0.58	-1.10	-1.72	-0.52	-1.22	-2.19
1 (no figure)	E-polarisation	-0.64	-1.21	-1.88	-0.67	-1.06	-1.52
	H-polarisation	-0.62	-1.05	-1.54	-0.66	-1.09	-1.78

Tab. 5.22: Asymptotic (α_{as}) and limiting (α_{lim}) convergence rate of the derived field components for E- and H-polarisation depending on the polynomial degree p of the basis functions. Adaptive mesh refinement.

5.4.4 Local Convergence

Fig. 5.42 displays convergence curves for linear ($p = 1$, +), quadratic ($p = 2$, ×) and cubic ($p = 3$, □) basis functions at a frequency of $f = 0.1\,\mathrm{Hz}$ for all DOF on the earth's surface (left-hand diagram) and the point $(0, 0)$ (right-hand diagram). The local convergence curves are less smooth than the global ones (cf. Fig. 5.34). However, the trend shows that the absolute value of the convergence rate α_{as} for third-order ($p = 3$) finite elements listed in Tab. 5.23 is significantly below the expected value of 2 (cf. section 4.4). For the higher and the lower frequency of $f = 1\,\mathrm{Hz}$ and $f = 0.01\,\mathrm{Hz}$, respectively, the convergence rates are closer to the predicted value again (cf. Figs 5.43 and 5.44) since, for the corresponding small and large skin depths, the layered-halfspace model appears to be a homogeneous halfspace. Adaptive mesh refinement leads to improved convergence rates as Fig. 5.45 and Tab. 5.24 illustrate. The absolute values of the local convergence rates are also increased compared to the global ones (cf. Tab. 5.20).

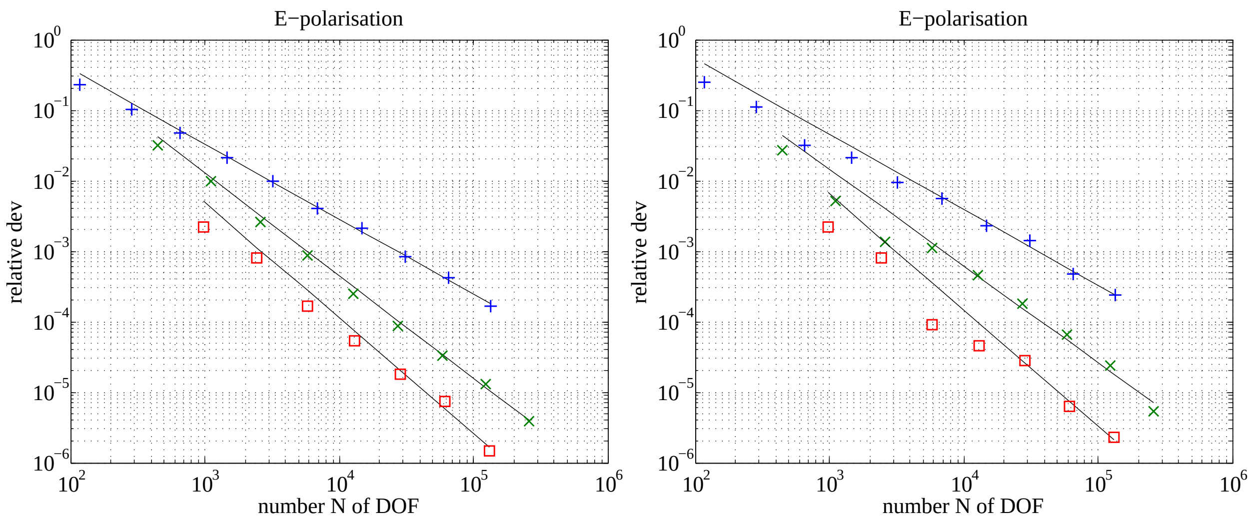

Fig. 5.42: Convergence curves of the local relative deviation of the electric field from the finest-grid solution for E-polarisation for all DOF on the earth's surface (left) and for the point $(0, 0)$ (right) using linear ($p = 1$,+), quadratic ($p = 2$, ×) and cubic ($p = 3$, □) basis functions. Black lines (–) indicate the linear trend of each convergence curve for sufficiently large N. The frequency is $f = 0.1\,\mathrm{Hz}$.

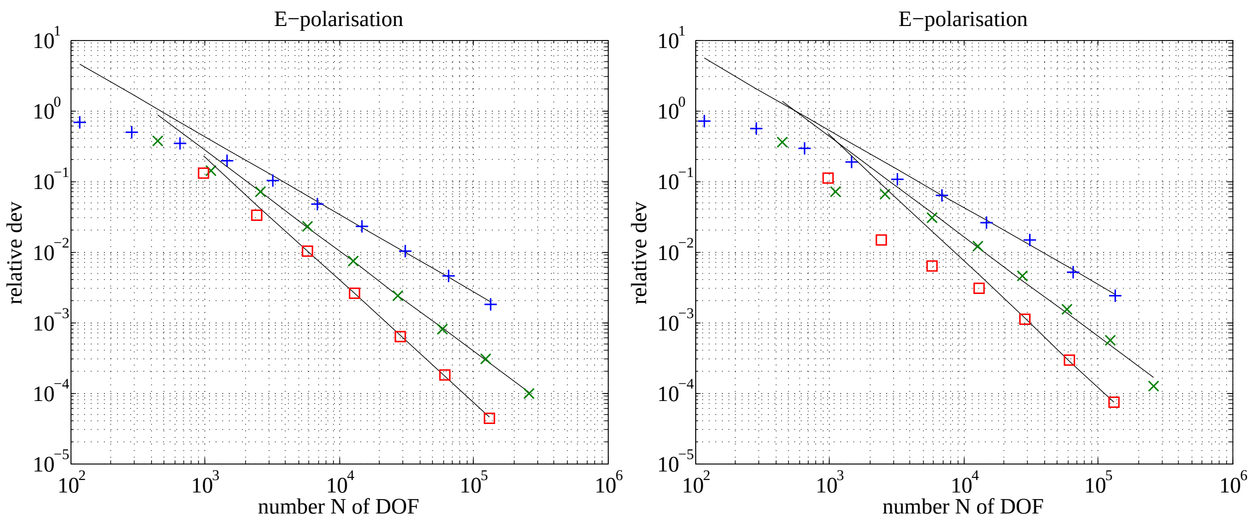

Fig. 5.43: Convergence curves of the local relative deviation of the electric field from the finest-grid solution for E-polarisation for all DOF on the earth's surface (left) and for the point $(0,0)$ (right) using linear ($p = 1$,+), quadratic ($p = 2$, ×) and cubic ($p = 3$, □) basis functions. Black lines (–) indicate the linear trend of each convergence curve for sufficiently large N. The frequency is $f = 1\,\mathrm{Hz}$.

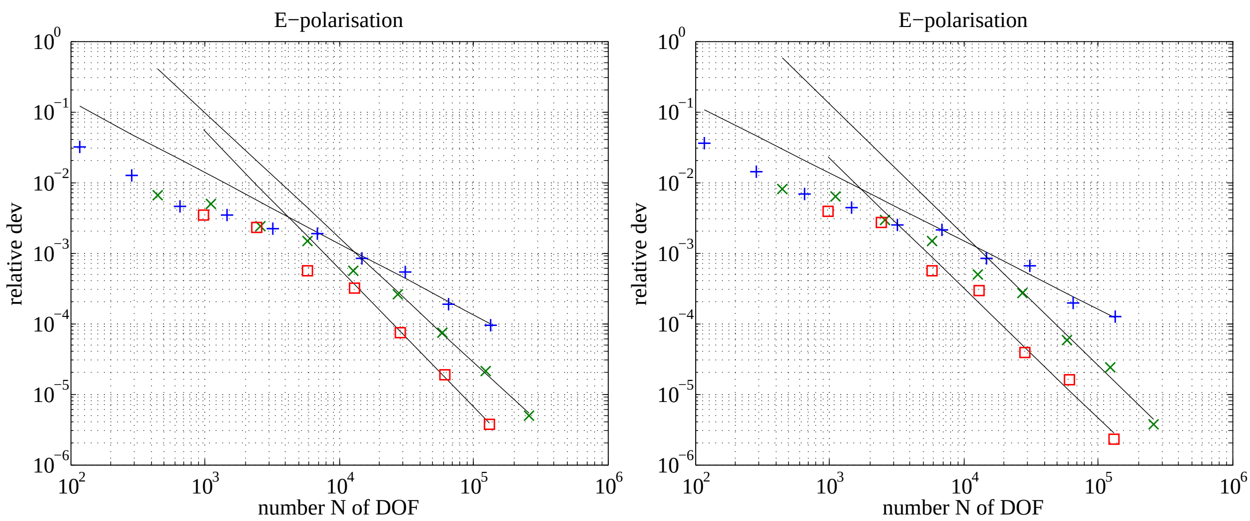

Fig. 5.44: Convergence curves of the local relative deviation of the electric field from the finest-grid solution for E-polarisation for all DOF on the earth's surface (left) and for the point $(0,0)$ (right) using linear ($p = 1$, +), quadratic ($p = 2$, ×) and cubic ($p = 3$, □) basis functions. Black lines (–) indicate the linear trend of each convergence curve for sufficiently large N. The frequency is $f = 0.01\,\mathrm{Hz}$.

		asymptotic conv. rate α_{as}			limiting conv. rate α_{lim}		
$f\,[\mathrm{Hz}]$	p	1 (linear)	2 (quadratic)	3 (cubic)	1 (linear)	2 (quadratic)	3 (cubic)
0.01	earth's surface	-1.01	-1.77	-1.95	-0.96	-1.97	-2.12
(Fig. 5.44)	$(0, 0)$	-0.96	-1.85	-1.83	-0.61	-2.50	-2.56
0.1	earth's surface	-1.06	-1.45	-1.63	-1.30	-1.65	-2.14
(Fig. 5.42)	$(0, 0)$	-1.07	-1.37	-1.65	-0.97	-2.06	-1.34
1	earth's surface	-1.10	-1.42	-1.74	-1.30	-1.57	-1.81
(Fig. 5.43)	$(0, 0)$	-1.09	-1.41	-1.79	-1.07	-2.00	-1.82

Tab. 5.23: Asymptotic (α_{as}) and limiting (α_{lim}) local convergence rate for the electric field in the case of E-polarisation at all DOF on the earth's surface and at the point $(0, 0)$ depending on the the polynomial degree p of the basis functions.

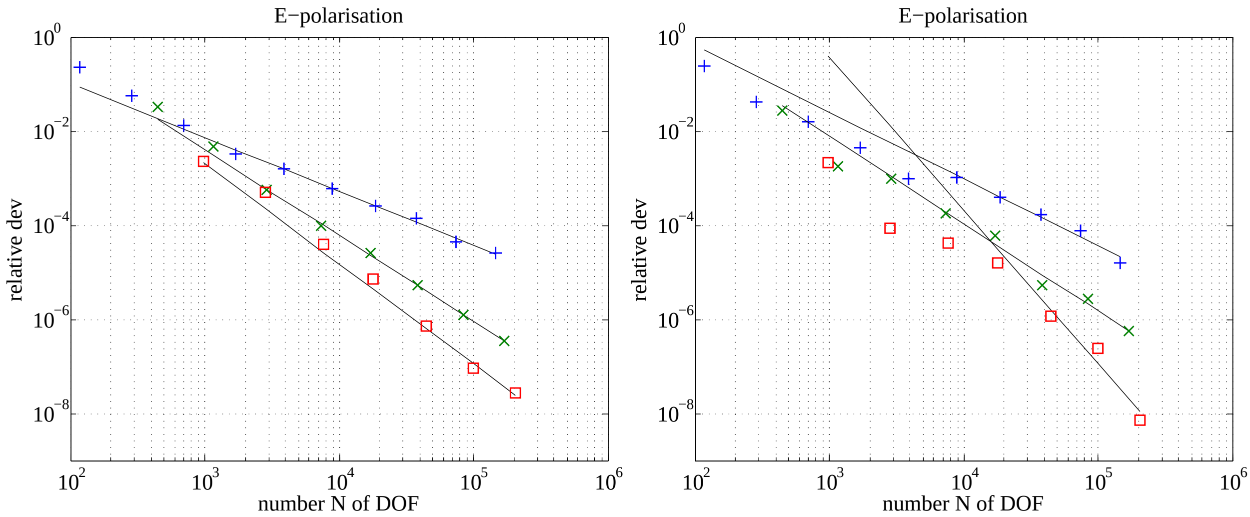

Fig. 5.45: Convergence curves of the local relative deviation of the electric field from the finest-grid solution for E-polarisation for all DOF on the earth's surface (left) and for the point $(0, 0)$ (right) using linear ($p = 1$,+), quadratic ($p = 2$, ×) and cubic ($p = 3$, □) basis functions. Black lines (–) indicate the linear trend of each convergence curve for sufficiently large N. The frequency is $f = 0.1\,\mathrm{Hz}$. Adaptive mesh refinement.

		asymptotic conv. rate α_{as}			limiting conv. rate α_{lim}		
$f\,[\mathrm{Hz}]$	p	1 (linear)	2 (quadratic)	3 (cubic)	1 (linear)	2 (quadratic)	3 (cubic)
0.01	earth's surface	-1.16	-1.83	-2.51	-1.19	-2.46	-3.10
(no figure)	$(0,0)$	-1.12	-1.60	-2.47	-2.34	-3.43	-2.88
0.1	earth's surface	-1.15	-1.81	-2.28	-0.81	-1.86	-1.71
(Fig. 5.45)	$(0,0)$	-1.41	-1.85	-3.25	-2.30	-2.31	-4.85
1	earth's surface	-1.18	-1.93	-2.53	-0.84	-1.81	-1.92
(no figure)	$(0,0)$	-1.08	-1.82	-2.28	-0.40	-2.28	-2.27

Tab. 5.24: Asymptotic (α_{as}) and limiting (α_{lim}) local convergence rate for the electric field in the case of E-polarisation at all DOF on the earth's surface and at the point $(0,0)$ depending on the the polynomial degree p of the basis functions. Adaptive mesh refinement.

Derived Field Components

The derived field components exhibit local convergence behaviour (cf. Figs 5.46 and 5.47 for E- and H-polarisation, respectively, and $f = 0.1\,\mathrm{Hz}$) that is hardly represented by a linear trend especially considering only the point $(0, 0)$ in the right-hand diagram. Here, the convergence curve is not even monotonic. However, if convergence rates are estimated nevertheless, convergence behaviour almost as predicted in section 4.4 can be observed (cf. Tab. 5.25). The absolute values of the local convergence rates are higher than the global ones for the layered-halfspace model (cf. Tab. 5.41). In most cases, adaptive mesh refinement leads to a further improvement of the convergence rate (cf. Figs 5.48, 5.49, and Tab. 5.26).

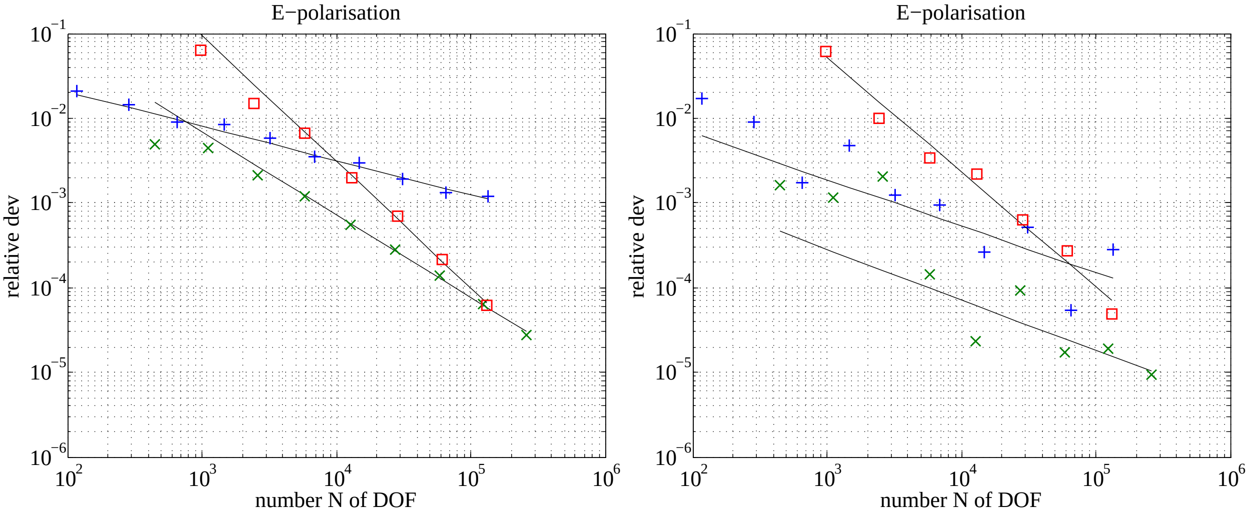

Fig. 5.46: Convergence curves of the local relative deviation of the derived field components for the earth's surface (left) and the point $(0, 0)$ (right) for E-polarisation using linear ($p = 1$, +), quadratic ($p = 2$, ×) and cubic ($p = 3$, □) basis functions. Black lines (–) indicate the linear trend of each convergence curve for sufficiently large N. The frequency is $f = 0.1\,\mathrm{Hz}$.

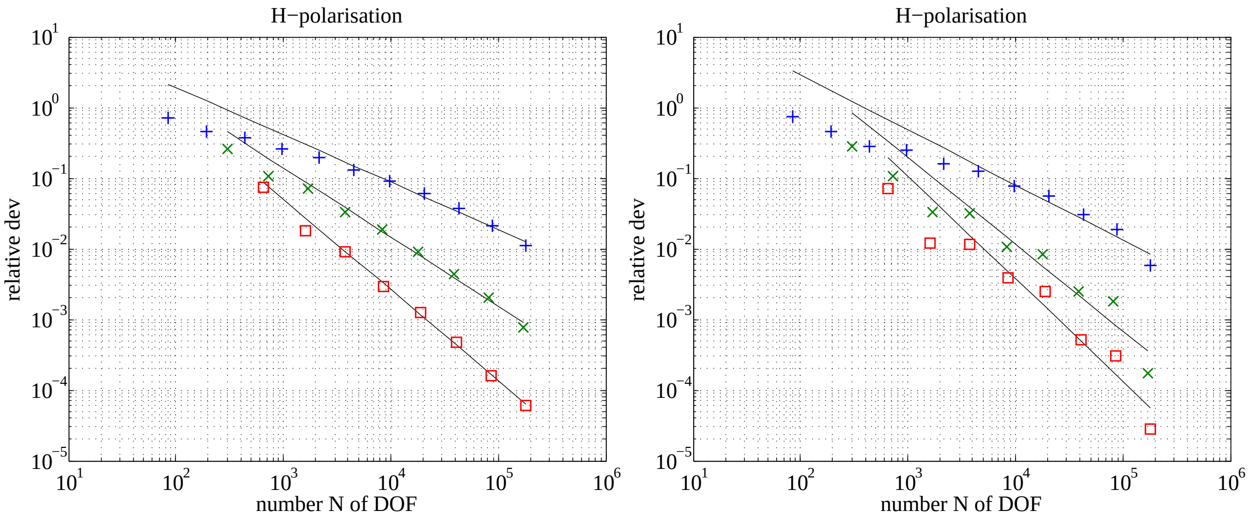

Fig. 5.47: Convergence curves of the local relative deviation of the derived field components for the earth's surface (left) and the point $(0, 0)$ (right) for H-polarisation using linear ($p = 1$, +), quadratic ($p = 2$, ×) and cubic ($p = 3$, □) basis functions. Black lines (–) indicate the linear trend of each convergence curve for sufficiently large N. The frequency is $f = 0.1\,\mathrm{Hz}$.

			asymptotic conv. rate α_{as}			limiting conv. rate α_{lim}		
f[Hz]		p	1 (linear)	2 (quadratic)	3 (cubic)	1 (linear)	2 (quadratic)	3 (cubic)
0.01	E-polarisation	earth's surface	-0.50	-1.55	-1.77	-0.26	-1.45	-1.80
	(no figure)	$(0,0)$	-0.75	-1.39	-1.49	1.78	-1.60	-2.22
	H-polarisation	earth's surface	-0.69	-1.07	-1.82	-0.88	-1.29	-1.71
	(no figure)	$(0,0)$	-0.80	-1.25	-2.18	-1.64	-3.23	-4.02
0.1	E-polarisation	earth's surface	-0.41	-0.98	-1.49	-0.18	-1.12	-1.65
	(Fig. 5.46)	$(0,0)$	-0.55	-0.60	-1.35	2.27	-0.95	-2.26
	H-polarisation	earth's surface	-0.67	-0.98	-1.28	-0.87	-1.29	-1.30
	(Fig. 5.47)	$(0,0)$	-0.78	-1.23	-1.45	-1.65	-2.20	-3.17
1	E-polarisation	earth's surface	-0.38	-0.82	-1.15	-0.11	-1.06	-1.59
	(no figure)	$(0,0)$	-0.63	-0.84	-1.12	1.17	-0.88	-2.26
	H-polarisation	earth's surface	-0.67	-0.95	-1.13	-0.85	-1.23	-1.30
	(no figure)	$(0,0)$	-0.75	-0.99	-1.01	-1.68	-3.14	-3.03

Tab. 5.25: Asymptotic (α_{as}) and limiting (α_{lim}) convergence rate of the derived field components for E- and H-polarisation on the earth's surface and in the point $(0,0)$ depending on the polynomial degree p of the basis functions.

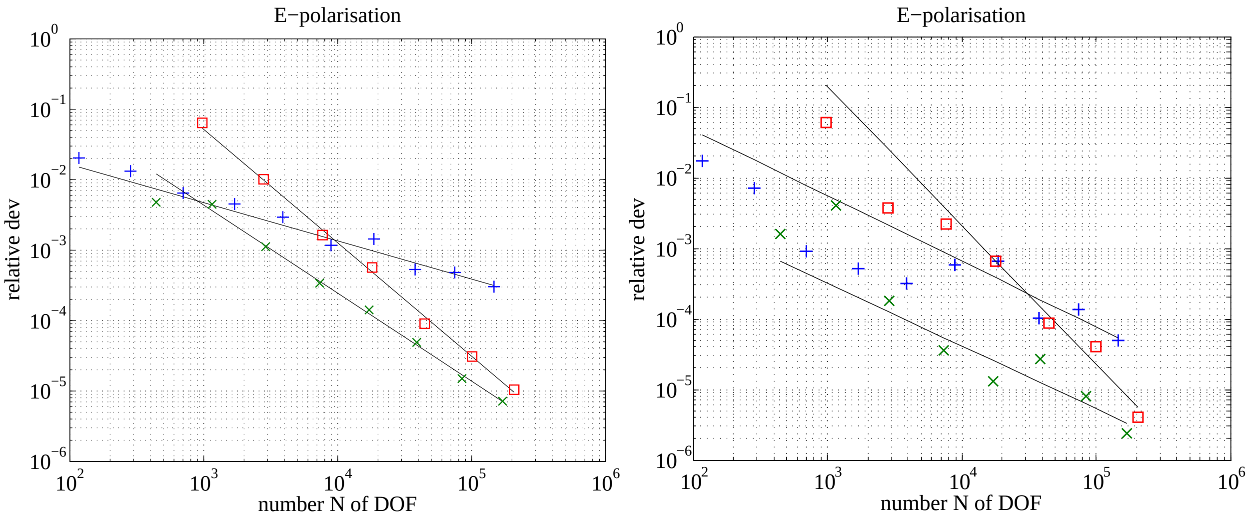

Fig. 5.48: Convergence curves of the local relative deviation of the derived field components on the earth's surface (left) and at the point $(0, 0)$ (right) for E-polarisation using linear ($p = 1$, +), quadratic ($p = 2$, ×) and cubic ($p = 3$, □) basis functions. Black lines (–) indicate the linear trend of each convergence curve for sufficiently large N. The frequency is $f = 0.1\,\mathrm{Hz}$. Adaptive mesh refinement.

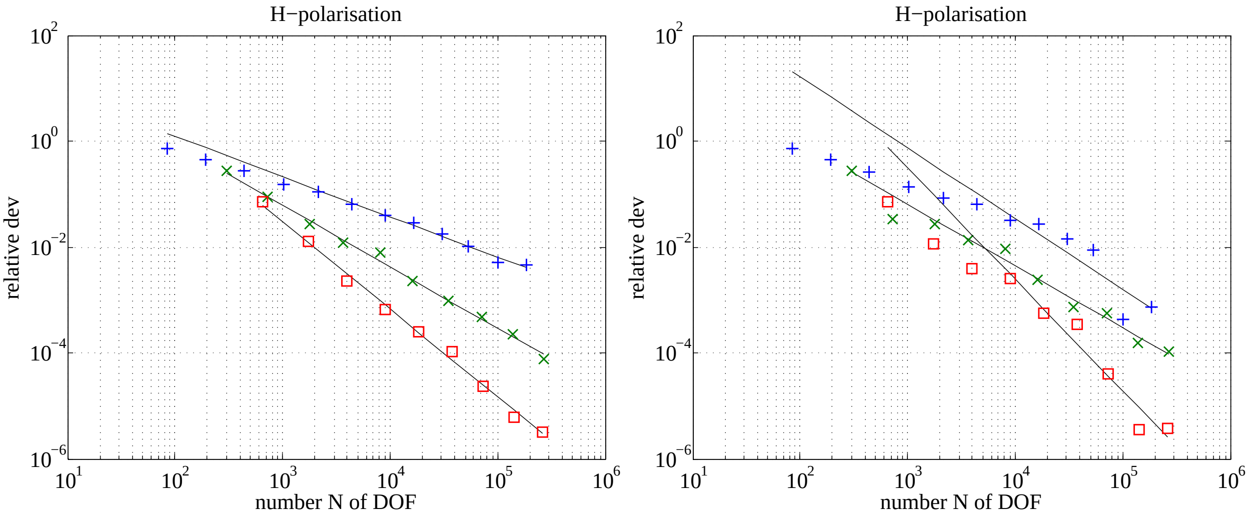

Fig. 5.49: Convergence curves of the local relative deviation of the derived field components on the earth's surface (left) and at the point $(0, 0)$ (right) for H-polarisation using linear ($p = 1$, +), quadratic ($p = 2$, ×) and cubic ($p = 3$, □) basis functions. Black lines (–) indicate the linear trend of each convergence curve for sufficiently large N. The frequency is $f = 0.1\,\mathrm{Hz}$. Adaptive mesh refinement.

			asymptotic conv. rate α_{as}			limiting conv. rate α_{lim}		
$f\,[\mathrm{Hz}]$		p	1 (linear)	2 (quadratic)	3 (cubic)	1 (linear)	2 (quadratic)	3 (cubic)
0.01	E-polarisation	earth's surface	-0.83	-1.33	-1.82	-1.01	-1.56	-1.88
	(no figure)	$(0,0)$	-0.99	-1.65	-1.75	-1.47	-2.70	-1.50
	H-polarisation	earth's surface	-0.88	-1.22	-1.56	-2.51	-1.83	-2.43
	(no figure)	$(0,0)$	-0.91	-1.34	-1.53	-3.16	-3.11	-1.43
0.1	E-polarisation	earth's surface	-0.54	-1.25	-1.61	-0.69	-1.06	-1.50
	(Fig. 5.48)	$(0,0)$	-0.93	-0.89	-1.96	-1.48	-1.72	-3.15
	H-polarisation	earth's surface	-0.76	-1.16	-1.66	-0.14	-1.64	-1.06
	(Fig. 5.49)	$(0,0)$	-1.34	-1.17	-2.11	0.94	-0.52	0.05
1	E-polarisation	earth's surface	-0.91	-1.29	-1.71	-0.75	-0.99	-1.78
	(no figure)	$(0,0)$	-2.40	-2.43	-1.83	3.76	-1.69	-2.63
	H-polarisation	earth's surface	-0.69	-1.25	-1.74	-0.71	-1.46	-2.23
	(no figure)	$(0,0)$	-0.71	-1.16	-1.91	-0.62	-0.63	-4.00

Tab. 5.26: Asymptotic (α_{as}) and limiting (α_{lim}) convergence rate for the derived field components in the case of E- and H-polarisation on the earth's surface and in the point $(0,0)$ depending on the polynomial degree p of the basis functions. Adaptive mesh refinement.

5.5 The COMMEMI 3-D-2 Model

We now turn to 3-D simulation. The following convergence studies are carried out for the COMMEMI 3-D-2 model composed of a conductive and a resistive block embedded in a layered-halfspace background model (cf. Fig. 5.50). The convergence of the numerical solutions of BVPs (i) (eqs (3.3)), (ii) (eqs (3.4)), (iii) (eqs (3.11)), (iv) (eqs (3.12)), and (v) (eqs (3.19)) to the appropriate numerical finest-grid solution is examined. Note that, first, the field components parallel to the normal electromagnetic

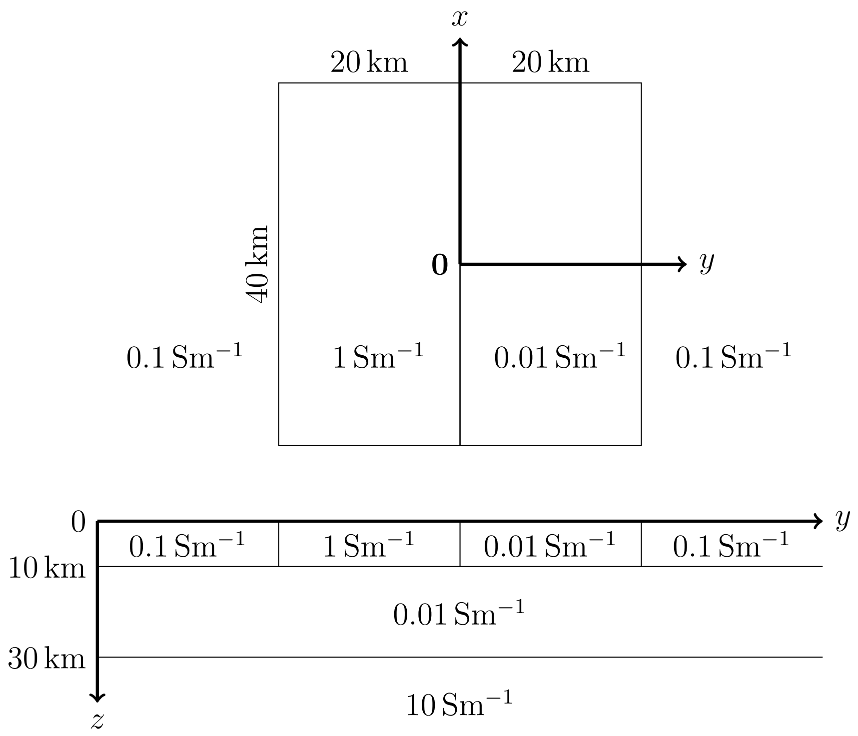

Fig. 5.50: COMMEMI model 3-D-2

fields for polarisation 1, i.e. E_x and H_y, are considered. Hence,

$$(\mathbf{u})_i = \begin{cases} \mathbf{u} \cdot \mathbf{e}_y = H_y & \text{for} \quad \text{BVP (i)} \\ \mathbf{u} \cdot \mathbf{e}_x = E_x & \text{for} \quad \text{BVP (ii) – BVP (v)} \end{cases} \tag{5.7}$$

and

$$(\nabla\times \mathbf{u})_i = \begin{cases} (\nabla\times \mathbf{u}) \cdot \mathbf{e}_x = E_x & \text{for} \quad \text{BVP (i)} \\ (\nabla\times \mathbf{u}) \cdot \mathbf{e}_y = H_y & \text{for} \quad \text{BVP (ii) – BVP (v)} \end{cases} \tag{5.8}$$

where $\mathbf{e}_x = (1, 0, 0)^T$ and $\mathbf{e}_y = (0, 1, 0)^T$ are unit vectors in x- and y-direction. The field components orthogonal to the normal fields, i.e. E_y, E_z, H_x, and H_z for polarisation 1, and the second direction of polarisation (polarisation 2) with the normal field components $\mathbf{E}_n = E_0 \cdot \mathbf{e}_y$ and $\mathbf{H}_n = H_0 \cdot \mathbf{e}_x$ are considered in the appropriate subsections.

5.5.1 h-Refinement versus p-Refinement

Figs 5.51 – 5.55 display the convergence curves for BVP (i) – (v) for the COMMEMI 3D-2 model. Tab. 5.27 summarises the appropriate convergence rates. The absolute values of the asymptotic con-

vergence rates do not exceed 0.7 even in the case of cubic ($p = 3$) basis functions for which eq. (4.88) predicts $\alpha = -1$. In contrast, for a 3-D model of a homogeneous halfspace with conductivity $\sigma = 0.01\,\mathrm{Sm}^{-1}$, the predicted convergence rate is almost reached for the simulated $(\mathbf{u})_i$ field components (cf. Figs 5.56 – 5.59 and Tab. 5.28). However, for quadratic ($p = 2$) and cubic ($p = 3$) basis functions, the convergence rates are difficult to estimate since the relative deviations diverge for large numbers N of DOF. Note that, BVP (v) is not applicable to the homogeneous-halfspace model since in the absence of lateral conductivity contrasts no anomalous vector potential occurs.
The presence of horizontal conductivity contrasts in the COMMEMI 3-D-2 model limits the convergence rate since electric charges accumulate there and the normal component of the electric field jumps. Hence, the regularity of the exact solution is reduced. For the homogeneous-halfspace model containing the air-earth interface as vertical conductivity contrast, only the absolute values of the convergence rates for the magnetic field component H_y ($(\mathbf{u})_i$ for BVP (i) and $(\nabla\times\mathbf{u})_i$ for BVPs (ii) – (iv)) are slightly reduced.

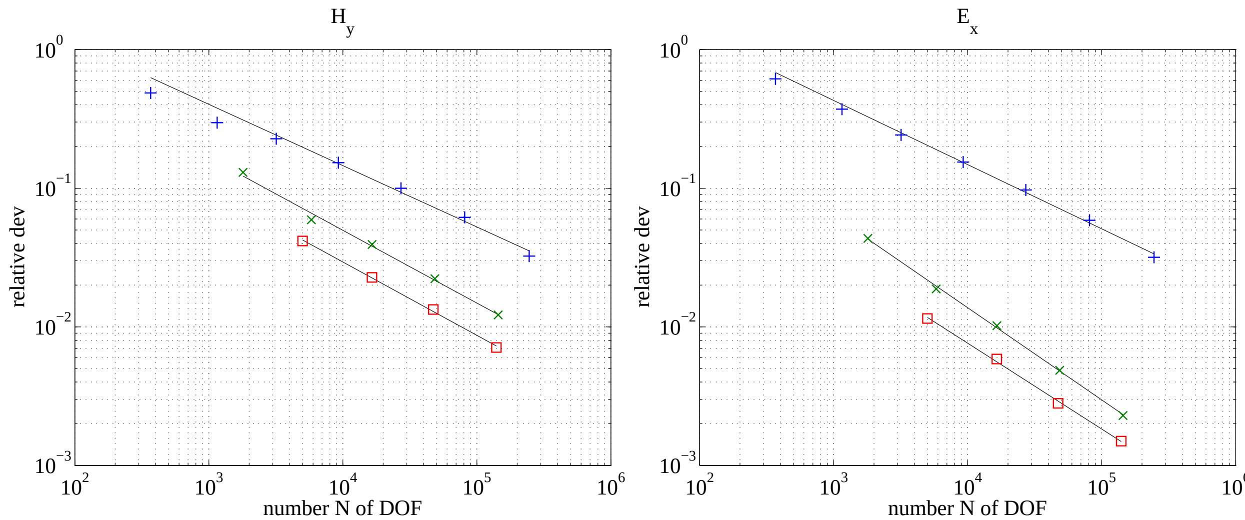

Fig. 5.51: Convergence curves for H_y (left) and E_x (right) computed from BVP (i) for the COMMEMI 3-D-2 model using linear ($p = 1$, +), quadratic ($p = 2$, ×) and cubic ($p = 3$, □) finite elements. Black lines (–) indicate the linear trend of each convergence curve for sufficiently large N. The frequency is $f = 0.1\,\mathrm{Hz}$. Polarisation 1.

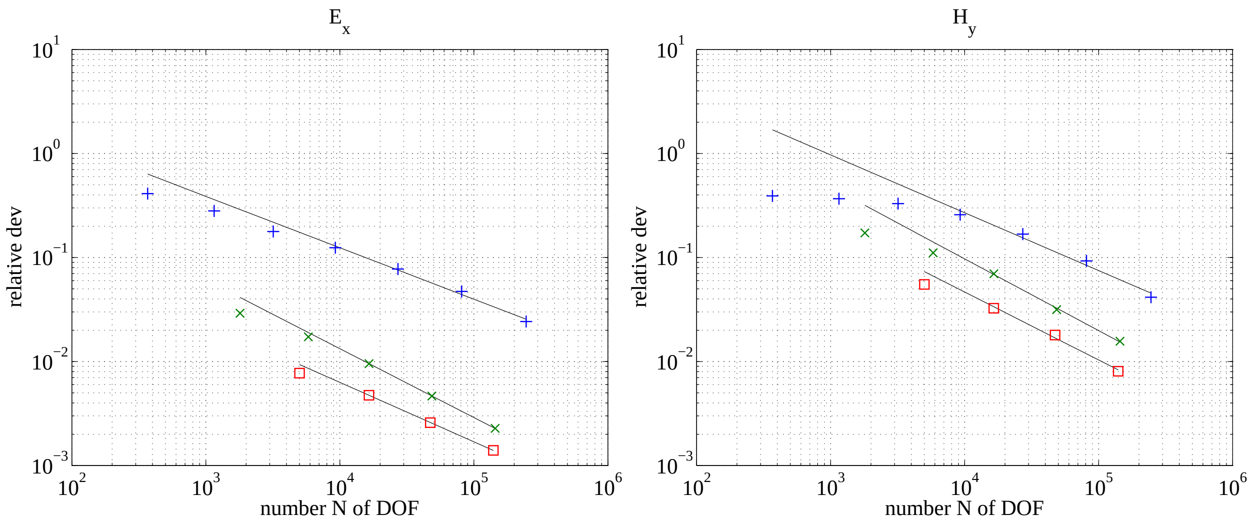

Fig. 5.52: Convergence curves for E_x (left) and H_y (right) computed from BVP (ii) for the COMMEMI 3-D-2 model using linear ($p = 1$, +), quadratic ($p = 2$, ×) and cubic ($p = 3$, □) finite elements. Black lines (–) indicate the linear trend of each convergence curve for sufficiently large N. The frequency is $f = 0.1\,\mathrm{Hz}$. Polarisation 1.

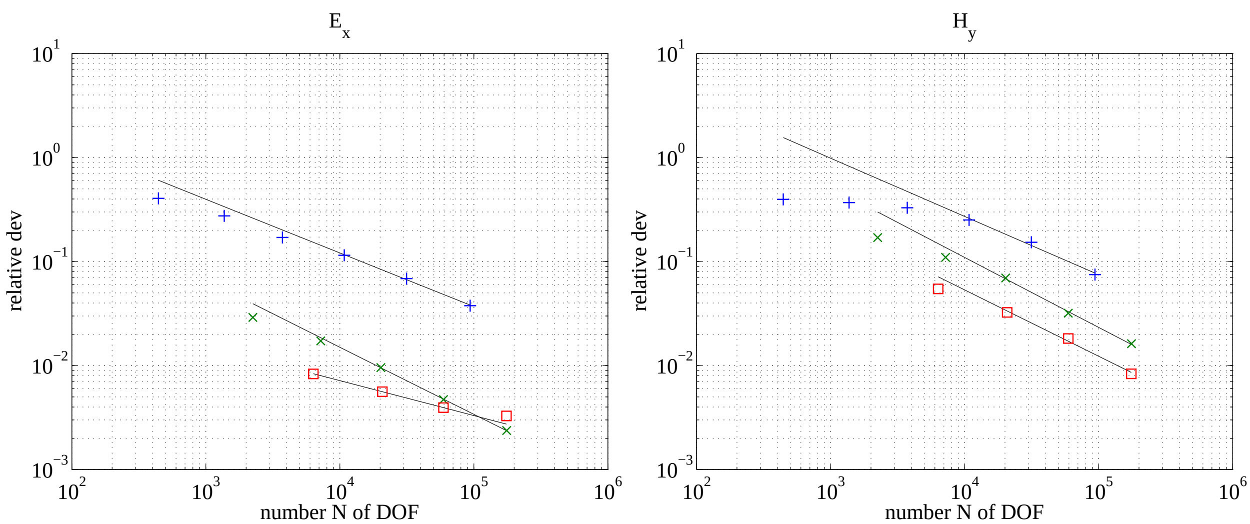

Fig. 5.53: Convergence curves for E_x (left) and H_y (right) computed from BVP (iii) for the COMMEMI 3-D-2 model using linear ($p = 1$, +), quadratic ($p = 2$, ×) and cubic ($p = 3$, □) finite elements. Black lines (–) indicate the linear trend of each convergence curve for sufficiently large N. The frequency is $f = 0.1\,\mathrm{Hz}$. Polarisation 1.

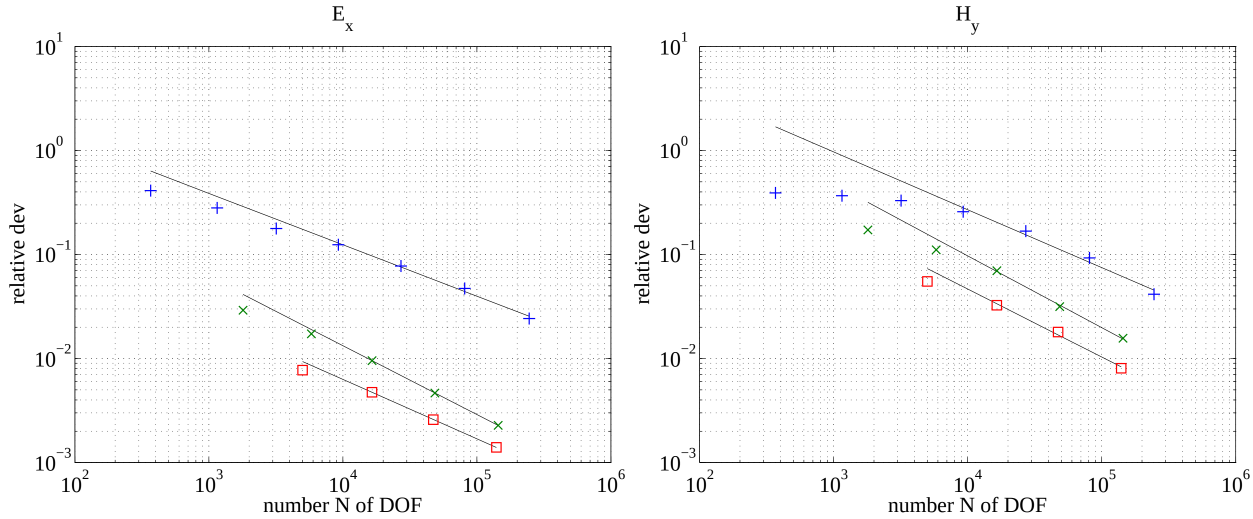

Fig. 5.54: Convergence curves for E_x (left) and H_y (right) computed from BVP (iv) for the COMMEMI 3-D-2 model using linear ($p = 1$, +), quadratic ($p = 2$, $\times$) and cubic ($p = 3$, $\square$) finite elements. Black lines (–) indicate the linear trend of each convergence curve for sufficiently large N. The frequency is $f = 0.1\,\mathrm{Hz}$. Polarisation 1.

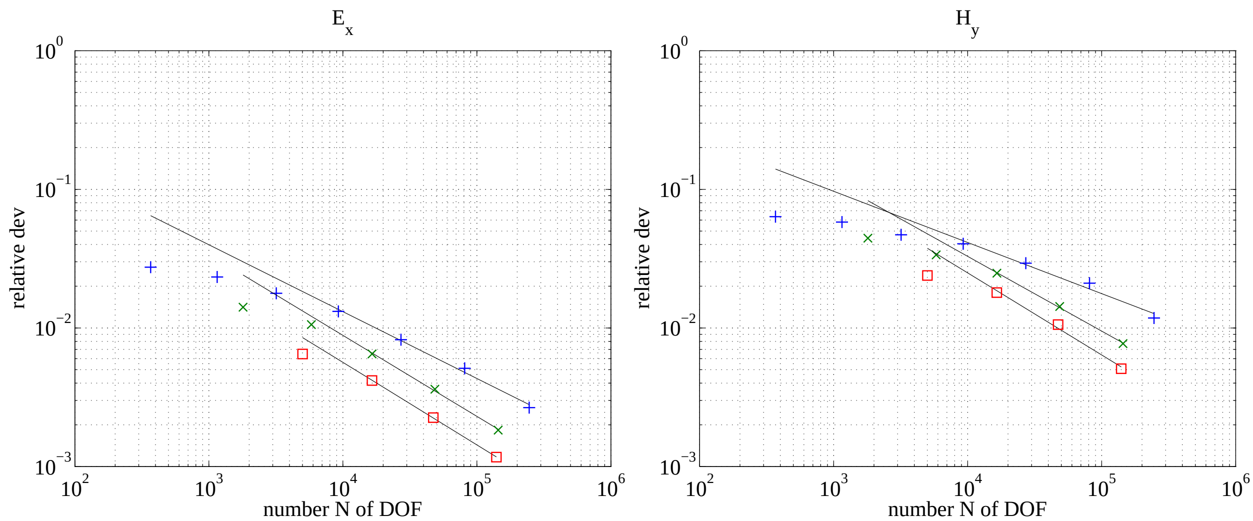

Fig. 5.55: Convergence curves for E_x (left) and H_y (right) computed from BVP (v) for the COMMEMI 3-D-2 model using linear ($p = 1$, +), quadratic ($p = 2$, $\times$) and cubic ($p = 3$, $\square$) finite elements. Black lines (–) indicate the linear trend of each convergence curve for sufficiently large N. The frequency is $f = 0.1\,\mathrm{Hz}$. Polarisation 1.

		asymptotic conv. rate α_{as}		limiting conv. rate α_{lim}	
	p	$(\mathbf{u})_i$	$(\nabla\times\mathbf{u})_i$	$(\mathbf{u})_i$	$(\nabla\times\mathbf{u})_i$
BVP (i)	1	-0.44	-0.46	-0.58	-0.56
	2	-0.53	-0.66	-0.55	-0.69
	3	-0.53	-0.62	-0.58	-0.58
BVP (ii)	1	-0.49	-0.56	-0.60	-0.73
	2	-0.66	-0.69	-0.66	-0.64
	3	-0.57	-0.65	-0.57	-0.74
BVP (iii)	1	-0.52	-0.56	-0.55	-0.66
	2	-0.64	-0.67	-0.63	-0.62
	3	-0.34	-0.64	-0.17	-0.72
BVP (iv)	1	-0.49	-0.56	-0.60	-0.73
	2	-0.66	-0.69	-0.66	-0.64
	3	-0.57	-0.65	-0.57	-0.74
BVP (v)	1	-0.48	-0.37	-0.59	-0.52
	2	-0.58	-0.54	-0.63	-0.57
	3	-0.60	-0.59	-0.61	-0.68

Tab. 5.27: Asymptotic (α_{as}) and limiting (α_{lim}) convergence rate of a field component of the numerical solution $(\mathbf{u})_i$ and its curl $(\nabla\times\mathbf{u})_i$ computed from BVPs (i) – (v) for the COMMEMI 3-D-2 model depending on the polynomial degree p of the basis functions. Polarisation 1. The frequency is $f = 0.1\,\text{Hz}$.

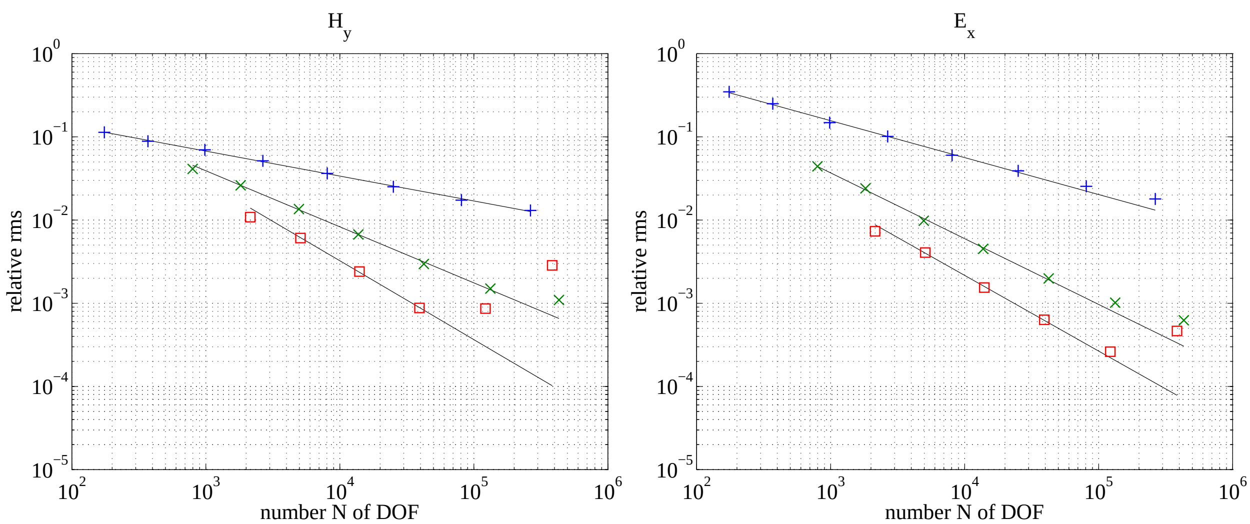

Fig. 5.56: Convergence curves for H_y (left) and E_x (right) computed from BVP (i) for the 3-D homogeneous-halfspace model using linear ($p = 1$, +), quadratic ($p = 2$, ×) and cubic ($p = 3$, □) finite elements. Black lines (–) indicate the linear trend of each convergence curve for sufficiently large N until it starts to diverge. The frequency is $f = 0.1\,\text{Hz}$. Polarisation 1.

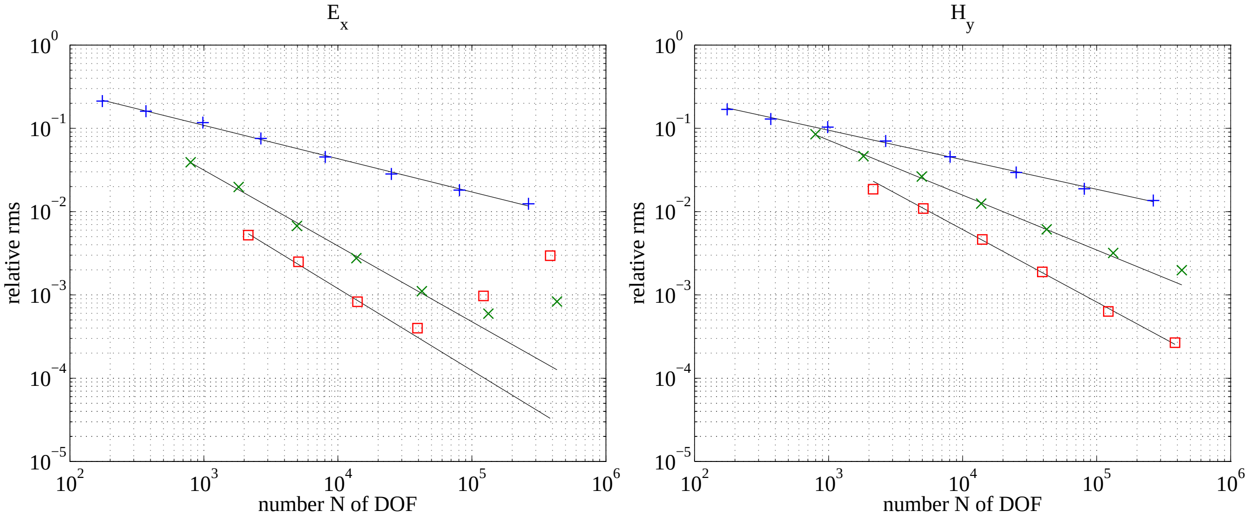

Fig. 5.57: Convergence curves for E_x (left) and H_y (right) computed from BVP (ii) for the 3-D homogeneous-halfspace model using linear ($p = 1$, +), quadratic ($p = 2$, ×) and cubic ($p = 3$, □) finite elements. Black lines (–) indicate the linear trend of each convergence curve for sufficiently large N until it starts to diverge. The frequency is $f = 0.1$ Hz. Polarisation 1.

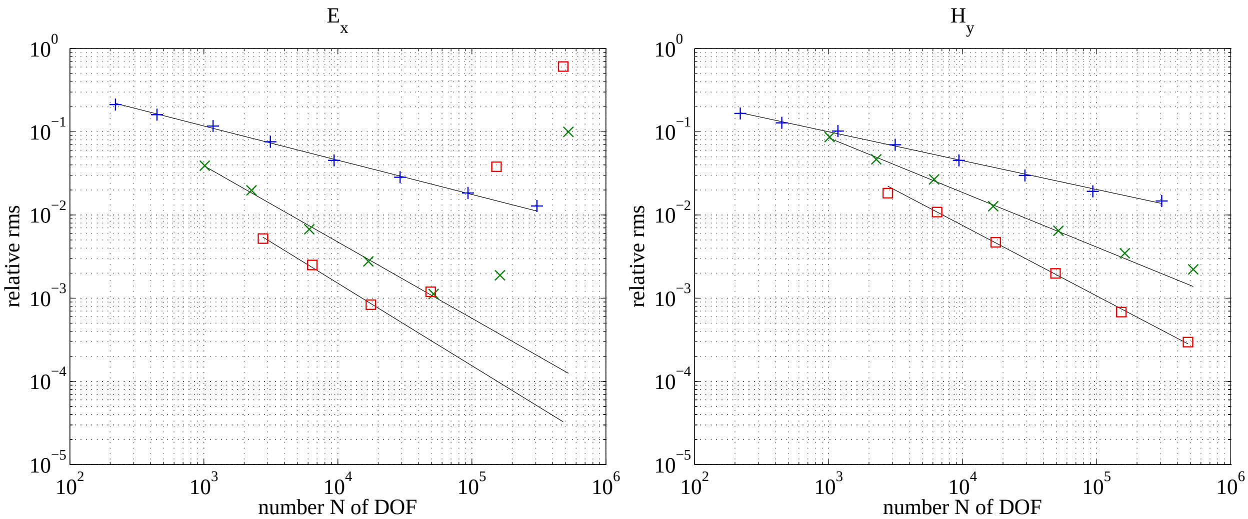

Fig. 5.58: Convergence curves for E_x (left) and H_y (right) computed from BVP (iii) for the 3-D homogeneous-halfspace model using linear ($p = 1$, +), quadratic ($p = 2$, ×) and cubic ($p = 3$, □) finite elements. Black lines (–) indicate the linear trend of each convergence curve for sufficiently large N until it starts to diverge. The frequency is $f = 0.1$ Hz. Polarisation 1.

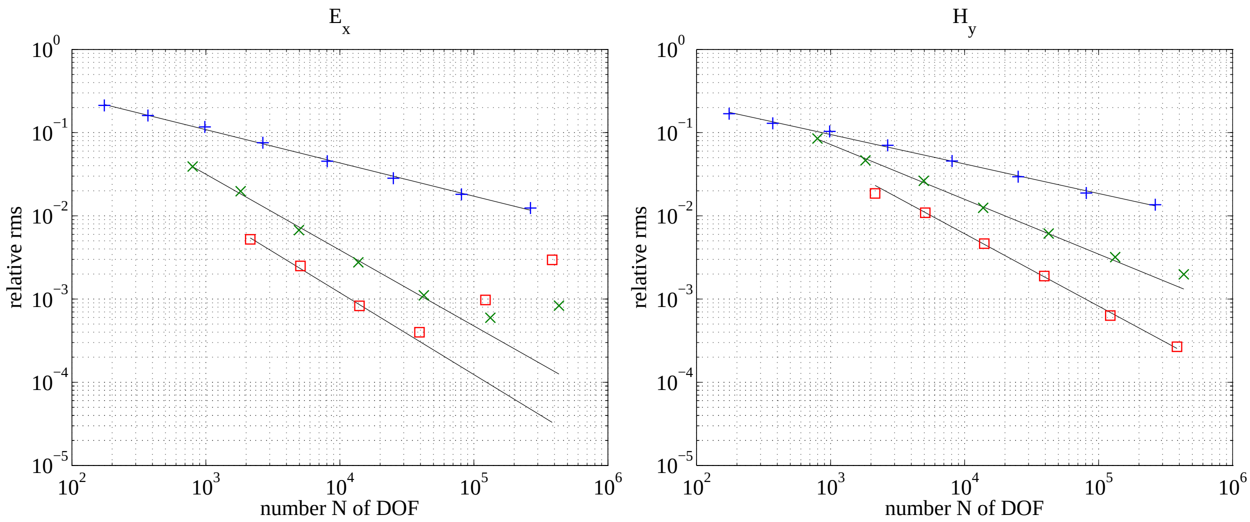

Fig. 5.59: Convergence curves for E_x (left) and H_y (right) computed from BVP (iv) for the 3-D homogeneous-halfspace model using linear ($p = 1$, +), quadratic ($p = 2$, ×) and cubic ($p = 3$, □) finite elements. Black lines (–) indicate the linear trend of each convergence curve for sufficiently large N until it starts to diverge. The frequency is $f = 0.1\,\mathrm{Hz}$. Polarisation 1.

		asymptotic conv. rate α_{as}		limiting conv. rate α_{lim}	
	p	$(\mathbf{u})_i$	$(\nabla\times\mathbf{u})_i$	$(\mathbf{u})_i$	$(\nabla\times\mathbf{u})_i$
BVP (i)	1	-0.30	-0.44	-0.24	-0.29
	2	-0.67	-0.79	-0.27	-0.41
	3	-0.95	-0.91	1.04	0.50
BVP (ii)	1	-0.40	-0.35	-0.32	-0.27
	2	-0.91	-0.66	0.28	-0.41
	3	-0.98	-0.87	0.97	-0.75
BVP (iii)	1	-0.41	-0.35	-0.31	-0.23
	2	-0.92	-0.66	3.37	-0.38
	3	-0.99	-0.85	2.42	-0.73
BVP (iv)	1	-0.40	-0.35	-0.32	-0.27
	2	-0.91	-0.66	0.28	-0.41
	3	-0.98	-0.87	0.97	-0.75

Tab. 5.28: Asymptotic (α_{as}) and limiting (α_{lim}) convergence rate of a field component of the numerical solution $(\mathbf{u})_i$ and its curl $(\nabla\times\mathbf{u})_i$ computed from BVPs (i) – (iv) for the 3-D homogeneous-halfspace model depending on the polynomial degree p of the basis functions. Polarisation 1. The frequency is $f = 0.1\,\mathrm{Hz}$.

5.5.2 Frequency Dependence

Figs 5.60 and 5.61 display convergence curves using third-order ($p = 3$) finte elements for $f = 0.01\,\mathrm{Hz}$ and $f = 1\,\mathrm{Hz}$, respectively. From Tabs 5.29 and 5.30 listing the convergence rates, it becomes apparent that the convergence rates depend on the frequency. Maximum absolute convergence rates of up to 0.95 for cubic basis functions are obtained for the highest frequency of $f = 1\,\mathrm{Hz}$ that features the smallest skin depth. For lower frequencies, the skin depth is larger and the convergence behaviour is more seriously affected by the conductivity contrasts. Approximate maximum absolute convergence rates for $f = 0.01\,\mathrm{Hz}$ and $f = 0.1\,\mathrm{Hz}$ are 0.50 and 0.65, respectively. For linear basis functions, however, superconvergence can be observed for all frequencies and BVPs, i.e. the absolute value of the estimated convergence rate is higher than predicted.

5.5.3 Most Efficient Formulation - BVP (v)

From Tabs 5.29 and 5.30, it is obvious that, in the case of conductivity contrasts affecting the convergence behaviour, BVP (v) yields best convergence rates. The anomalous potential approach is well-suited to approximate the electromagnetic fields in the vicinity of jumps in the electrical conductivity. In the absence of the normal field components, the anomaly effect can be computed very accurately. Among BVP (i) – (iv) representing total field or potential approaches, BVP (i) approximating the magnetic field is advantageous in terms of convergence rates (cf. Tabs 5.29 and 5.30). BVP (iii), however, exhibits serious stability problems. For $f = 0.01\,\mathrm{Hz}$ and $p \geq 2$, the electric field component does not converge at all. The electric field is calculated from the magnetic vector potential $\mathbf{A}$ and the electric scalar potential V which is computed as part of a stabilisation term to introduce the null-space of the $\nabla\times\nabla\times$ -operator to the system of equations especially for low frequencies. V is observed to be in the order of $10^8\,\mathrm{V}$ for the second-finest grid which is far to large to be due to physical phenomena. A stabilised electric field approach by which the electric field components are computed directly as described by Schwarzbach (2009) seems to be more promising.

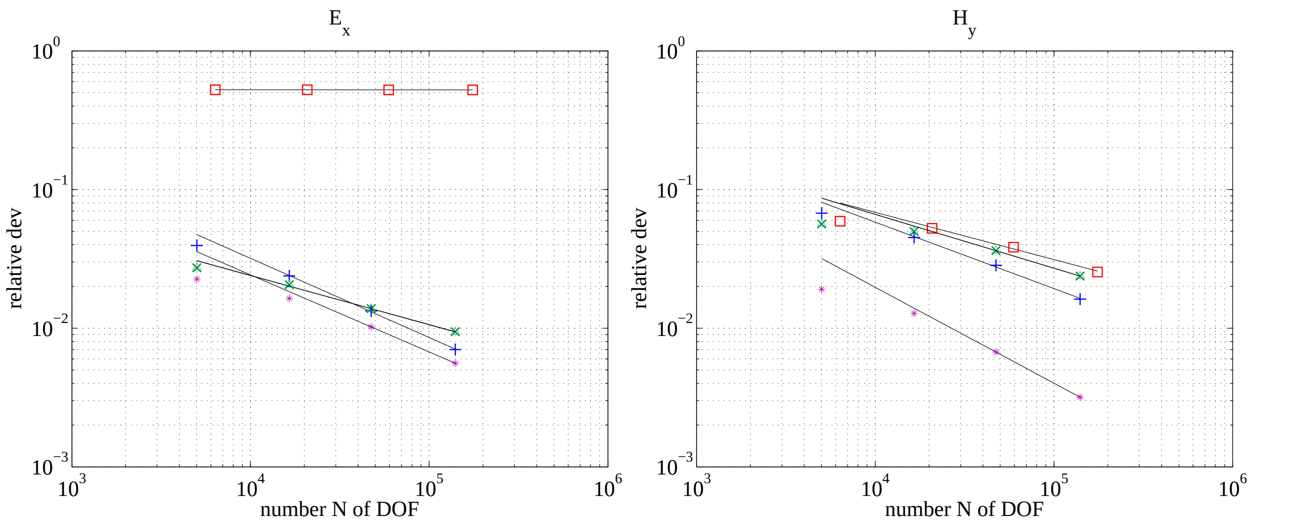

Fig. 5.60: Convergence curves for E_x (left) and H_y (right) computed for the COMMEMI 3-D-2 model from BVP (i) (+), BVP (ii) (×), BVP (iii) (□), BVP (iv) (△) and BVP (v) ($*$) using cubic ($p = 3$) finite elements. Black lines (–) indicate the linear trend of each convergence curve for sufficiently large N. The frequency is $f = 0.01\,\mathrm{Hz}$.

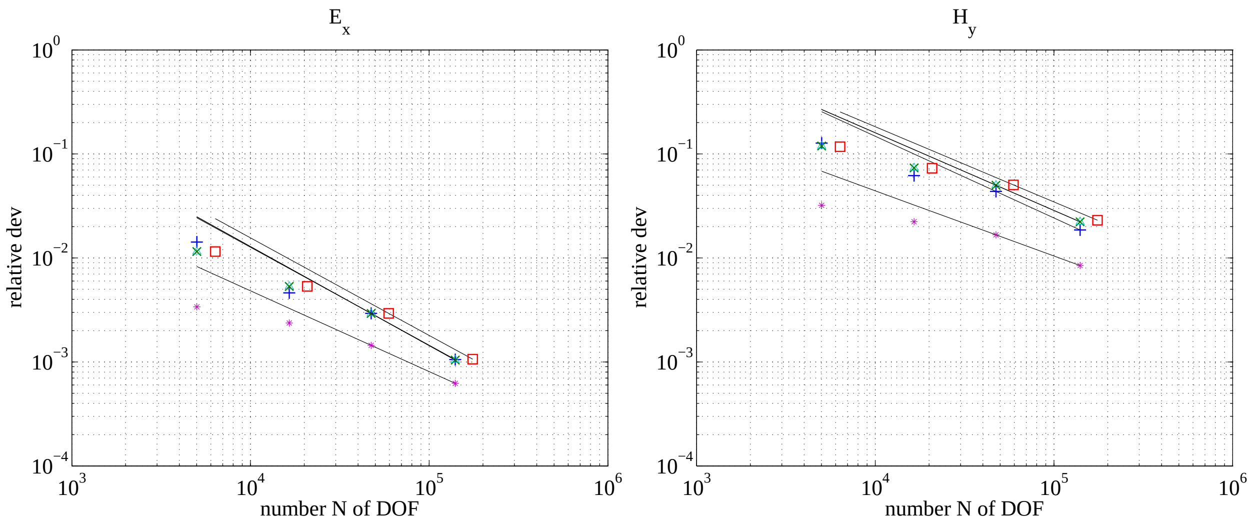

Fig. 5.61: Convergence curves for E_x (left) and H_y (right) computed for the COMMEMI 3-D-2 model from BVP (i) (+), BVP (ii) (×), BVP (iii) (□), BVP (iv) (△) and BVP (v) (∗) using cubic ($p = 3$) finite elements. Black lines (–) indicate the linear trend of each convergence curve for sufficiently large N. The frequency is $f = 1\,\mathrm{Hz}$.

		asymptotic conv. rate α_{as}		limiting conv. rate α_{lim}	
p	BVP	$(\mathbf{u})_i$	$(\nabla\times\mathbf{u})_i$	$(\mathbf{u})_i$	$(\nabla\times\mathbf{u})_i$
1	i	-0.39	-0.43	-0.49	-0.52
	ii	-0.43	-0.46	-0.55	-0.49
	iii	-0.44	-0.53	-0.50	-0.53
	iv	-0.43	-0.46	-0.55	-0.49
	v	-0.45	-0.47	-0.53	-0.54
2	i	-0.38	-0.53	-0.42	-0.53
	ii	-0.46	-0.28	-0.53	-0.34
	iii	$-1.5\cdot10^{-2}$	-0.27	$-7.9\cdot10^{-3}$	-0.34
	iv	-0.46	-0.28	-0.53	-0.34
	v	-0.48	-0.54	-0.54	-0.60
3	i	-0.48	-0.57	-0.52	-0.59
	ii	-0.35	-0.39	-0.35	-0.39
	iii	$-2.6\cdot10^{-4}$	-0.34	$-5.8\cdot10^{-5}$	-0.38
	iv	-0.36	-0.39	-0.36	-0.39
	v	-0.57	-0.69	-0.56	-0.69

Tab. 5.29: Asymptotic (α_{as}) and limiting (α_{lim}) convergence rate of the numerical solution $(\mathbf{u})_i$ and its curl $(\nabla\times\mathbf{u})_i$ computed from BVPs (i) – (v) for the COMMEMI 3-D-2 model depending on the polynomial degree p of the basis functions. Polarisation 1. The frequency is $f = 0.01\,\mathrm{Hz}$.

		asymptotic conv. rate α_{as}		limiting conv. rate α_{lim}	
p	BVP	$(\mathbf{u})_i$	$(\nabla\times\mathbf{u})_i$	$(\mathbf{u})_i$	$(\nabla\times\mathbf{u})_i$
1	i	-0.44	-0.45	-0.58	-0.59
	ii	-0.43	-0.36	-0.58	-0.45
	iii	-0.46	-0.36	-0.51	-0.36
	iv	-0.43	-0.36	-0.58	-0.45
	v	-0.41	-0.34	-0.54	-0.41
2	i	-0.56	-0.77	-0.55	-0.71
	ii	-0.75	-0.50	-0.79	-0.55
	iii	-0.75	-0.49	-0.78	-0.53
	iv	-0.75	-0.50	-0.79	-0.55
	v	-0.65	-0.47	-0.65	-0.47
3	i	-0.79	-0.94	-0.79	-0.94
	ii	-0.95	-0.75	-0.95	-0.75
	iii	-0.94	-0.75	-0.94	-0.75
	iv	-0.95	-0.75	-0.95	-0.75
	v	-0.78	-0.63	-0.78	-0.63

Tab. 5.30: Asymptotic (α_{as}) and limiting (α_{lim}) convergence rate of the numerical solution $(\mathbf{u})_i$ and its curl $(\nabla\times\mathbf{u})_i$ computed from BVPs (i) – (v) for the COMMEMI 3-D-2 model depending on the polynomial degree p of the basis functions. Polarisation 1. The frequency is $f = 1\,\text{Hz}$.

The following considerations regarding

- the second direction of polarisation (polarisation 2), i.e. the normal electromagnetic fields are $\mathbf{E}_n = E_0 \cdot \mathbf{e}_y$ and $\mathbf{H}_n = H_0 \cdot \mathbf{e}_x$ instead of $\mathbf{E}_n = E_0 \cdot \mathbf{e}_x$ and $\mathbf{H}_n = H_0 \cdot \mathbf{e}_y$ (cf. Fig. 5.62, Tab. 5.31),
- the convergence of field components that are not parallel to the normal electromagnetic fields (cf. Fig. 5.63, Tab. 5.32),
- the effect of adaptive mesh refinement on the convergence behaviour (Fig. 5.64, Tab. 5.33), and
- local convergence (Figs 5.65, 5.66, 5.67, Tab. 5.34)

are restricted to BVP (v) due to its advantages mentioned above.

Polarisation 2

Considering polarisation 2, the electromagnetic field components parallel to the normal fields are E_y and H_x. Hence, for BVP (v) we have

$$(\mathbf{u})_i = \mathbf{u} \cdot \mathbf{e}_y \quad = E_y \quad \text{and} \quad (\nabla\times \mathbf{u})_i = (\nabla\times \mathbf{u}) \cdot \mathbf{e}_x \quad = H_x. \tag{5.9}$$

Fig. 5.62 ($f = 0.1\,\mathrm{Hz}$) and Tab. 5.31 illustrate that similar convergence behaviour can be observed for both directions of polarisation although the frequency dependence of the convergence rates is less significant for polarisation 2 (cf. Fig. 5.55 and Tabs 5.27, 5.29, 5.30). This might be due to the different orientation of the normal field components relative to the lateral conductivity contrasts. In the following, convergence studies are restricted to polarisation 1, however, qualitatively they similarly refer to the appropriate field components occuring in the case of polarisation 2.

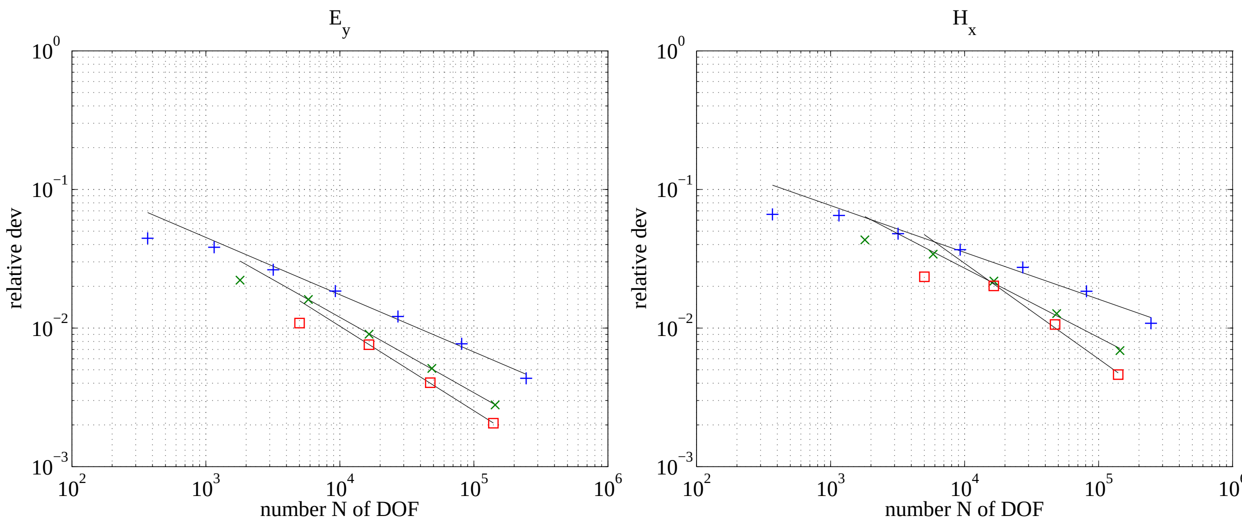

Fig. 5.62: Convergence curves for E_y (left) and H_x (right) computed from BVP (v) for the COMMEMI 3-D-2 model using linear ($p = 1$, +), quadratic ($p = 2$, ×) and cubic ($p = 3$, □) finite elements. Polarisation 2. Black lines (–) indicate the linear trend of each convergence curve for sufficiently large N. The frequency is $f = 0.1\,\mathrm{Hz}$.

		asymptotic conv. rate α_{as}		limiting conv. rate α_{lim}	
f[Hz]	p	$(\mathbf{u})_i$	$(\nabla\times\mathbf{u})_i$	$(\mathbf{u})_i$	$(\nabla\times\mathbf{u})_i$
0.01	1	-0.43	-0.50	-0.51	-0.56
	2	-0.50	-0.64	-0.50	-0.66
	3	-0.53	-0.78	-0.57	-0.77
0.1	1	-0.41	-0.34	-0.52	-0.48
	2	-0.54	-0.50	-0.56	-0.57
	3	-0.61	-0.69	-0.62	-0.77
1	1	-0.38	-0.29	-0.48	-0.38
	2	-0.52	-0.39	-0.58	-0.47
	3	-0.69	-0.46	-0.73	-0.54

Tab. 5.31: Asymptotic (α_{as}) and limiting (α_{lim}) convergence rate of a field component of the numerical solution $(\mathbf{u})_i$ and its curl $(\nabla\times\mathbf{u})_i$ computed from BVPs (i) – (v) for the COMMEMI 3-D-2 model depending on the polynomial degree p of the basis functions. Polarisation 2. The frequency is $f = 0.1\,\text{Hz}$.

Non-Parallel-to-the-Normal-Field Components

The field components which are not parallel to the normal electromagnetic fields, i.e. E_y, H_x, E_z, and H_z for polarisation 1, exhibit a slightly different convergence behaviour than the components parallel to the normal electromagnetic fields. The convergence curves are less steep. Here, the asymptotic convergence rates hardly reach -0.6 in comparison to -0.7 for the parallel-to-the-normal-field components. Additionally, the convergence rates are less dependent on the frequency (cf. Fig. 5.63 and Tab. 5.32). The frequency dependence is caused by conductivity contrasts affecting the convergence behaviour for different skin depths to varying degrees. Moreover, the orientation of the field components relative to the conductivity contrasts seems to influence the convergence behaviour as well. In Fig. 5.63, E_y and E_z are considered. Convergence rates for E_x are more seriously affected by the frequency. Same effect may be obvious comparing E_x for polaristion 1 and E_y in the case of polarisation 2, although it is less significant.

		asymptotic conv. rate α_{as}				limiting conv. rate α_{lim}			
		$(\mathbf{u})_i$		$(\nabla\times\mathbf{u})_i$		$(\mathbf{u})_i$		$(\nabla\times\mathbf{u})_i$	
f[Hz]	p	E_y	E_z	H_x	Hz	E_y	E_z	H_x	H_z
0.01	1	-0.39	-0.31	-0.41	-0.44	-0.52	-0.39	-0.47	-0.56
	2	-0.37	-0.37	-0.52	-0.53	-0.44	-0.58	-0.58	-0.61
	3	-0.47	-0.41	-0.62	-0.67	-0.60	-0.41	-0.63	-0.73
0.1	1	-0.39	-0.33	-0.33	-0.37	-0.49	-0.46	-0.42	-0.51
	2	-0.43	-0.42	-0.37	-0.42	-0.53	-0.56	-0.43	-0.47
	3	-0.47	-0.45	-0.56	-0.59	-0.59	-0.48	-0.63	-0.74
1	1	-0.41	-0.35	-0.34	-0.29	-0.45	-0.49	-0.41	-0.39
	2	-0.55	-0.51	-0.34	-0.31	-0.69	-0.55	-0.47	-0.42
	3	-0.50	-0.55	-0.45	-0.40	-0.57	-0.64	-0.63	-0.49

Tab. 5.32: Asymptotic (α_{as}) and limiting (α_{lim}) convergence rate of a field component of the numerical solution $(\mathbf{u})_i$ and its curl $(\nabla\times\mathbf{u})_i$ computed from BVP (v) for the COMMEMI 3-D-2 model depending on the frequency f and polynomial degree p of the basis functions.

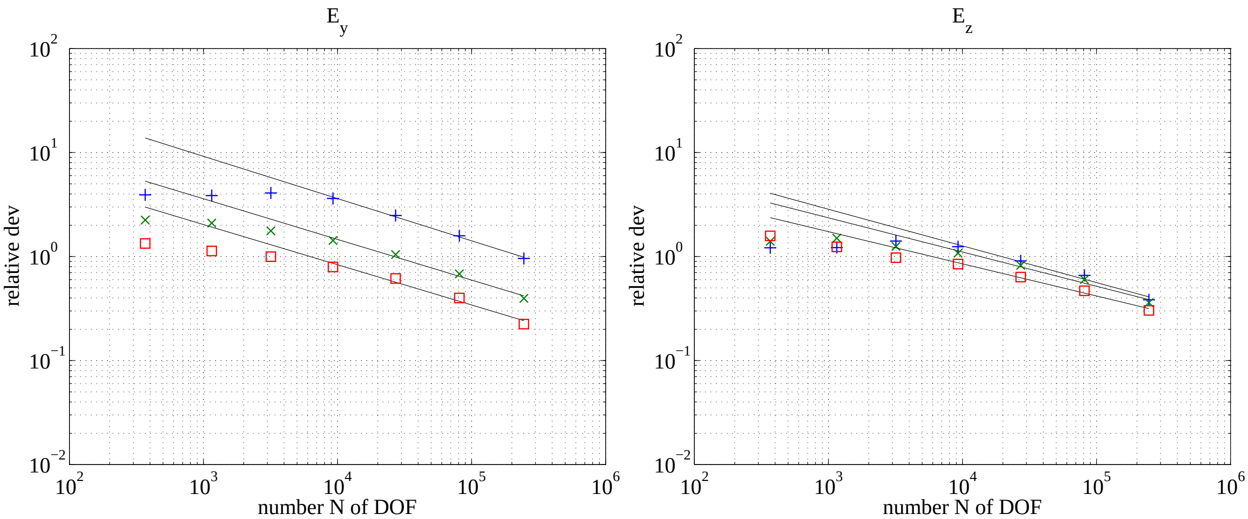

Fig. 5.63: Convergence curves for E_y (left) and E_z (right) computed from BVP (v) for the COMMEMI 3-D-2 model using linear ($p = 1$) finite elements for $f = 1$ Hz (+), $f = 0.1$ Hz (×) and $f = 0.01$ Hz (□). Black lines (–) indicate the linear trend of each convergence curve for sufficiently large N.

Adaptive Mesh Refinement

Fig. 5.64 and Tab. 5.33 illustrate similar convergence behaviour for adaptive mesh refinement as for uniformly refined meshes (cf. Fig. 5.55 for $f = 0.1\,\mathrm{Hz}$ and Tab. 5.27). However, here, convergence rates are less dependent on the frequency. In the adaptive mesh refinement process, the skin depth of the electromagnetic fields is accounted for in the way that the mesh is refined where strong variations in the solution occur. Hence, the accuracy and, therefore, the convergence of the FE solution is less seriously affected by the frequency in this case. Note that, third-order ($p = 3$) finite elements are not available under COMSOL Multiphysics® for adaptive mesh refinement. Therefore, they are not discussed here.
For the simulated electric field, largest relative deviations occur for the lowest frequency of $f = 0.01\,\mathrm{Hz}$ (□). This feature also becomes clear by comparing Figs 5.55, 5.60, and 5.61 for cubic ($p = 3$) basis functions in the case of uniform mesh refinement. It might be due to the 3-D conductivity distribution, since for the homogeneous halfspace the lowest frequency yields the smallest errors. In this case, for a given mesh most DOF are located within the length of one skin depth.

Local Convergence

Fig. 5.65 displays convergence curves for the electric field component E_x in all DOF on the earth's surface and the point $(0, 0, 0)$ using quadratic ($p = 2$) basis functions. Contrary to the electric field, the magnetic field component H_y exhibits at least a slight frequency-dependence (cf. Figs 5.66 and 5.67). The estimation of convergence rates for the point $(0, 0, 0)$ is impossible for H_y due to the non-monotonical behaviour of the relative deviation. It is even hard to speak of convergence at all. Asymptotic convergence rates for E_x in the point $(0, 0, 0)$ are $\alpha_{\text{as}}(f = 1\,\mathrm{Hz}) = -0.47$, $\alpha_{\text{as}}(f = 0.1\,\mathrm{Hz}) = -0.74$, $\alpha_{\text{as}}(f = 0.01\,\mathrm{Hz}) = -0.52$. They are in the range of the global convergence rates for adaptive mesh refinement (cf. Fig. 5.33) although difficult to estimate because of the small number of data points. The convergence rates for the electromagnetic field components on the earth's surface are listed in Tab. 5.34.

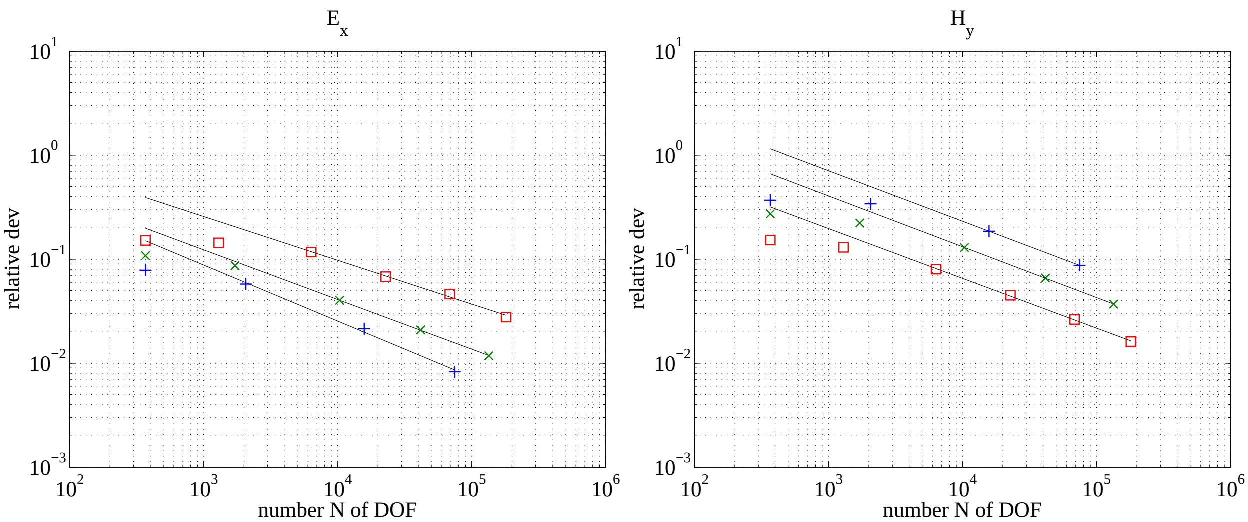

Fig. 5.64: Convergence curves for E_x (left) and H_y (right) computed from BVP (v) for the COMMEMI 3-D-2 model using first-order ($p = 1$) finite elements for $f = 1\,\mathrm{Hz}$ (+), $f = 0.1\,\mathrm{Hz}$ (×) and $f = 0.01\,\mathrm{Hz}$ (□). Adaptive mesh refinement. Black lines (–) indicate the linear trend of each convergence curve for sufficiently large N.

		asymptotic conv. rate α_{as}		limiting conv. rate α_{lim}	
f[Hz]	p	E_x	H_y	E_x	H_y
0.01	1	-0.42	-0.48	-0.53	-0.50
	2	-0.64	-0.74	-0.64	-0.74
0.1	1	-0.48	-0.49	-0.49	-0.49
	2	-0.50	-0.72	-0.50	-0.72
1	1	-0.54	-0.49	-0.61	-0.49
	2	-0.55	-0.38	-0.55	-0.38

Tab. 5.33: Asymptotic (α_{as}) and limiting (α_{lim}) convergence rate for E_x and H_y computed from BVP (v) for the COMMEMI 3-D-2 model depending on the frequency f and polynomial degree p of the basis functions. Adaptive mesh refinement.

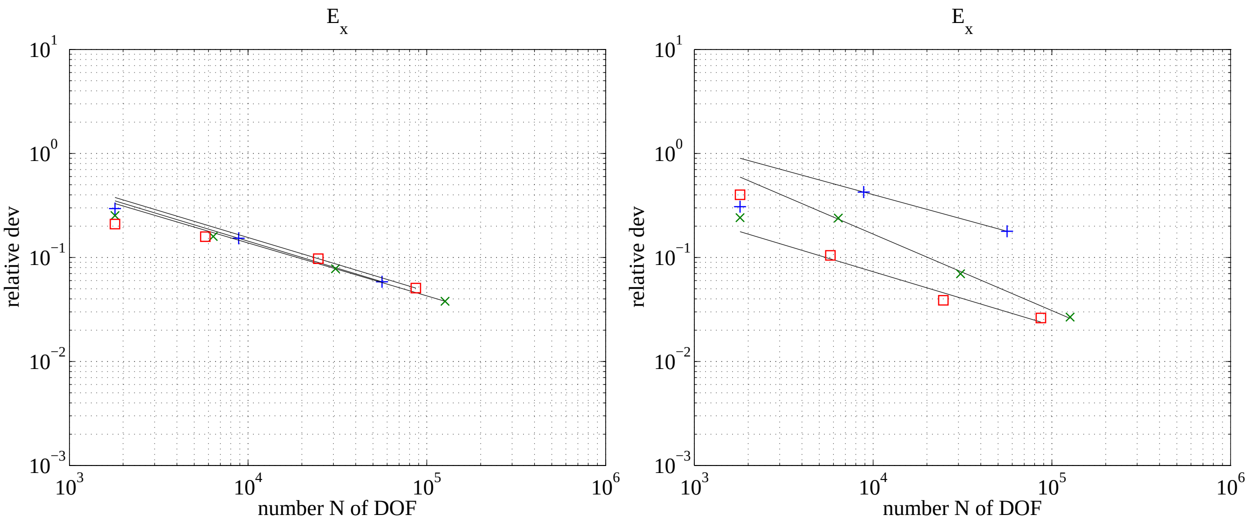

Fig. 5.65: Convergence curves for E_x computed from BVP (v) for the COMMEMI 3-D-2 model for all DOF on the earth's surface (left) and the point $(0, 0, 0)$ (right) using second-order ($p = 2$) finite elements for $f = 1\,\text{Hz}$ (+), $f = 0.1\,\text{Hz}$ (×) and $f = 0.01\,\text{Hz}$ (□). Adaptive mesh refinement. Black lines (–) indicate the linear trend of each convergence curve for sufficiently large N.

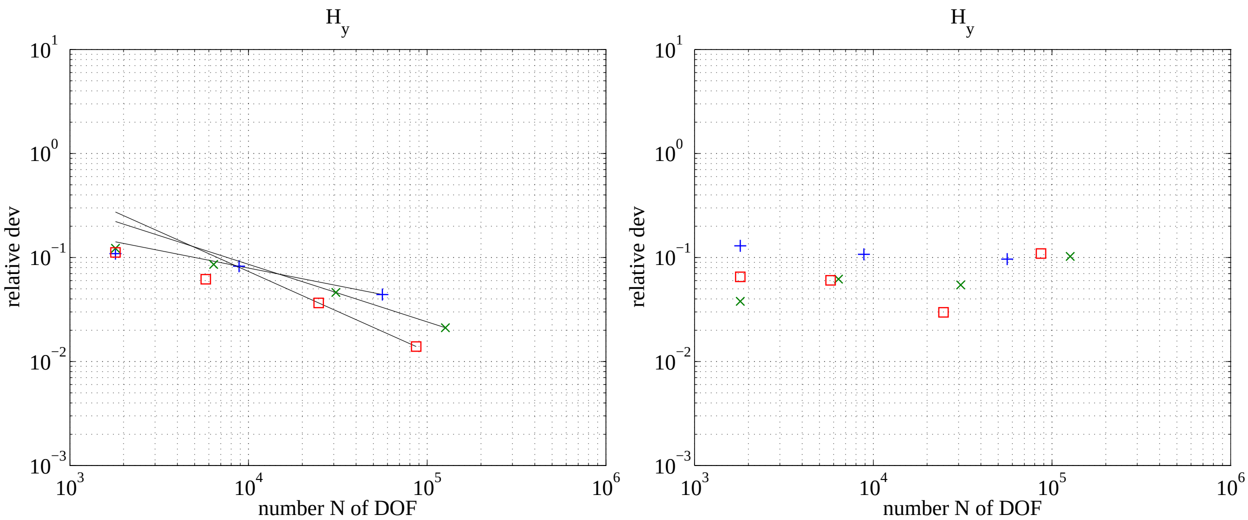

Fig. 5.66: Convergence curves for H_y computed from BVP (v) for the COMMEMI 3-D-2 model for all DOF on the earth's surface (left) and the point $(0,0,0)$ (right) using second-order ($p = 2$) finite elements for $f = 1\,\mathrm{Hz}$ (+), $f = 0.1\,\mathrm{Hz}$ (×) and $f = 0.01\,\mathrm{Hz}$ (□). Adaptive mesh refinement. Black lines (–) indicate the linear trend of each convergence curve for sufficiently large N.

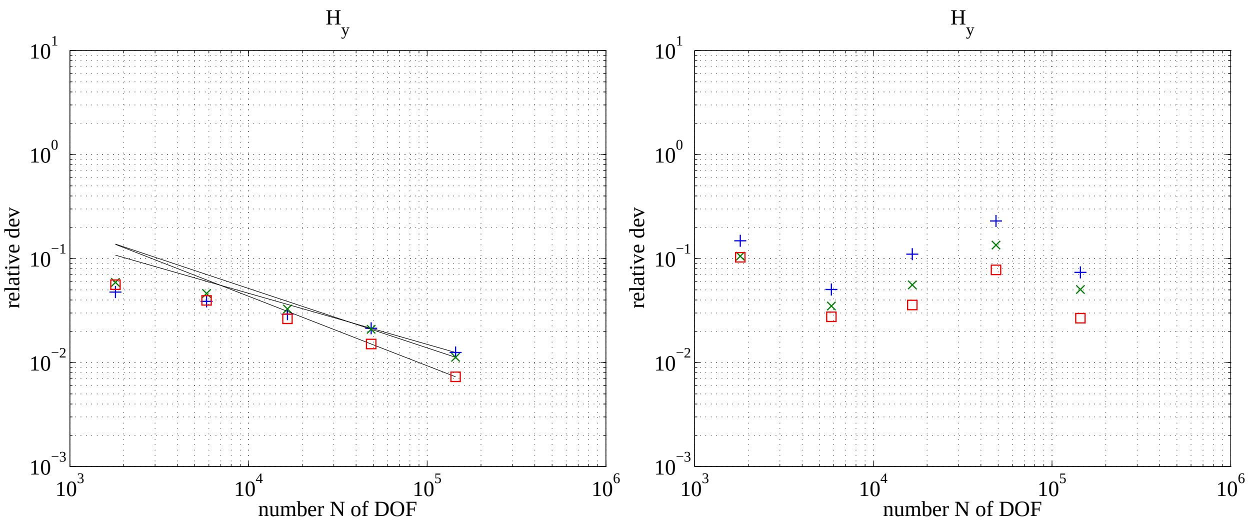

Fig. 5.67: Convergence curves for H_y computed from BVP (v) for the COMMEMI 3-D-2 model for all DOF on the earth's surface (left) and the point $(0,0,0)$ (right) using second-order ($p = 2$) finite elements for $f = 1\,\mathrm{Hz}$ (+), $f = 0.1\,\mathrm{Hz}$ (×) and $f = 0.01\,\mathrm{Hz}$ (□). Uniform mesh refinement. Black lines (–) indicate the linear trend of each convergence curve for sufficiently large N.

			asymptotic conv. rate α_{as}		limiting conv. rate α_{lim}	
mesh refinement	f [Hz]	p	E_x	H_y	E_x	H_y
adaptive	0.01	1	−0.41	−0.54	−0.47	−0.52
		2	−0.52	−0.77	−0.52	−0.77
	0.1	1	−0.45	−0.59	−0.49	−0.66
		2	−0.51	−0.55	−0.51	−0.55
	1	1	−0.69	−0.48	−0.69	−0.48
		2	−0.52	−0.34	−0.52	−0.34
uniform	0.01	1	−0.41	−0.43	−0.59	−0.57
		2	−0.52	−0.67	−0.78	−0.67
		3	−0.46	−0.72	−0.47	−0.81
	0.1	1	−0.45	−0.35	−0.61	−0.61
		2	−0.58	−0.57	−0.78	−0.57
		3	−0.49	−0.64	−0.49	−0.77
	1	1	−0.50	−0.17	−0.62	−0.25
		2	−0.52	−0.49	−0.71	−0.49
		3	−0.56	−0.45	−0.74	−0.55

Tab. 5.34: Asymptotic (α_{as}) and limiting (α_{lim}) convergence rate for E_x and H_y on the eath's surface computed from the solution of BVP (v) for the COMMEMI 3-D-2 model depending on the frequency f and polynomial degree p of the basis functions.

5.6 Conclusions

In general, from the 2-D and 3-D convergence studies, we can conclude that the relative rms error and the relative rms deviation introduced by eqs (5.1) and (5.4) are well suited to perform convergence studies. An area integration as necessary for the computation of the L^2-norm is not required following the strategy described in the beginning of this chapter.

For the 2-D convergence studies, reduced absolute values of the limiting convergence rates indicate a limit of the discretisation error. However, due to the limitation of the available computer memory, it could not be quantified.

The convergence towards the finest-grid solution perfectly reflects the convergence behaviour with respect to the analytical solution. Hence, convergence studies enable us to estimate the accuracy of any numerical solution and to verify its significance even in the case the exact solution is unknown.

For a sufficiently large number of data points, local convergence is similar to global convergence behaviour. Therefore, convergence studies may also provide estimates of the local accuracy of numerical simulation results. Moreover, they can be used to verify the local significance of any numerical solution. This is of special interest in the case of complicated-structured models incorporating surface topography which may induce unexpected geo-electromagnetic effects or generate numerical artefacts. Geo-electromagnetic phenomena are expected to be present throughout all mesh refinement steps, whereas numerical artefacts may occur more spontaneously for certain grids.

From the 3-D convergence studies, it becomes clear that even simple 3-D conductivity structures as occuring in the COMMEMI 3-D-2 model seriously affect the convergence behaviour. Due to electrical charge accumulation at lateral conductivity contrasts influencing the regularity of the true solution, the maximum absolute convergence rate is reduced. In this case, higher-order finite elements do not necessarily result in faster convergence and higher accuracy. However, geometrical adaptive mesh refinement has proved to be advantageous especially when 3-D conductivity structures are present. It partially compensates the frequency effect on the convergence rate that arises from the decrease of the accuracy of the numerical solution due to an enlarged skin depth.

Finally, among BVP (i) – (v), BVP (v) proved to be advantageous in terms of convergence rates, stability, and accuracy.

6 Simulation of Magnetotelluric Fields at Stromboli

Stromboli volcano arises with very steep slopes from the Mediterranean Sea off the west coast of Italy. In her diploma thesis, Kütter (2009) showed that, for magnetotelluric (MT) data strong three-dimensional (3-D) effects may be expected from topographic and bathymetric undulations as well as the adjacent islands of the Aeolian archipelago. Data from digital elevation models were successfully incorporated into the finite element (FE) simulation of MT fields using COMSOL Multiphysics®, however, it has not been possible to assess the accuracy and significance of the numerical results so far. To verify the results, the FE solution for the simplified model of a frustum surrounded by sea water was analysed regarding its symmetry and compared to the solution of another FE code (Schwarzbach, 2009) and the finite-difference solution computed by Mackie (cf. Mackie et al., 1994). Now, convergence studies enable us to prove the significance of the simulation results and to even estimate the accuracy of the numerical solution.
Based on the experience from the 3-D convergence studies in chapter 5, most efficient boundary value problem (BVP) BVP (v) is chosen to simulate the anomalous magnetic vector potential at Stromboli. Due to the complicated-structured model of Stromboli area incorporating surface topography and bathymetry, reliable convergence studies are carried out only for uniform mesh refinement using linear basis functions.

6.1 Stromboli Model

The model of the area of interest is chosen to be similar to the so-called bathymetry-topography model in Kütter (2009). It extends from 38.4° to 39.2° N and 14.7° to 15.7° E, i.e. $86.51\,\mathrm{km}$ in west-east (x) and $88.76\,\mathrm{km}$ in north-south (y) direction. Two sets of digital elevation data were adapted to yield the model depicted in Fig. 6.1. The ETOPO1 data set is a 1 arc-minute model and provides elevation values for both land and sea. It is available online at the National Geophysical Data Center (http://www.ngdc.noaa.gov) and gives a good approximation for the regional bathymetry. Since, however, its spatial data density is not sufficient to describe Stromboli's topography, a second data set was used. These data are available from the Shuttle Radar Topography Mission (SRTM), a project to obtain high-resolution topographic data (http://srtm.csi.cgiar.org/). To keep the model used for the simulation at moderate size on the one hand and to still reflect the main topographic features on the other hand, a subset of the digital elevation data with a resolution of $1.44\,\mathrm{km}$ in x- and $1.85\,\mathrm{km}$ in y-direction was extracted (cf. Fig. 6.2, right-hand side). The final 3-D model of Stromboli area depicted in the left-hand panel of Fig. 6.2 was completed by surrounding points at an average elevation of $1.54\,\mathrm{km}$.
The conductivity distribution in the model is as follows

- air layer: $\sigma_0 = 10^{-9}\,\mathrm{Sm}^{-1}$,
- sea layer: $\sigma_1 = 5\,\mathrm{Sm}^{-1}$,

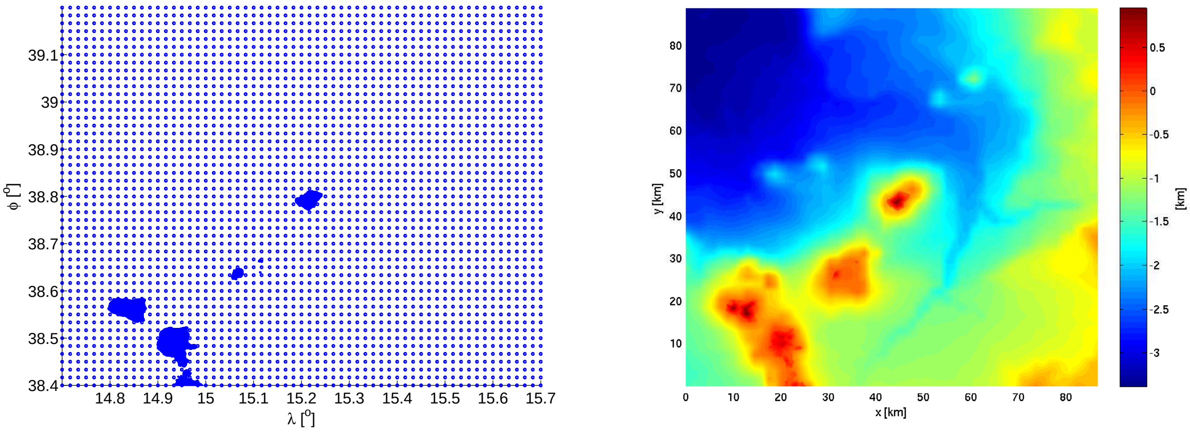

Fig. 6.1: Density of digital elevation data (left) and resulting digital elevation model (right). Pictures from Kütter (2009).

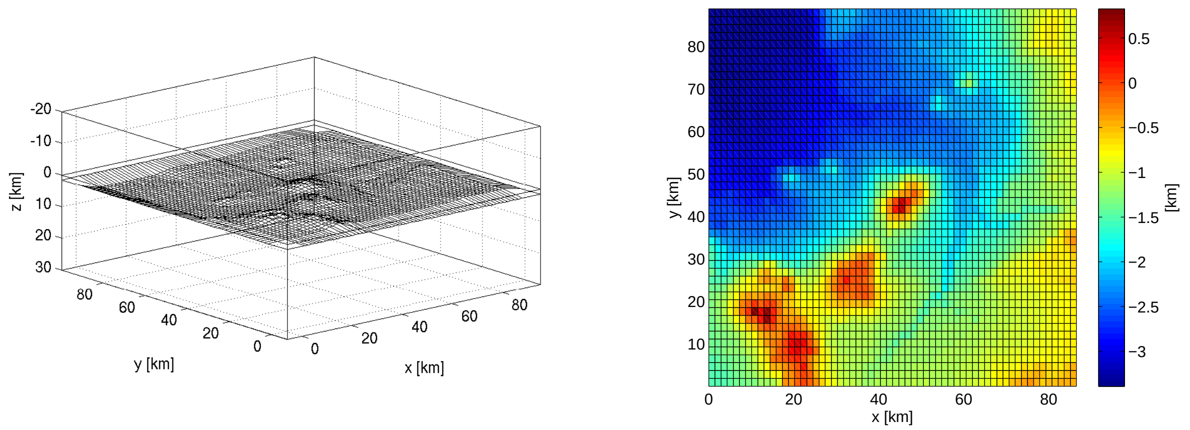

Fig. 6.2: Stromboli 3-D model (left) including digital elevation data (right). Pictures from Kütter (2009).

- halfspace, Stromboli volcano, islands: $\sigma_2 = 0.01\,\mathrm{Sm}^{-1}$.

6.2 Simulated Data and Convergence Studies

Exemplarily, data on profiles 'yE' and 'yW' are examined (cf. Fig. 6.3, left-hand side). They run on the seafloor south and north of Stromboli volcano which is located in the center of the area and follow the island's topography. The profiles consisting of 1177 data points are assumed to include a sufficiently large number of locations which are considered for the convergence studies. The air-sea interface is aligned with $z = 0$. The results from Kütter (2009) exhibit strong anomalies in the apparent resistivity ρ_{xy} and the phase ϕ_{xy} (cf. Fig. 6.3, right-hand side). Convergence studies enable the verification or falsification of their significance.
The results for ρ_{xy} and ϕ_{xy} using a more recent version of COMSOL Multiphysics® (3.5a instead of 3.3a) are displayed in Fig. 6.4 in terms of the apparent resistivity ρ_{xy} and the phase ϕ_{xy} on the left-hand side and ρ_{yx} and ϕ_{yx} on the right-hand side, respectively. The simulations are performed using $1.3 \cdot 10^6$ DOF on a 2.4 GHz shared memory computer utilizing 8 of 32 nodes. The results mainly differ in that,

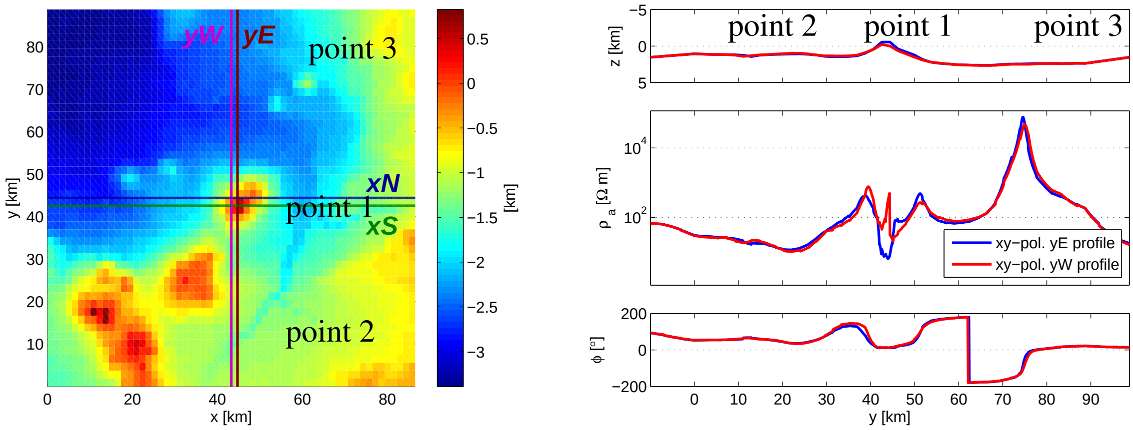

Fig. 6.3: Locations of data points and profiles in the Stromboli model (left). ρ_{xy} and ϕ_{xy} computed using COMSOL Multiphysics® 3.3a on profiles 'yE' and 'yW' and related topography on top (right). Pictures from Kütter (2009).

the anomalies in the southern part of the profiles ($-20\,\mathrm{km} \leq y \leq 40\,\mathrm{km}$) are more pronounced, whereas the anomalies in the northern part ($50\,\mathrm{km} \leq y \leq 100\,\mathrm{km}$) including the local and the global maximum of the apparent resistivity and the phase jump have completely disappeared. The recent results in Fig. 6.4 seem more plausible since the strong variations south of the volcanic island can be attributed to bathymetric undulations and lateral effects from the near-by islands of the Aeolian archipelago, whereas in the northern part of the profiles the seafloor resides almost constantly at a larger depth. There, the data nicely reproduce the resistivity $\rho_2 = {\sigma_2}^{-1} = 100\,\Omega\mathrm{m}$ of the underlying halfspace.

Analysing the electromagnetic field components parallel to the normal fields, i.e. E_x and H_y for polarisation 1, exemplarily for profile 'yE' in Fig. 6.5 the effects of bathymetry and topography become clear. The behaviour of the magnetic field (right-hand diagram) obviously reflects bathymetric undulations since the field value is attenuated according to the depth of the sea floor. For $-20\,\mathrm{km} \leq y \leq 40\,\mathrm{km}$, the thickness of the sea layer significantly varies, whereas for $50\,\mathrm{km} \leq y \leq 100\,\mathrm{km}$ it is more or less constant at a larger depth. The real part of the electric field component (left-hand diagram) shows similar behaviour, its imaginary part, however, exhibits significant variations only in the vicinity of the volcano. The field components orthogonal to the normal fields, i.e. E_y and H_x for polarisation 1, are orders of magnitude smaller than E_x and H_y. Hence, they do not affect apparent resistivity and phase significantly. For polarisation 2, the appropriate field components behave similarly since, along the profile, the conductivity contrasts are distributed symmetrically with respect to the direction of the normal field components.

After having discussed the plausibility of the numerical results computed for the 3-D model of Stromboli area, in the following, the results will be further verified by local convergence studies. Due to the undulating topographic and bathymetric relief generating a large complicated-structured initial mesh with an already considerable number of DOF, only uniform mesh refinement and linear ($p = 1$) basis functions are applied. The use of higher-order finite elements implies only one step of mesh refinement that is not sufficient to perform reliable convergence studies.

Fig. 6.6 displays convergence curves for E_x (+) and H_y (×) on the profiles 'yE' (left-hand diagram) and 'yW' (right-hand diagram). E_x and H_y converge on both profiles, however, H_y exhibits very slow convergence on profile 'yW'.

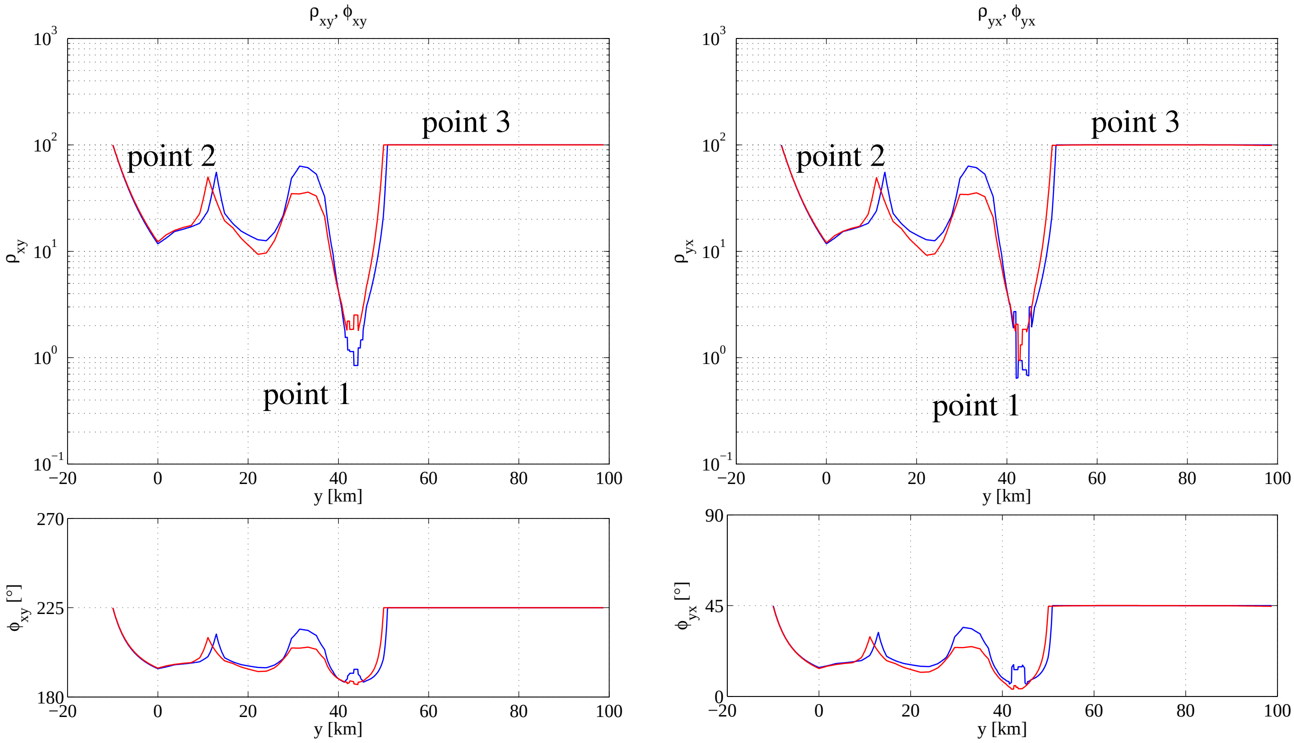

Fig. 6.4: Apparent resistivities ρ_{xy} (left) and ρ_{yx} (right) at the top and phases ϕ_{xy} (left) and ϕ_{yx} (right) at the bottom computed using COMSOL Multiphysics® 3.5a on profiles 'yE' (–) and 'yW' (–).

To evaluate the numerical results for the apparent resistivity and the phase, it seems more reasonable to consider convergence studies for the impedance. Fig. 6.7 shows the appropriate convergence curves for the off-diagonal elements Z_{xy} (+) and Z_{yx} (×) of the impedance tensor on profiles 'yE' (left-hand side) and 'yW' (right-hand side). Z_{xy} and Z_{yx} converge, although convergence of Z_{yx} on profile 'yE' is slow. Tab. 6.1 summarizes the convergence rates on both profiles. The simulation results there seem to be reasonable and accurate to approximately 10^{-2} times the finest-grid solution on average.

The simulation results for the points 1, 2, and 3 on profile 'yE' indicated in Figs 6.3 and 6.4 seem to be even more reliable since all convergence rates for Z_{xy} and Z_{yx} are negative (cf. Figs 6.8 – 6.10 and Tab. 6.2). The locations of points 1 and 2 are chosen to represent the local maxima of the apparent resistivity and phase on the sea floor south of Stromboli and the global minimum of the apparent resistivity on the volcano itself, respectively. Point 3 is situated on the sea floor north of Stromboli. The convergence curves for points 2 and 3 both located on the sea floor suggest local accuracy of 10^{-5} times the finest-grid solution there (cf. Figs 6.9, 6.10). For point 1 on top of Stromboli volcano (cf. Fig. 6.8), the magnetic field component H_y does not converge, however, Z_{xy} and Z_{yx} exhibit convergence to the local accuracy of 10^{-2} times the finest-grid solution there.

	'yE'	'yW'
Z_{xy}	-0.36	-0.47
Z_{yx}	-0.09	-0.41
E_x	-0.36	-0.03
H_y	-1.75	-0.81

Tab. 6.1: Convergence rates for profiles 'yE' and 'yW'.

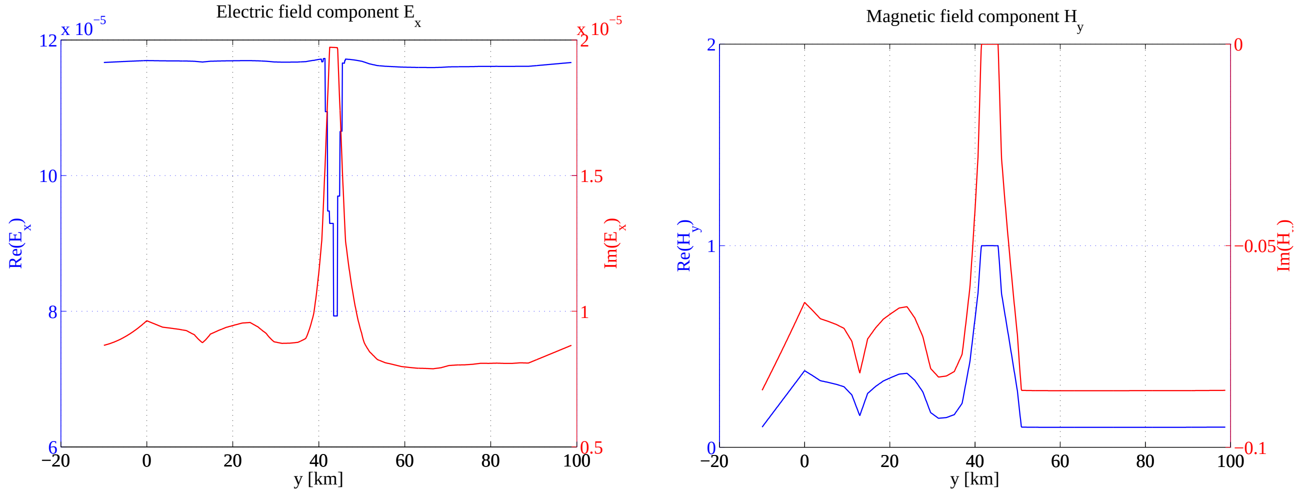

Fig. 6.5: Real (Re, –) and imaginary (Im, –) part of the electric E_x (left) and magnetic H_y (right) field component for polarisation 1 on profile 'yE'.

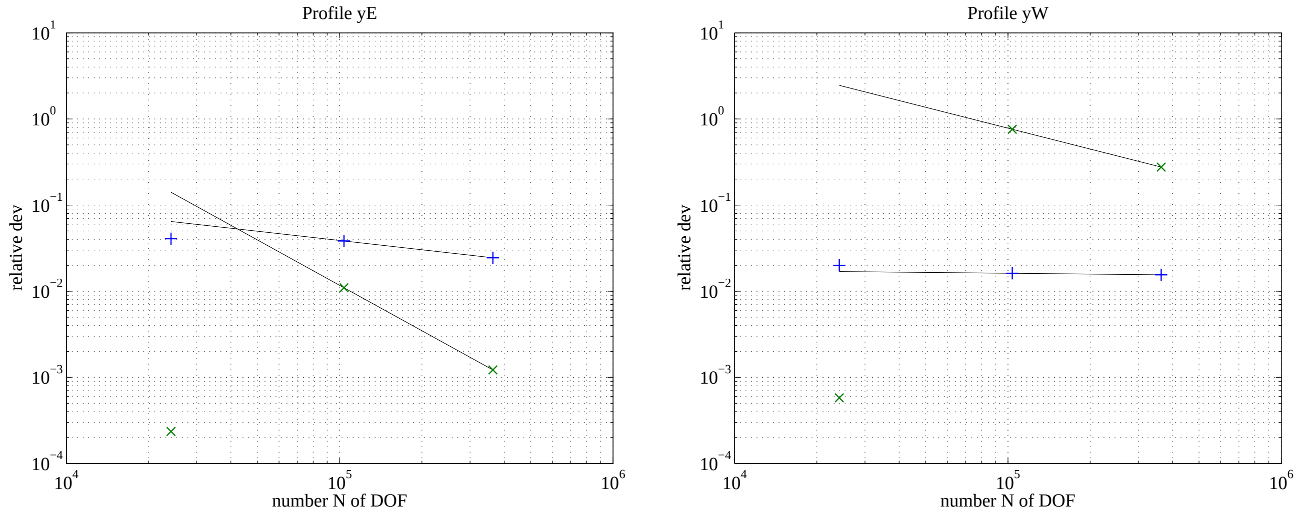

Fig. 6.6: Convergence of the field components E_x (+) and H_y (×) on profiles 'yE' (left) and 'yW' (right).

Fig. 6.11 shows a cross section of the triangulation of the model of Stromboli volcano. Tetrahedrons on bottom of the figure are relatively large whereas small and acute-angled elements occur in the upper part. Meshes triangulating models with steep topography are not expected to be of high quality. Especially in this case convergence studies are important to verify the simulation results. However, a tensor product grid as used for finite difference simulations is not able to incorporate such huge and small cells at the same time.

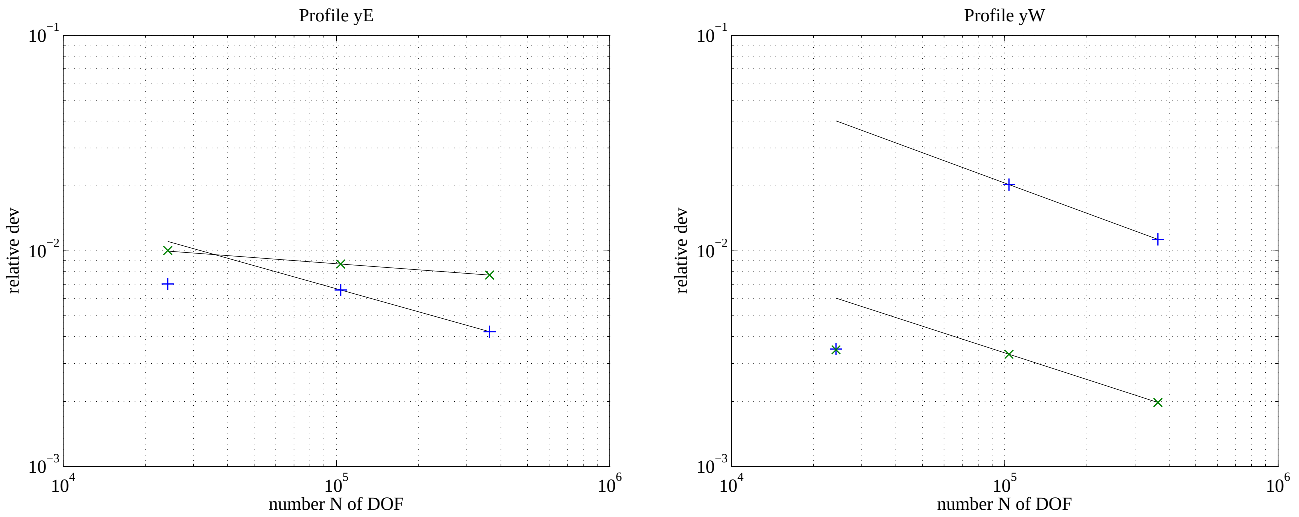

Fig. 6.7: Convergence of the impedances Z_{xy} (+) and Z_{yx} (×) on profiles 'yE' (left) and 'yW' (right).

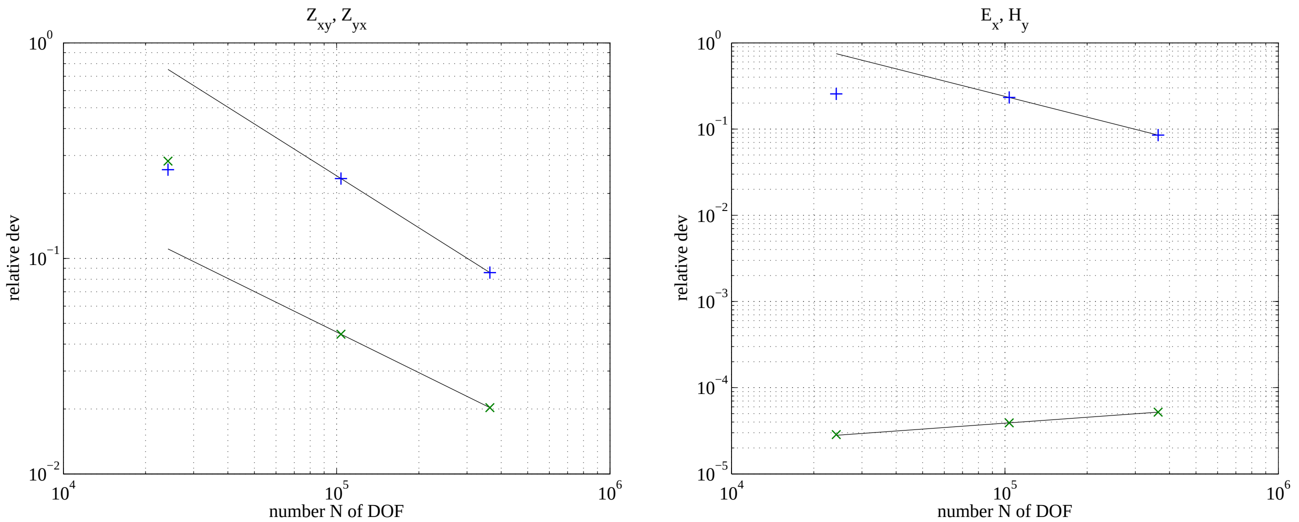

Fig. 6.8: Convergence of the impedances Z_{xy} (+) and Z_{yx} (×) (left) and the electric and the magnetic field components E_x (+) and H_y (×) (right) in point 1 at $x = 44.7\,\mathrm{km}$, $y = 42.5\,\mathrm{km}$, $z = -0.55\,\mathrm{km}$.

	point 1	point 2	point 3
Z_{xy}	-0.80	-0.66	-0.48
Z_{yx}	-0.63	-0.24	-0.85
E_x	-0.80	-2.37	-0.84
H_y	0.23	-0.49	-0.45

Tab. 6.2: Convergence rates for points 1 – 3.

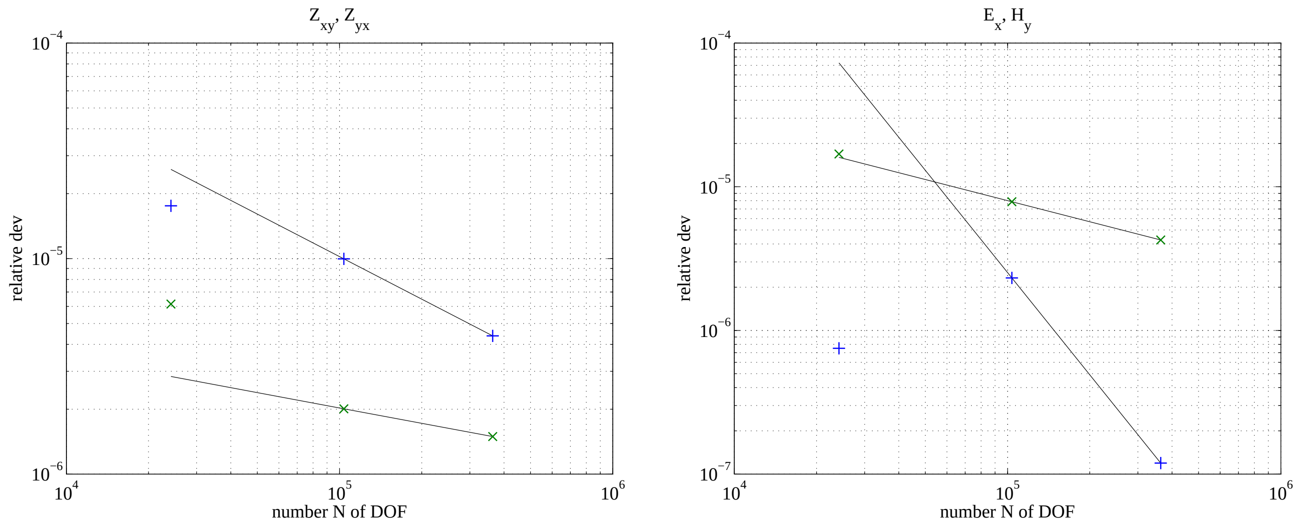

Fig. 6.9: Convergence of the impedances Z_{xy} (+) and Z_{yx} (×) (left) and the electric and the magnetic field components E_x (+) and H_y (×) (right) in point 2 at $x = 44.7\,\mathrm{km}$, $y = 13.0\,\mathrm{km}$, $z = 1.44\,\mathrm{km}$.

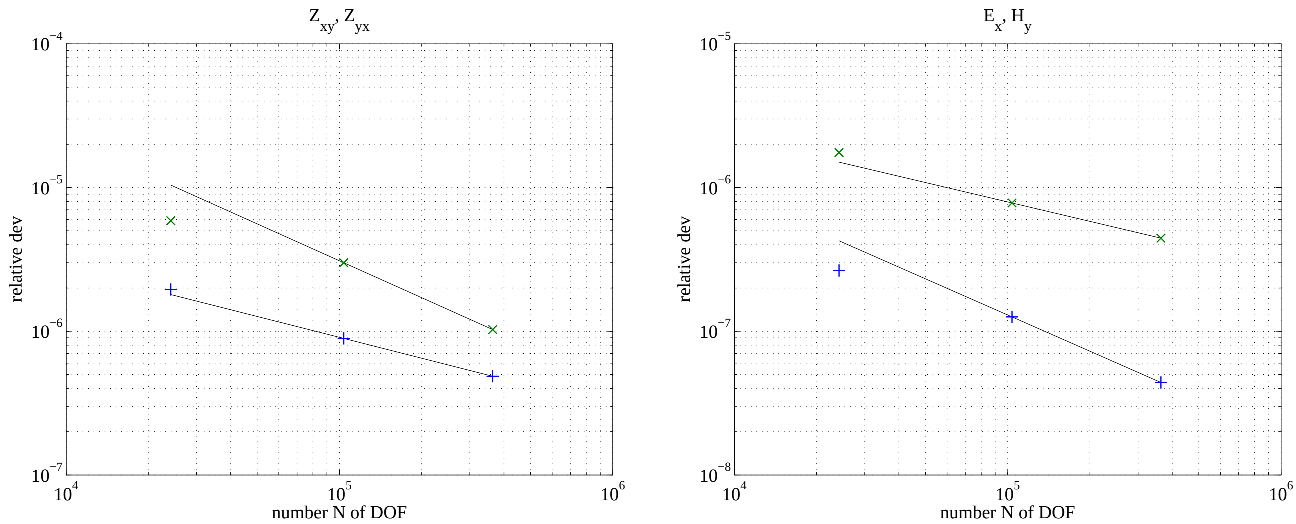

Fig. 6.10: Convergence of the impedances Z_{xy} (+) and Z_{yx} (×) (left) and the electric and the magnetic field components E_x (+) and H_y (×) (right) in point 3 at $x = 44.7\,\mathrm{km}$, $y = 80.4\,\mathrm{km}$, $z = 2.38\,\mathrm{km}$.

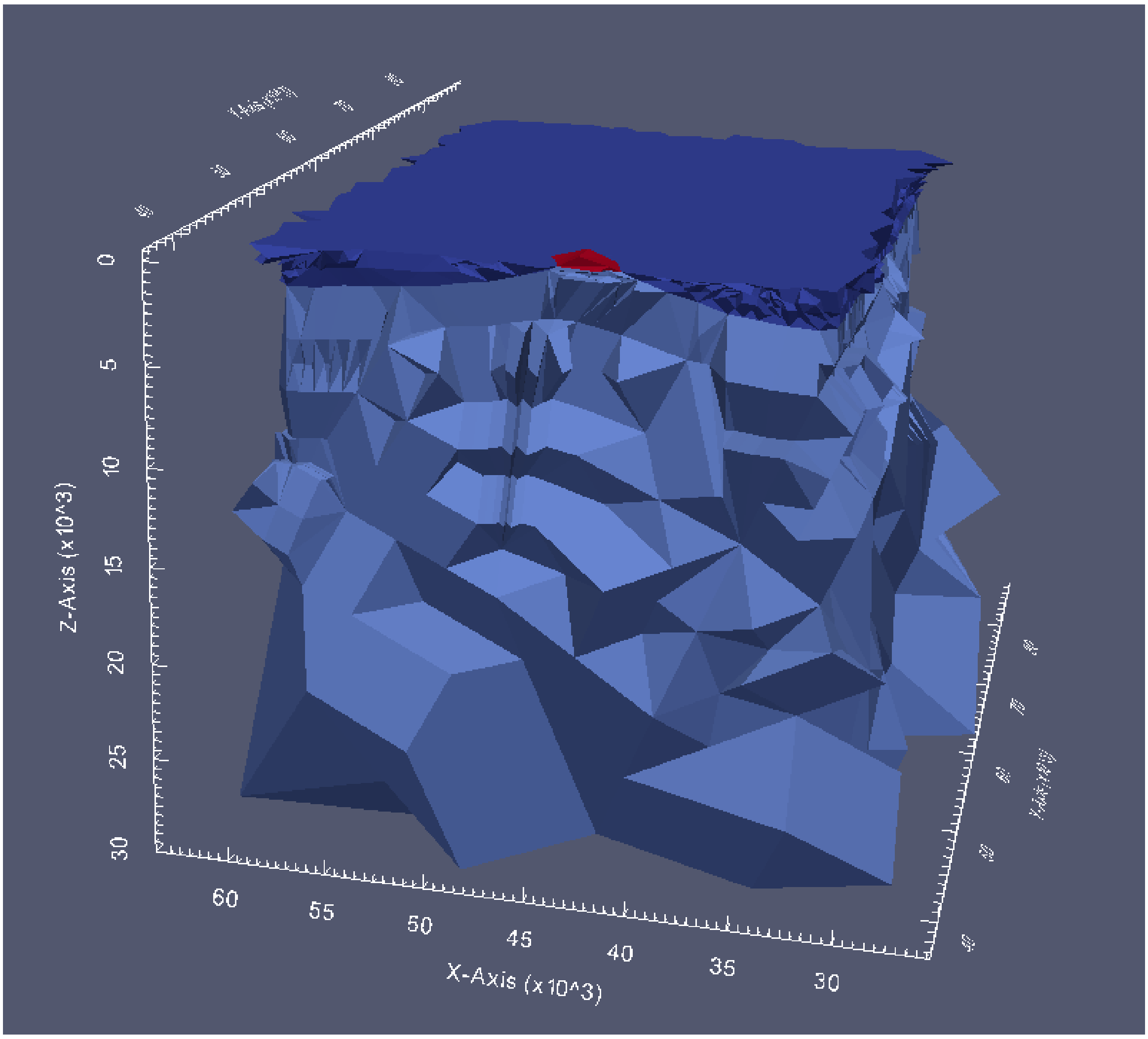

Fig. 6.11: Cross section of the finite element triangulation of Stromboli model: Stromboli island in red, sea-water layer in dark blue, underlying halfspace in light blue.

7 Summary

In the presented work, the finite element method was applied to numerically solve various boundary value problems that describe the propagation of magnetotelluric fields. The two- and three-dimensional boundary value problems in terms of the electric or the magnetic field, the magnetic vector potential and the electric scalar potential, the magnetic vector potential only, or the anomalous magnetic vector potential were derived from Maxwell's equations. Based on the application of convergence theory to the finite element solution, convergence studies were performed for the two-dimensional models of a homogeneous and a layered halfspace as well as the three-dimensional COMMEMI 3-D-2 model. Moreover, for a close-to-reality model of Stromboli area including digital terrain data, convergence studies were utilized to obtain local error estimates for the numerical results. The convergence studies for the two-dimensional models helped to understand the convergence behaviour for the three-dimensional models that is seriously affected by the three-dimensional conductivity distribution.

The boundary value problem formulated for the anomalous magnetic vector potential proved to be advantageous in terms of convergence rates, stability, and accuracy.

The convergence studies showed that the estimation of the accuracy of any numerical solution is possible even without knowing the exact solution. This is especially important for complex-structured models incorporating surface topography and sea floor bathymetry since on the one hand the discretisation error cannot be computed from the comparison with an analytical or semi-analytical solution and on the other hand the significance of the simulation results needs to be evaluated. The approximation of surface and sea floor undulations may induce unexpected geo-electromagnetic effects that consolidate throughout the mesh refinement steps or generate numerical artefacts that are expected to occur more spontaneously for certain grids.

For the example of Stromboli volcano, convergence studies revealed local pointwise relative accuracy of 10^{-5} and 10^{-2} for data points located on the sea floor and on top of the volcano, respectively.

References

Ashcraft, C., & Liu, J. W. H. (1998). Robust ordering of sparse matrices using multisection. *SIAM Journal on Matrix Analysis and Applications*, *19*(3), 816–832.

Ashcraft, C., Pierce, D., Wah, D., & Wu, J. (1999, February). The reference manual for spooles, release 2.2 [Computer software manual].

Babuška, I., & Aziz, A. K. (1972). *Survey lectures on the mathematical foundations of the finite element method with applications to partial differential equations* (A. K. Aziz, Ed.). Academic Press, New York.

Beck, R., Hiptmair, R., Hoppe, R., & Wohlmuth, B. (2000). Residual based a posteriori error estimators for eddy current computation. *Mathematical Modelling and Numerical Analysis*, *34*(1), 159-182.

Botha, M. M., & Davidson, D. B. (2005, November). An Explicit *A Posteriori* Error Indicator for Electromagnetic, Finite Element-Boundary Integral Analysis. *IEEE Transactions on Antennas and Propagation*, *53*(11), 3717-3725.

Cagniard, L. (1953). Basic theory of the magneto-telluric method of geophysical prospecting. *Geophysics*, *18*, 605-635.

Ciarlet, P. G. (1978). *The finite element method for elliptic problems*. North-Holland.

COMSOL. (2006, August). COMSOL Multiphysics® User's Guide, Version 3.3 [Computer software manual].

Davis, T. A. (2004a, June). Algorithm 832: Umfpack - an unsymmetric-pattern multifrontal method. *ACM Transactions on Mathematical Software*, *30*(2), 196-199.

Davis, T. A. (2004b, June). A column pre-ordering strategy for the unsymmetric-pattern multifrontal method. *ACM Transactions on Mathematical Software*, *30*(2), 165-195.

Davis, T. A., & Duff, I. S. (1997, January). An unsymmetric-pattern multifrontal method for sparse lu factorization. *SIAM Journal of Matrix Analysis and Applications*, *18*(1), 140-158.

Farquharson, C. G., & Miensopust, M. P. (2011). Three-dimensional finite-element modelling of magnetotelluric data with a divergence correction. *Journal of Applied Geophysics*, *75*, 699-710.

Franke, A., Börner, R., & Spitzer, K. (2007). Adaptive unstructured grid finite element simulation of two-dimensional magnetotelluric fields for arbitrary surface and seafloor topography. *Geophysical Journal International*, *171*(1), 71–86.

Haber, E., Ascher, U., Aruliah, D., & Oldenburg, D. (2000). Fast simulation of 3d electromagnetic problems using potentials. *Journal of Computational Physics*, *163*(1), 150–171.

Hiptmair, R. (1998). Multigrid method for Maxwell's equations. *SIAM Journal on Numerical Analysis*, *36*(1), 204–225.

Jin, J. (1993). *The Finite Element Method in Electromagnetics*. John Wiley & Sons, Inc.

Johnson, C. (1987). *Numerical Solution of Partial Differential Equations by the Finite Element Method*. Studentlitteratur, Lund, Sweden.

Key, K., & Weiss, C. (2006). Adaptive fiinite-element modeling using unstructured grids: The 2d magnetotelluric example. *Geophysics*, *71*, G291-G299.

Kütter, S. (2009). *Three-dimensional finite element simulation of magnetotelluric fields incorporating digital elevation models*. Unpublished master's thesis, TU Bergakademie Freiberg.

Mackie, R., Madden, T., & Wannamaker, P. (1993). Three-dimensional magnetotelluric modeling using finite-difference equations - theory and comparison to integral equation solutions. *Geophysics*, *58*, 215-226.

Mackie, R., Smith, J., & Madden, T. (1994). Three-dimensional electromagnetic modeling using finite-difference equations: the magnetotelluric example. *Radio Science*, *29*, 923-935.

Mitsuhata, Y., & Uchida, T. (2004). 3D magnetotelluric modelling using the T-Ω finite-element method. *Geophysics*, *69*(1), 108-119.

Mogi, T. (1996). Three-dimensional electromagnetic modeling of magnetotelluric data using finite element method. *Journal of Applied Geophysics*, *35*, 185-189.

Monk, P. (2003). *Finite Element Methods for Maxwell's Equations*. Oxford University Press.

Nam, M., Kim, H., Song, Y., Lee, T., Son, J.-S., & Suh, J. (2007). 3d magnetotelluric modelling including surface topography. *Geophysical Prospecting*, *55*, 277-287.

Newman, G. A., & Alumbaugh, D. L. (1996). *Three-dimensional electromagnetic modeling and inversion of massively parallel computers* (Tech. Rep.). Sandia National Laboratories.

Saad, Y., & Schultz, M. H. (1986). Gmres: A generalized minimal residual algorithm for solving nonsymmetric linear systems. *SIAM Journal on Scientific and Statistical Computing*, *7*, 856-869.

Schenk, O., & Gärtner, K. (2004). Solving unsymmetric sparse systems of linear equations with pardiso. *Journal of Future Generation Computer Systems*, *20*(3), 475-487.

Schenk, O., & Gärtner, K. (2006). On fast factorization pivoting methods for symmetric indefinite systems. *Elec. Trans. Numer. Anal.*, *23*, 158-179.

Schwarzbach, C. (2009). *Stability of finite element solutions to maxwell's equations in frequency domain*. Unpublished doctoral dissertation, TU Bergakademie Freiberg.

Siripunvaraporn, W., Egbert, G., & Lenbury, Y. (2002). Numerical accuracy of magnetotelluric modeling: a comparison of finite difference approximations. *Earth, Planets and Space*, *54*, 721-725.

Strang, G., & Fix, G. J. (1973). *An analysis of the finite element method*. Prentice-Hall, Inglewood Cliffs.

Tikhonov, A. N. (1950). On the determination of electric characteristics of deep layers of the earth's crust. *Dokl. Akad. Nauk. SSSR*, *73*, 295-297.

Verfürth, R. (1996). *A review of a posteriori error estimation and adaptive mesh-refinement techniques*. Wiley-Teubner, Chichester (Engl.), Stuttgart.

Wait, J. R. (1953). Propagation of Radio Waves over a Stratified Ground. *Geophysics*, *20*, 416-422.

Wannamaker, P., Hohmann, G., & SanFilipo, W. (1984). Electromagnetic modeling of three-dimensional bodies in layered earths using integral equations. *Geophysics*, *49*(1), 60–74.

Wannamaker, P. E. (1989). PW2DIS Finite Element Program for Solution of Magnetotelluric Responses and Sensitivities of two-dimensional Earth Resistivity Structures, User Documentation [Computer software manual].

Acknowledgements

First of all, I would like to thank Prof. Dr. Klaus Spitzer for his supervision, perpetual support, and patience.
I am also thankful to Prof. Dr. Phil Wannamaker for the fruitful communication we had on workshops and via email.
Many thanks go to Prof. Dr. Oliver Ernst and Martin Afanasjew for inspiring discussions.
I am grateful to my friends and colleagues Wenke Wilhelms and Christoph Schwarzbach for always encouraging me when it was necessary.
My deep gratitude goes to my dad, my husband Ralph, and my daughter Clara for their support.